Antenna Array Systems: Propagation and Performance

Richard B. Ertel

Dissertation submitted to the Faculty of the
Virginia Polytechnic Institute and State University
in partial fulfillment of the requirements for the degree of

Doctor of Philosophy
in
Electrical Engineering

Jeffrey H. Reed, Chair
Brian D. Woerner
William H. Tranter
Theodore S. Rappaport
Chistopher A. Beattie

July, 1999
Blacksburg, Virginia

Keywords: Antenna Arrays, Propagation Modeling, Diversity Systems, Adaptive Beamforming

Antenna Array Systems: Propagation and Performance

Richard B. Ertel

(ABSTRACT)

Due to the enormous performance gains associated with the use of antenna arrays in wireless networks, it is inevitable that these technologies will become an integral part of future systems. This report focuses on signal propagation modeling for antenna array systems and on its relationship to the performance of these systems. Accurate simulation and analytical models are prerequisite to the characterization of antenna array system performance. Finally, an understanding of the performance of these systems in various environments is needed for effective overall network design.

This report begins with an overview of the fundamentals of antenna array systems. A survey of vector channel models is presented. Angle of arrival and time of arrival statistics for the circular and elliptical (Liberti's Model) models are derived. A generalized optimum output SINR analysis is derived for space-time processing structures in frequency selective fading channels. The hardware and software of the MPRG Antenna Array Testbed (MAAT) is described. A literature review of previous antenna array propagation measurements is given. Antenna array measurement results obtained with the MAAT are used to compare the properties of the received signal vector in the various environmental conditions. The influence of channel parameters on the ability of antenna arrays to separate the signals of two users on the reverse link is studied using simulation. Finally, forward link beamforming techniques are reviewed.

Funded by the Bradley Fellowship Endowment, LG Information and Communications (LGIC), Texas Instruments (TI), Sprint PCS, Defense Advanced Research Projects Agency (DARPA).

Acknowledgements

The completion of this research project would have been impossible without the support of many people. First of all I would like to express my sincere appreciation to my advisor, Professor Jeffrey H. Reed for his support and guidance throughout the duration of this work. It has been a pleasure working under his supervision and I am looking forward to maintaining a continued friendship with him.

Also, I would like to acknowledge the support of several students at the MPRG and CWT. Tom Biedka in particular has been especially helpful. He has provided valuable feedback on most of the material presented in this work. Raqibul Mostafa, Zhong Hu, and Carl Dietrich all have provided much needed assistance in the collection of antenna array measurements. I would also like to thank them for insights that they provided during various technical discussions. Paul Petrus provided input on vector channel models in the early stages of this work. Don Breslin designed the RF front end for the antenna array system that was needed for data collection. I would like to thank Kim Phillips for her help in writing the DSP code used in the MAAT system. Also, I would like to thank all of the MPRG students for making my time at Virginia Tech a pleasant experience. Finally, I would like to thank the MPRG staff. Hilda Reynolds in particular has been especially helpful during the past few years.

I am grateful for the financial support that I have received. Special thanks goes to the late Marion Bradley Via whose generous donation has blessed me through the Harry Lynde Bradley Fellowship. It is a great honor to receive this fellowship. I am also grateful for the support provided by LGIC, Texas Instruments (TI), Defense Advanced Research Projects Agency (DARPA), and Sprint PCS, and for the advice provided by Radix Technologies. Also I would like to express my appreciation to the MPRG affiliates whose contributions have provided valuable support to all of the MPRG students.

Finally, I would like to express my appreciation to family and close friends. Their love and support has helped me through difficult times and the challenges of completing this work.

Contents

List of Figures

List of Tables

Chapter 1

Overview and Contributions

1.1 Introduction

The use of antenna array systems is thought to be one of the last remaining frontiers that promises to provide a substantial increase in the capacity of wireless systems. Antenna arrays offer the ability to improve signal reception, signal detection, and parameter estimation [1]. Of these, the most important to the wireless communications industry is improving signal reception. This is accomplished by providing a large antenna gain to desired signals while simultaneously reducing the antenna gain to interfering signals. This fundamental capability of antenna arrays leads to increased system capacity, extended mobile battery life, increased range, improved coverage, and improved signal quality, making the use of antenna arrays highly attractive to the wireless communication system designer.

Until recently the cost of employing antenna array systems has inhibited their widespread use. However, with today's availability of high performance digital signal processing components and the increased demands on the available spectrum, the wireless industry is showing a surge of interest in developing and utilizing antenna array technologies. Today, commercial antenna array systems are available from a number of vendors and several are already functioning in existing cellular networks. With the substantial benefits that the antenna array systems offer, it is inevitable that they will become an integral part of future wireless networks.

Integration of antenna arrays into today's wireless networks will require an evaluation of the performance of antenna array systems which fundamentally impacts network design parameters such as cell size, placement of base stations, antenna heights, etc. The performance of antenna arrays is highly dependent upon the propagation environment. Therefore, prior to an evaluation of antenna array performance there must be an understanding of the propagation environment. Fig. 1.1 highlights the relationship which exists between network design, antenna array performance, and the propagation environment. The focus of this report is on the propagation environment as sensed by an antenna array and its relationship to antenna array system performance.

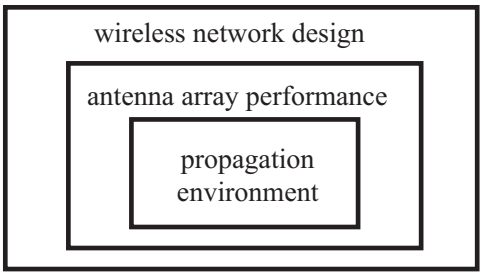

Figure 1.1: Relationships among wireless network design, antenna array performance, and propagation environment.

1.2 Report Outline

This report is organized as follows. In Chapter 2 fundamentals of antenna array systems are covered. General models are given for propagating plane waves for both wideband and narrowband signals. These models are then extended to the more general multiple user multipath propagation environment. The concepts of adaptive beamforming and spatial diversity are described. The optimum beamforming solutions of several performance criteria are derived. The chapter concludes with a description and some analysis showing the benefits of utilizing antenna arrays in wireless networks.

Chapter 3 provides a brief description of multipath propagation mechanisms and a survey of several proposed vector channel models. The various vector channel models are classified into two classes, geometrically based and statistically based depending upon whether or not the location of scattering objects is specified by the model.

Details of two of these models, the circular and elliptical (Liberti's Model) models are presented in Chapter 4. Here the joint TOA-AOA, marginal TOA, and marginal AOA probability density functions are derived. Also derived is the Doppler spectrum which results from the proposed scattering models when path-loss is applied to the multipath components.

In Chapter 5 a generalized optimum output SINR analysis is used to evaluate the performance of various space-time processing structures under different channel conditions.

The MPRG Antenna Array Testbed (MAAT) is described in Chapter 6. Hardware details and data collection limitations of the present system are given. Also presented is the antenna array calibration procedure which is used to compensate for hardware amplitude and phase variations of the different branches of the array.

In Chapter 7 a survey of antenna array propagation measurements is presented. The propagation measurement results include measurements of the envelope correlations observed at two antenna elements, changes in spatial signature vectors, angle spread, and joint TOA-AOA channel properties.

Antenna array measurement results obtained with the MAAT are presented in Chapter 8. Data were collected in four different channel environments. Various characteristics of the received signal vectors are compared.

In Chapter 9, the ability of an antenna array to separate two received signals is considered. Simulations demonstrate the ability of an antenna array system to improve signal quality even if an interferer has multipath with identical AOA to that of the desired user. Also, it is shown that two user's with identical line-of-sight AOA can be adequately separated provided that the angular spreading of the users' multipath is sufficiently high. Finally, the impact of angle spread and number of path components is explored through simulation.

Forward link beamforming techniques are reviewed in Chapter 10. Simulation results show the increase in received signal power at the mobile unit that is possible using forward link beamforming.

Finally, Chapter 11 concludes this report with summary of work completed and a list of suggested future research topics.

1.3 Contributions

Several contributions regarding antenna arrays propagation models and their relationship to system performance have been made in this dissertation. Portions of these contributions have been published or have been submitted for publication. Below is a list of contributions to date and corresponding publications.

- Original contributions related to antenna array propagation modeling.

    1. First is the completion of a comprehensive overview of vector channel models. This material was written as an invited paper to *IEEE Personal Communications Magazine* [2]. Portions of this material were also presented at the *Stanford Smart Antennas Workshop* [3].
    2. Next the Doppler spectrum was derived for the circular scattering model and Liberti's elliptical scattering model when path-loss is applied to the multipath components. The Doppler spectrum results derived for Liberti's model are published in [4].
    3. The derivations in Chapter 4 of the joint TOA-AOA, marginal AOA, and marginal TOA probability density functions for the circular scattering region model are original contributions of this work. These results and the corresponding results for Liberti's model have been accepted for publication in [5].
    4. In Chapter 4 an efficient algorithm is proposed for placing scatterers inside an ellipse assuming a uniform distribution. This algorithm is useful for providing scatterer locations for Liberti's elliptical channel model.
    5. In Chapter 7 several different metrics for determining the difference of two spatial signature vectors are proposed. We derive the relationships among the various spatial signature vector difference metrics and show that they may all be expressed in terms of the normalized cross-correlation between the two vectors.
    6. Finally, the analysis of the antenna array measurements in Chapter 8 which reveals a relationship between envelope correlations, rate of change of spatial signature vectors, and eigenvalue distributions is a fundamental contribution of this work.

- Contributions involving the relationship between propagation and performance. These results still need to be submitted for publication to either a journal or conference as appropriate.

    1. A key analytical contribution is the generalized optimum output SINR closed formed expression derived in Chapter 5 for various space-time processing structure in frequency selective fading channels.
    2. Simulation results demonstrate the ability of an antenna array system to improve signal quality even if an interferer has multipath with identical AOA to that of the desired user.
    3. Simulations show that two user's with identical line-of-sight AOA can be adequately separated provided that the angular spreading of the users' multipath is sufficiently high.
    4. The impact of angle spread and number of path components on the ability to separate the signals of two used is explored through simulation.
    5. Finally, simulations show the increase in the received signal power at the mobile for both the optimum and dominant path forward link beamforming techniques.

- Other contributions involving antenna arrays.

    1. The analysis of the coverage improvement offered by an antenna array over a single element receiver is also an original contribution.
    2. A procedure is described for calibrating the signal splitter used for array calibration based on the complex baseband array outputs [6].
    3. The hardware interface used to collect data from the array and store it on the TI320EVM board as well as all of the supporting software are original contributions of this work.

Chapter 2

Antenna Array Fundamentals

The purpose of this chapter is to present fundamental antenna array concepts. In particular this chapter covers array data signal modeling, multipath propagation, adaptive beamforming, spatial diversity, optimum performance criteria for adaptive combining, and a discussion of the benefits of using antenna arrays in wireless networks. The reader who is well versed in antenna array theory may wish to skip this chapter with the possible exception of Section 2.7.3, which presents an original analysis of the coverage improvement provided by antenna array systems.

2.1 Definition

An antenna array system is composed of a collection of spatially separated antenna elements the outputs of which are combined by a multiple input transceiver as shown in Fig. 2.1. The multiple antenna elements function as a spatial aperture through which spatio-temporal signals are observed. In contrast to single antenna receivers which combine the signals present at their antenna aperture in a fixed manner, the antenna array system has the ability to dynamically adjust the combining mechanism in order to improve system performance. For this reason antenna arrays are often referred to as *smart antennas* which may be thought of as a single antenna whose characteristics may be adjusted automatically as needed.

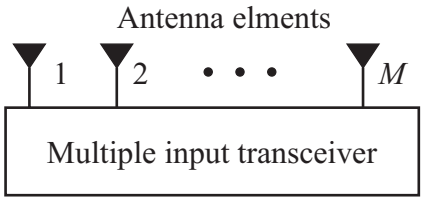

Figure 2.1: Antenna array systems composed of M spatially diverse antenna elements and a multiple input transceiver.

2.2 Sensor Array Modeling

The outputs of the M antenna elements are conveniently described by the received signal vector,

$$\mathbf{x}(t) = \begin{bmatrix} x_1(t) \\ x_2(t) \\ \vdots \\ x_M(t) \end{bmatrix}, \tag{2.1}$$

where $x_i(t)$ denotes the signal observed at the ith antenna. Assuming linearity of the array elements, the received signal vector may be decomposed into a signal vector $\mathbf{s}(t)$ and noise vector $\mathbf{n}(t)$ as,

$$\mathbf{x}(t) = \mathbf{s}(t) + \mathbf{n}(t). \tag{2.2}$$

In general, the signal vector $\mathbf{s}(t)$ may be the superposition of several signal vectors which correspond to various incident plane waves in the environment.

The additive noise vector $\mathbf{n}(t)$ accounts for both interference and noise present at the sensor outputs. Depending upon ones perspective the various signals that are present in the environment may be included in either $\mathbf{s}(t)$ or $\mathbf{n}(t)$. This is especially true for directional interference signals.

In this work the following assumptions will be made regarding the signals impinging upon the array: (1) signals are composed of a finite number of plane waves, (2) the medium surrounding the antenna array is homogeneous, (3) signal attenuation across the extent of the array is negligible, and (4) signals arriving at the array originate from sources in the far-field of the array. For a discussion concerning antenna array systems in the more general case when these assumptions are not imposed see Chapter 2 of [1].

2.2.1 Propagating Plane Waves

Space time signals may be expressed as $s(x, y, z, t)$ where x, y, and z are the Cartesian coordinate spatial variables, and t denotes time. Fundamentally, it is Maxwell's equations which govern electromagnetic field propagation. In free space the source-free wave equation for the electric field intensity $\vec{E}$ is

$$\nabla^2 \vec{E} - \frac{1}{c^2} \frac{\partial^2 \vec{E}}{\partial t^2} = 0, \tag{2.3}$$

where c is the speed of light [7]. The monochromatic plane wave solution of the wave equation in Cartesian coordinates takes on the form,

$$s(x, y, z, t) = A \exp[j(\omega t - k_x x - k_y y - k_z z)], \tag{2.4}$$

where A is a complex constant, and k_x, k_y, k_z and ω are real constants with $\omega \geq 0$. Additionally, these constants must satisfy the constraint

$$k_x^2 + k_y^2 + k_z^2 = \frac{\omega^2}{c^2}. \tag{2.5}$$

For notational convenience we will define the position vector $\vec{x} = (x, y, z)$. Similarly, let $\vec{k} = (k_x, k_y, k_z)$ denote the wavenumber vector which points in the direction the plane wave is propagating. Using this simplified notation we may express the propagating plane wave as

$$s(\vec{x}, t) = A \exp[j(\omega t - \vec{x} \cdot \vec{k})]. \tag{2.6}$$

Finally, if we define $\vec{\alpha} = \vec{k}/\omega$ then we may express the spatiotemporal signal $s(\vec{x}, t)$ as

$$s(\vec{x}, t) = s(t - \vec{\alpha} \cdot \vec{x}) = A \exp[j\omega(t - \vec{\alpha} \cdot \vec{x})], \tag{2.7}$$

where $s(u) = A \exp[j\omega u]$ [1]. The vector $\vec{\alpha}$ is referred to as the *slowness vector* the magnitude of which is given by $|\vec{\alpha}| = \frac{1}{c}$.

More generally, any Fourier transformable space time propagating plane wave solution of the wave equation may be expressed as

$$s(\vec{x}, t) = s(t - \vec{\alpha} \cdot \vec{x}) = \frac{1}{2\pi} \int_{-\infty}^{\infty} S(\omega) \exp[j\omega(t - \vec{\alpha} \cdot \vec{x})] d\omega, \tag{2.8}$$

where $S(\omega)$ is the Fourier transform of $s(t)$ [1].

2.2.2 Wideband Signal Model

Letting $\vec{x}_1, \vec{x}_2, \cdots, \vec{x}_M$ denote the position vectors of the M sensors in the array, then from (2.7) or (2.8) the received signal vector will be given by,

$$\mathbf{s}(t) = \begin{bmatrix} s(\vec{x}_1, t) \\ s(\vec{x}_2, t) \\ \vdots \\ s(\vec{x}_M, t) \end{bmatrix} = \begin{bmatrix} s(t - \vec{\alpha} \cdot \vec{x}_1) \\ s(t - \vec{\alpha} \cdot \vec{x}_2) \\ \vdots \\ s(t - \vec{\alpha} \cdot \vec{x}_M) \end{bmatrix} = \begin{bmatrix} s(t - \tau_1) \\ s(t - \tau_2) \\ \vdots \\ s(t - \tau_M) \end{bmatrix}, \tag{2.9}$$

where $\tau_i = \vec{\alpha} \cdot \vec{x}_i$ are the delay times due to the finite propagation speed of the signal. As should be expected, spatially sampling a propagating plane wave in a lossless homogeneous medium results in delayed versions of the original signal.

Often it is useful to relate the signal delays to the azimuth and elevation angles of arrival denoted as θ and ϕ, respectively (See Fig. 2.2). Since $|\vec{\alpha}| = \frac{1}{c}$ then $\vec{u} = c\vec{\alpha}$ is a unit vector in the direction of signal propagation. The delay at each sensor may then be expressed as $\tau_i = \frac{\vec{u} \cdot \vec{x}_i}{c}$ where $\vec{u}$ is given by $\vec{u} = (\sin\phi\cos\theta, \sin\phi\sin\theta, \cos\phi)$ [8]. Therefore, the signal delay observed at the ith sensor may be written as

$$\tau_i = \frac{\vec{u} \cdot \vec{x}_i}{c} = \frac{1}{c}(x_i \sin\phi\cos\theta + y_i \sin\phi\sin\theta + z_i \cos\phi). \tag{2.10}$$

Following the discussion given in Chapter 3 of [9], when $s(\vec{x}, t)$ is an analytic signal corresponding to a real sinusoid then a delay is equivalent to a phase shift of $-\omega\tau$. In this case, from (2.9)

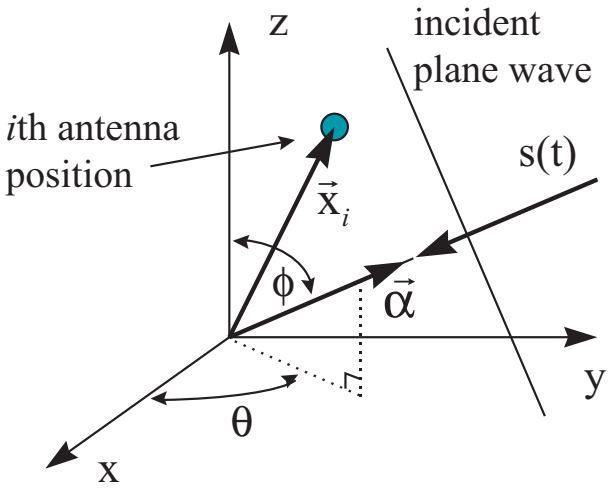

Figure 2.2: Propagation delay associated with an incident plane wave in a homogeneous medium.

we may write,

$$\mathbf{s}(t) = \begin{bmatrix} \exp[j\psi_1(\vec{\alpha},\omega)] \\ \exp[j\psi_2(\vec{\alpha},\omega)] \\ \vdots \\ \exp[j\psi_M(\vec{\alpha},\omega)] \end{bmatrix} s(t), \tag{2.11}$$

where $\psi_i(\vec{\alpha},\omega) = -\omega\tau_i$. So far we have assumed that each of the sensors in the array have identical responses. In the more general case each sensor may have different directional and frequency dependent amplitude and phase responses [9]. Letting $g_i(\vec{\alpha},\omega)$ and $\zeta_i(\vec{\alpha},\omega)$ denote the amplitude and phase responses of the ith sensor, respectively, the received signal vector may be expressed,

$$\mathbf{s}(t) = \begin{bmatrix} g_1(\vec{\alpha},\omega)\exp[j(\psi_1(\vec{\alpha},\omega)+\zeta_1(\vec{\alpha},\omega))] \\ g_2(\vec{\alpha},\omega)\exp[j(\psi_2(\vec{\alpha},\omega)+\zeta_2(\vec{\alpha},\omega))] \\ \vdots \\ g_M(\vec{\alpha},\omega)\exp[j(\psi_M(\vec{\alpha},\omega)+\zeta_M(\vec{\alpha},\omega))] \end{bmatrix} s(t) = \mathbf{a}(\vec{\alpha},\omega)s(t). \tag{2.12}$$

The vector $\mathbf{a}(\vec{\alpha},\omega)$ which defines the array response to a sinusoidal propagating plane wave with frequency ω arriving from the direction of $\vec{\alpha}$ is referred to as the *array response vector*. The set of array response vectors over all signal propagation directions and frequencies is known as the *array manifold*.

For the general Fourier transformable space time propagating plane wave $s(\vec{x},t)$, signal delays cause frequency dependent phase shifts. In this case we may write the Fourier transform of the

received signal vector as

$$\mathbf{S}(\omega) = \begin{bmatrix} g_1(\vec{\alpha},\omega)\exp[j(\psi_1(\vec{\alpha},\omega)+\zeta_1(\vec{\alpha},\omega))] \\ g_2(\vec{\alpha},\omega)\exp[j(\psi_2(\vec{\alpha},\omega)+\zeta_2(\vec{\alpha},\omega))] \\ \vdots \\ g_M(\vec{\alpha},\omega)\exp[j(\psi_M(\vec{\alpha},\omega)+\zeta_M(\vec{\alpha},\omega))] \end{bmatrix} S(\omega) = \mathbf{a}(\vec{\alpha},\omega)S(\omega). \tag{2.13}$$

In the time domain, the signal present at the ith sensor may be expressed,

$$s_i(t) = \frac{1}{2\pi}\int_{-\infty}^{\infty} g_i(\vec{\alpha},\omega)S(\omega)\exp[j(\omega t+\psi_i(\vec{\alpha},\omega)+\zeta_i(\vec{\alpha},\omega)]d\omega, \tag{2.14}$$

which cannot be expressed as a scalar times the original signal as was the case for sinusoidal signals.

2.2.3 Narrowband Model

When the propagating signal is sufficiently narrowband and the maximum delay is sufficiently small then it is possible to approximate $\mathbf{a}(\vec{\alpha},\omega) \approx \mathbf{a}(\vec{\alpha},\omega_c)$ over the bandwidth of the signal, where ω_c is the carrier frequency in radians per second. Suppose that $s(t)$ has a nonzero power spectral density only in the range $[\omega_c - \frac{B}{2}, \omega_c + \frac{B}{2}]$. Then considering only the positive frequency components, (2.8) may be written

$$s(\vec{x},t) = s(t-\vec{\alpha}\cdot\vec{x}) = \frac{1}{2\pi}\int_{\omega_c-\frac{B}{2}}^{\omega_c+\frac{B}{2}} S(\omega)\exp[j\omega(t-\vec{\alpha}\cdot\vec{x})]d\omega. \tag{2.15}$$

Now if the $(\omega_c - \frac{B}{2})\tau \approx (\omega_c + \frac{B}{2})\tau$ then the corresponding phase term may be pulled outside of the integral resulting in the narrowband signal model,

$$s(t-\tau) \approx s(t)e^{j\omega_c\tau}. \tag{2.16}$$

In this case the received signal vector may be written as

$$\mathbf{s}(t) = \mathbf{a}(\vec{\alpha},\omega_c)s(t) = \mathbf{a}(\vec{\alpha})s(t), \tag{2.17}$$

which is identical to the wideband signal model for sinusoidal signals. Therefore, although $s(t)$ is not sinusoidal, it is sufficiently narrowband that the spatial response of the array is approximately equal to the response of a sinusoid.

The narrowband model is valid when $B\tau = B\vec{\alpha}\cdot\vec{x} \approx 0$. Suppose that $|\vec{x}| < k\lambda_c = k(2\pi c/\omega_c)$ where λ_c is the carrier wavelength given by $\lambda_c = 2\pi/\omega_c$. In this case $B\tau$ is bounded by

$$B\tau < \frac{Bk\lambda_c}{c} = 2\pi k\frac{B}{\omega_c}. \tag{2.18}$$

This final expression suggests that the narrowband signal model is valid when the fractional signal bandwidth defined as $\frac{B}{\omega_c}$ is sufficiently small. Also it indicates that its validity is determined by the element spacing. For further details regarding the validity of the narrowband model see Chapter 3 of [9].

2.3 Multipath Propagation Environment

The models derived in the previous section describe the received signal vector of a single incident plane wave. In this section, the more general case involving multiple users in a multipath environment is considered. Let N denote the total number of users with signals impinging upon the array, and let $\mathbf{x}_k(t)$ denote the $M \times 1$ received signal vector corresponding to the kth user. When the incoming plane waves lie in the xy plane then the array response vectors may be expressed in terms of the azimuth angle of arrival only. This is a reasonable approximation for many cellular systems where the mobiles are far away from the antenna array. In this case the array response vector may be expressed as a function of θ as $\mathbf{a}(\theta)$. In a LOS environment, $\mathbf{x}_k(t)$ may be expressed

$$\mathbf{x}_k(t) = \alpha_k \mathbf{a}(\theta_k) s_k(t), \tag{2.19}$$

where α_k is the scalar complex path amplitude, $\mathbf{a}(\theta_k)$ is the array response vector in the direction of θ_k towards the kth user, and $s_k(t)$ is the complex baseband signal impinging upon the array.

The total received signal vector at the array is given by

$$\mathbf{x}(t) = \sum_{k=1}^{N} \mathbf{x}_k(t) + \eta(t), \tag{2.20}$$

where $\eta(t)$ accounts for receiver noise as well as background channel noise and is typically modeled as both spatially and temporarily white Gaussian noise. It is convenient to define the matrix

$$\mathbf{A} = \left[\begin{array}{cccc} \mathbf{a}(\theta_1) & \mathbf{a}(\theta_2) & \cdots & \mathbf{a}(\theta_N) \end{array} \right] \tag{2.21}$$

and the signal vector

$$\bar{\mathbf{s}}(t) = \left[\begin{array}{c} s_1(t) \\ s_2(t) \\ \vdots \\ s_N(t) \end{array} \right]. \tag{2.22}$$

The received signal vector may then be expressed as

$$\mathbf{x}(t) = \mathbf{A}\bar{\mathbf{s}}(t) + \eta(t). \tag{2.23}$$

When the received signal from each user is the summation of several multipath signals, the received signal vector for the kth user may be expressed

$$\mathbf{x}_k(t) = \sum_{l=1}^{L_k} \alpha_{k,l} \mathbf{a}(\theta_{k,l}) s_k(t - \tau_{k,l}), \tag{2.24}$$

where L_k is the number of multipath components of the kth user, $\tau_{k,l}$ is the excess path delay, and the remaining variables are as defined above.

The expression given in (2.24) is general in the sense that it accounts for frequency selective fading. Depending upon whether or not the multipath channel experiences frequency selective

fading, the impact of the multipath on the performance of the antenna array will vary. When the delay differences between the multipath components are sufficiently small relative to the reciprocal of the signal bandwidth then the channel experiences flat fading. For a flat fading environment, (2.24) reduces to

$$\mathbf{x}_k(t) = \sum_{l=1}^{L_k} \alpha_{k,l} e^{-j\omega_c \tau_{k,l}} \mathbf{a}(\theta_{k,l}) s_k(t), \tag{2.25}$$

where ω_c is the carrier frequency in radians per second. The complex baseband signal may be factored out of the expression to give,

$$\mathbf{x}_k(t) = \left[\sum_{l=1}^{L_k} \alpha_{k,l} e^{-j\omega_c \tau_{k,l}} \mathbf{a}(\theta_{k,l}) \right] s_k(t) = \mathbf{v}_k s_k(t), \tag{2.26}$$

where

$$\mathbf{v}_k = \sum_{l=1}^{L_k} \alpha_{k,l} e^{-j\omega_c \tau_{k,l}} \mathbf{a}(\theta_{k,l}) \tag{2.27}$$

is the *spatial signature vector* of user k.

In this case the total received signal vector may be expressed in the compact form

$$\mathbf{x}(t) = \mathbf{V}\bar{\mathbf{s}}(t) + \eta(t), \tag{2.28}$$

where

$$\mathbf{V} = \begin{bmatrix} \mathbf{v}_1 & \mathbf{v}_2 & \cdots & \mathbf{v}_N \end{bmatrix} \tag{2.29}$$

is the matrix whose ith column consists of the spatial signature vector of the ith user and $\bar{\mathbf{s}}(t)$ is given by (2.22).

2.4 Adaptive Beamforming

The objective of the receiver is to use the information present at each antenna element to improve system performance. For narrowband signals in flat fading channels, the narrowband adaptive beamformer shown in Fig. 2.3 is typically employed. The output of the narrowband adaptive beamformer is a weighted linear combination of the received signal vector components which may be expressed,

$$y(t) = \mathbf{w}^H(t)\mathbf{x}(t), \tag{2.30}$$

where

$$\mathbf{w}(t) = \begin{bmatrix} w_1(t) \\ w_2(t) \\ \vdots \\ w_M(t) \end{bmatrix} \tag{2.31}$$

is known as the beamforming *weight vector*.

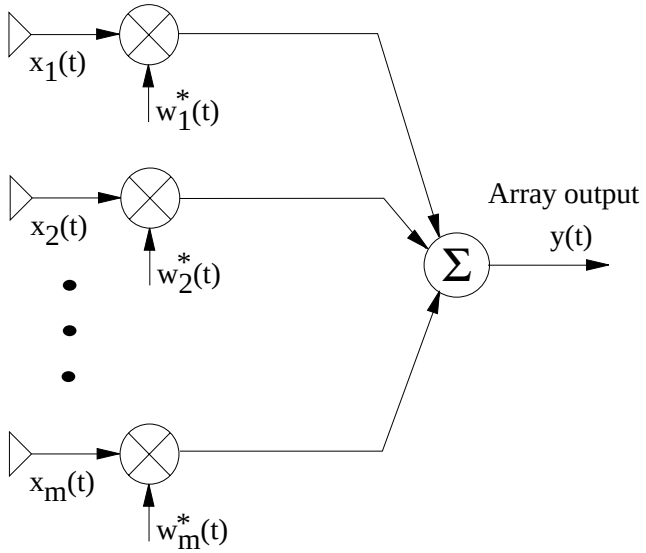

Figure 2.3: Structure of a narrowband adaptive beamformer.

The best way to demonstrate the ability of an adaptive beamformer to improve system performance is with an example. Consider a two element antenna array with $\lambda/2$ spacing between the elements. Suppose that the desired user is array broadside[1] at zero degrees and that an interferer is located at 45 degrees from broadside. Assuming omni-directional elements, the corresponding complex matrix A defined above in (2.21) is given by

$$\mathbf{A} = \left[\begin{array}{cc} \mathbf{a}(0) & \mathbf{a}(\pi/4) \end{array} \right] = \left[\begin{array}{cc} 1 & 1.0000 \\ 1 & -0.6057 - 0.7957i \end{array} \right] \tag{2.32}$$

where the location of the first element is selected as the zero phase reference.

The beamformer seeks to increase the antenna gain in the direction towards the desired user while simultaneously reducing the antenna gain in the direction of the interferer. The ideal weight vector $\mathbf{w}$ will satisfy $\mathbf{w}^H\mathbf{a}(0) = 1$ and $\mathbf{w}^H\mathbf{a}(\pi/4) = 0$. Expressing this requirement in matrix form gives

$$\mathbf{w}^H \left[\begin{array}{cc} 1 & 1.0000 \\ 1 & -0.6057 - 0.7957i \end{array} \right] = \left[\begin{array}{cc} 1 & 0 \end{array} \right], \tag{2.33}$$

which has a unique solution,

$$\mathbf{w} = \left[\begin{array}{c} 0.5000 - 0.2478i \\ 0.5000 + 0.2478i \end{array} \right]. \tag{2.34}$$

The resulting beampattern is shown in Fig. 2.4. This example demonstrates the ability of a narrowband antenna array to adapt its antenna gain to enhance signals of interest while reducing or completely cancelling signals which are not of interest.

[1]Broadside is defined as the direction perpendicular to a line which joins the elements.

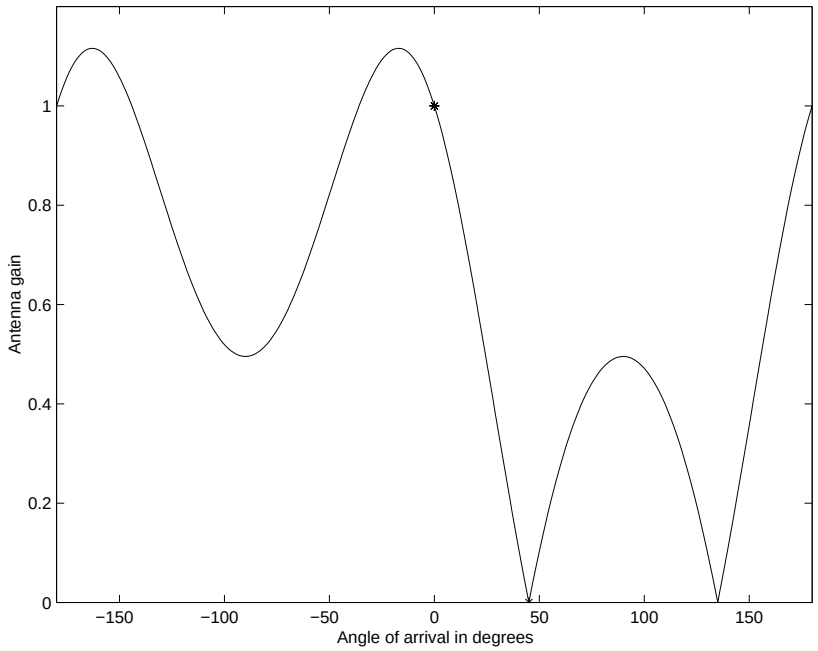

Figure 2.4: Antenna gain versus angle of arrival. The desired user is at 0 degrees and the interferer is located at 45 degrees.

For wideband signals, the wideband adaptive beamformer shown in Fig. 2.5 is more appropriate. Wideband antenna arrays are also referred to as joint space-time processors. Following the discussion in [8] the two dimensional array structure can be molded into a standard linear array model by forming the length MB vector

$$\acute{\mathbf{x}}(t) = \begin{bmatrix} \mathbf{x}(t) \\ \mathbf{x}(t - t_c) \\ \vdots \\ \mathbf{x}(t - (B-1)t_c) \end{bmatrix},$$

and then forming the length MB weight vector

$$\acute{\mathbf{w}}(t) = \begin{bmatrix} \mathbf{w}_0(t) \\ \mathbf{w}_1(t) \\ \vdots \\ \mathbf{w}_B - 1(t) \end{bmatrix},$$

where

$$\mathbf{w}_i(t) = [\mathbf{w}_{1,i}(t), \mathbf{w}_{2,i}(t), \cdots, \mathbf{w}_{M,i}(t)]^T. \tag{2.35}$$

and B is the number of taps in the wideband array. Using these definitions, the array output maybe expressed as

$$y(t) = \acute{\mathbf{w}}^H(t)\acute{\mathbf{x}}(t),$$

which is identical in form to the array output of the narrowband antenna array receiver described above.

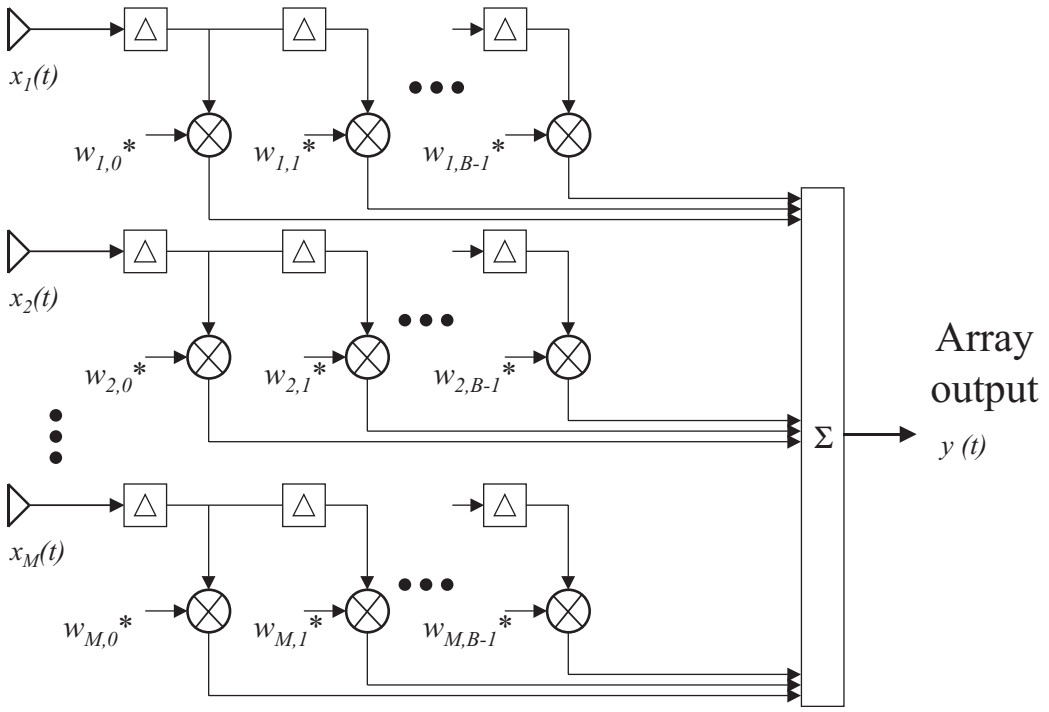

Figure 2.5: Wideband adaptive beamformer receiver structure.

2.5 Spatial Diversity

Unlike beamforming systems which attempt to steer beams in the direction of desired signals and nulls in the directions of interference signals, spatial diversity systems focus primarily on mitigating multipath fading. The multipath signals which are present in the environment have random phases, and hence the various signal components may combine both coherently or destructively. When the signal components combine destructively the received signal power made be extremely low, and it is said that the signal is experiencing a *fade*.

When the receiver is equipped with an antenna array, it is possible that the signal power fades at different times on the various antenna elements. If this is the case then there is nearly always good signal reception on at least one of the antenna elements, and therefore the combined signal at the output of the multiple input transceiver will generally have good SNR.

The degree by which the multiple input transceiver is able to combat the multipath fading is dependent upon the cross-correlation of the fading envelopes observed at the various elements of the antenna array as well as the mean signal powers which are present. In general the smaller the cross-correlation and the more equal the mean signal powers, the higher is the diversity gain. Both of these results are intuitive. When the cross-correlation between the fading envelopes is low then the likelihood that signals will fade at the same instant is low and therefore at least one of the antenna elements is likely to have good reception. Also, if one considers an extreme case when one branch has a large mean power level and a second branch has a small mean power level, as one might expect the variation in the signal power of the one with the larger

power will typically dominate the instantaneous output power. Therefore, it is almost as if only one branch were available. Hence, when the ratio of mean signal power levels is large there is little diversity gain.

The distinction between adaptive beamforming and spatial diversity systems is a subtle one and in some instances they are in fact identical. In general adaptive beamforming is employed for interference rejection whereas diversity systems are primarily thought of as a method of combating multipath fading. However, regardless of whether the system employs an adaptive beamforming approach or spatial diversity, typically interference is rejected and multipath fading is mitigated. Furthermore, when one considers the optimum SINR solution of either system the result is identical.

There are several different algorithms that are used to implement spatial diversity. Among the most common are selection diversity, equal gain combining, maximum ratio combining, and optimum combining [10]. A brief description of each of these combining schemes is given below. For further details regarding diversity combining techniques see [10–14].

2.5.1 Selection and Switched Diversity

In a *selection diversity* system the receiver selects the antenna output of only a single antenna element at any given instant of time. Ideally, the receiver would select the branch with the largest instantaneous SNR. However, this selection requires that the receiver has knowledge of the SNR at each antenna at each instant of time. To avoid the system complexity associated with estimating each branch's SNR, most practical systems monitor only the currently selected branch's SNR and then switch branches only when the SNR goes below some threshold. This technique is referred to as switched diversity.

2.5.2 Maximum Ratio Combining

When the received signal vector contains the desired signal with additive white noise, then the the maximum SNR is achieved using *maximum ratio combining* which weights the co-phased desired signal on each antenna element by the individual branch SNR and sums together the resulting signals [10]. Implementing maximum ratio combining may be difficult due to the need to estimate the instantaneous SNR at each branch of the receiver. The use of equal gain combining described next overcomes this difficulty.

2.5.3 Equal Gain Combining

Equal gain combining is a diversity technique in which the signals present at each antenna element are co-phased and then added together. Not weighting the signals by the corresponding SNR eliminates the need to estimate the SNR at each branch. The performance lost using equal gain combining when compared to maximum ratio combining is approximately 1 dB [13].

2.5.4 Optimum Combining

Optimum combining refers to the diversity combining method which yields the maximum output SINR. This solution is identical to maximum ratio combining only when the noise and interference is white. However, in the presence of correlated interference, the optimum combiner will seek to maximize SNR and reduce interference. The performance gained by using optimum combining as compared to maximum ratio combining is highly dependent upon the properties of the signals. The derivation of the optimum combining vector or weight vector is covered in the next section. Finally, it is worth noting that optimum combining is identical to optimum beamforming.

2.6 Optimum Performance Criteria

The first step in attempting to find an optimum solution to a problem is to define the performance criteria. In this section the most commonly selected performance criterion are introduced and the corresponding optimum weight vectors are derived. It will be shown that the solutions of the selected performance criteria all result in the maximum output SINR under certain conditions. The derivations given here are a combination of the results found in [8] and [15].

2.6.1 Maximum Signal-to-Interference and Noise Ratio

One performance criteria is to maximize the signal-to-interference and noise ratio (SINR). It will be shown that this method requires knowledge of both the desired signal's and the interference correlation matrix. As stated above, for narrowband antenna arrays the array output may be expressed as[2]

$$y = \mathbf{w}^H \mathbf{x} = \mathbf{w}^H (\mathbf{a}s + \eta) = \mathbf{w}^H \mathbf{a}s + \mathbf{w}^H \eta = y_s + y_\eta, \tag{2.36}$$

where $y_s = \mathbf{w}^H \mathbf{a}s$ is the desired signal output and $y_\eta = \mathbf{w}^H \eta$ is the interference output. The average output SINR is then

$$\text{SINR} = E\left\{\frac{|y_s|^2}{|y_\eta|^2}\right\} = E\left\{\frac{\mathbf{w}^H \mathbf{a}s(\mathbf{a}s)^H \mathbf{w}}{\mathbf{w}^H \eta\eta^H \mathbf{w}}\right\} = \frac{\mathbf{w}^H \mathbf{R}_s \mathbf{w}}{\mathbf{w}^H \mathbf{R}_i \mathbf{w}}, \tag{2.37}$$

where $\mathbf{R}_s = E\left\{\mathbf{a}s(\mathbf{a}s)^H\right\}$ and $R_i = E\left\{\eta\eta^H\right\}$. The optimum weight vector $\mathbf{w}_{opt}$ is the vector which maximizes (2.37).

An elegant solution may be found by first observing that if $\mathbf{w}_0$ maximizes (2.37) then $c\mathbf{w}_0$ is also a solution which will maximize (2.37), where c is a scalar constant. Therefore, requiring the additional constraint on $\mathbf{w}$ that

$$\mathbf{w}^H \mathbf{R}_i \mathbf{w} = 1, \tag{2.38}$$

will not change the maximum SINR. Using this approach our new objective is to maximize the quantity

$$Q = \mathbf{w}^H \mathbf{R}_s \mathbf{w} \tag{2.39}$$

[2]The dependence on time in the notation is suppressed for convenience.

subject to the constraint imposed by (2.38). Formulating the problem in terms of Lagrange multipliers, gives [16]

$$L = \mathbf{w}^H \mathbf{R}_s \mathbf{w} + \lambda(1 - \mathbf{w}^H \mathbf{R}_i \mathbf{w}). \tag{2.40}$$

where λ is a real constant. Taking the gradient of (2.40) with respect to $\mathbf{w}^*$ (See Appendix A) and setting it equal to zero results in,

$$\mathbf{R}_s \mathbf{w} = \lambda \mathbf{R}_i \mathbf{w}. \tag{2.41}$$

This is the well-known generalized eigenvalue problem [17]. If $\mathbf{R}_i$ is invertable then 2.41 may be written as

$$\mathbf{R}_i^{-1} \mathbf{R}_s \mathbf{w} = \lambda \mathbf{w}, \tag{2.42}$$

which is an ordinary eigenvalue problem the solution of which requires that $\mathbf{w}$ be an eigenvector of $\mathbf{R}_i^{-1}\mathbf{R}_s$.

To decide which eigenvector to choose we observe that (2.37) is in standard quadratic form and hence is bound by the eigenvalues of $\mathbf{R}_i^{-1}\mathbf{R}_s$. Therefore, the eigenvector which maximizes (2.37) is the one with the largest corresponding eigenvalue. To see this another way, we may set the gradient of (2.37) equal to zero to get

$$\mathbf{R}_s \mathbf{w} = \frac{\mathbf{w}^H \mathbf{R}_s \mathbf{w}}{\mathbf{w}^H \mathbf{R}_i \mathbf{w}} \mathbf{R}_i \mathbf{w} = \text{ SINR} \cdot \mathbf{R}_i \mathbf{w}. \tag{2.43}$$

Equating the right-hand sides of (2.41) and (2.43) gives

$$\lambda = \text{SINR} = \frac{\mathbf{w}^H \mathbf{R}_s \mathbf{w}}{\mathbf{w}^H \mathbf{R}_i \mathbf{w}}. \tag{2.44}$$

Therefore, the eigenvalue which solves (2.41) is itself the SINR. Therefore, the optimum weight vector $\mathbf{w}_{opt}$ is the eigenvector with the largest corresponding eigenvalue.

Finally, from (2.43),

$$\mathbf{w}_{opt} = \frac{\mathbf{R}_i^{-1}\mathbf{R}_s \mathbf{w}_{opt}}{\text{SINR}} = \frac{\mathbf{R}_i^{-1}\mathbf{a}s(\mathbf{a}s)^H \mathbf{w}_{opt}}{\text{SINR}} = \frac{\mathbf{R}_i^{-1}\mathbf{a}\mathbf{a}^H \mathbf{w}_{opt}\sigma_s^2}{\text{SINR}} = \beta_{opt}\mathbf{R}_i^{-1}\mathbf{a}. \tag{2.45}$$

where $\sigma_s^2 = E\{|s|^2\}$ and $\beta_{opt} = \sigma_s^2 \mathbf{a}^H \mathbf{w}_{opt}/\text{SINR}$.

2.6.2 Minimum Mean-Square Error

Next we consider the *Minimum Mean-Square Error* (MMSE) criteria, in which the average squared error (difference between the desired system output and the actual output) is minimized. Let d denote the desired output signal, which corresponds to the signal transmitted by the desired user. Assuming that the adaptive array output is given by $y = \mathbf{w}^H \mathbf{x}$, where $\mathbf{w}$ is the weight vector and $\mathbf{x}$ is the input signal vector then the error may be expressed

$$e = d - y = d - \mathbf{w}^H \mathbf{x}. \tag{2.46}$$

The MMSE performance criteria stated above is to minimize the quantity,

$$E\{|e|^2\} = E\{ee^*\} = E\{(d - \mathbf{w}^H\mathbf{x})(d - \mathbf{w}^H\mathbf{x})^H\}. \tag{2.47}$$

Expanding the terms inside the expectation gives

$$\begin{aligned} E\{|e|^2\} &= E\{dd^H - d(\mathbf{w}^H\mathbf{x})^H - \mathbf{w}^H\mathbf{x}d^H + \mathbf{w}^H\mathbf{x}(\mathbf{w}^H\mathbf{x})^H\} & (2.48)\\ &= E\{dd^H - d\mathbf{x}^H\mathbf{w} - \mathbf{w}^H\mathbf{x}d^H + \mathbf{w}^H\mathbf{x}\mathbf{x}^H\mathbf{w}\}. & (2.49)\end{aligned}$$

Taking the gradient with respect to $\mathbf{w}^*$ gives

$$\nabla_{\mathbf{w}^*} E\{|e|^2\} = E\{-\mathbf{x}d^H + \mathbf{x}\mathbf{x}^H\mathbf{w}\}. \tag{2.50}$$

Setting the gradient equal to zero and solving for $\mathbf{w}$ gives

$$\mathbf{w} = (E\{\mathbf{x}\mathbf{x}^H\})^{-1}E\{d^H\mathbf{x}\}. \tag{2.51}$$

Since d is a scalar, $d^H = d^*$. Defining $\mathbf{R}_{xx} = E\{\mathbf{x}\mathbf{x}^H\}$ (known as the correlation matrix of $\mathbf{x}$) and $\mathbf{r}_{xd} = E\{d^*\mathbf{x}\}$ then (2.51) becomes,

$$\mathbf{w}_{\text{MMSE}} = \mathbf{R}_{xx}^{-1}\mathbf{r}_{xd}. \tag{2.52}$$

This result is commonly referred to in the literature as the Wiener-Hopf equation or the optimum Wiener solution [15]. Substituting (2.52) into (2.49) the optimum MMSE becomes

$$\text{MMSE} = E\{|e|^2\} = E\{|d|^2\} - \mathbf{r}_{xd}^H\mathbf{R}_{xx}^{-1}\mathbf{r}_{xd}. \tag{2.53}$$

In order to show that all of the performance criteria lead to the optimum SINR solution it will first be shown that the solutions may be expressed in a common form. Let the input signal vector be given by

$$\mathbf{x} = \mathbf{a}s + \eta, \tag{2.54}$$

where $\mathbf{a}$ is the array response vector[3], s is transmitted communication signal, and η is zero mean noise plus interference vector. Assuming that the desired signal is orthogonal to the interference then the received correlation matrix may be expressed

$$\mathbf{R}_{xx} = \sigma_s^2\mathbf{a}\mathbf{a}^H + \mathbf{R}_i, \tag{2.55}$$

where $\sigma_s^2 = E\{|s|^2\}$ and $\mathbf{R}_i = E\{\eta\eta^H\}$. Also, from the form of $\mathbf{x}$, when $d = s$ then

$$\mathbf{r}_{xd} = E\{s^*(\mathbf{a}s + \eta)\} = \sigma_s^2\mathbf{a}. \tag{2.56}$$

Applying the matrix inversion lemma (see Appendix B) to $\mathbf{R}_{xx}$ and multiplying through by $\mathbf{a}$ gives,

$$\mathbf{R}_{xx}^{-1}\mathbf{r}_{xd} = \mathbf{R}_{xx}^{-1}\mathbf{a} = \left[\frac{1}{1 + \sigma_s^2\mathbf{a}^H\mathbf{R}_i^{-1}\mathbf{a}}\right]\mathbf{R}_i^{-1}\mathbf{a}. \tag{2.57}$$

Therefore, the optimum MMSE weight vector may also be expressed as

$$\mathbf{w}_{\text{MMSE}} = \beta_{\text{MMSE}}\mathbf{R}_i^{-1}\mathbf{a}, \tag{2.58}$$

where

$$\beta_{\text{MMSE}} = \frac{\sigma_s^2}{1 + \sigma_s^2\mathbf{a}^H\mathbf{R}_i^{-1}\mathbf{a}}. \tag{2.59}$$

[3]For flat fading multipath environments the array response vector should be replaced with the spatial signature vector

2.6.3 Minimum Variance

The *minimum variance* (also commonly referred to as linearly constrained minimum variance (LCMV)) performance criterion constrains the gain of the array in the direction of the desired user while minimizing the variance of the array output.

As shown above, the array output may be expressed as

$$y = \mathbf{w}^H \mathbf{x} = \mathbf{w}^H (\mathbf{a}s + \eta) = \mathbf{w}^H \mathbf{a}s + \mathbf{w}^H \eta. \tag{2.60}$$

The gain in the direction of the desired signal is constrained by forcing [4]

$$\mathbf{w}^H \mathbf{a} = G. \tag{2.61}$$

Subject to this constraint the array output becomes

$$y = Gs + \mathbf{w}^H \eta. \tag{2.62}$$

The expected value of the array output is $E\{y\} = Gs$, since by assumption $E\{\eta\} = 0$. The array output variance is then

$$\sigma_y^2 = E\{(y - Gs)(y - Gs)^H\} = E\{\mathbf{w}^H \eta (\mathbf{w}^H \eta)^H\} = \mathbf{w}^H \mathbf{R}_i \mathbf{w}. \tag{2.63}$$

Using Lagrange multipliers, the quantity that must be minimized is

$$L = \mathbf{w}^H \mathbf{R}_i \mathbf{w} - \lambda(G - \mathbf{w}^H \mathbf{a}). \tag{2.64}$$

Taking the gradient with respect to $\mathbf{w}^*$ and setting it to zero gives,

$$\mathbf{R}_i \mathbf{w} = \lambda \mathbf{a}. \tag{2.65}$$

When $\mathbf{R}_i$ is nonsingular we may write

$$\mathbf{w} = \lambda \mathbf{R}_i^{-1} \mathbf{a}. \tag{2.66}$$

Eq. 2.66 is the desired form of the solution, however, λ still needs to be determined by imposing the constraint given by (2.61). Multiplying through by $\mathbf{a}^H$ and observing that $\mathbf{a}^H \mathbf{w} = G^*$ we have

$$\mathbf{a}^H \mathbf{w} = \lambda \mathbf{a}^H \mathbf{R}_i^{-1} \mathbf{a} = G^*. \tag{2.67}$$

Solving for λ results in

$$\lambda = \frac{G^*}{\mathbf{a}^H \mathbf{R}_i^{-1} \mathbf{a}}. \tag{2.68}$$

Therefore, we may write

$$\mathbf{w}_{LCMV} = \beta_{LCMV} \mathbf{R}_i^{-1} \mathbf{a}, \tag{2.69}$$

where $\beta_{LCMV} = G^* / \mathbf{a}^H \mathbf{R}_i^{-1} \mathbf{a}$.

[4] When $G = 1$ the performance criteria is referred to as the minimum variance distortionless response (MVDR) since the desired component of the array output is equal to s itself.

2.6.4 Maximum Likelihood

With the *maximum likelihood* performance criteria the desired signal is treated as a deterministic but unknown parameter which is to be estimated [8]. Again, we express the input signal vector as before

$$\mathbf{x} = \mathbf{a}s + \eta. \tag{2.70}$$

The maximum likelihood estimate of s denoted as $\hat{s}$ is the value of s which maximizes the probability density function

$$f_{\mathbf{x};s}(\mathbf{x}; s), \tag{2.71}$$

where the notation is meant to emphasize that the probability density function of $\mathbf{x}$ is itself a function of s. In order to proceed the probability density function $f_{\mathbf{x};s}(\mathbf{x}; s)$ must be known.

If we assume that η is a zero mean multivariate Gaussian distribution, then $f_{\mathbf{x};s}(\mathbf{x}; s)$ is a multivariate Gaussian distribution with mean $\mathbf{a}s$ and covariance matrix given by

$$\mathbf{C}_x = E\{(\mathbf{x} - \mathbf{a}s)(\mathbf{x} - \mathbf{a}s)^H\} = E\{\eta\eta^H\} = \mathbf{R}_i. \tag{2.72}$$

The multivariate Gaussian probability density function of $\mathbf{x}$ is [16]

$$f_{\mathbf{x};s}(\mathbf{x}; s) = \frac{1}{\pi^M |\mathbf{R}_i|} e^{-(\mathbf{x}-\mathbf{a}s)\mathbf{R}_i^{-1}(\mathbf{x}-\mathbf{a}s)^H}, \tag{2.73}$$

where M is the length of $\mathbf{x}$. Our objective is to find s to maximize (2.73) for a given observation vector $\mathbf{x}$. Since the natural logarithm is monotone increasing maximizing $\ln(f_{\mathbf{x};s}(\mathbf{x}; s))$ is equivalent to maximizing $f_{\mathbf{x};s}(\mathbf{x}; s)$. Therefore we may choose to maximize the quantity,

$$L = \ln\left(\frac{1}{\pi^M |\mathbf{R}_i|}\right) - (\mathbf{x} - \mathbf{a}s)\mathbf{R}_i^{-1}(\mathbf{x} - \mathbf{a}s)^H. \tag{2.74}$$

Setting the partial derivative of L with respect to s^* equal to zero and then solving for s, gives

$$\hat{s} = \frac{\mathbf{a}^H \mathbf{R}_i^{-1}}{\mathbf{a}^H \mathbf{R}_i^{-1} \mathbf{a}} \mathbf{x}. \tag{2.75}$$

Hence, the maximum likelihood array output is of the form

$$y = \hat{s} = \mathbf{w}_{ML}^H \mathbf{x} \tag{2.76}$$

with the optimum weight vector given by [5]

$$\mathbf{w}_{ML} = \frac{\mathbf{R}_i^{-1}\mathbf{a}}{\mathbf{a}^H \mathbf{R}_i^{-1} \mathbf{a}}, \tag{2.77}$$

Finally, the optimum maximum likelihood weight vector may be expressed

$$\mathbf{w}_{ML} = \beta_{ML} \mathbf{R}_i^{-1} \mathbf{a}, \tag{2.78}$$

where $\beta_{ML} = 1/\mathbf{a}^H \mathbf{R}_i^{-1} \mathbf{a}$. It is interesting to note that this solution is identical to the solution found above for the LCMV when $G = 1$.

[5] Note that $\mathbf{R}_i^{-1}$ is hermitian symmetric since $\mathbf{R}_i$ is hermitian symmetric.

2.6.5 Steady-State SINR

In the previous sections it was found that the optimum weight vectors for each of the performance criteria may be expressed as

$$\mathbf{w} = \beta \mathbf{R}_i^{-1}\mathbf{a}, \tag{2.79}$$

where β is a scalar quantity dependent upon the selected criteria. In this section we will show that the steady-state SINR value that results from using the optimum weight vector for each criteria is independent of the value of β and hence are all equal. Therefore, regardless of which performance criteria is selected, the output SINR is optimum.[6] Substituting (2.79) into (2.37) gives the optimum SINR:

$$\text{SINR}_{opt} = \frac{(\beta \mathbf{R}_i^{-1}\mathbf{a})^H \mathbf{R}_s (\beta \mathbf{R}_i^{-1}\mathbf{a})}{(\beta \mathbf{R}_i^{-1}\mathbf{a})^H \mathbf{R}_i (\beta \mathbf{R}_i^{-1}\mathbf{a})} = \frac{\mathbf{a}^H (\mathbf{R}_i^{-1})^H E\{|s|^2\}\mathbf{a}\mathbf{a}^H (\mathbf{R}_i^{-1}\mathbf{a})}{\mathbf{a}^H (\mathbf{R}_i^{-1})^H \mathbf{a}} = \sigma_s^2 \mathbf{a}^H \mathbf{R}_i^{-1}\mathbf{a}. \tag{2.80}$$

2.6.6 Summary of Optimum Performance Criteria

Table 2.1 summarizes the key quantities for each of the performance criteria described above.

Table 2.1: Summary of optimum performance criteria.

Criteria	Cost Function	Solution
Maximum SINR	$\text{SINR} = \frac{\mathbf{w}^H \mathbf{R}_s \mathbf{w}}{\mathbf{w}^H \mathbf{R}_i \mathbf{w}}$	$\mathbf{R}_i^{-1}\mathbf{R}_s \mathbf{w}_{opt} = \lambda_{max}\mathbf{w}_{opt}$
Minimum Mean Square Error	$E\{\lvert(d - \mathbf{w}^H\mathbf{x})\rvert^2\}$	$\mathbf{w}_{MMSE} = \mathbf{R}_{xx}^{-1}\mathbf{r}_{xd}$
Minimum Variance	$\mathbf{w}^H \mathbf{R}_i \mathbf{w}$	$\mathbf{w}_{LCMV} = \frac{G^*}{\mathbf{a}^H \mathbf{R}_i^{-1}\mathbf{a}} \mathbf{R}_i^{-1}\mathbf{a}$
Maximum Likelihood	$f_{\mathbf{x};s}(\mathbf{x}; s)$	$\mathbf{w}_{ML} = \frac{1}{\mathbf{a}^H \mathbf{R}_i^{-1}\mathbf{a}} \mathbf{R}_i^{-1}\mathbf{a}$

2.7 Benefits of Using an Antenna Array in a Wireless Network

As noted above the fundamental capability of the antenna array that is of most interest to the wireless industry is the ability to improve signal reception, although the ability to estimate the angle of arrival of signals is also often of interest. The ability to improve signal reception can be used to improve various aspects of the wireless network. Several of these system performance enhancements are qualitatively and quantitatively described below.

2.7.1 Increased System Capacity

Let us consider a typical cellular network which utilizes frequency division multiple access (FDMA), where by users are able to share the wireless communication channel by transmitting in non-overlapping frequency bands. With a fixed amount of available spectrum, there is a limit

[6] Inclusion of the maximum likelihood solution in this statement requires the assumption that the received signal vector assumes a multivariate Gaussian distribution.

on the number of users that may be communicating at each instant of time. However, due to the attenuation experienced by the signals as they propagate through space, it is possible to *reuse* the frequency spectrum in distant regions in space. In order to provide good coverage near the edge of these spatial regions, referred to as *cells*, it is typically necessary not to use the same set of frequencies in adjacent cells. For convenience hexagonal cell shapes are often used to represent the region over which a particular set of frequencies is allocated. A typical cell pattern with a frequency reuse factor of $\frac{1}{7}$ is shown in Figure 2.6. The entire available spectrum is divided into seven different frequency bands, each of which is allocated to the corresponding cell in the network layout. Within each cell, a single user is assigned a particular frequency channel. The same frequency is re-used in the six surrounding co-channel cells that have the same available frequency band, indicated in the figure by the regions with the same number. Provided that the distance to the co-channel cells is sufficiently large, then the interferer's signal power will be attenuated to an acceptable level before it reaches the desired user's base station.

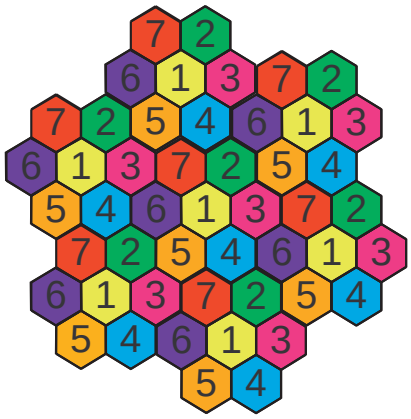

Figure 2.6: Example frequency reuse pattern with a frequency reuse of $\frac{1}{7}$.

Reducing the cluster size (the reciprocal of the frequency reuse), will provide an increase in the overall system capacity since more frequency bands can be used within each cell. However, reducing the cluster size brings the co-channel interference base stations closer to the desired cell and hence will yield a greater level of interference power. Therefore, for a fixed cell size, there is a limit to the number of channels that may be used in each cell which is determined by the level of co-channel interference. The use of an antenna array to improve signal reception causes a reduction in co-channel interference. With the capability to reduce co-channel interference it becomes possible to reduce the cluster size without a severe degradation in the signal quality.

In addition to increasing the system capacity by increasing frequency reuse, with antenna arrays it is possible to have several users in the same cell using the same frequency. This provides an additional multiple access scheme known as spatial division multiple access (SDMA), in which mobiles in the same cell with different locations have access to the base station resources. The utilization of SDMA systems will increase the system capacity by a factor equal to the number

of users which may be supported by the same cell, using the same frequency.

2.7.2 Range Extension

Range refers to the maximum distance a user may be displaced from the base station and still have sufficient signal quality. The ability of the antenna array to increase range results from its ability to increase the received signal to noise ratio. Suppose that we have an M element antenna array, and that the system is primarily noise limited. Simply co-phasing the received signals and combing will provide an M fold increase in the SNR, since the desired signal power increases by M^2 whereas the noise increases only by a factor of M.

Let γ_{min} denote the minimum acceptable SNR, which may be expressed

$$\gamma_{min} = \frac{P_{min}(d_1)}{N_0}, \tag{2.81}$$

where $P_{min}(d_1)$ denotes the required received signal power for a single element receiver with corresponding T-R separation of d_1, and N_0 is the noise power. To analyze the improvement offered by the antenna array, let us consider the received signal power as a function of distance which is typically expressed,

$$P_{min}(d) = P_0 \left(\frac{d_0}{d}\right)^n, \tag{2.82}$$

where P_0 is the reference power at a distance d_0 in the far-field, d is the T-R separation, and n is the path loss exponent [10]. When an M element antenna array is used the minimum acceptable SNR may be expressed

$$\gamma_{min} = \frac{M^2 P_{min}(d_M)}{M N_0} = \frac{M P_{min}(d_M)}{N_0}, \tag{2.83}$$

where d_M denotes the maximum range of the M element array. Equating (2.81) and (2.83) and solving for $P_{min}(d_M)$ we find that

$$P_{min}(d_M) = \frac{1}{M} P_{min}(d_1). \tag{2.84}$$

From (2.82) and (2.84), we have

$$\frac{P_{min}(d_1)}{P_{min}(d_M)} = \left(\frac{d_1}{d_M}\right)^n = M. \tag{2.85}$$

Finally, solving for d_M gives

$$d_M = M^{1/n} d_1. \tag{2.86}$$

Figure 2.7 shows the factor of improvement in range as a function of the number of antenna elements for various path loss exponents. The results indicate that greater range extension is achieved in environments with a lower path loss exponent.

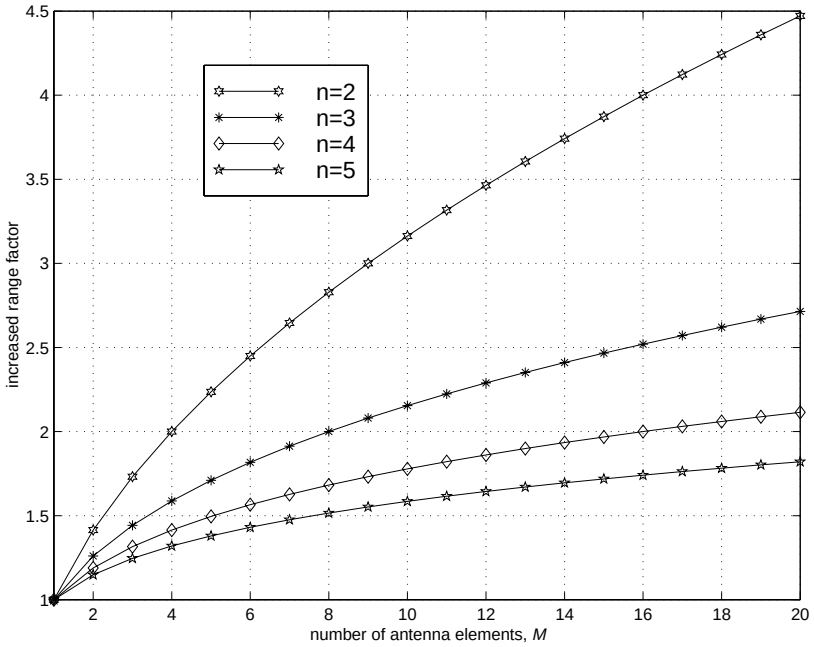

Figure 2.7: Increase in the factor of range improvement as a function of the path loss exponent and the number of antenna elements in the array.

2.7.3 Increased Coverage

In this section, we show that the antenna array can also be used to increase the percentage of the area of the cell that will have an acceptable signal level which is referred to as *coverage*. Here we assume that the size of the cell remains unchanged and that the mobile transmit power is held fixed regardless of the number of antenna elements used at the receiver.

Coverage with a Single Antenna Element Receiver

Before showing the improvement in coverage offered by the antenna array, first the derivation of coverage for a single antenna element is presented. The coverage increase achieved by the antenna array is a straight-forward extension of the result derived for a single antenna element system.

Typically, it is assumed that the signal strength at a given distance from the base station is described by a log-normal distribution [11]. Therefore, when expressing the received signal power P in dB, the probability density function of the received signal power is

$$f(P) = \frac{1}{\sigma\sqrt{2\pi}} \exp\left[\frac{-(P-\bar{P})^2}{2\sigma^2}\right], \tag{2.87}$$

where $\bar{P}$ is the mean received signal power and σ is the standard deviation in dB. The probability

that the signal power exceeds a desired threshold β is given by

$$P_\beta = P_r[P \geq \beta] = \int_\beta^\infty f(P)dP = \frac{1}{2} - \frac{1}{2}\text{erf}\left(\frac{\beta - \bar{P}}{\sigma\sqrt{2}}\right), \tag{2.88}$$

where $\text{erf}(x)$ is the standard error function [18]. Equation (2.88) gives the probability of acceptable signal quality when the received signal power is described by (2.87). However, due to path loss we would expect that the mean received signal will vary with distance from the transmitter. Often it is assumed that the path loss is proportional to d^{-n}, where d is the base to mobile separation distance and n is the path loss exponent, in which case the mean received signal strength may be expressed [10]

$$\bar{P} = \alpha - 10n\log_{10}\frac{d}{R}, \tag{2.89}$$

where α (expressed in dB) is related to the transmit power and antenna properties and R is the radius of the circular cell. Combining (2.88) and (2.89) we may express the probability that the signal level is above the required threshold as a function of distance d as

$$P_\beta(d) = \frac{1}{2} - \frac{1}{2}\text{erf}\left(\frac{\beta - \alpha + 10n\log_{10}\frac{d}{R}}{\sigma\sqrt{2}}\right). \tag{2.90}$$

Substituting $a = (\beta - \alpha)/\sigma\sqrt{2}$ and $b = 10n\log_{10} e/\sigma\sqrt{2}$ gives the compact expression

$$P_\beta(d) = \frac{1}{2} - \frac{1}{2}\text{erf}\left(a + b\ln\frac{d}{R}\right). \tag{2.91}$$

The fraction of the circular cell in which the signal strength exceeds the required threshold can now be found by integrating (2.91) over the area of the cell and normalizing by the area, resulting in

$$F_u = \frac{1}{\pi R^2}\int_0^R\int_0^{2\pi} \zeta P_\beta(\zeta)\, d\theta\, d\zeta. \tag{2.92}$$

Making the variable substitution $t = a + b\ln(d/R)$, F_u may be expressed [10]

$$F_u = \frac{1}{2}\left[1 - \text{erf}(a) + \exp\left(\frac{1-2ab}{b^2}\right)\left(1 - \text{erf}\left(\frac{1-ab}{b}\right)\right)\right]. \tag{2.93}$$

Typically, a family of coverage curves for various fractional coverage at the cell boundary versus the quantity σ/n is given [10, 19, 11]. In doing so, one finds that the parameter a determines the fractional coverage at the cell boundary, leaving only the parameter b which is a function of σ/n. However, as we shall see shortly, when comparing the coverage achievable with an antenna array to the coverage obtained with a single antenna element receiver, the individual values of σ and n are needed, and not just their ratio. Therefore, we shall proceed by simply assuming that $n = 4$ and then plotting F_u versus σ.

Figure 2.8 shows the resulting coverage versus the standard deviation of the log-normal fading σ. The various curves are labeled with the corresponding fractional coverage at the cell boundary. As expected the coverage within the cell increases with an increase in the coverage at the cell boundary. Also, as shown the cell coverage decreases with an increase in the standard deviation of the log-normal shadowing.

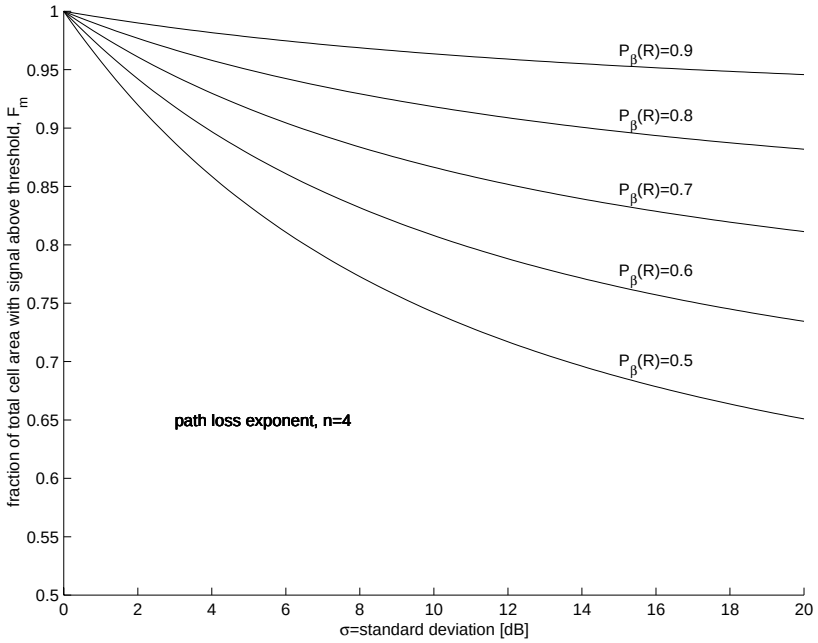

Figure 2.8: Fractional cell coverage for single antenna element receiver.

Coverage Improvement with an Antenna Array

Assuming that the cell radius remains constant, and that the system is noise limited, then it is possible to find the increase in the coverage of the cell obtained by using an antenna array. Again it is assumed that the antenna array increases the signal power by a factor of M^2 and the noise power by a factor of M. This result is only valid when the noise at each element is uncorrelated with the noise at the other elements.

Since the noise power increases by a factor of M, in order to maintain the same level of acceptable SNR then the signal power threshold must also increase by a factor of M. Therefore, the power level threshold in dB for the array system becomes

$$\beta_m = \beta + 10 \log_{10} M, \tag{2.94}$$

where β was the original signal threshold for the single element receiver. Fortunately, by using the array to coherently combine the desired signal at each of the antenna elements the desired signal power increases by M^2. The resulting desired signal output power is still log-normally distributed with a standard deviation of σ and with a mean in dB given by

$$\bar{P}_m = 20 \log_{10} M + \bar{P}. \tag{2.95}$$

Hence, the probability that the desired signal power at the array output exceeds β_m is given by

$$\begin{aligned} P_{\beta_m} &= P_r[P_m \geq \beta_m] \\ &= \frac{1}{2} - \frac{1}{2}\text{erf}\left(\frac{\beta_m - \bar{P}_m}{\sigma\sqrt{2}}\right) \end{aligned}$$

$$= \frac{1}{2} - \frac{1}{2}\text{erf}\left(\frac{\beta - 10\log_{10} M - \bar{P}}{\sigma\sqrt{2}}\right)$$
$$= \frac{1}{2} - \frac{1}{2}\text{erf}\left(\frac{\beta - 10\log_{10} M - \alpha + 10n\log_{10}\frac{d}{R}}{\sigma\sqrt{2}}\right). \quad (2.96)$$

Making the substitution $a_m = (\beta - \alpha - 10\log_{10} M)/\sigma\sqrt{2}$ and $b = 10n\log_{10} e/\sigma\sqrt{2}$ then (2.96) becomes

$$P_{\beta_m}(d) = \frac{1}{2} - \frac{1}{2}\text{erf}\left(a_m + b\ln\frac{d}{R}\right). \quad (2.97)$$

This expression is identical to (2.91) with a being replaced by a_m. Therefore, we may use the expression for F_u above to find the percentage coverage of the total area when an antenna array is employed F_m simply by replacing a by a_m.

Figure 2.9 shows the fraction of the cell area with the signal power above the required threshold as a function of σ, with $n = 4$ and $M = 4$ for various values of fractional coverage at the cell boundary when a single element receiver is used. One may compare Fig. 2.9 with Fig. 2.8 to find the improvement in coverage provided by the antenna array system. From these figures we may find the percentage improvement in the fractional coverage of the cell area.

The percentage improvement in the fractional coverage is given by

$$G = \frac{F_m - F_u}{F_u}. \quad (2.98)$$

The percentage improvement in the coverage within the cell is shown in Figure 2.10 for $n = 4$ and $M = 4$. Figure 2.11 shows the percentage improvement in the fraction of the coverage area within the cell as a function of the number of elements in the array for $n = 4$ and $\sigma = 10dB$.

2.7.4 Reduction in Mobile Transmit Power

Due to the increased antenna gain achievable at the base station, the transmit power at the mobile may be reduced by roughly a factor of M. The reduction in required mobile transmit power can be directly related to an increase in the mobile battery life and/or a reduction in the required battery size, both of which are of major benefit to handheld units.

2.7.5 Improved Signal Quality

The use of antenna arrays to increase the received SINR results in a reduced BER in digital systems. For voice or video applications the reduced BER yields a corresponding improvement in the received signal quality. In general, for noise limited channels, the minimum signal thresholds are reduced by $10\log_{10} M$, where M is the number of antenna elements in the array [15].

2.7.6 Higher Data Rates

The increase in the SINR can be used to increase the number of bits per symbol in the digital modulation by switching over to higher order modulation formats. This results in an increased

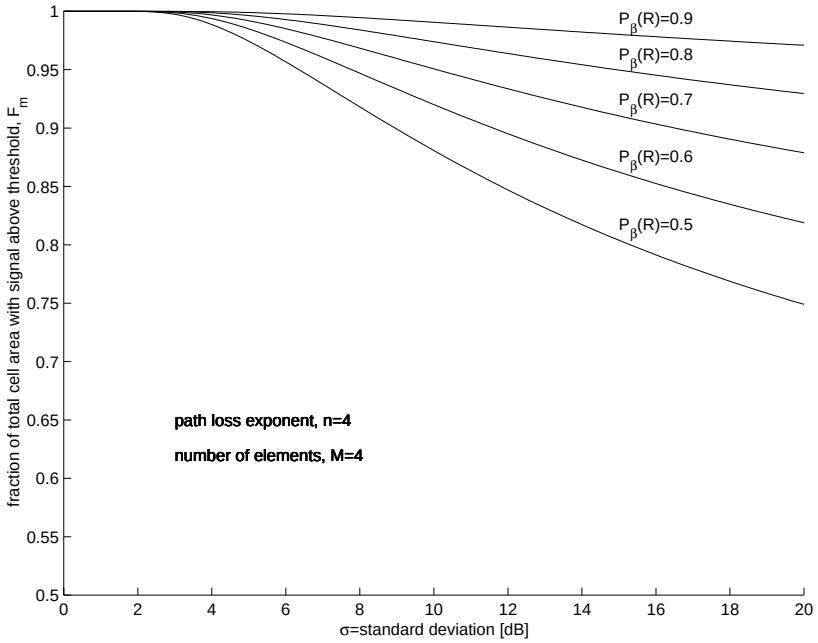

Figure 2.9: Percentage cell coverage for a four element antenna array.

bit rate with a corresponding increase in the capacity of the channel.

2.8 Summary

This chapter provided a review of fundamental antenna array concepts. A general wideband signal model was developed. It was shown that under certain conditions a more simplistic narrowband signal model can be used. The extension of these models to multiple users in a multipath environment was shown.

Both the narrowband and wideband adaptive structures were described. It was shown that the array output of the wideband adaptive array model could be expressed in the same form as the array output of the narrowband model. A brief overview of spatial diversity and diversity combining techniques was given.

Four commonly used optimum performance criteria were applied to the solution of a narrowband adaptive array. It was found that under certain conditions regardless of the performance criterion which is selected, all solutions provide maximum SINR.

Finally, the ability of an antenna arrays to improve system capacity, extend maximum range, increase coverage, reduce mobile transmit power, improve signal quality, and increase data rates was explored. Straight-forward analytical results could be obtained by assuming that the antenna array increases the received SNR by a factor M. An original analysis of the coverage improvement provided by antenna arrays was presented.

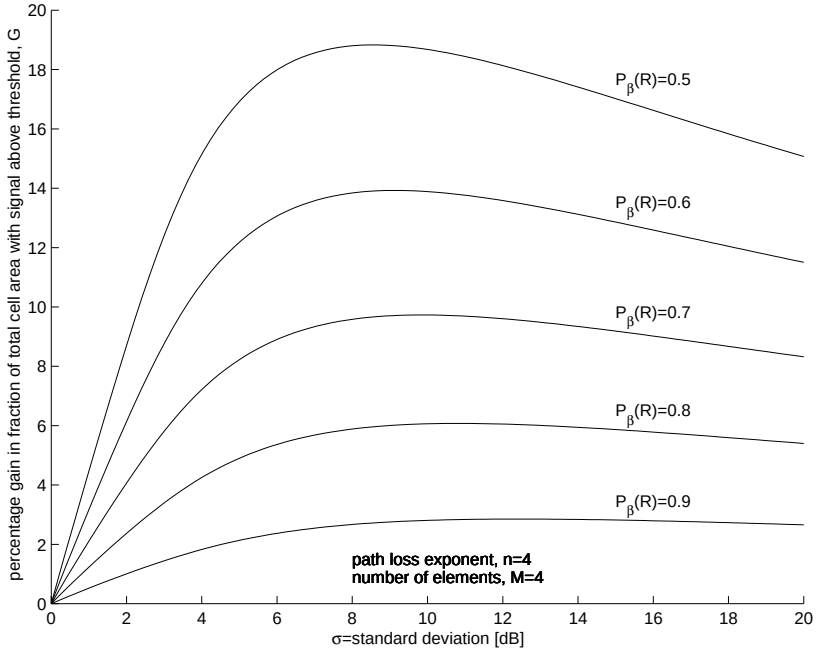

Figure 2.10: Percentage improvement in cell coverage for a four element antenna array.

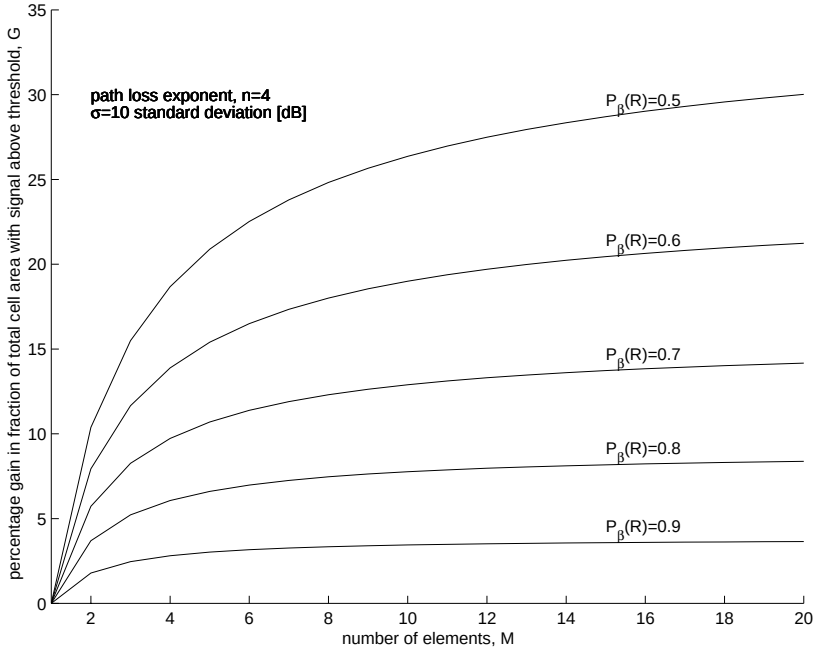

Figure 2.11: Percentage improvement in cell coverage for an M element antenna array.

Chapter 3

Overview of Vector Channel Models

The performance of antenna array systems is highly dependent upon the characteristics of the wireless channel. In some environments the antenna array may offer large performance gains, whereas in other environments an antenna array may provide only modest performance gains. Understanding how the environment will impact antenna array performance is essential to the design of these systems.

To obtain reliable estimates of the performance of antenna array systems, accurate vector channel models are needed. These models must provide all of the temporal channel properties of classical channel models as well as spatial information. There has been a wide variety of vector channel models presented in the literature.

In this chapter the various multipath propagation mechanisms are described. Also presented is a survey of vector channel models. Section 3.1 describes the propagation environment and defines terms used to describe propagation mechanisms. Section 3.2 defines two classes of vector channel models, geometrically based and statistical models. In Sections 3.3 and 3.4 a brief description of each of the vector channel models is given.

3.1 Description of the Signal Environment

In a wireless system, the signal which is transmitted into the channel interacts with the environment in a complex manner. The signal observed at the receiver is in general a summation of both a direct line-of-sight and several multipath signal components. *Multipath* signal components occur due to scattering, reflecting, and diffraction of the transmitted signal. A brief description of each of these multipath propagation mechanisms is described below.

3.1.1 Reflection

Reflection occurs when the signal impinges upon an object with dimensions larger than the signal wavelength. If the object is a perfect conductor, then all of the signal energy is reflected,

otherwise a portion of the energy is transmitted through the object [11]. According to Snells's law of reflection the angle of reflection equals the angle of incidence [7]. However, if the surface of the object is not perfectly smooth then surface scattering results which causes the signal energy to be transmitted in diverse directions [20].

For reflected signals, the path-loss will be determined by the sum of the distance from the transmitter to the reflector and the distance from the reflector to the receiver plus the loss associated with the reflection coefficient. For rough surfaces, the reflection coefficient is scaled by the scattering loss factor.

3.1.2 Scattering

Scattering occurs when the dimensions of the object or facets on the object are smaller than the signal wavelength. The signal energy that is received by the scatterer is re-radiated in all directions away from the scatterer [11]. In the case of scattering the path loss observed from the transmitter to the receiver will be the product of the distance from the transmitter to the scatterer and the distance from the scatterer to the receiver, plus the additional loss associated with the scattering coefficient [21]. Typically the path-loss associated with scattering is much greater than that associated with reflection.

3.1.3 Diffraction

The mechanism that allows signal energy to propagate around objects is called *diffraction*. It is based upon Huygen's principle which states that all points on a wavefront behave as point sources. The energy transmitted from the point sources allows the signal to arrive in shadowed regions which have no line-of-sight from the transmitter. In general the path-loss can be obtained by considering the obstruction of the Fresnel zones [11].

3.1.4 Dominant Reflectors, Scattering Clusters, and Local Scatterers

In the various vector channel models the terms reflectors and scatterers are used somewhat loosely. In order to provide a more consistent description of the propagation mechanisms being modeled the following terms will be used to describe the physical structures with which the signal interacts, and the multipath mechanism that is occurring. The various multipath propagation mechanisms are illustrated in Fig. 3.1.

- *Scattering cluster* - A region containing a number of scatterers such that the signal components from scatterers are confined within a narrow time delay and angle of arrival. Also known as remote scatterers, scattering clusters may give rise to large delay and angle spreads [22, 23]. The path-loss associated with the product of the distances should be applied (product path-loss).
- *Local scatterers* - The scatterers in the vicinity of the mobile which gives rise to independent fading signals in different directions away from the mobile.

- *Scatterers local to the base station* - The scatterers in the vicinity of the base station including objects on nearby roof-tops, the antenna tower structure, etc. These scatterers may cause severe angle spreading [22, 23].
- *Dominant reflectors* - Refers to a structure that gives rise to a significant multipath component at the receiver. The reflection may be both specular or diffuse. For diffuse reflection, the reflected signal may be treated as the summation of a number of point sources which give rise to a nonzero angular spread at the receiver. As with scattering clusters, the presence of dominant reflectors may give rise to large delay and angle spreading. A path-loss dependent upon the total propagation distance (sum path-loss) occurs.
- *Object* - Any physical structure that interacts with the propagating signal. The signal may experience scattering and/or reflection from the object.

The key difference between dominant reflectors and scattering clusters is in the type of path-loss which is applied.

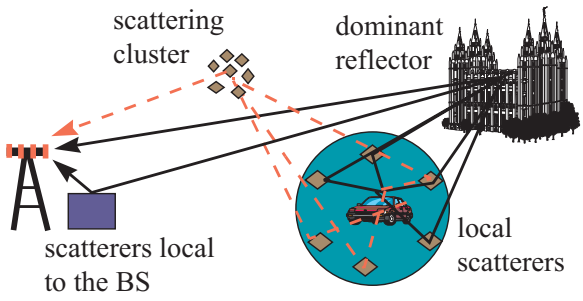

Figure 3.1: General propagation environment.

3.2 Vector Channel Model Classification

Since there are many similarities between some of the models it is convenient to define classes of vector channel models such that the models within a given class have a common attribute. Here we define two classes of vector channel models, *geometrically based* and *statistically based*. Further details regarding these defined classes are given below.

3.2.1 Geometrically Based Vector Channel Models

Geometrically based vector channel models are defined as those models which specify both a region in space where objects are distributed and the distribution of those objects. The objects give rise to scattering and/or reflection. Typically the interaction of the signal with the objects is such that each multipath signal only interacts with a single object. This interaction may be viewed as a single-bounce from the transmitter to the receiver, and the term geometrically based single-bounce (GBSB) models is often used when referring to these models [24, 25].

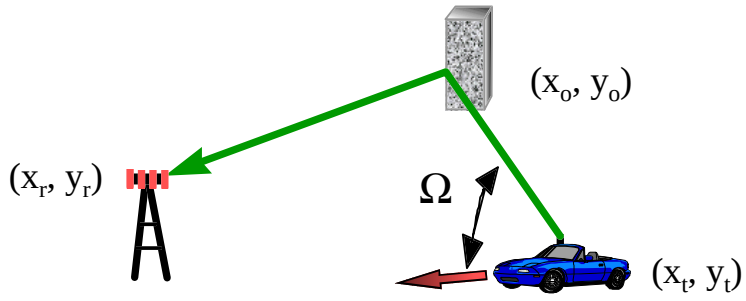

Figure 3.2: Geometrically based single bounce models notation.

Figure 3.2 shows the geometry of the GBSB propagation, and notation for the receiver, transmitter, and object coordinates. From the known coordinates the time of arrival, angle of arrival, and signal power level may be found. Let $d_{to} = \sqrt{(x_t - x_o)^2 + (y_t - y_o)^2}$ and $d_{or} = \sqrt{(x_o - x_r)^2 + (y_o - y_r)^2}$ denote the distance from the transmitter to the object and the distance from the object to the receiver, respectively. The total signal delay from transmitter to receiver is then

$$\tau = \frac{d_{to} + d_{or}}{c} \tag{3.1}$$

where c is the speed of light. If reflection is considered then the path-loss will be a function of τ. For scattering the path-loss will be a function of the product $d_{to}d_{or}$. From the coordinates of the object and the receiver, the angle of arrival observed at the receiver is

$$\theta = \text{atan}\left(\frac{y_o - y_r}{x_o - x_r}\right). \tag{3.2}$$

The majority of the GBSB channel models specify time invariant coordinates for the mobile and each of the objects. These models do, however, provide Doppler fading simply by treating each of the objects as an oscillator (applying a rotating phase) the frequency of which is dependent upon the angle between the direction the mobile is traveling and the ray towards the object, Ω. This angle may be expressed

$$\Omega = \text{atan}\left(\frac{y_o - y_m}{x_o - x_m}\right). \tag{3.3}$$

The corresponding Doppler frequency is

$$\omega_d = \frac{v_s f_c}{c}\cos(\Omega), \tag{3.4}$$

where v_s is the speed of the mobile, f_c is the carrier frequency, and c is the speed of light.

Since the Doppler frequencies are dependent upon an angle measured relative to the mobile, the Doppler spectrum and corresponding fading are dependent upon the angular distribution of objects about the mobile. The classical Doppler spectrum results when equal power signal components are uniformly distributed about the mobile [11]. When the object distribution is not uniform about the mobile, something other than the classical U-shaped Doppler spectrum

will result. When a path distance dependent path-loss is applied to each multipath component, the signal amplitude will vary about the angle of departure relative to the mobile, and hence even uniform object distributions about the mobile may not produce the classical U-shaped Doppler spectrum. This amplitude variation is more prominent when the maximum excess delay is large, or when the path-loss exponent is high.

The expected power delay profiles for the GBSB channel models are determined by the concentration of objects on concentric ellipses, defined such that the transmitter and receiver are placed at the foci. Each ellipse corresponds to a particular delay. Therefore, it is possible to predict the power delay profile simply from the geometry of the model.

In general the geometrically based vector channel models do not provide much flexibility in the independent selection of channel parameters. In fact some of the models have only one degree of freedom. Furthermore, some of the models are only appropriate for specific environments. When simulating different environments different channel model structures may be needed. This lack of flexibility inherent in the geometrical models is the major disadvantage of using such a model.

An advantage of the geometrical models is that they provide in a very compact form the complete specification of the joint AOA/TOA statistics of the channel. For example, simply specifying that scatterers are uniformly distributed within a circular region about the mobile of radius 20m is all that is needed to specify the spatial aspects of the channel. Additionally, many of the models seamlessly adjust to different T-R separation distances. For example, with the circular model, the angle spread will automatically decrease with an increase in the T-R separation as desired.

Another potential advantage of these models is that by placing objects in space the resulting channel at least in some sense is modeling a physical property of the real world. However, the actual phenomenon which is occurring is extremely difficult to characterize, and hence using a highly idealized physical model of the channel may not give an accurate representation of what is actually happening. In this case, it may be best to consider the statistical characterization of measurement data rather than attempt to model the physical mechanism behind the data.

3.2.2 Statistical Vector Channel Models

Statistically based vector channel models do not rely upon the specification of a geometrical region, but rather signal parameters are obtained directly from some statistical distribution. Maximum flexibility is provided by the models since the user is free to choose any arbitrary distribution for the various channel parameters. In fact it is possible to generate signals which match any arbitrary desired power delay profile, Doppler spectrum, and angle spread using statistical models.

The major difficulty in implementing these models is in deciding what parameter values should be used. In particular from the results that have been published in the literature it is difficult to determine what the angular distribution should be, and how it should vary from one environment to another. Favorably, this limitation is not a fundamental limitation of the model, but rather is simply a consequence of a lack of extensive measurement data. After sufficient data

has been collected to characterize the various statistical properties of the channel, statistical channel models can be created which match the measured data.

3.3 Geometrically Based Vector Channel Models

In this section a brief description of each of the geometrically based channel models that have appeared in the literature is given. Of most importance is the defining geometry of the models, and not in the exact details about how path-loss, shadowing, and other affects are accounted for since one is free to select these aspects independent of the geometry. Hence, our focus here is on the former.

3.3.1 Circular

The circular vector channel model assumes that objects are uniformly distributed within some radius about the mobile as shown in Fig. 3.3 [10,26–29]. The circular region of scatterers model was used in [10] to derive theoretical results for the correlation observed between two antenna elements as a function of the element spacing. Later it was used in [27] to study the effects of beamwidth on the fading rate.

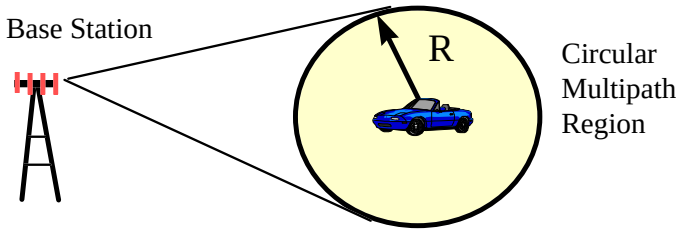

Figure 3.3: Geometry of the circular scattering channel model. Scatterers are uniformly distributed within a circle centered at the mobile.

The model is most appropriate for macrocells in rural or suburban environments where the base station antenna height is above the local clutter, and no large reflectors away from the vicinity of the mobile are visible at the base.

3.3.2 Typical Urban

The typical urban vector channel model is a special case of the circular model in that the radius of the multipath region is specified as 1 km, and the number of scatterers is 120 [30–32]. The maximum delay observed with the typical urban model occurs when the multipath signal is bounced off of an object on the far side of the circle relative to the base station. The corresponding excess path distance is $2R$ where R is the radius of the circular region. For $R = 1$ km, $\tau_m = 6.67\mu s$ which is close to the maximum delay of 7 μs specified in the GSM 05.05 standard (hence the motivation for R=1 km).

There is a subtle difference between the circular model described above, and the typical urban model involving the manner in which the Doppler frequency shift is accounted for. In the circular model the location of the mobile and objects are fixed and each object is treated as an oscillator. In the typical urban model the coordinates of the mobile continuously vary with time, and it is the time-varying path length which naturally gives rise to the Doppler shifts. In this way the typical urban model is more realistic. However, in order to prevent the mobile from leaving the scattering region, after the mobile as moved a distance of 5m, the coordinates of the scatterers are adjusted so that the scatterers are again in their origin position relative to the mobile. At the same time the scatterers are assigned a new random phase so that each fading realization is unique.

3.3.3 Bad Urban

The Bad Urban (BU) model is identical to the Typical Urban with the addition of a secondary cluster of scatterers which is off-set from the first by 45 degrees [30–32]. The mean power level of the log-normal shadowing of the secondary cluster is 5 dB below the original cluster. Figure 3.4 shows the geometry for a T-R separation of 2 km. In this case the two clusters overlap in space.

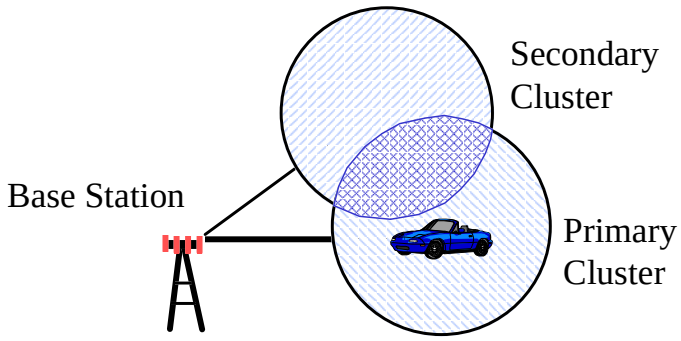

Figure 3.4: Bad urban vector model geometry. The model consists of an overlap of two circular scattering regions.

3.3.4 Hierarchical Circular

In [33] the authors propose a hierarchical subdivision of the propagation environment into circular regions as shown in Fig. 3.5. In this model the propagation environment is subdivided into regions without scatterers, and circular areas with scatterers. Within each circular scattering area are circular scattering clusters, which contain the actual scattering points. The number and diameter of the scattering areas and the number and diameter of scattering clusters are variables of the models. Additionally, the placement of the scattering areas may be varied to accommodate different propagation environments. In [33] five different default configurations are suggested for the various environments including a rural model, two urban models, a microcellular model, and a picocellular model. All of the models use two main scattering areas,

with the exception of the rural model which has only a single scattering area. In all cases the first scattering area is centered at the mobile.

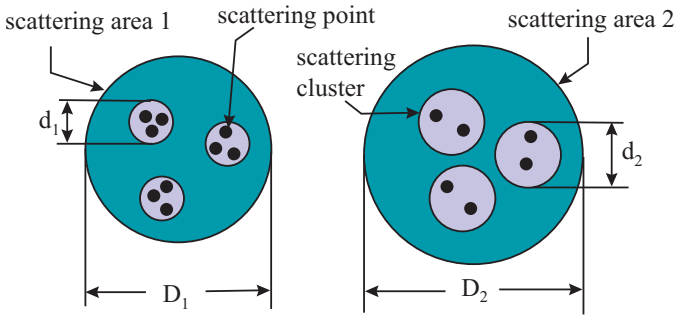

Figure 3.5: Hierarchical circular subdivision of the propagation environment with two scattering areas. The diameter of the first and second scattering area are D_1 and D_2 respectively. Similarly, the diameter of the scattering clusters in the first and second scattering area are denoted d_1 and d_2, respectively.

The suggested use of the model is for Monte Carlo simulation to obtain BER estimates. A selected set of parameters is used to generate a large ensemble of propagation environments. For each realization the mobile is allowed to move a distance of 10 wavelengths and the corresponding BER is determined. The resulting BER values are then used as a measure of the expected BER distribution.

3.3.5 Elliptical (Liberti's Model)

The elliptical vector channel model (Liberti's Model) uniformly distributes objects in an ellipse defined such that the base station and the mobile are located at the foci of the ellipse as shown in Figure 3.6 [24, 25, 29]. The size of the ellipse is selected to provide a fixed maximum delay, τ_m. The motivation behind an elliptical multipath region is that all single bounce multipath components with a delay up to and including τ_m are accounted for.

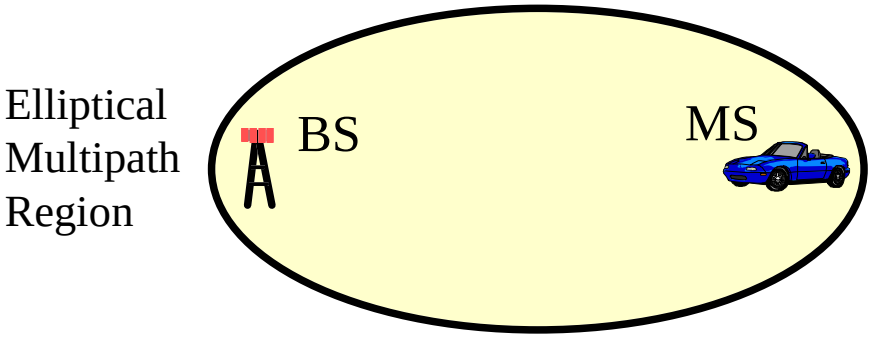

Figure 3.6: Elliptical scattering channel model geometry.

The model is thought to be appropriate for microcells with low antenna heights, and hence observable clutter in the vicinity of the base station. The elliptical model provides a much greater angle spread than the models presented above, and hence one would expect less correlation at two antenna elements with a fixed element spacing.

3.3.6 Elliptical Sub-regions

The previous models do not allow the user to specify parameters of the power delay profile with the exception of the maximum excess delay time. In contrast, the elliptical sub-regions model described in [34] provides this flexibility. As shown in Figure 3.7, the model separates the ellipse of maximum delay into S elliptical sub-regions. Each sub-region accounts for multipath components with a corresponding delay. By adjusting the number of signal components within the various sub-regions, it is possible to obtain any desired power delay profile.

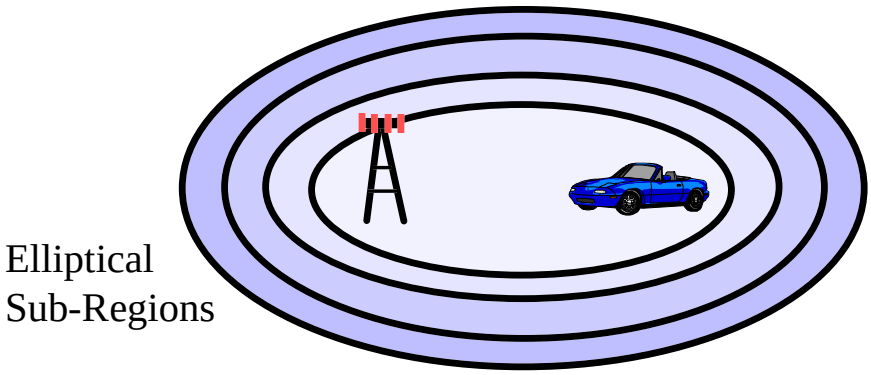

Figure 3.7: Elliptical sub-regions channel model geometry.

The total number of multipath components, L, is selected from a Poisson distribution. The number of dominant reflectors in the ith sub-region is selected from Poisson distribution with mean given by,

$$\Lambda_i = p_i L, \tag{3.5}$$

where p_i is the probability of a path arriving with excess delay in the range defined by the ith elliptical sub-region. In particular, if $p_r(\tau)$ denotes the probability of a path component with excess delay τ, then

$$p_i = \int_{(i-1)\Delta\tau}^{i\Delta\tau} p_r(\tau) d\tau. \tag{3.6}$$

Each of the dominant reflectors is composed of a number of reflecting points, the number of which is again selected from a Poisson distribution. The delay times of the additional reflecting points within the dominant reflector assume an exponential distribution. Also, the angle of arrival observed at the base station is assumed to be Gaussian within each dominant reflector.

3.3.7 Lee's and Modified Lee's Model

Lee's model provides a simple model to determine the correlation that exists between two antenna elements as a function of the element spacing [35,36]. The model assumes that scatterers are uniformly spaced on a radius about the mobile as shown in Figure 3.8. From the resulting angular distribution that is observed at the base station is it possible to derive the spatial correlation function.

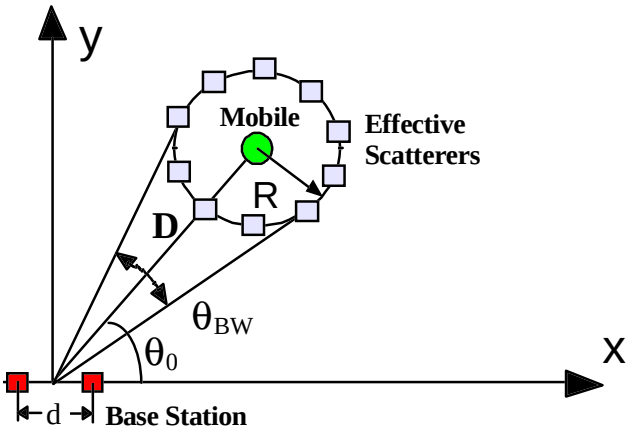

Figure 3.8: Lee's model geometry.

Modified Lee's model uses the same geometry as Lee's model, but imposes an angular velocity on the scatterers to provide Doppler frequency shifts [37,38].

3.3.8 Norklit's Model

The object distribution of Norklit's model [39] (previously referred to as the uniform sector model) is shown in Figure 3.9. Objects are uniformly distributed in the region specified by a finite angular and radial distance range with respect to the base station. The magnitude and phase of the scatterers are selected from uniform distributions over $[0,1]$ and $[0,2\pi]$ respectively. As the number of scatterers approaches infinity samples from the signal envelope become Rayleigh distributed. The major advantage of this model is that the angle of arrival at the base station is from a uniform distribution and hence could be used to provide tractable analytic results.

3.3.9 Jake's Fading Model with Angle Spread

Jake's fading model [10] which consists of uniformly spaced oscillators has been used extensively for generation of Rayleigh fading envelopes. However, when a ring of scatterers is used to generate angle of arrival information, the resulting angle of arrival probability density function observed at the base is U-shaped as opposed to having the expected bell-shape [40]. In [40] an efficient method is proposed to generate Rayleigh fading signals, with angle of arrival statistics

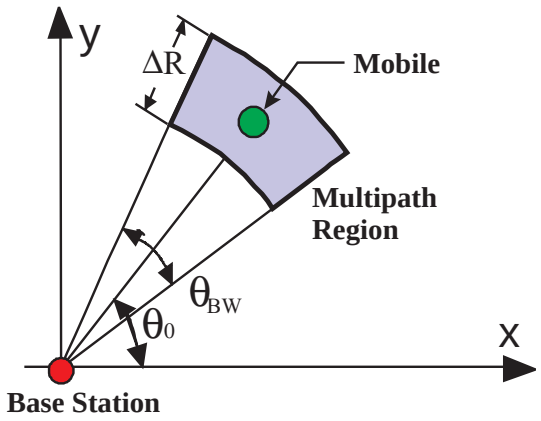

Figure 3.9: Norklit's model geometry.

which closely match those of the circular scatterer model described above. The model proposes placing several scatterers on spokes of equal Doppler centered at the mobile as shown in Figure 3.10. In this way, only a single oscillator per spoke is needed while the spatial properties of the spoke are accounted for by use of the spoke's effective signature vector.

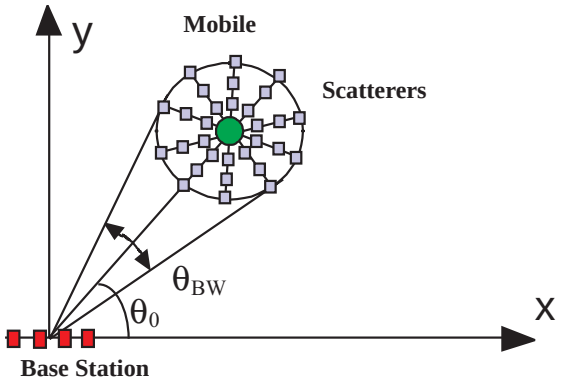

Figure 3.10: Jake's fading model with angle spread.

3.3.10 Raleigh's Model

Raleigh's model accounts for two propagation mechanisms as shown in Figure 3.11 [41]. There is local scattering that occurs in the vicinity of the mobile, the effect of which is to cause the signal envelope to experience uncorrelated Rayleigh fading at different angles away from the mobile. The signals leaving the local scatterers then interact with dominant reflectors, the distribution of which determines the angle spread at the base station. The number of such dominant reflectors and the distribution is left as a parameter of the model for the user to

choose. Note, that the fading properties can be selected independently from the AOA and TOA properties since the fading is attributed to the scatterers local to the mobile and not the dominant reflectors.

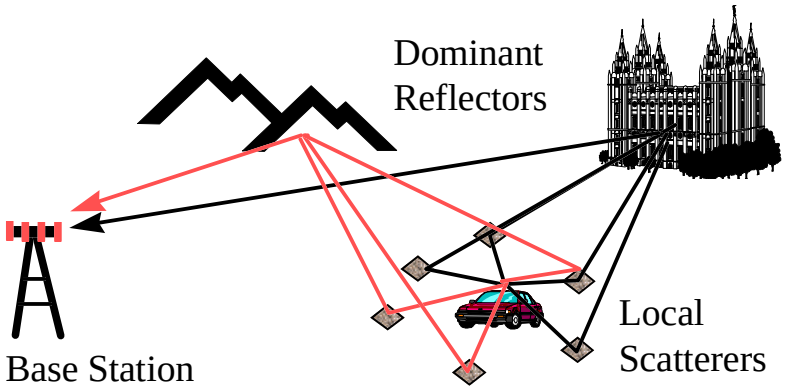

Figure 3.11: Raleigh's channel model geometry. The model consists of local scatterers near the mobile and dominant reflectors at distant locations.

3.4 Statistical Vector Channel Models

In this section various statistical vector channel models that have appeared in the literature are presented.

3.4.1 Gaussian Wide Sense Stationary Uncorrelated Scattering

The Gaussian Wide Sense Stationary Uncorrelated Scattering (GWSSUS) vector channel model assumes that the objects are grouped into S uncorrelated clusters as shown in Figure 3.12 [30, 31]. The delays of the multipath within each cluster are non-resolvable within the signal bandwidth. Each of the clusters has many scattering components. The received signal vector may be expressed,

$$\mathbf{x(t)} = \sum_{\mathbf{k=1}}^{\mathbf{S}} \mathbf{v_k s(t - \tau_k)}, \tag{3.7}$$

where

$$\mathbf{v}_k = \sum_{i=1}^{N_k} \alpha_{k,i} \mathbf{a}(\theta_{0k} - \theta_{k,i}) \tag{3.8}$$

is the effective signature vector, τ_k is the delay, and θ_{0k} is the mean angle of arrival of the kth cluster, respectively. N_k is the number of scatterers in the kth cluster, $\alpha_{k,i}$ is the complex amplitude and $\theta_{k,i}$ is the angle deviation from θ_{0k} of the ith path of the kth cluster.

Provided that the number of scattering components is sufficiently large the signature vector for each cluster can be modeled as a multi-variant Gaussian distribution defined by its mean

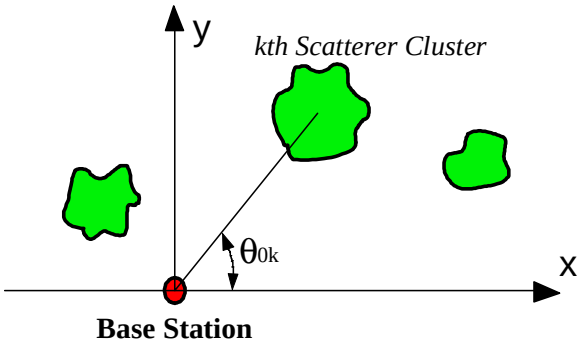

Figure 3.12: GWSSUS model geometry.

and covariance matrix. When there is no line-of-sight component the mean of the signature vector is zero. If a line-of-sight component is present the mean of the signature vector will be proportional to the array response vector in the direction towards the mobile. The covariance matrix of the k^{th} cluster may be expressed as,

$$\mathbf{R}_k = E\left\{\mathbf{v}_k \mathbf{v}_k^H\right\} = \sum_{i=1}^{N_k} E\left\{\mathbf{a}(\theta_{0k} - \theta_{k,i})\mathbf{a}^H(\theta_{0k} - \theta_{k,i})\right\}. \tag{3.9}$$

3.4.2 Gaussian Angle of Arrival

A special case of the GWSSUS vector channel model is the Gaussian Angle of Arrival (GAA) model shown in Figure 3.13. It assumes that only a single cluster is present, centered about the mobile, and that the angle of arrival statistics of the signal components within the cluster assume a Gaussian distribution [42,30,31]. Measurements indicate that the standard deviation in the angle of arrival is typically between 2 to 6 degrees at a T-R separation of 1 km, and is inversely proportional to the T-R separation [42].

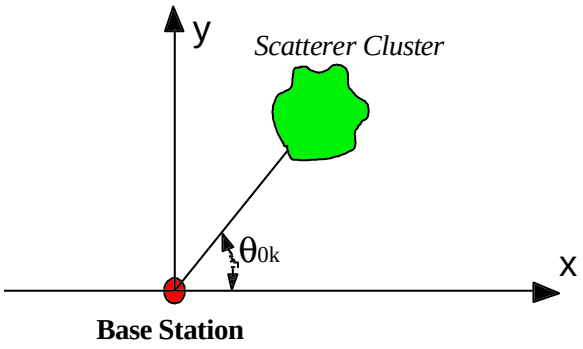

Figure 3.13: GAA model geometry.

3.4.3 Modified Saleh-Valenzuela

The final statistical channel model is the Modified Saleh-Valenzuela model [43, 44]. The model was developed by characterizing joint angle of arrival and time of arrival measurements that were taken inside two campus buildings. The model assumes that both the AOA and TOA statistics are independent, and that the signal arrives at the base-station in clusters in both AOA and TOA.

The time of arrival of both clusters and the rays within each cluster assume a Poisson distribution. Additionally it was found that the AOA of the clusters was uniformly distributed over the range $[0, 2\pi]$, and that the AOA of the rays within each cluster were well modeled by a Laplacian distribution.

3.5 Summary

In this chapter various propagation mechanisms including reflection, scattering, and diffraction were considered. One possible classification of vector channel models into geometrically based or statistically based models was described. Finally a brief description of several vector channel models was given. Further details of two of these models, the circular model and Liberti's model are presented in the next chapter.

Chapter 4

Details of Two Vector Channel Models

In this chapter further details of the circular and Liberti's elliptical vector channel models that were presented in the previous chapter are derived. These models were selected for further analysis due to their popularity for modeling macrocell and microcell environments respectively. The joint AOA-TOA, marginal AOA, and marginal TOA probability density functions (pdfs) as seen from both the base station and the mobile are found. The pdfs for the elliptical model were previously derived in [24]. However, here a more general approach is used that allows the density functions for both models to be derived using a common approach. The derived pdfs corresponding to the circular model are original contributions of this work.

Also derived is a novel approach for calculating the Doppler spectrum from the joint power-Doppler density function. Typically, the signal power is assumed to be independent of the Doppler frequency. However, based on the geometrically based channel model, the signal power and Doppler frequency are not independent. A method to determine the Doppler spectrum in the presence of correlation between the signal power level and Doppler frequency is derived, and applied to both the circular and elliptical models. Finally, an efficient procedure is given that can be used to generate samples from these models.

4.1 Notation and Geometry

Figure 4.1 shows the geometry and notation used to derive the geometrically based single bounce channel models. The mobile is separated from the base by the distance, D. Although only one scatter is shown in the figure it is assumed that there exists some statistical scatterer density function, $f_{x,y}(x, y)$. Hence, the results derived here apply to the ensemble of randomly located scatterers and make no assumptions about the number of multipath components present at any one time.

The following assumptions are common to both the elliptical and circular models [26].

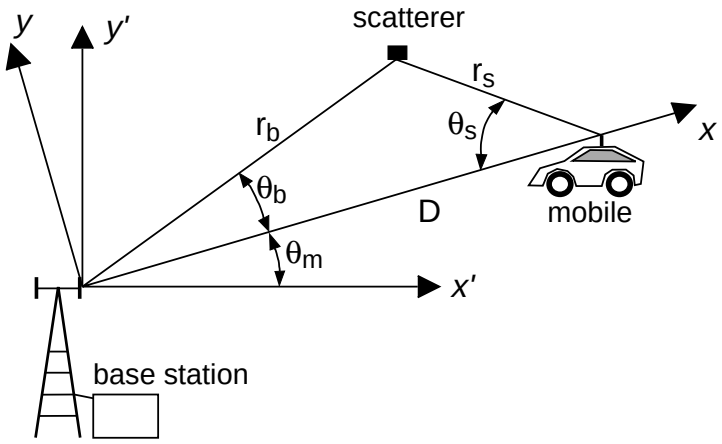

Figure 4.1: Notation and Scatterer geometry.

1. The signals received at the base station are plane waves propagating along the horizon, ie.) there is no vertical component to the signal propagation.
2. Scatterers are omni-directional re-radiating elements.
3. The signals that are scattered from each scatterer are not affected by the presence of the other scatterers in the channel.
4. The scatterers have identical scattering coefficients.
5. Received signals experience an exponential path loss model in the channel characterized by the path loss exponent, n.

4.2 Joint TOA-AOA Density Function

We first derive an expression for the most general joint pdfs and then show how these density functions simplify for particular scatterer densities. Let the joint scatterer density function be denoted by $f_{x,y}(x,y)$, where for convenience we have defined the xy coordinate system such that the mobile lies on the x-axis as shown in Figure 4.1. It will be useful to express the joint scatterer density function with respect to the polar coordinates, (r_b, θ_b) as an intermediate step before deriving the joint TOA-AOA density function. The polar coordinates are related to the rectangular coordinates via the following set of equations,

$$r_b = \sqrt{x^2 + y^2} \tag{4.1}$$

$$\theta_b = \text{atan}\left(\frac{y}{x}\right) \tag{4.2}$$

$$x = r_b \cos(\theta_b) \tag{4.3}$$

$$y = r_b \sin(\theta_b), \tag{4.4}$$

where (x, y) denotes the location of the scatterer.

The joint density $f_{r_b,\theta_b}(r_b,\theta_b)$ is found using [18]

$$f_{r_b,\theta_b}(r_b,\theta_b) = \left.\frac{f_{x,y}(x,y)}{|J(x,y)|}\right|_{\substack{x=r_b\cos(\theta_b)\\ y=r_b\sin(\theta_b)}} \tag{4.5}$$

where $J(r_s,\theta_s)$ is the Jacobian of the transformation given by

$$J(x,y) = \begin{vmatrix} \frac{\partial x}{\partial r_b} & \frac{\partial x}{\partial \theta_b} \\ \frac{\partial y}{\partial r_b} & \frac{\partial y}{\partial \theta_b} \end{vmatrix}^{-1} = \begin{vmatrix} \cos(\theta_b) & -r_b\sin(\theta_b) \\ \sin(\theta_b) & r_b\cos(\theta_b) \end{vmatrix}^{-1} = \frac{1}{r_b}. \tag{4.6}$$

Substituting (4.6) into (4.5) gives,

$$f_{r_b,\theta_b}(r_b,\theta_b) = |r_b|\, f_{x,y}(r_b\cos(\theta_b), r_b\sin(\theta_b)). \tag{4.7}$$

If we restrict r_b to be positive then (4.7) reduces to,

$$f_{r_b,\theta_b}(r_b,\theta_b) = r_b\, f_{x,y}(r_b\cos(\theta_b), r_b\sin(\theta_b)). \tag{4.8}$$

The next step is to derive the joint TOA-AOA density function $f_{\tau,\theta}(\tau,\theta)$ where τ is the delay of the particular multipath component. Applying the law of cosines to the triangle shown in Figure 4.1 gives,

$$r_s^2 = D^2 + r_b^2 - 2r_bDcos(\theta_b). \tag{4.9}$$

The total path propagation distance is given by,

$$d = r_b + r_s = r_b + \sqrt{D^2 + r_b^2 - 2r_bD\cos(\theta_b)}. \tag{4.10}$$

Squaring both sides of (4.10), and solving for r_b gives the following relationship between the polar coordinate radius, r_b and the propagation distance d:

$$r_b = \frac{D^2 - d^2}{2(D\cos(\theta_b) - d)}. \tag{4.11}$$

The time of arrival of the signal, τ is related to the propagation distance by the velocity of propagation c by the relationship $d = \tau c$. Substituting $d = \tau c$ into (4.11) gives

$$r_b = \frac{D^2 - \tau^2c^2}{2(D\cos(\theta_b) - \tau c)}. \tag{4.12}$$

The joint density is given by

$$f_{\tau,\theta_b}(\tau,\theta_b) = \left.\frac{f_{r_b,\theta_b}(r_b,\theta_b)}{|J(r_b,\theta_b)|}\right|_{r_b=\frac{D^2-\tau^2c^2}{2(D\cos(\theta_b)-\tau c)}}. \tag{4.13}$$

where $J(x,y)$ is the Jacobian transformation given by

$$J(r_b,\theta_b) = \left|\frac{\partial r_b}{\partial \tau}\right|^{-1}. \tag{4.14}$$

Taking the reciprocal of the partial derivative of Eq. (4.12) with respect to τ gives the Jacobian,

$$J(r_b, \theta_b) = \frac{2(D\cos(\theta_b) - \tau c)^2}{D^2 c + \tau^2 c^3 - 2\tau c^2 D\cos(\theta_b))}. \tag{4.15}$$

Substituting (4.15) into (4.13) gives

$$f_{\tau,\theta_b}(\tau, \theta_b) = \frac{D^2 c + \tau^2 c^3 - 2\tau c^2 D\cos(\theta_b)}{2(D\cos(\theta_b) - \tau c)^2} f_{r_b,\theta_b}\left(\frac{D^2 - \tau^2 c^2}{2(D\cos(\theta_b) - \tau c)}, \theta_b\right) \tag{4.16}$$

Next, we may express the joint TOA-AOA density in terms of the original joint scatterer density function using Eq. (4.8) and (4.12). The resulting joint density function becomes,

$$f_{\tau,\theta_b}(\tau, \theta_b) = \frac{(D^2 - \tau^2 c^2)(D^2 c + \tau^2 c^3 - 2\tau c^2 D\cos(\theta_b))}{4(D\cos(\theta_b) - \tau c)^3} f_{x,y}(r_b\cos(\theta_b), r_b\sin(\theta_b)) \tag{4.17}$$

where r_b is given by Eq. (4.12). Eq. (4.17) expresses the joint TOA/AOA observed at the base station in terms of a general joint scatterer density. The special case of a uniform scatter density will be explored in the next section.

4.2.1 Uniform Scatterer Densities

When the scatterers are distributed based upon a uniform pdf within an arbitrarily shaped region, R_A, with area, A, then the joint scatterer density function is given by,

$$f_{x,y}(x, y) = \begin{cases} \frac{1}{A} & : \quad x \text{ and } y \in R_A \\ 0 & : \quad else. \end{cases} \tag{4.18}$$

In this special case the joint TOA/AOA density function reduces to

$$f_{\tau,\theta_b}(\tau, \theta_b) = \frac{(D^2 - \tau^2 c^2)(D^2 c + \tau^2 c^3 - 2\tau c^2 D\cos(\theta_b))}{4A(D\cos(\theta_b) - \tau c)^3}, \tag{4.19}$$

where the appropriate range of τ and θ are assumed.

Eq. (4.19) gives the joint TOA-AOA pdf related to the base station. Since the form of the original uniform scatterer density is independent of a rotation and translation of the coordinate system and the relationship between r_b and τ is identical in form to the relationship between r_s and τ, namely,

$$r_s = \frac{D^2 - \tau^2 c^2}{2(D\cos(\theta_s) - \tau c)}, \tag{4.20}$$

repeating the derivation with respect to the angle of arrival at the mobile gives

$$f_{\tau,\theta_s}(\tau, \theta_s) = \frac{(D^2 - \tau^2 c^2)(D^2 c + \tau^2 c^3 - 2\tau c^2 D\cos(\theta_s))}{4A(D\cos(\theta_s) - \tau c)^3}. \tag{4.21}$$

Hence, $f_{\tau,\theta_b}(\tau, \theta_b)$ and $f_{\tau,\theta_s}(\tau, \theta_s)$ have the same form. However, the range of θ_b for which Eq. (4.19) is valid will in general be different from the range over which θ_s is valid in Eq. (4.21).

Figure 4.2 shows the shape of the general joint pdf on a log scale corresponding to a uniform scatterer density function. The plot assumes that the entire x-y plane has a uniform scatterer density. When uniform scatterers are restricted to a given region in the x-y plane, then the corresponding points in the general joint pdf will be present in the new joint pdf (ie., the shape will be the same where the new pdf is nonzero, but there will be regions that are zero in the new pdf that are not zero in the general pdf). Clearly the amplitude will be scaled when considering different regions, but the relative amplitudes will remain constant.

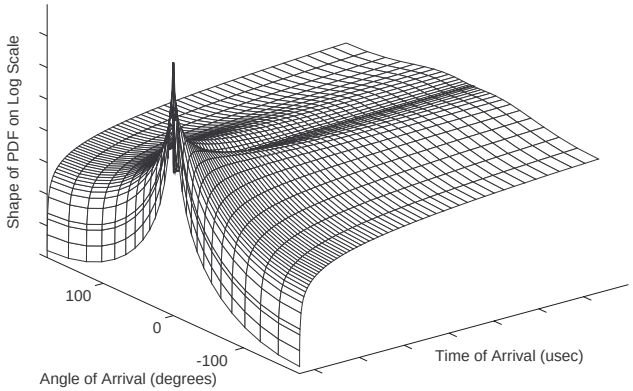

Figure 4.2: Shape of joint TOA-AOA pdf for uniform scatterers (log-scale).

4.3 Marginal Densities

4.3.1 AOA Density Function

Although the marginal AOA density function could possibly be found by integrating the joint AOA-TOA density function over τ, a more promising approach is to integrate the polar coordinate system representation of the scatterer density function given in (4.8) with respect to r_b over the range $r_{b1}(\theta_b)$ to $r_{b2}(\theta_b)$,

$$f_{\theta_b}(\theta_b) = \int_{r_{b1}(\theta_b)}^{r_{b2}(\theta_b)} f_{r_b,\theta_b}(r_b,\theta_b)dr_b = \int_{r_{b1}(\theta_b)}^{r_{b2}(\theta_b)} r_b f_{x,y}(r_b\cos(\theta_b), r_b\sin(\theta_b))dr_b. \tag{4.22}$$

Figure 4.3 shows the definitions of $r_{b1}(\theta_b)$ and $r_{b2}(\theta_b)$ for an arbitrary scatterer region. For a uniform scatterer density with $f_{x,y}(x,y) = \frac{1}{A}$, then

$$f_{\theta_b}(\theta_b) = \int_{r_{b1}(\theta_b)}^{r_{b2}(\theta_b)} \frac{1}{A} r_b \; dr_b = \frac{1}{2A}\left(r_{b2}^2(\theta_b) - r_{b1}^2(\theta_b)\right). \tag{4.23}$$

The functions $r_{b1}(\theta_b)$ and $r_{b2}(\theta_b)$ may be obtained from the polar coordinate representations of the scatterer density functions. When the base station is located within the scatterer region

then $r_{b1}(\theta_b) = 0$ and the marginal AOA density function reduces to

$$f_{\theta_b}(\theta_b) = \frac{1}{2A} r_{b2}^2(\theta_b). \tag{4.24}$$

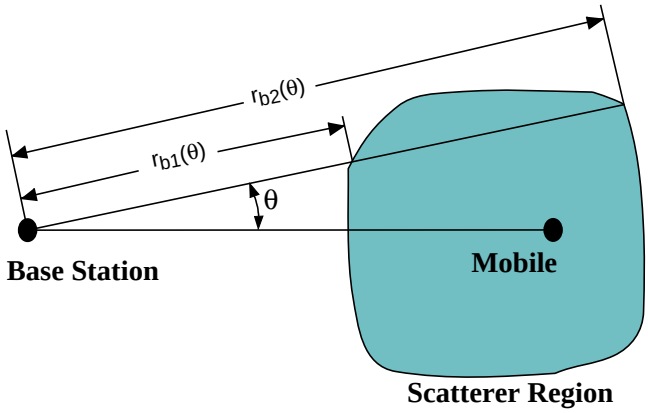

Figure 4.3: Geometry used to calculate the AOA pdf.

The same equations apply at the mobile when the joint scatterer density is referred to the polar coordinate system, (r_s, θ_s) defined at the mobile. Hence the marginal AOA pdf at the mobile may be found by,

$$f_{\theta_s}(\theta_s) = \frac{1}{2A} \left(r_{s2}^2(\theta_s) - r_{s1}^2(\theta_s) \right) \tag{4.25}$$

where the functions $r_{s2}(\theta_s)$ and $r_{s1}(\theta_s)$ define the boundary of the uniform scatterer region. When the mobile is located inside of the scatterer region then $r_{s1}(\theta_s) = 0$ and the marginal AOA pdf at the mobile becomes

$$f_{\theta_s}(\theta_s) = \frac{1}{2A} r_{s2}^2(\theta_s). \tag{4.26}$$

These results will be used to find the AOA pdfs for the elliptical and circular models in the corresponding sections below.

4.3.2 TOA Density Function

Deriving a general TOA density function for a generic scatterer density function is difficult. An obvious approach would be to integrate the joint TOA-AOA pdf over the angle of arrival. However, even for the case of a uniform scatterer density function integrating the joint TOA-AOA pdf is nearly intractable and does not yield manageable results.

Another approach is to first derive the TOA cumulative distribution function (cdf). The TOA cdf function may be calculated as the probability of a scatterer being placed in the region contained in an ellipse corresponding to a delay equal to τ. Taking the derivative of the TOA cdf function with respect to τ gives the desired TOA marginal density function. The area of overlap of the ellipse with the scatterer region is illustrated in Figure 4.4. In general the

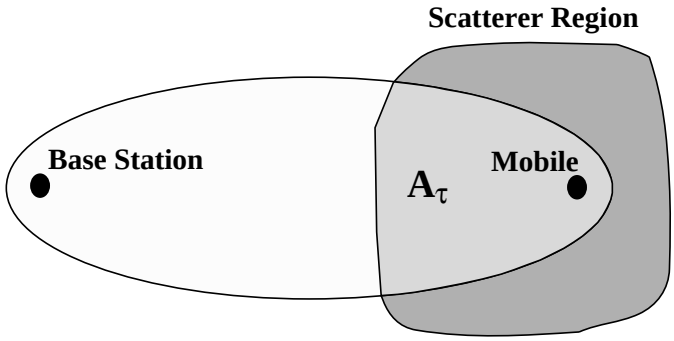

Figure 4.4: Geometry used to calculate TOA cdf.

probability associated with the area (which is equal to the TOA cdf) will involve the double integral over the joint scatterer density function.

For the case of a uniform scatterer density function the TOA cdf will be given by

$$F(\tau) = \frac{A_\tau(\tau)}{A} \tag{4.27}$$

where $A_\tau(\tau)$ is the area of intersection of the scatterer region with the ellipse with delay of τ. Taking the derivative with respect to τ gives the desired TOA density function,

$$f_\tau(\tau) = \frac{1}{A}\frac{d}{d\tau}\left(A_\tau(\tau)\right). \tag{4.28}$$

The function $A_\tau(\tau)$ and the approach used to find this area is dependent upon the form of the scatterer density function.

A final comment regarding the TOA density function is that the TOA density function observed at the base station is exactly the same as the TOA density function seen at the mobile. This is true since the distance traveled between the mobile and the base station for a given scatterer is independent of the perspective.

4.4 Doppler Spectrum Analysis

In this section a novel approach to calculating the Doppler spectrum from the joint power-Doppler density is derived that accounts for correlations between the signal power and the Doppler frequency. If an exponential path loss model is assumed then multipath components that travel a shorter distance will have greater power. Since the TOA statistics vary with AOA, the signal power level, being a function of TOA, will be dependent upon AOA. Furthermore, since the Doppler frequency is a function of the AOA, the signal power level may also be viewed as a function of the Doppler frequency.

The Doppler shift is given by $f_d = f_m \cos(\theta_s - \theta_v)$, where $f_m = v/\lambda$ is the maximum Doppler shift, θ_s is angle of arrival of the signal, and θ_v is the direction the mobile is traveling [11]. For

a continuous wave signal, the baseband received signal representation is

$$r(t) = \alpha e^{j2\pi f_d t}, \tag{4.29}$$

where α is the complex amplitude of the received signal that is a function of both the transmit power and path loss. The power spectral density of the signal is given by [45]

$$S_r(f) = \lim_{T\to\infty} \frac{1}{2T} E\{\mathcal{F}_T(f)\mathcal{F}_T^*(f)\}, \tag{4.30}$$

where $\mathcal{F}_T(f)$ is the finite time Fourier transform of $r(t)$. The finite time Fourier transform of $r(t)$ is

$$\begin{aligned}
\mathcal{F}_T(f) &= \int_{-T}^{T} \alpha e^{j2\pi f_d t} e^{-j2\pi f t} dt = \int_{-T}^{T} \alpha e^{j2\pi (f_d - f) t} dt && (4.31)\\
&= \frac{\alpha}{j2\pi(f_d - f)} \left[e^{j2\pi(f_d - f)T} - e^{-j2\pi(f_d - f)T} \right] && (4.32)\\
&= \frac{\alpha}{\pi(f_d - f)} \sin(2\pi(f_d - f)T) = 2\alpha T \frac{\sin(2\pi(f_d - f)T)}{2\pi(f_d - f)T}. && (4.33)
\end{aligned}$$

Substituting (4.33) into (4.30) gives,

$$\begin{aligned}
S_r(f) &= \lim_{T\to\infty} \frac{1}{2T} E\left\{ 2\alpha T \frac{\sin(2\pi(f_d - f)T)}{2\pi(f_d - f)T} \cdot 2\alpha^* T \frac{\sin(2\pi(f_d - f)T)}{2\pi(f_d - f)T} \right\}, && (4.34)\\
&= \lim_{T\to\infty} \frac{1}{2T} E\left\{ 4|\alpha|^2 T^2 \left(\frac{\sin(2\pi(f_d - f)T)}{2\pi(f_d - f)T} \right)^2 \right\} && (4.35)\\
&= E\left\{ 4|\alpha|^2 \cdot \lim_{T\to\infty} \frac{T}{2} \left(\frac{\sin(2\pi(f_d - f)T)}{2\pi(f_d - f)T} \right)^2 \right\} && (4.36)\\
&= E\left\{ |\alpha|^2 \delta(f_d - f) \right\}. && (4.37)
\end{aligned}$$

Previously it was assumed that $|\alpha|$ is a constant which is then pulled outside of the expectation [24]. However, a more general result can be obtained by assuming that α and f_d are indeed correlated with each other. The power associated with a complex exponential is $p = |\alpha|^2$. Substituting p into the expression for the PSD gives,

$$\begin{aligned}
S_r(f) &= E\left\{ p\ \delta(f_d - f) \right\} && (4.38)\\
&= \int_{-\infty}^{\infty} \int_{-\infty}^{\infty} p\ \delta(f_d - f)\ f_{p,f_d}(p, f_d)\ dp\ df_d && (4.39)\\
&= \int_{-\infty}^{\infty} \int_{-\infty}^{\infty} p\ \delta(f_d - f)\ \frac{f_{p,f_d}(p, f_d)}{f_{f_d}(f_d)}\ f_{f_d}(f_d)\ dp\ df_d && (4.40)\\
&= \int_{-\infty}^{\infty} \int_{-\infty}^{\infty} p\ \delta(f_d - f)\ f_{p|f_d}(p|f_d)\ f_{f_d}(f_d)\ dp\ df_d && (4.41)
\end{aligned}$$

$$= \int_{-\infty}^{\infty} \left[\int_{-\infty}^{\infty} p f_{p|f_d}(p|f_d) dp \right] \delta(f_d - f)\ f_{f_d}(f_d)\ df_d \tag{4.42}$$

$$= \int_{-\infty}^{\infty} E\{p|f_d\}\, \delta(f_d - f)\ f_{f_d}(f_d)\ df_d \tag{4.43}$$

$$= E\{p|f\} \cdot f_{f_d}(f), \tag{4.44}$$

where $f_{p,f_d}(p, f_d)$ is the joint power-Doppler density function, $f_{f_d}(f_d)$ is the marginal Doppler density function, and $f_{p|f_d}(p|f_d)$ is the conditional power density function given the Doppler frequency. Using Eq. (4.44) the Doppler PSD that occurs when the signal power is correlated with the Doppler frequency can be determined.

For simplicity, one may consider the Doppler spectrum corresponding to only a single component. Generalization of the result to account for an arbitrary number of scattering points is straightforward, provided that each of the multipath components are independent. With this restriction the PSD that will result for L multipath signals is simply L times the PSD of a single path since the power of independent signals is additive.

When viewed from the perspective of a joint power-Doppler density function, (4.44) is an intuitive result. Clearly, the long term average power associated with a given frequency component is equal to the average power associated with the particular frequency multiplied by the probability of the occurrence of the frequency.

The PSD can be related to the joint power-Doppler density function, $f_{p,f_d}(p, f_d)$ by using the definition of the conditional expectation,

$$PSD = E\{p|f\} \cdot f_{f_d}(f) = \int_{p_l}^{p_u} p\ f_{p|f_d}(p|f_d)\ f_{f_d}(f)\ dp = \int_{p_l}^{p_u} p\ f_{p,f_d}(p, f_d)\ dp, \tag{4.45}$$

where the upper and lower limits, p_u and p_l, are in general functions of the Doppler frequency, f_d.

To evaluate (4.45) we begin by calculating the joint angle-power density function, $f_{p,\theta_s}(p, \theta_s)$. Here we will consider only a uniform scatterer density. The power will be related to the multipath propagation distance, d, by

$$p = p_0 \left(\frac{d}{D} \right)^{-n} = p_0 \left(\frac{\tau c}{D} \right)^{-n}, \tag{4.46}$$

where p_0 is the power level of the direct path signal (at distance D), and n is the path loss exponent. Solving (4.46) for τ gives,

$$\tau = \frac{D}{c} \left(\frac{p}{p_0} \right)^{-\frac{1}{n}}. \tag{4.47}$$

The joint density $f_{p,\theta_s}(\tau, \theta_s)$ is found using

$$f_{p,\theta_s}(p, \theta_s) = \left. \frac{f_{\tau,\theta_s}(\tau, \theta_s)}{|J(\tau, \theta_s)|} \right|_{\tau = \frac{D}{c}\left(\frac{p}{p_0}\right)^{-\frac{1}{n}}} \tag{4.48}$$

where $|J(\tau,\theta_s)| = \frac{n\ c\ p_0}{D}\left(\frac{p}{p_0}\right)^{\frac{n+1}{n}}$ is the Jacobian transformation. Hence, the joint power-angle pdf is given by

$$f_{p,\theta_s}(p,\theta_s) = \frac{D^2\left(1-\left(\frac{p}{p_0}\right)^{-2/n}\right)\left(1+\left(\frac{p}{p_0}\right)^{-2/n}-2\left(\frac{p}{p_0}\right)^{-1/n}\cos(\theta_s)\right)}{4Anp_0\left(\frac{p}{p_0}\right)^{(n+1)/n}\left(\cos(\theta_s)-\left(\frac{p}{p_0}\right)^{-1/n}\right)^3}. \tag{4.49}$$

The next step is to determine the joint power-Doppler frequency pdf using the fact that the Doppler frequency is given by

$$f_d = f_m\cos(\theta_s-\theta_v), \tag{4.50}$$

where $f_m = \frac{v}{\lambda}$ is the maximum possible Doppler shift, v is the speed of the mobile, λ is the carrier wavelength, and θ_v is the direction the mobile is traveling. Using this transformation of variables the joint density becomes,

$$f_{p,f_d}(p,f_d) = \sum_{i=1}^{2}\frac{D^2\left(1-\left(\frac{p}{p_0}\right)^{-2/n}\right)\left(1+\left(\frac{p}{p_0}\right)^{-2/n}-2\left(\frac{p}{p_0}\right)^{-1/n}\cos(\theta_i)\right)}{4Anp_0\left(\frac{p}{p_0}\right)^{(n+1)/n}\left(\cos(\theta_i)-\left(\frac{p}{p_0}\right)^{-1/n}\right)^3 f_m\sqrt{1-(f_d/f_m)^2}}, \tag{4.51}$$

where

$$\theta_{s_i} = \theta_i = \begin{cases} \theta_v + \operatorname{acos}(\frac{f_d}{f_m}) & : \quad i=1 \\ \theta_v - \operatorname{acos}(\frac{f_d}{f_m}) & : \quad i=2. \end{cases}$$

Substituting (4.51) into (4.45) gives

$$PSD(f_d) = \int_{p_l}^{p_u}\sum_{i=1}^{2}\frac{pD^2\left(1-\left(\frac{p}{p_0}\right)^{-2/n}\right)\left(1+\left(\frac{p}{p_0}\right)^{-2/n}-2\left(\frac{p}{p_0}\right)^{-1/n}\cos(\theta_i)\right)}{4Anp_0\left(\frac{p}{p_0}\right)^{(n+1)/n}\left(\cos(\theta_i)-\left(\frac{p}{p_0}\right)^{-1/n}\right)^3 f_m\sqrt{1-(f_d/f_m)^2}}dp. \tag{4.52}$$

Since the nonzero region of the pdf is dependent upon the AOA, when moving the integration inside the summation it is necessary to denote the limits of integration as $p_u(i)$ and $p_l(i)$ to give,

$$PSD(f_d) = \sum_{i=1}^{2}\int_{p_l(i)}^{p_u(i)}\frac{pD^2\left(1-\left(\frac{p}{p_0}\right)^{-2/n}\right)\left(1+\left(\frac{p}{p_0}\right)^{-2/n}-2\left(\frac{p}{p_0}\right)^{-1/n}\cos(\theta_i)\right)}{4Anp_0\left(\frac{p}{p_0}\right)^{(n+1)/n}\left(\cos(\theta_i)-\left(\frac{p}{p_0}\right)^{-1/n}\right)^3 f_m\sqrt{1-(f_d/f_m)^2}}dp. \tag{4.53}$$

Making the variable substitution, $x = \left(\frac{p}{p_0}\right)^{-1/n}$ simplifies the integral considerably

$$PSD(f_d) = \sum_{i=1}^{2}\int_{x_l(i)}^{x_u(i)}\frac{-D^2(1-x^2)(1+x^2-2x\cos(\theta_i))}{4Ax^n(\cos(\theta_i)-x)^3 f_m\sqrt{1-(f_d/f_m)^2}}dx, \tag{4.54}$$

where $x_l(i) = \left(\frac{p_l(i)}{p_0}\right)^{-1/n}$ and $x_u(i) = \left(\frac{p_u(i)}{p_0}\right)^{-1/n}$. Taking terms that do not depend upon x outside of the integral results in

$$PSD(f_d) = \frac{-D^2}{4Af_m\sqrt{1-(f_d/f_m)^2}} \sum_{i=1}^{2} \int_{x_l(i)}^{x_u(i)} \frac{(1-x^2)(1+x^2-2x\cos(\theta_i))}{x^n(\cos(\theta_i)-x)^3} dx. \tag{4.55}$$

To simplify this expression further let us define the variables,

$$K = \frac{-D^2 p_0}{4Af_m\sqrt{1-(f_d/f_m)^2}} \tag{4.56}$$

and

$$C_i = \cos(\theta_i) \tag{4.57}$$

so that the Doppler PSD may be expressed in the compact form

$$PSD(f_d) = K \sum_{i=1}^{2} \int_{x_l(i)}^{x_u(i)} \frac{(1-x^2)(1+x^2-2xC_i)}{x^n(C_i-x)^3} dx. \tag{4.58}$$

Finding a closed form expression for (4.58) when the path loss exponent, n, is left variable does not appear tractable. However, for integer path loss exponents it is possible to obtain a closed form expression using Matlab's Symbolic Toolbox (or partial fraction expansion if you prefer). For $n = 2$, then

$$\begin{aligned} PSD(f_d) &= K \sum_{i=1}^{2} \left[\frac{-2\ C_i^2 + 3}{C_i^4} \ln(x) + \frac{C_i^4 + 2\ C_i^2 - 3}{C_i^4} \ln(C_i - x) \right. \\ &+ \left. \frac{(4\ C_i^2 - 6)x^2 + (C_i^5 - 4\ C_i^3 + 9\ C_i)x - 2\ C_i^2}{2\ C_i^3 x^3 - 4\ C_i^4 x^2 + 2\ C_i^5 x} \right]_{x_l(i)}^{x_u(i)}. \end{aligned}$$

For $n = 4$, then

$$\begin{aligned} PSD(f_d) = K \sum_{i=1}^{2} \left[\frac{2\ C_i^4 - 12\ C_i^2 + 10}{C_i^6} (\ln(x) - \ln(C_i - x)) \right. \\ \left. - \frac{(12\ C_i^4 - 72\ C_i^2 + 60)x^4 + (-15\ C_i^{15} + 108\ C_i^3 - 90\ C_i)x^3 + (-24\ C_i^4 + 20\ C_i^2)x^2 + (-6\ C_i^5 + 5\ C_i^3)x + 2\ C_i^4}{6\ C_i^5 x^3 (-C + x)^2} \right]_{x_l(i)}^{x_u(i)}. \end{aligned} \tag{4.59}$$

The values $x_u(i)$ and $x_l(i)$ are themselves functions of the Doppler frequency the form of which is dependent upon the original scatterer region, $f_{x,y}(x, y)$.

The functions derived in this section will be used to calculate the Doppler Spectrum for the elliptical and circular models. The results are verified by plotting a normalized histogram generated by simulation against the analytical results.

4.5 Geometrically Based Elliptical Model (Liberti's Microcell Model)

The assumed geometry for the elliptical model is shown in Figure 4.5. Scatterers are uniformly distributed throughout the ellipse with a major axis of $c\tau_m$, where τ_m is the maximum delay associated with scatterers within the ellipse and c is the speed of light, and with foci at the base station and the mobile. The model is appropriate for microcell environments where antenna heights are relatively low. With low antennas the base station may receive multipath reflections from locations near the base station as well as around the mobile. The elliptical model has the nice physical interpretation that multipath components which arrive with a maximum delay of τ_m are accounted for by the model. One justification of the model is that signals with longer delays will experience greater path loss and hence will have relatively low power compared to those with shorter delays. Therefore, provided that τ_m is chosen sufficiently large, nearly all of the power of any multipath signals in the environment will be included in the model.

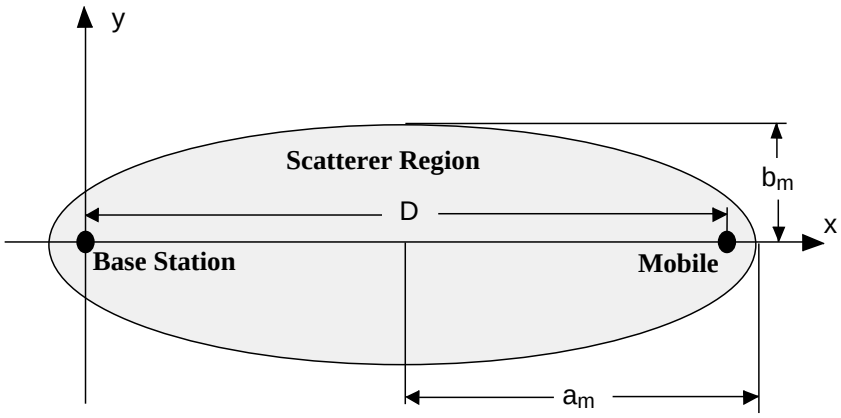

Figure 4.5: Elliptical scatterer density geometry.

The primary parameter of the model is the choice of τ_m, the maximum TOA to be considered. The parameters a_m and b_m are the semimajor axis and semiminor axis values which are given by

$$a_m = \frac{c\ \tau_m}{2} \tag{4.60}$$

$$b_m = \frac{1}{2}\sqrt{c^2\tau_m^2 - D^2}. \tag{4.61}$$

The ellipse shown in Figure 4.5 may be described by either the Cartesian equation

$$\frac{(x - \frac{D}{2})^2}{a_m^2} + \frac{y^2}{b_m^2} = 1, \tag{4.62}$$

or by the polar coordinate equation [46]

$$r_b = \frac{c^2\tau_m^2 - D^2}{2c\tau_m - 2D\cos(\theta_b)}. \tag{4.63}$$

For each of the pdfs shown below, the T-R separation was $1000m$ and the maximum delay was $\tau_m = 5u$sec. Each of the histograms that is shown to validate the closed form expressions of the pdfs is generated by placing 50,000 scatterers uniformly into the ellipse, measuring the desired property (AOA or TOA), and then creating a histogram containing 75 bins. Finally the number of points in each bin is divided by the total number of points to give the normalized histogram. In all cases there is good agreement between the closed form expression and the normalized histogram. Finally, the amplitudes of the pdfs are scaled to reflect the units shown on the independent axis.

4.5.1 Joint AOA-TOA Density Function (Elliptical Model)

Joint TOA-AOA Density Function at the Base Station

The joint AOA and TOA density function was derived in Section 4.2.1 for the case of a uniform scatterer density. The result given in (4.19) is repeated here for convenience,

$$f_{\tau,\theta_b}(\tau,\theta_b) = \frac{(D^2-\tau^2c^2)(D^2c+\tau^2c^3-2\tau c^2 D\cos(\theta_b))}{4A(D\cos(\theta_b)-\tau c)^3}. \tag{4.64}$$

The area of an ellipse is given by $A = \pi a_m b_m$. Substituting this expression into (4.64) and explicitly stating the range of validity gives

$$f_{\tau,\theta_b}(\tau,\theta_b) = \begin{cases} \frac{(D^2-\tau^2c^2)(D^2c+\tau^2c^3-2\tau c^2 D\cos(\theta_b))}{4\pi a_m b_m (D\cos(\theta_b)-\tau c)^3} & : \ \frac{D}{c} \le \tau \le \tau_m, \theta_b \neq 0 \\ \frac{c(D+\tau c)}{4\pi a_m b_m} & : \ \frac{D}{c} \le \tau \le \tau_m, \theta_b = 0 \\ 0 & : \ else. \end{cases} \tag{4.65}$$

Figures 4.6a and 4.6b show the joint TOA-AOA density function that is observed at the base station for $D = 1000m$ and $\tau_m = 5u$sec. Figure 4.6a is a plot of the closed form expression for the joint density. Figure 4.6b is a scatter plot created by placing 10000 scatterers and then plotting the corresponding TOA-AOA pairs. The plots show that there is a high concentration of scatterers with relatively small delays near the line-of-sight.

Joint TOA-AOA Density Function at the Mobile

Due to the symmetry of the ellipse with respect to the base station and the mobile, by inspection the same TOA-AOA density function will be valid when related to the angle of arrival at the mobile. The resulting joint pdf is

$$f_{\tau,\theta_s}(\tau,\theta_s) = \begin{cases} \frac{(D^2-\tau^2c^2)(D^2c+\tau^2c^3-2\tau c^2 D\cos(\theta_s))}{4\pi a_m b_m (D\cos(\theta_s)-\tau c)^3} & : \ \frac{D}{c} \le \tau \le \tau_m, \theta_s \neq 0 \\ \frac{c(D+\tau c)}{4\pi a_m b_m} & : \ \frac{D}{c} \le \tau \le \tau_m, \theta_s = 0 \\ 0 & : \ else. \end{cases} \tag{4.66}$$

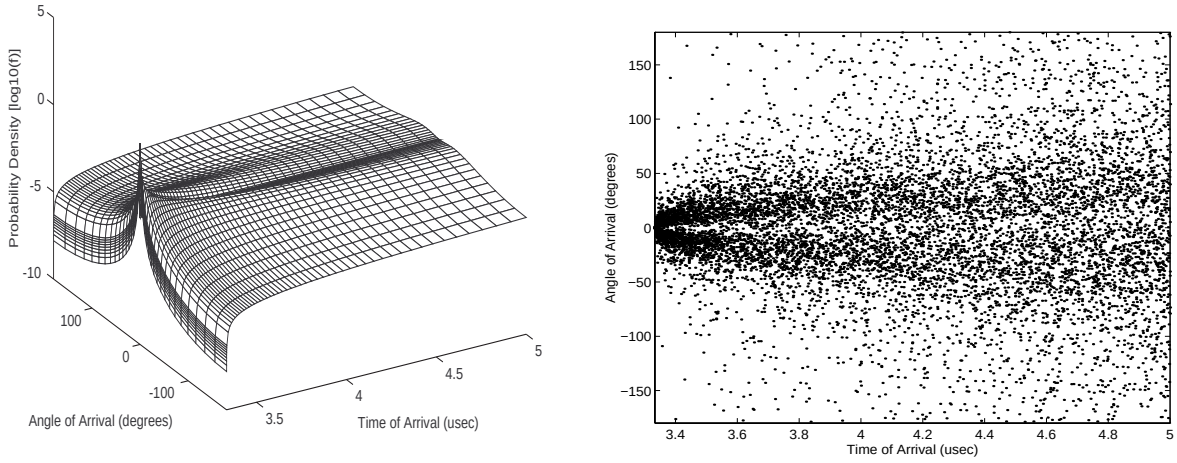

(a) pdf Closed Form Expression (Log-Scale)

(b) Scatter Plot

Figure 4.6: Joint TOA-AOA pdf for Liberti's elliptical scattering model with $D = 1000m$ and $\tau_m = 5u$sec.

4.5.2 AOA Marginal Density Function (Elliptical Model)

AOA Density Function at the Base Station

The polar equation defining the boundary of the scatterer region is

$$r_b = \frac{\tau_m^2 c^2 - D^2}{2\tau_m c - 2D\cos(\theta_b)}. \tag{4.67}$$

Since the base station is located inside the scatterer region using (4.24) the AOA pdf is

$$f_{\theta_b}(\theta_b) = \frac{1}{2A} r_{b2}^2(\theta_b) = \begin{cases} \frac{1}{8\pi a_m b_m} \left(\frac{\tau_m^2 c^2 - D^2}{\tau_m c - D\cos(\theta_b)} \right)^2 . & : \quad \theta_b \neq 0 \\ \frac{\tau_m c + D}{8\pi a_m b_m} & : \quad \theta_b = 0. \end{cases} \tag{4.68}$$

The elliptical AOA marginal pdf and the normalized histogram is plotted in Figure 4.7 for the case of $D = 1000m$ and $\tau_m = 5u$sec. As expected from the joint density function, Figure 4.7 shows that the scatterers are concentrated near line-of-sight, but all AOA are possible.

AOA Density Function at the Mobile (Elliptical Model)

Again due to the symmetry of the ellipse, the same pdf applies at the mobile, namely,

$$f_{\theta_s}(\theta_s) = \frac{1}{2A} r_{s2}^2(\theta_s) = \begin{cases} \frac{1}{8\pi a_m b_m} \left(\frac{\tau_m^2 c^2 - D^2}{\tau_m c - D\cos(\theta_s)} \right)^2 . & : \quad \theta_s \neq 0 \\ \frac{\tau_m c + D}{8\pi a_m b_m} & : \quad \theta_s = 0 \end{cases} \tag{4.69}$$

where $\theta_s = 0$ in the direction towards the mobile and increases in a clockwise direction.

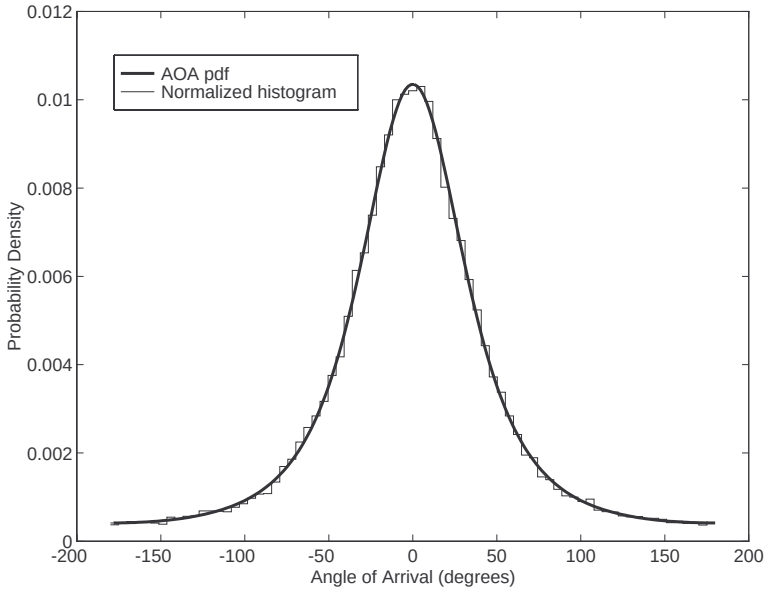

Figure 4.7: AOA pdf for the elliptical scattering model.

4.5.3 TOA Marginal Density Function (Elliptical Model)

As derived above, the marginal TOA density function may be calculated using

$$f_\tau(\tau) = \frac{1}{A}\frac{d}{d\tau}\left(A_\tau(\tau)\right), \tag{4.70}$$

where $A_\tau(\tau)$ is the area of intersection of the ellipse corresponding to a delay of τ with the uniform scatterer region. For the case of a concentric elliptical scatterer density, $A_\tau(\tau)$ is the area of the ellipse itself. The area of an ellipse is given by

$$A_\tau(\tau) = \pi a_\tau b_\tau = \frac{\pi\tau c}{4}\sqrt{\tau^2c^2 - D^2}. \tag{4.71}$$

Taking the derivative with respect to τ and simplifying gives,

$$\frac{d}{d\tau}\left(A_\tau(\tau)\right) = \frac{\pi c(2\tau^2c^2 - D^2)}{4\sqrt{\tau^2c^2 - D^2}} \tag{4.72}$$

Dividing by $A = \pi a_m b_m$ gives the marginal TOA density function,

$$f_\tau(\tau) = \begin{cases} \frac{c(2\tau^2c^2 - D^2)}{4a_m b_m\sqrt{\tau^2c^2 - D^2}} & : \quad \frac{D}{c} \le \tau \le \tau_m \\ 0 & : \quad else \end{cases} \tag{4.73}$$

Figure 4.8 is a plot of the TOA marginal pdf function and the normalized histogram. Figure 4.8 shows that there is a high density of scatterers with relatively small delays.

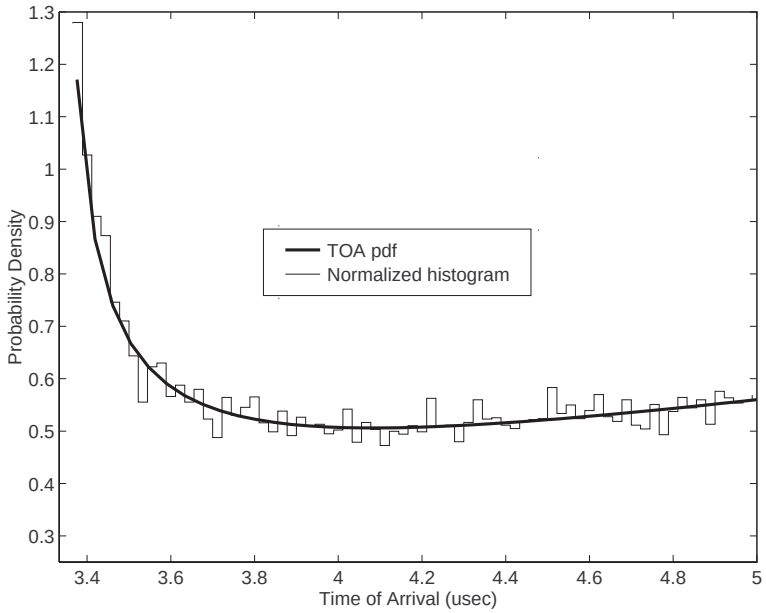

Figure 4.8: TOA pdf for the elliptical scattering model.

4.5.4 Doppler Spectrum (Elliptical Model)

The Doppler spectrum was derived above in Section 4.4 for uniform scatterer density functions. The only parameters that were not specified above were the values of $x_u(i)$ and $x_l(i)$. In this section, these functions are evaluated for the special case of the elliptical scatterer density function. In the derivation above, for convenience the variable substitution,

$$x = \left(\frac{p}{p_0}\right)^{-\frac{1}{n}} \tag{4.74}$$

was made. The functions that we are seeking $x_u(i)$ and $x_l(i)$ are the resulting upper and lower limits respectively, where the original limits were p_u and p_l which are the maximum and minimum signal power levels as a function of the Doppler frequency, respectively. By plugging the original limits into (4.74) we may express the new limits in terms of p_u and p_l. This results in,

$$x_u(i) = \left(\frac{p_u}{p_0}\right)^{-\frac{1}{n}} \tag{4.75}$$

and

$$x_l(i) = \left(\frac{p_l}{p_0}\right)^{-\frac{1}{n}}. \tag{4.76}$$

Regardless of the geometry, the maximum power will correspond to the line of site components. For convenience this power was set to p_0, hence

$$x_u(i) = p_0. \tag{4.77}$$

Note that although technically only the Doppler frequency which corresponds to scatterers along the line-of-sight will have the maximum power of p_0, the maximum power for all other Doppler frequencies will be $p_0 - \epsilon$, where ϵ may be made arbitrarily small since each ray from the mobile may be made arbitrarily close to the line-of-sight and thus (4.77) is justified.

The lower limit is dependent upon the minimum power at the Doppler frequency of interest. For the elliptical geometry, regardless of AOA at the mobile, the minimum power will given by

$$p_l = p_0 \left(\frac{\tau_m c}{D} \right)^{-n} \tag{4.78}$$

and the corresponding limit for x is

$$x_l(i) = \left(\frac{p_l}{p_0} \right)^{-1/n} = \frac{\tau_m c}{D}. \tag{4.79}$$

Substituting these values into the expression derived in Section 4.4 for path loss exponents of $n = 2$ and $n = 4$ gives the desired closed form expression for the Doppler PSD.

Figures 4.9a and 4.9b show the Doppler PSD that results for a path loss exponent of $n = 2$, with $\theta_v = 0$ and $\theta_v = \frac{\pi}{2}$ respectively. Similarly, Figures 4.10a and 4.10b show the Doppler PSD that results for a path loss exponent of $n = 4$, with $\theta_v = 0$ and $\theta_v = \frac{\pi}{2}$ respectively. For convenience p_0=1W. Also shown in the figures are normalized histograms that were generated using simulation to validate the mathematical expressions. The Doppler frequency is normalized by f_m, the maximum Doppler frequency.

Also shown in Figures 4.9 and 4.10 are the Doppler spectrums that result assuming Clarke's Model, and assuming the the power is independent of the Doppler frequency as was done in [24]. Clarke's Model assumes that the AOA pdf is uniformly distributed about the mobile and that the signal power level is some fixed constant. Clarke's model gives [24],

$$PSD = \frac{A_0^2}{\pi f_m \sqrt{1 - (f/f_m)^2}}, |f| \leq f_m, \tag{4.80}$$

where A_0^2 is a function of the signal amplitudes. The uncorrelated power allows for an arbitrary AOA pdf, but assumes that the signal power is independent of AOA. The resulting PSD is [24],

$$PSD = \frac{A_0^2}{f_m \sqrt{1 - (f/f_m)^2}} \left[f_{\theta_s}(\theta_v + |\text{acos}(f/f_m)|) + f_{\theta_s}(\theta_v - |\text{acos}(f/f_m)|) \right]. \tag{4.81}$$

Although a method is shown in [24] of how to account for directional antennas which will result in a dependence of the effective signal amplitude on the Doppler frequency, the phenomena being modeled is the antenna pattern and not the multipath scattering environment. The dependence on signal amplitude with direction of arrival due to the path-loss model was not considered in the calculation of the Doppler spectrum [24].

For comparison, the constant power used for Clarke's Model and for the uncorrelated power plots was set equal to the average power found for the geometrically based elliptical model that assumes a path loss model. There is a significant difference in the Doppler spectrum when $\theta_v = \frac{\pi}{2}$ and only a subtle difference when $\theta_v = 0$ between the path loss model and the uncorrelated power models.

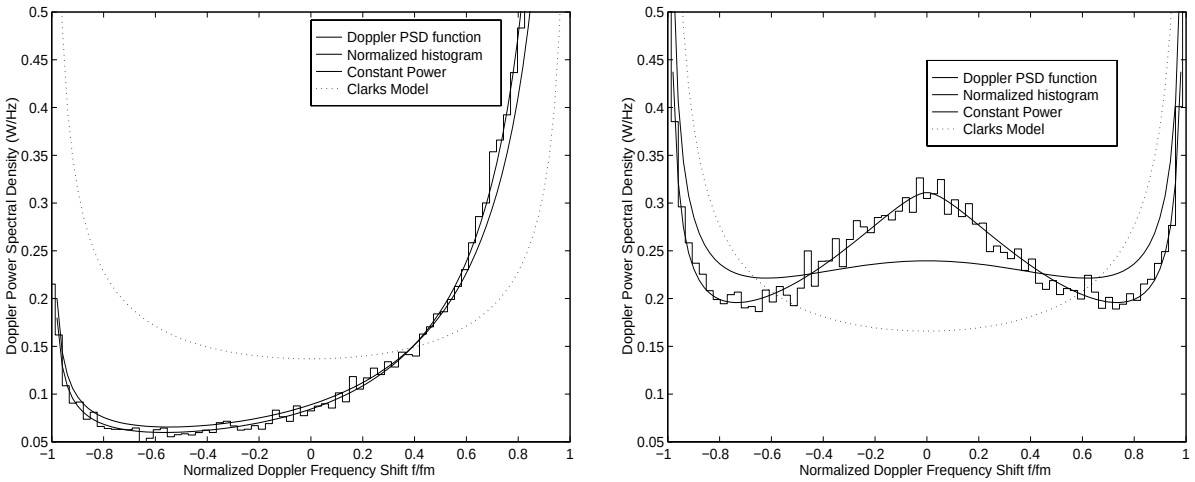

(a) $\theta_v = 0$ (b) $\theta_v = \frac{\pi}{2}$

Figure 4.9: Doppler PSD for the elliptical scattering model for $n = 2$.

4.5.5 Generation of Samples of the Elliptical Model

For simulation purposes, it is useful to develop an efficient algorithm for generating samples from the model. It is possible to generate samples from the joint density functions as described in [25]. However, it turns out that a much more efficient procedure can be obtained by using the definition of the original scatterer geometry. The process is to simply uniformly place scatterers in the ellipse and then derive the relevant signal parameters from the coordinates of the scatterer.

To uniformly place samples in an ellipse of the form,

$$\frac{x^2}{a_m^2} + \frac{y^2}{b_m^2} = 1, \tag{4.82}$$

we begin by first uniformly placing samples in a circle with unit radius and then scaling the resulting x and y coordinates by a_m and b_m respectively. The resulting random variables will be uniformly distributed in the desired ellipse.

A detailed algorithm that may be used to carry out the steps described above for each scattering component is given below. Here it is assumed that the programmer has access to a uniform random number generator over the interval [0,1].

1. Let u_1 be uniformly distributed in [0,1].
2. Calculate $\phi = 2\pi(u_1 - 0.5)$.
3. Let u_2 be uniformly distributed in [0,1].
4. Calculate $r = \sqrt{u_2}$.

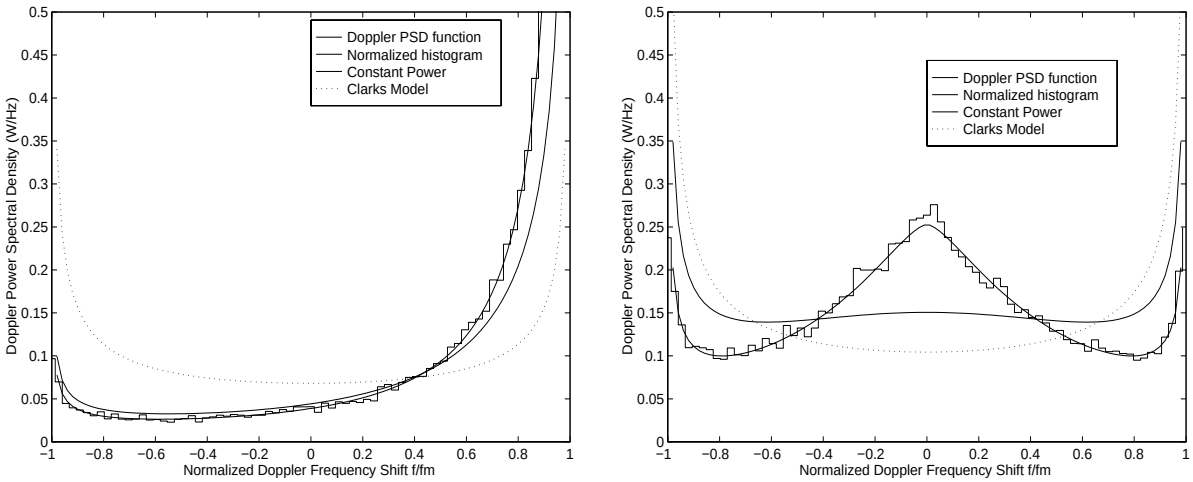

(a) $\theta_v = 0$ (b) $\theta_v = \frac{\pi}{2}$

Figure 4.10: Doppler PSD for the elliptical scattering model for $n = 4$.

5. Calculate $x_e = a_m\ r\cos(\phi) + \frac{D}{2}$ and $y_e = b_m\ r\sin(\phi)$.
6. Calculate path distance, $d = \sqrt{x_e^2 + y_e^2} + \sqrt{(D - x_e)^2 + y_e^2}$.
7. The transmit to receive delay will be $\tau = d/c$.
8. Angle of arrival at the mobile is $\theta = \text{atan}(y_e/(x_e - D))$.
9. Angle of arrival at the base station is $\beta = \text{atan}(y_e/x_e)$.

4.6 Geometrically Based Circular Model (Macrocell Model)

The geometry of the geometrically based circular model (GBCM) (also referred to as the geometrically based single bounce macrocell model [26]) is shown in Figure 4.11. The model assumes that the scatterers lie within a radius, R_m about the mobile. Often the requirement that $R_m < D$ is imposed. The GBCM is based upon the assumption that in macrocell environments where antenna heights are relatively high there will be no signal scattering from locations near the base station.

Although it is relatively easy to extend the density functions derived below to allow any value of R_m, to maintain the premise of the model that scatterers are not located about the mobile, we consider here only the case where $R_m < D$. Each of the histograms that is shown to validate the closed form expressions of the pdfs were generated as described above for the elliptical model. Again there is good agreement between all of the normalized histograms and the corresponding pdfs.

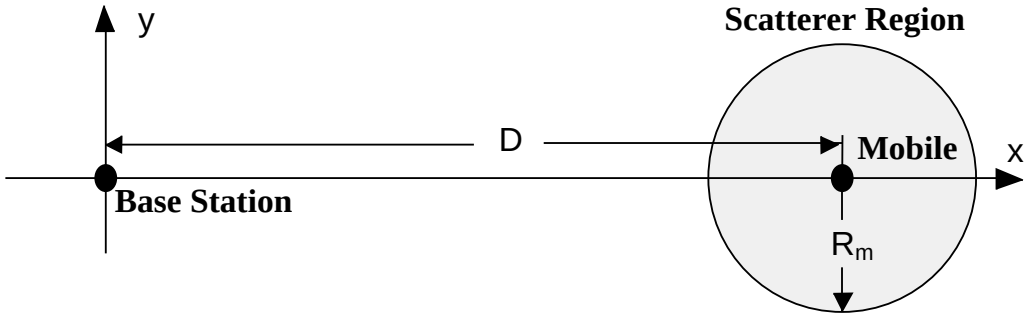

Figure 4.11: Circular scatterer density geometry.

4.6.1 Joint TOA-AOA Density Function (Circular Model)

Joint TOA-AOA Density Function at the Base Station

When the scatter region is uniformly distributed within a radius, R_m about the mobile, then the area of the scatterer region is $A = \pi R_m^2$. Substituting this expression into (4.19) gives

$$f_{\tau,\theta_b}(\tau,\theta_b) = \begin{cases} \frac{(D^2-\tau^2c^2)(D^2c+\tau^2c^3-2\tau c^2 D\cos(\theta_b))}{4\pi R_m^2(D\cos(\theta_b)-\tau c)^3} & : \quad \frac{D^2-2\tau cD\cos(\theta_b)+\tau^2c^2}{\tau c-D\cos(\theta_b)} \le 2R_m, \quad \theta_b \neq 0 \\ \frac{c(D+\tau c)}{4\pi R_m^2} & : \quad \frac{D}{c} \le \tau \le \frac{D+2R_m}{c}, \quad \theta_b = 0 \\ 0 & : \quad else, \end{cases} \tag{4.83}$$

where the range of τ and θ_b for which $f_{\tau,\theta_b}(\tau,\theta_b) \neq 0$ was found by considering the condition on the original scatterer density, namely,

$$(x-D)^2 + y^2 \le R_m^2. \tag{4.84}$$

Expanding and then transforming into polar coordinates gives

$$r_b^2 - 2r_bD\cos(\theta_b) + D^2 \le R_m^2. \tag{4.85}$$

Substituting the expression for r_b found in (4.12) and then simplifying results in the condition

$$\frac{D^2 - 2\tau cD\cos(\theta_b) + \tau^2c^2}{\tau c - D\cos(\theta_b)} \le 2R_m. \tag{4.86}$$

Figures 4.12a and 4.12b show the joint TOA-AOA density function that is observed at the base station for $D = 1000m$ and $R_m = 100m$. Figure 4.12.a is a plot of the closed form expression for the joint density. Figure 4.12.b is a scatter plot created by placing 10000 scatterers and then plotting the corresponding TOA-AOA pairs. There is good agreement between the amplitude of the joint probability density function shown in Fig. 4.12a with the concentration of scatter points in Fig. 4.12b.

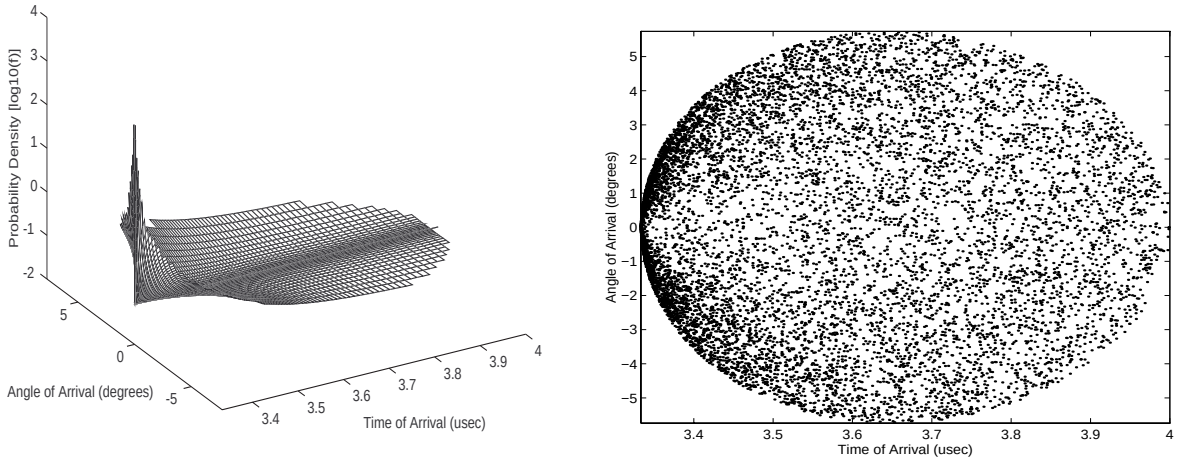

(a) pdf Closed Form Expression (Log-Scale)

(b) Scatter Plot

Figure 4.12: Joint TOA-AOA pdf for the circular scattering model from the base station perspective.

Joint TOA-AOA Density Function at the Mobile

As stated in Section 4.2.1, the joint AOA-TOA density function observed at the mobile will have the same form as the joint density function observed at the base station with only the range of parameters where $f_{\tau,\theta_b}(\tau,\theta_b) \neq 0$ being different. The joint AOA-TOA function observed at the mobile is

$$f_{\tau,\theta_s}(\tau,\theta_s) = \begin{cases} \frac{(D^2-\tau^2c^2)(D^2c+\tau^2c^3-2\tau c^2 D\cos(\theta_s))}{4\pi R_m^2 (D\cos(\theta_s)-\tau c)^3} & : \quad \frac{D^2-\tau^2c^2}{2(D\cos(\theta_s)-\tau c)} \leq R_m, \quad \theta_s \neq 0 \\ \frac{c(D+\tau c)}{4\pi R_m^2} & : \quad \frac{D}{c} \leq \tau \leq \frac{D+2R_m}{c}, \quad \theta_s = 0 \\ 0 & : \quad else. \end{cases} \tag{4.87}$$

The range of τ and θ_s for which $f_{\tau,\theta_s}(\tau,\theta_s) \neq 0$ is again found by considering the condition on the original scatterer density, namely,

$$x_c^2 + y^2 \leq R_m^2, \tag{4.88}$$

where for convenience the new Cartesian coordinate system (x_c, y) is defined at the mobile such that $x_c = -x + D$. With this definition, then the inequality given in (4.88) may be expressed as,

$$r_s^2 \leq R_m^2, \tag{4.89}$$

where $r_s = \sqrt{x_c^2 + y^2}$ is the radius of the polar coordinate system defined at the mobile. Substituting (4.20) into (4.89) gives the desired result,

$$\left(\frac{D^2 - \tau^2 c^2}{2(D\cos(\theta_s) - \tau c)} \right)^2 \leq R_m^2. \tag{4.90}$$

Figures 4.13a and 4.13b show the joint TOA-AOA pdf observed at the mobile, and a scatter plot of 10,000 TOA-AOA samples from the circular model. There is good agreement between the two plots.

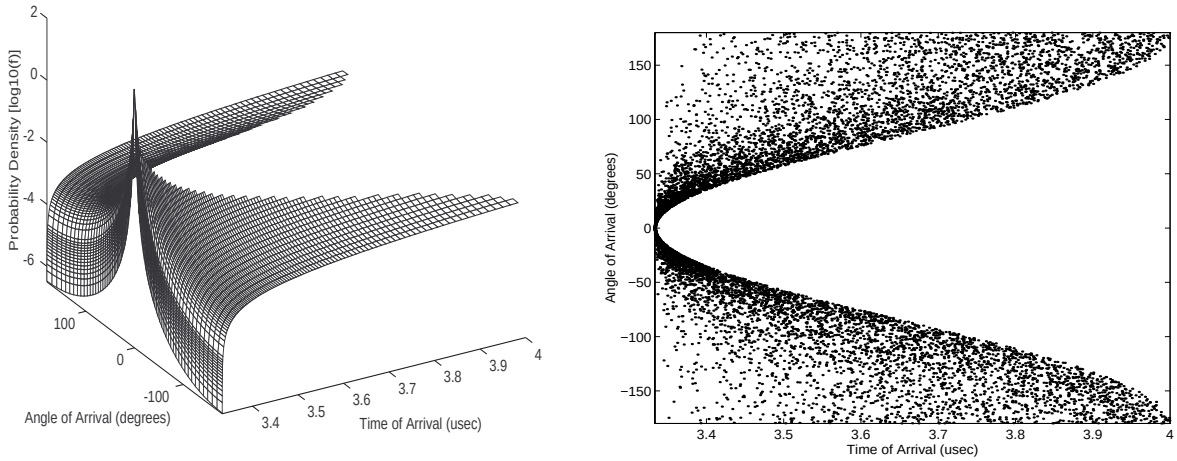

(a) pdf Closed Form Expression (Log-Scale)

(b) Scatter Plot

Figure 4.13: Joint TOA-AOA pdf for the circular scattering model from the mobile station perspective.

4.6.2 AOA Density Function (Circular Model)

AOA Density Function at the Base Station

The general expression for the AOA density function was derived in Section 4.3.1. In this section, the AOA density function corresponding to a circular scatterer density function is derived. The polar coordinate expression for a circle center at $(0, D)$ with a radius, R_m is described by

$$r_b^2 - 2D\cos(\theta_b)r_b + D^2 - R_m^2 = 0. \tag{4.91}$$

Using the quadratic formula,

$$r_b = D\cos(\theta_b) \pm \sqrt{D^2\cos^2(\theta_b) - D^2 + R_m^2}, \tag{4.92}$$

which implies that

$$r_{b1}(\theta_b) = D\cos(\theta_b) - \sqrt{D^2\cos^2(\theta_b) - D^2 + R_m^2} \tag{4.93}$$

$$r_{b2}(\theta_b) = D\cos(\theta_b) + \sqrt{D^2\cos^2(\theta_b) - D^2 + R_m^2}. \tag{4.94}$$

Substituting (4.93) and (4.94) into (4.23) with $A = \pi R_m^2$ and simplifying, results in

$$f_{\theta_b}(\theta_b) = \begin{cases} \frac{2D\cos(\theta_b)\sqrt{D^2\cos^2(\theta_b) - D^2 + R_m^2}}{\pi R_m^2} & : \quad -\sin^{-1}(\frac{R_m}{D}) \leq \theta_b \leq \sin^{-1}(\frac{R_m}{D}) \\ 0 & : \quad else. \end{cases} \tag{4.95}$$

Figure 4.14 shows the AOA pdf observed at the base for the case of $D = 1000m$ and $R_m = 100m$.

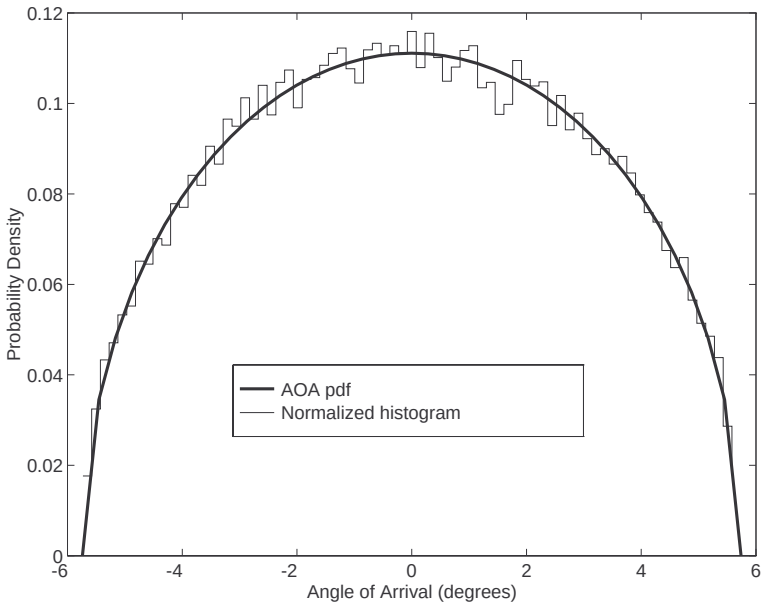

Figure 4.14: AOA pdf for the circular scattering model at the base.

The ensemble average AOA angle spread at the base station (variance of θ_b) to some degree will determine the performance of adaptive antenna array systems. Furthermore, theoretical vs measured AOA angle spread can be used to determine an appropriate value for the radius of scatterers. The ensemble AOA spread is simply the standard deviation of θ_b given by [24]

$$\sigma_\theta = \sqrt{E\{\theta_b^2\} - E\{\theta_b\}^2} \tag{4.96}$$

The angle spread is shown in Figure 4.15 as a function of R_m/D and was found by evaluating the variance numerically and taking the square root.

A good fit to the angle spread curve is

$$\sigma_\theta = 31\left(\frac{R_m}{D}\right). \tag{4.97}$$

In [42] it is claimed that experimental results presented in [47] indicate that for $R_m \approx 1km$, $\sigma_\theta \approx 1$ to 6 degrees and for $R_m = 4km$, $\sigma_\theta \approx 0.5$ to 1.1 degrees. Although in [42] the AOA

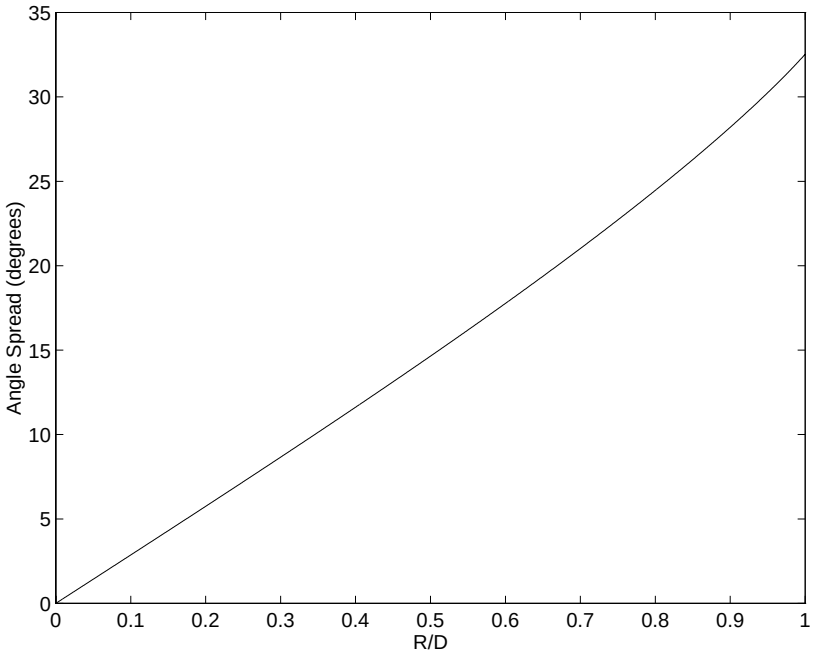

Figure 4.15: Angle spread at the observed at the base station as a function of R/D.

pdf was assumed Gaussian, a good first order estimate of R_m may be obtained by equating the expression for the angle spread found above with the angle spread values given in [42]. The motivation behind this approach is to match the angle spread of the model with the angle spread found through measurements. Under this criterion we may select an appropriate value for R_m.

Solving (4.97) for R_m and assuming that σ_θ= 1 degrees at $D = 1km$, implies that $R_m \approx 30m$. For $\sigma_\theta = 6$ degrees at $D = 1km$, then $R_m \approx 200m$. The angle spreads that result for $R_m = 30m$, $R_m = 100m$, and $R_m = 200m$ is shown in Fig. 4.16 as a function of T-R separation distance.

For the purposes of this report, a scatterer radius of 100 m will be assumed unless otherwise stated. Using this value of R_m, the angle spread in degrees may be expressed,

$$\sigma_\theta = \frac{3100}{D}, \tag{4.98}$$

where D is in meters.

AOA Density Function at the Mobile

The AOA density function observed at the mobile is trivial. Since the scatterers are uniformly distributed within a radius about the mobile, the AOA density will be independent of angle. The resulting density function is,

$$f_{\theta_s}(\theta_s) = \frac{1}{2\pi}. \tag{4.99}$$

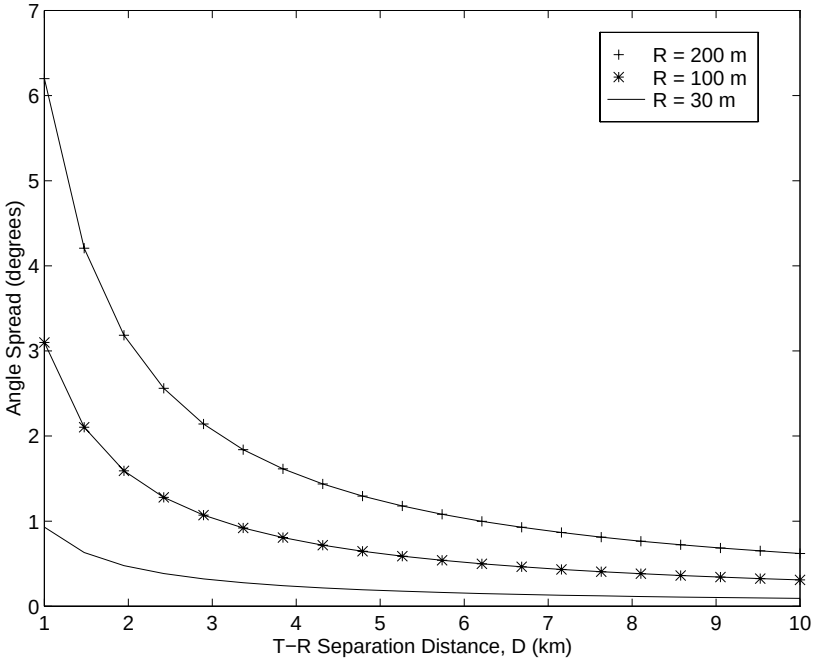

Figure 4.16: Angle spread at the base for various R_m values.

4.6.3 TOA Density Function (Circular Model)

Deriving the marginal TOA density function is nontrivial. The approach to be taken is to find the area of the intersection of an ellipse with majoraxis equal to τc with the circular scatterer region. The derivative of the resulting function of τ divided by the area gives the desired pdf (See Section 4.3.2),

$$f_\tau(\tau) = \frac{1}{A}\frac{d}{d\tau}\left(A_\tau(\tau)\right). \tag{4.100}$$

The area of intersection of the ellipse with the circular scatterer region is most easily derived using the polar coordinate equations of the circle and ellipse referred to the polar coordinate system defined at the mobile, (r_s, θ_s). (Note the nonconventional orientation of this coordinate system which is used for convenience, namely θ_s increases in the clockwise direction). With respect to this coordinate system the ellipse and the circle are described by the following two polar coordinate equations respectively,

$$r_{s_e} = \frac{c^2\tau^2 - D^2}{2c\tau - 2D\cos(\theta_s)}, \tag{4.101}$$

$$r_{s_c} = R_m. \tag{4.102}$$

Figure 4.17 shows the situation being considered. The area of intersection is divided into the two separate regions, A_1 and A_2, by the rays from the mobile to the points of intersection of the circle with the ellipse. The angle from the mobile to the points of intersection labeled α

may be determined by substituting α for θ_s and solving (4.101) and (4.102) simultaneously for α. The resulting positive value of α is

$$\alpha = \text{acos}\left(\frac{D^2 + 2R_m\tau c - \tau^2 c^2}{2R_m D}\right). \tag{4.103}$$

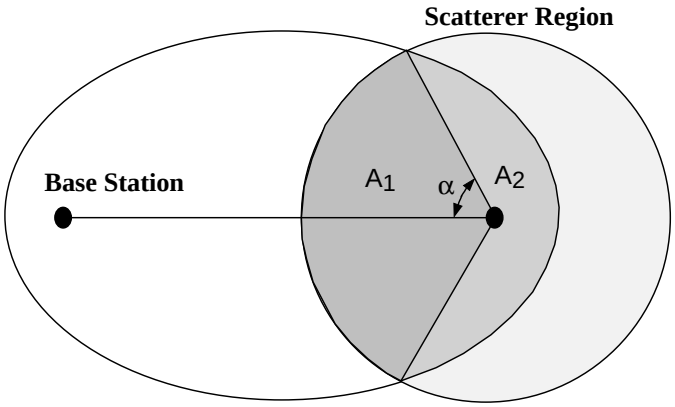

Figure 4.17: Geometry and notation used to calculate the TOA cdf for the circular scattering model.

Since there is symmetry about the x-axis, it is possible to find the overall area of intersection by multiplying the area of intersection above the x-axis by two. Hence, the overall area of intersection may be expressed,

$$\begin{aligned} A_\tau(\tau) &= A_1 + A_2 && (4.104)\\ &= 2\int_0^\alpha \frac{1}{2} r_{s_c}^2(\theta)d\theta \;+\; 2\int_\alpha^\pi \frac{1}{2} r_{s_e}^2(\theta)d\theta && (4.105)\\ &= \int_0^\alpha R_m^2 d\theta \;+\; \int_\alpha^\pi \left(\frac{c^2\tau^2 - D^2}{2c\tau - 2D\cos(\theta)}\right)^2 d\theta. && (4.106)\\ &= R_m^2\alpha \;+\; \int_\alpha^\pi \left(\frac{c^2\tau^2 - D^2}{2c\tau - 2D\cos(\theta)}\right)^2 d\theta. && (4.107) \end{aligned}$$

The last term may be integrated using integral formulas given in [48]. The resulting expression for the area as a function of τ becomes

$$\begin{aligned} A_\tau(\tau) &= R_m^2\alpha \\ &\quad + \tfrac{D^2-\tau^2c^2}{4}\left[\tfrac{-\pi\tau c}{\sqrt{\tau^2c^2-D^2}} + \tfrac{D\sin(\alpha)}{\tau c - D\cos(\alpha)} + \tfrac{2\tau c}{\sqrt{\tau^2c^2-D^2}}\text{atan}\left(\tfrac{\sqrt{\tau^2c^2-D^2}\tan(\frac{\alpha}{2})}{\tau c - D}\right)\right]. \end{aligned} \tag{4.108}$$

Substituting the expression for α given in (4.103), taking the derivative with respect to τ with the aid of Matlab's Symbolic Toolbox, and then dividing by $A = \pi R_m^2$ gives the marginal TOA

density function,

$$f_\tau(\tau) = \frac{c}{\pi R_m^2}\left[\frac{\pi\tau^2c^2k_2 - \tau ck_2^2 + \pi k_2k_1^2 + \tau ck_1^2 - 2R_mk_1^2}{4k_1k_2} + \frac{\tau^2c^2k_0k_4 + \tau ck_0k_1^2}{2k_4^2 + 2k_0^2k_1^2}\right.$$
$$\left. + \frac{\tau^2c^2 + k_1^2}{2k_1}\text{atan}\left(\frac{k_0k_1}{k_4}\right) - \frac{R_m - \tau c}{(4R_m^2D^2 - k_3^2)^{\frac{1}{2}}}\left(2R_m^2 + \frac{\tau ck_1^2k_4(1+k_0^2)}{2k_4^2 + 2k_0^2k_1^2}\right)\right] \quad (4.109)$$

where

$$k_0 = \tan\left(\tfrac{1}{2}\text{acos}\left(\tfrac{-\tau^2c^2+D^2+2R_m\tau c}{2R_mD}\right)\right)$$
$$k_1 = \sqrt{\tau^2c^2 - D^2}$$
$$k_2 = \sqrt{D^2 - 4R_m^2 - \tau^2c^2 + 4R_m\tau c}$$
$$k_3 = -\tau^2c^2 + D^2 + 2R_m\tau c$$
$$k_4 = D - \tau c$$

This expression is valid for only for $\frac{D}{c} < \tau \leq \frac{D+2R_m}{c}$. When $\tau = \frac{D}{c}$, then $k_0 = 0$, $k_1 = 0$, and $k_4 = 0$ and a few of the terms result in an indeterminate $\frac{0}{0}$ condition. Although it may be possible to apply Hospital's rule and find the limit as $\tau \to \frac{D}{c}$, we'll take the easier route and just restrict that τ is strictly larger than $\frac{D}{c}$.

Figure 4.18 shows the TOA density function and a simulated normalized histogram for $D = 1000m$ and $R_m = 100m$.

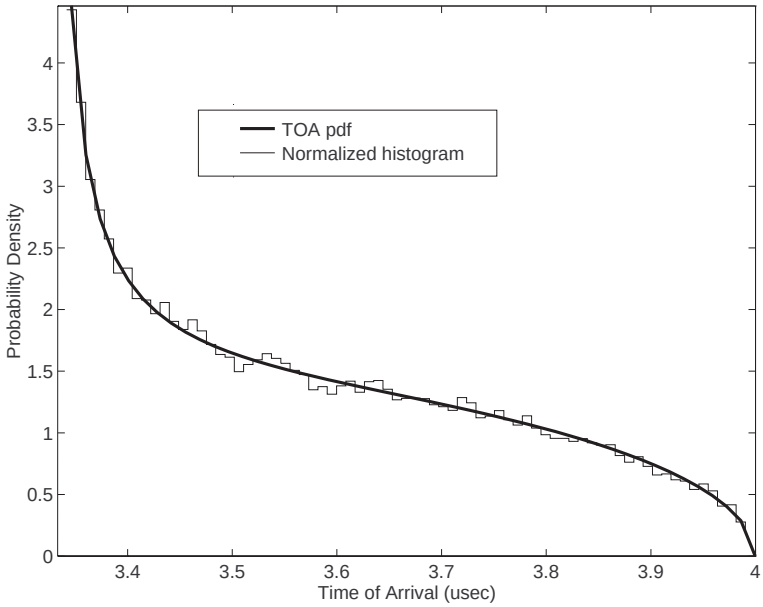

Figure 4.18: TOA pdf for the circular scattering model ($D = 1000m$, $R_m = 100m$).

4.6.4 Doppler Spectrum (Circular Model)

The upper and lower limits $x_u(i)$ and $x_l(i)$ needed to determine the PSD in Eq. 4.58 that apply to the circular model are determined in this section. The limits on x are related to the original limits over which the power was integrated by

$$x_u(i) = \left(\frac{p_u}{p_0}\right)^{-\frac{1}{n}} \tag{4.110}$$

and

$$x_l(i) = \left(\frac{p_l}{p_0}\right)^{-\frac{1}{n}}. \tag{4.111}$$

Regardless of the geometry, the maximum power will correspond to the line of site components. For convenience this power was set to p_0, hence

$$x_u(i) = p_0. \tag{4.112}$$

The lower limit is dependent upon the minimum power at the Doppler frequency of interest. For the circular geometry, the minimum power at any given AOA at the mobile will be due to scatterers on the edge of the circle. Applying Eq. 4.10 to the polar coordinates defined at the mobile with $r_s = R_m$ gives,

$$d = R_m + \sqrt{D^2 + R_m^2 - 2R_m D\cos(\theta_s)}. \tag{4.113}$$

Hence, the power associated with the scatterer at coordinates (R_m, θ_s) will be

$$p_l = p_0\left(\frac{d}{D}\right)^{-n} = p_0\left(\frac{R_m + \sqrt{D^2 + R_m^2 - 2R_m D\cos(\theta_s)}}{D}\right)^{-n} \tag{4.114}$$

For each Doppler frequency there are two possible AOA's which are given by

$$\theta_{s_i} = \theta_i = \begin{cases} \theta_v + \text{acos}(\frac{f_d}{f_m}) & : \quad i = 1 \\ \theta_v - \text{acos}(\frac{f_d}{f_m}) & : \quad i = 2 \end{cases}$$

Substituting θ_i into (4.114) gives the corresponding lower limits of p,

$$p_l(i) = p_0\left(\frac{R_m + \sqrt{D^2 + R_m^2 - 2R_m D\cos(\theta_i)}}{D}\right)^{-n} \tag{4.115}$$

The corresponding limit for x is

$$x_l(i) = \left(\frac{p_l(i)}{p_0}\right)^{-1/n} = \frac{R_m + \sqrt{D^2 + R_m^2 - 2R_m D\cos(\theta_i)}}{D}. \tag{4.116}$$

Substituting these values into the expression derived in Section 4.4 for path loss exponents of $n = 2$ and $n = 4$ gives the desired closed form expression for the Doppler PSD.

Figures 4.19a and 4.19b show the Doppler PSD that results for a path loss exponent of $n = 2$, with $\theta_v = 0$ and $\theta_v = \frac{\pi}{2}$ respectively. Similarly, Figures 4.20a and 4.20b show the Doppler PSD that results for a path loss exponent of $n = 4$, with $\theta_v = 0$ and $\theta_v = \frac{\pi}{2}$ respectively. For convenience p_0=1W. Also shown in the figures are normalized histograms that were generated using simulation to validate the mathematical expressions. The Doppler frequency is normalized by f_m, the maximum Doppler frequency.

For comparison Clarke's model is plotted (which is the same as the uncorrelated power model mentioned above since the AOA is uniform at the mobile for the circular model). For the circular model the difference between Clarke's model and the path loss amplitude model is negligible.

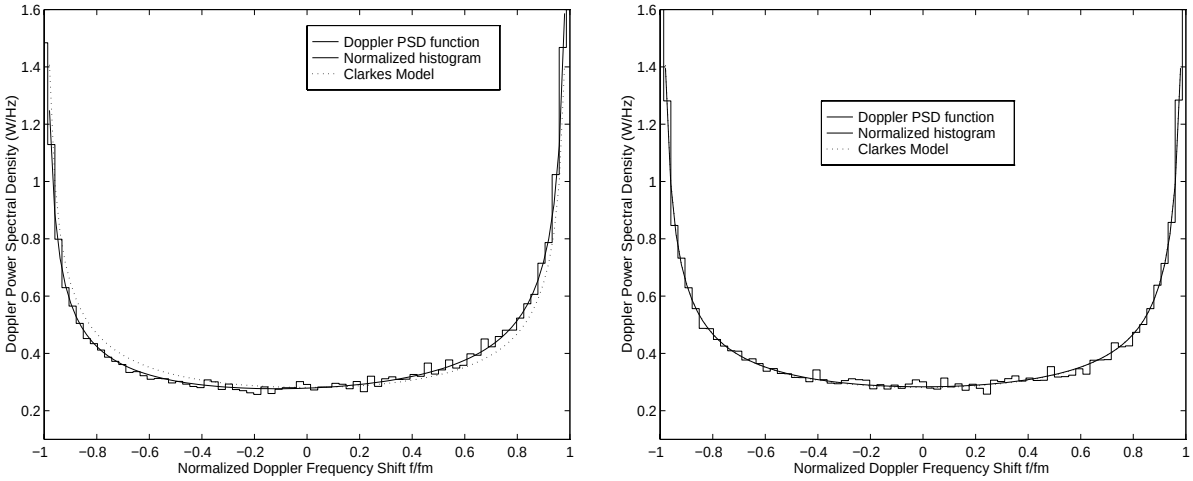

(a) $\theta_v = 0$ (b) $\theta_v = \frac{\pi}{2}$

Figure 4.19: Doppler PSD for the circular scattering model with $n = 2$.

4.6.5 Generation of Samples of the Circular Model

The algorithm for generating samples of the GBCM is similar to that developed above for generating samples from the GBEM except that now it is not necessary to scale x and y by the a_m and b_m parameters. The resulting algorithm for the GBCM becomes:

1. Let u_1 be uniformly distributed in [0,1].
2. Calculate $\phi = 2\pi(u_1 - 0.5)$.
3. Let u_2 be uniformly distributed in [0,1].
4. Calculate $r = \sqrt{u_2}$.
5. Calculate $x_c1 = r\cos(\phi)$ and $y_c = r\sin(\phi)$.
6. Let $x_c = x_{c1} + \frac{D}{2}$.

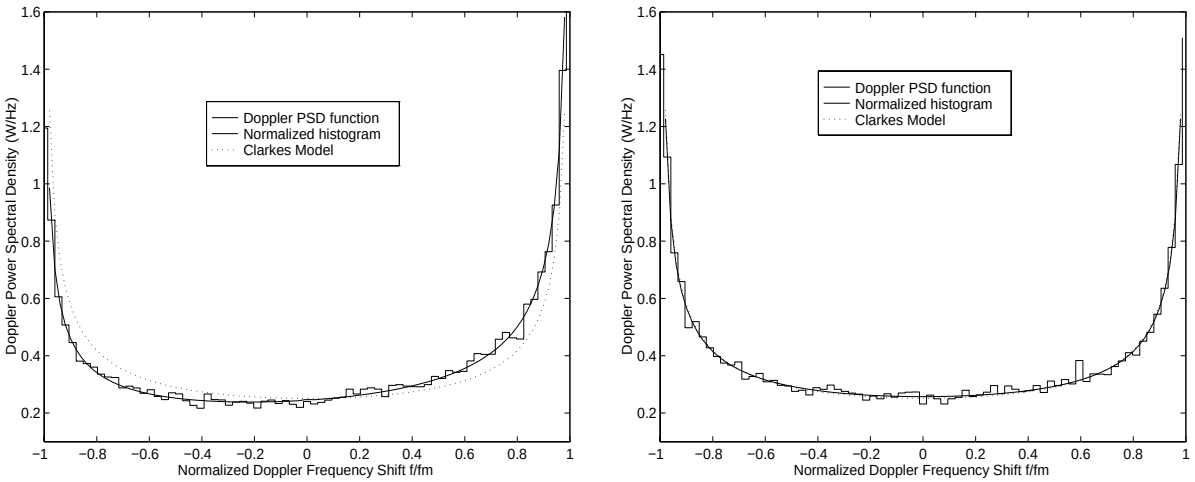

(a) $\theta_v = 0$ (b) $\theta_v = \frac{\pi}{2}$

Figure 4.20: Doppler PSD for the circular scattering model with $n = 4$.

7. Calculate path distance, $d = \sqrt{x_c^2 + y_c^2} + \sqrt{(D - x_c)^2 + y_c^2}$.
8. The transmit to receive delay will be $\tau = \frac{d}{c}$.
9. Angle of arrival at the mobile is $\theta = \text{atan}(y_c/(x_c - D))$.
10. Angle of arrival at the base station is $\beta = \text{atan}(y_c/x_c)$.

4.7 Summary

The joint TOA-AOA, marginal AOA, and marginal TOA density functions were derived for the circular and elliptical vector channel models. Also derived was the Doppler spectrum which results from the geometry of scatterers when a path dependent path-loss is assumed. Finally, efficient algorithms were given that can be used to simulate these models.

Chapter 5

Generalized Optimum Output SINR Analysis

With the introduction of antenna array receivers into third-generation high-bandwidth wireless data communication systems comes the need to quantify the performance of such systems. Due to the relatively high bandwidth of the proposed systems it is expected that frequency selective fading channels will occur frequently. In such channels it is beneficial to utilize space-time filters. In this chapter the derivation of optimum output SINR presented in Section 2.6 is extended to the more general case of space-time processing structures in frequency selective fading channels.

The derivation relies on the decomposition of the received signal vector into two components, one which is correlated with the desired signal and one which is not, as suggested in [49]. This signal decomposition can be used to cast the received signal vector of various space-time processing structures in frequency selective fading environments into the form of a narrowband antenna array in a flat fading channel, to which the results of [8] may be directly applied.

In Section 5.1 we introduce the matrix representation of a frequency selective fading channel and its simplification for flat fading channels. In Section 5.2 the well known closed form expression for the performance of spatial filtering in flat fading channels is reviewed. The results of Section 5.2 are extended to the case of frequency selective fading channels in Section 5.3. In Section 5.4 the optimum output SINR for joint space-time processors is derived. In Sections 5.5 and 5.6 the performance of two sub-optimum space time processor structures is derived. The derived expressions for optimum output SINR performance are used to compare the performance of the selected receiver structures in various multipath channel environments in Section 5.7. Finally, a chapter summary is given in Section 5.8.

5.1 Signal Model

For simplicity we consider only the multipath signals of a single user. Extension of the analysis to multi-user environments in which the signals of the various users are assumed to be uncorrelated

with one another is straightforward. The difference between the single user case and the multi-user case is the form of the interference plus noise covariance matrix. When only a single user is present then the interference plus noise covariance matrix is typically a scaled identity matrix. For the multi-user case, the interference plus noise covariance matrix will depend on the signal format as well as the channel properties. In either case the derivation below is valid, assuming that the correct interference plus noise covariance matrix is used, and that the signals of the interfering users are uncorrelated with the desired user's signal.

As shown in Chapter 2, in a LOS environment, $\mathbf{x}(t)$ may be expressed as

$$\mathbf{x}(t) = \alpha \mathbf{a}(\theta) s(t) + \eta(t), \tag{5.1}$$

where α is the scalar complex path amplitude, $\mathbf{a}(\theta)$ is the array response vector in the direction of θ towards the user, and $s(t)$ is the complex analytic signal impinging upon the array. The additive term $\eta(t)$ accounts for receiver noise as well as background channel noise and is typically modeled as both spatially and temporarily white Gaussian noise. When the received signal is the summation of several multipath signals, the received signal vector may be expressed as

$$\mathbf{x}(t) = \sum_{l=1}^{L} \alpha_l \mathbf{a}(\theta_l) s(t - \tau_l) + \eta(t), \tag{5.2}$$

where L is the number of multipath components, τ_l is the excess path delay, and the remaining variables are as defined above. It is sometimes convenient to express (5.2) in vector form as

$$\mathbf{x}(t) = \mathbf{A} \bar{\alpha} \mathbf{s}(t) + \eta(t). \tag{5.3}$$

where

$$\mathbf{A} = \left[\begin{array}{cccc} \mathbf{a}(\theta_1) & \mathbf{a}(\theta_2) & \cdots & \mathbf{a}(\theta_L) \end{array} \right], \tag{5.4}$$

$$\bar{\alpha} = \mathrm{diag}\left(\alpha_1 \ \alpha_2 \ \cdots \ \alpha_L \right), \tag{5.5}$$

and

$$\mathbf{s}(t) = \left[\begin{array}{c} s(t - \tau_1) \\ s(t - \tau_2) \\ \vdots \\ s(t - \tau_L) \end{array} \right]. \tag{5.6}$$

When the delay differences between the multipath components are sufficiently small relative to the reciprocal of the signal bandwidth, then the channel experiences flat fading. For a flat fading environment, (5.2) reduces to

$$\mathbf{x}(t) = \sum_{l=1}^{L} \alpha_l e^{-j\omega_c \tau_l} \mathbf{a}(\theta_l) s(t) + \eta(t), \tag{5.7}$$

where ω_c is the carrier frequency in radians per second. The complex baseband signal may be factored out of the expression to give,

$$\mathbf{x}(t) = \left[\sum_{l=1}^{L} \alpha_l e^{-j\omega_c \tau_l} \mathbf{a}(\theta_l) \right] s(t) + \eta(t) = \mathbf{v} s(t) + \eta(t), \tag{5.8}$$

where

$$\mathbf{v} = \sum_{l=1}^{L} \alpha_l e^{-j\omega_c \tau_l} \mathbf{a}(\theta_l) \tag{5.9}$$

is the *spatial signature vector*.

5.2 Spatial Filtering Performance in Flat Fading Channels

It is well known that when the received signal vector is expressed as

$$\mathbf{x}(t) = \mathbf{v}s(t) + \eta(t), \tag{5.10}$$

that the optimum output SINR performance of a spatial filter is given by [8]

$$\text{SINR}_{SFF} = \mathbf{v}^H \mathbf{R}_{ii}^{-1} \mathbf{v} \tag{5.11}$$

where $\mathbf{v}$ is the spatial signature vector of the desired user as defined above and $\mathbf{R}_{ii} = \text{E}\left\{\eta(t)\eta^H(t)\right\}$ is the interference plus noise covariance matrix. The assumptions made in deriving (5.11) are that $\text{E}\{s(t)s^*(t)\} = 1$ and that $\text{E}\{s(t)\eta^*(t)\} = 0$.

5.3 Spatial Filtering Performance in Frequency Selective Channels

In this section, we extend the results of the previous section to the more general case of frequency selective fading channels. The approach that we take is to decompose the received signal vector into two components, one which is correlated with the desired signal and one which is not. The effective signature vector of the correlated signal component is used in place of the spatial signature vector in the expression for the optimum output SINR. The corresponding interference plus noise covariance matrix is found from the expression for the uncorrelated signal component and the original additive noise covariance matrix.

Let $d(t)$ denote the desired signal and let $x(t)$ denote the actual received signal present at one of the antenna elements of the array. For convenience assume that $\text{E}\{d(t)d^*(t)\} = 1$. We may express $x(t)$ as

$$x(t) = x(t) - \text{E}\{x(t)d^*(t)\}\, d(t) + \text{E}\{x(t)d^*(t)\}\, d(t) = x_o(t) + x_c(t). \tag{5.12}$$

where

$$x_o(t) = x(t) - \text{E}\{x(t)d^*(t)\}\, d(t) \tag{5.13}$$

is orthogonal to $d(t)$, and

$$x_c(t) = \text{E}\{x(t)d^*(t)\}\, d(t) \tag{5.14}$$

is correlated with $d(t)$. By inspection, $\text{E}\{x_o(t)d^*(t)\} = 0$. Hence, $x_o(t)$ is orthogonal to $d^*(t)$ as desired. In the derivation below, we will take $x_c(t)$ as the desired signal component, and we will treat $x_o(t)$ as the interference plus noise signal component.

Using this approach, we may decompose the the signal vector $\mathbf{s}(t)$ given in (5.6) into correlated and uncorrelated components to obtain,

$$\mathbf{s}(t) = \left\{ \begin{bmatrix} s(t-\tau_1) \\ s(t-\tau_2) \\ \vdots \\ s(t-\tau_L) \end{bmatrix} - \begin{bmatrix} \mathrm{E}\{s(t-\tau_1)d^*(t)\} \\ \mathrm{E}\{s(t-\tau_2)d^*(t)\} \\ \vdots \\ \mathrm{E}\{s(t-\tau_L)d^*(t)\} \end{bmatrix} d(t) \right\} + \begin{bmatrix} \mathrm{E}\{s(t-\tau_1)d^*(t)\} \\ \mathrm{E}\{s(t-\tau_2)d^*(t)\} \\ \vdots \\ \mathrm{E}\{s(t-\tau_L)d^*(t)\} \end{bmatrix} d(t). \quad (5.15)$$

For the case under consideration, $d(t) = s(t-\tau_r)$, where τ_r is the delay of the reference signal. The choice of τ_r is dependent upon which signal delay would allow the maximum correlated signal power at the receiver. Assuming that $s(t)$ is wide sense stationary, then we may define the signal autocorrelation function of $s(t)$ as $R_d(\tau) = \mathrm{E}\{s(t)s^*(t-\tau)\}$. Using this definition we find that

$$\mathrm{E}\{s(t-\tau_i)d^*(t)\} = \mathrm{E}\{s(t-\tau_i)s^*(t-\tau_r)\} = \mathrm{E}\{s(t-\tau_i+\tau_r)s^*(t)\} = R_d^*(\tau_i-\tau_r) \quad (5.16)$$

Substituting this result into (5.15) we obtain

$$\mathbf{s}(t) = \begin{bmatrix} s(t-\tau_1) \\ s(t-\tau_2) \\ \vdots \\ s(t-\tau_L) \end{bmatrix} - \begin{bmatrix} R_d^*(\tau_1-\tau_r) \\ R_d^*(\tau_2-\tau_r) \\ \vdots \\ R_d^*(\tau_L-\tau_r) \end{bmatrix} s(t-\tau_r) + \begin{bmatrix} R_d^*(\tau_1-\tau_r) \\ R_d^*(\tau_2-\tau_r) \\ \vdots \\ R_d^*(\tau_L-\tau_r) \end{bmatrix} s(t-\tau_r). \quad (5.17)$$

Finally, we may define

$$\mathbf{s}_o(t) = \begin{bmatrix} s(t-\tau_1) \\ s(t-\tau_2) \\ \vdots \\ s(t-\tau_L) \end{bmatrix} - \begin{bmatrix} R_d^*(\tau_1-\tau_r) \\ R_d^*(\tau_2-\tau_r) \\ \vdots \\ R_d^*(\tau_L-\tau_r) \end{bmatrix} s(t-\tau_r) \quad (5.18)$$

and

$$\mathbf{s}_c(t) = \begin{bmatrix} R_d^*(\tau_1-\tau_r) \\ R_d^*(\tau_2-\tau_r) \\ \vdots \\ R_d^*(\tau_L-\tau_r) \end{bmatrix} s(t-\tau_r). \quad (5.19)$$

which are the uncorrelated and correlated signal vector components of $\mathbf{s}(t)$ respectively.

Finally, we may express the received signal vector as

$$\mathbf{x}(t) = \mathbf{A}\bar{\alpha}\mathbf{s}(t) + \eta(t) = \mathbf{A}\bar{\alpha}\mathbf{s}_c(t) + \mathbf{A}\bar{\alpha}\mathbf{s}_o(t) + \eta(t) = \hat{\mathbf{v}}s(t) + \hat{\eta}(t), \quad (5.20)$$

where

$$\hat{\mathbf{v}} = \mathbf{A}\bar{\alpha} \begin{bmatrix} R_d^*(\tau_1-\tau_r) \\ R_d^*(\tau_2-\tau_r) \\ \vdots \\ R_d^*(\tau_L-\tau_r) \end{bmatrix} \quad (5.21)$$

and

$$\hat{\eta}(t) = \mathbf{A}\bar{\alpha}\mathbf{s}_o(t) + \eta(t) \tag{5.22}$$

Since, (5.20) is of the same form as (5.10) we may write the optimum output SINR performance of a narrowband antenna array in a frequency selective environment as

$$\text{SINR}_{NBFS} = \hat{\mathbf{v}}^H \hat{\mathbf{R}}_{ii}^{-1} \hat{\mathbf{v}} \tag{5.23}$$

where $\hat{\mathbf{R}}_{ii} = \text{E}\left\{\hat{\eta(t)}\hat{\eta(t)}^H\right\}$.

Next a closed form expression for $\hat{\mathbf{R}}_{ii}$ is derived. From (5.22) we may write,

$$\hat{\mathbf{R}}_{ii} = \text{E}\left\{[\mathbf{A}\bar{\alpha}\mathbf{s}_o(t) + \eta(t)][\mathbf{A}\bar{\alpha}\mathbf{s}_o(t) + \eta(t)]^H\right\} = \mathbf{A}\bar{\alpha}\text{E}\left\{\mathbf{s}_o(t)\mathbf{s}_o(t)^H\right\}\bar{\alpha}^H\mathbf{A}^H + \sigma_n^2\mathbf{I}_m \tag{5.24}$$

For convenience we define $\mathbf{R}_{sso} = \text{E}\left\{\mathbf{s}_o(t)\mathbf{s}_o(t)^H\right\}$ so that we may write

$$\hat{\mathbf{R}}_{ii} = \mathbf{A}\bar{\alpha}\mathbf{R}_{sso}\bar{\alpha}^H\mathbf{A}^H + \sigma_n^2\mathbf{I}_m \tag{5.25}$$

The $(i,j)^{th}$ entry of $\mathbf{R}_{sso}$ is given by

$$\begin{aligned} R_{i,j} &= \text{E}\{s_{oi}(t)s_{oj}(t)^*\} \\ &= \text{E}\{[s(t-\tau_i) - \mathbf{R}_d^*(\tau_i - \tau_r)s(t-\tau_r)][s(t-\tau_j) - \mathbf{R}_d^*(\tau_j - \tau_r)s(t-\tau_r)]^*\} \end{aligned}$$

where $s_{oi}(t)$ denotes the ith component of the the vector $\mathbf{s}_o(t)$. After expanding and rearranging we find that

$$R_{i,j} = R_d(\tau_j - \tau_i) - R_d^*(\tau_i - \tau_r)R_d(\tau_j - \tau_r). \tag{5.26}$$

Finally, using (5.21) to find the effective spatial signature vector and using (5.25) and (5.26) to find the effective interference plus noise covariance matrix we obtain a closed form expression for the optimum output SINR for a narrowband antenna array in a frequency selective environment. In the following section we extend this result to the more general wideband antenna array receiver in frequency selective fading channels.

5.4 Extension to Joint Space-Time Processors

The joint space-time processor structure (wideband antenna array) is shown in Fig. 2.5 on page 14. In this case the sampled signal vector may be expressed as

$$\mathbf{x}[n] = \sum_{l=1}^{L} \alpha_l \mathbf{a}(\theta_l)s(nT_s - \tau_l) + \eta(nT_s), \tag{5.27}$$

In a wideband array several samples of the received signal vector are processed jointly to obtain the desired array output.

Suppose that the depth of the wideband processor is B. For convenience we may define the wideband received signal vector

$$\acute{\mathbf{x}}[n] = \begin{bmatrix} \mathbf{x}[n] \\ \mathbf{x}[n-1] \\ \vdots \\ \mathbf{x}[n-(B-1)] \end{bmatrix} = \begin{bmatrix} \mathbf{A}\bar{\alpha}\mathbf{s}[n] \\ \mathbf{A}\bar{\alpha}\mathbf{s}[n-1] \\ \vdots \\ \mathbf{A}\bar{\alpha}\mathbf{s}[n-(B-1)]) \end{bmatrix} \tag{5.28}$$

where

$$\mathbf{s}[n] = \begin{bmatrix} s(nT_s - \tau_1) \\ s(nT_s - \tau_2) \\ \vdots \\ s(nT_s - \tau_L) \end{bmatrix} \tag{5.29}$$

Next we may decompose each of the $\mathbf{s}[n-l]$ signal vectors into desired and undesired signal components. In this case the desired sampled signal is given by

$$d[n] = s(nT_s - \tau_r). \tag{5.30}$$

Defining the autocorrelation function of the sampled signal, $s(nT_s)$ as

$$R_d(\tau) = \mathrm{E}\left\{s(nT_s)s^*(nT_s - \tau)\right\} \tag{5.31}$$

we obtain

$$\mathbf{s}[n-l] = \mathbf{s}_o[n-l] + \mathbf{s}_c[n-l] \tag{5.32}$$

where

$$\mathbf{s}_o[n-l] = \mathbf{s}[n-l] - \begin{bmatrix} R_d^*(\tau_1 + lT_s - \tau_r) \\ R_d^*(\tau_2 + lT_s - \tau_r) \\ \vdots \\ R_d^*(\tau_L + lT_s - \tau_r) \end{bmatrix} d[n] \tag{5.33}$$

and

$$\mathbf{s}_c(n-l) = \begin{bmatrix} R_d^*(\tau_1 + lT_s - \tau_r) \\ R_d^*(\tau_2 + lT_s - \tau_r) \\ \vdots \\ R_d^*(\tau_L + lT_s - \tau_r) \end{bmatrix} d[n] \tag{5.34}$$

For convenience we define the vector

$$\mathbf{R}_d(l) = \begin{bmatrix} R_d^*(\tau_1 + lT_s - \tau_r) \\ R_d^*(\tau_2 + lT_s - \tau_r) \\ \vdots \\ R_d^*(\tau_L + lT_s - \tau_r) \end{bmatrix} \tag{5.35}$$

This gives

$$\mathbf{s}_o[n-l] = \mathbf{s}[n-l] - \mathbf{R}_d(l)d[n] \tag{5.36}$$

and

$$\mathbf{s}_c[n-l] = \mathbf{R}_d(l)d[n] \tag{5.37}$$

Therefore we may express $\acute{\mathbf{x}}[n]$ as

$$\acute{\mathbf{x}}[n] = \begin{bmatrix} \mathbf{A}\bar{\alpha}\mathbf{R}_d(0) \\ \mathbf{A}\bar{\alpha}\mathbf{R}_d(1) \\ \vdots \\ \mathbf{A}\bar{\alpha}\mathbf{R}_d(B-1)) \end{bmatrix} d[n] + \begin{bmatrix} \mathbf{A}\bar{\alpha}\mathbf{s}_o[n] \\ \mathbf{A}\bar{\alpha}\mathbf{s}_o[n-1] \\ \vdots \\ \mathbf{A}\bar{\alpha}\mathbf{s}_o[n-(B-1)]) \end{bmatrix} + \begin{bmatrix} \eta[n] \\ \eta[n-1] \\ \vdots \\ \eta[n-(B-1)] \end{bmatrix}. \tag{5.38}$$

Defining

$$\hat{\mathbf{v}} = \begin{bmatrix} \mathbf{A}\bar{\alpha}\mathbf{R}_d(0) \\ \mathbf{A}\bar{\alpha}\mathbf{R}_d(1) \\ \vdots \\ \mathbf{A}\bar{\alpha}\mathbf{R}_d(B-1)) \end{bmatrix} \tag{5.39}$$

and

$$\hat{\eta}[n] = \begin{bmatrix} \mathbf{A}\bar{\alpha}\mathbf{s}_o[n] \\ \mathbf{A}\bar{\alpha}\mathbf{s}_o[n-1] \\ \vdots \\ \mathbf{A}\bar{\alpha}\mathbf{s}_o[n-(B-1)]) \end{bmatrix} + \begin{bmatrix} \eta[n] \\ \eta[n-1] \\ \vdots \\ \eta[n-(B-1)] \end{bmatrix} \tag{5.40}$$

we obtain the following compact expression:

$$\acute{\mathbf{x}}[n] = \hat{\mathbf{v}}d[n] + \hat{\eta}[n]. \tag{5.41}$$

Since equation (5.38) is of the same form as (5.10) we may write the optimum output SINR performance of a wideband antenna array as

$$\mathrm{SINR}_{JSTF} = \hat{\mathbf{v}}^H \hat{\mathbf{R}}_{ii}^{-1} \hat{\mathbf{v}}. \tag{5.42}$$

where again $\hat{\mathbf{R}}_{ii} = \mathrm{E}\left\{\hat{\eta[t]}\hat{\eta[t]}^H\right\}$.

The closed form expression for $\hat{\mathbf{R}}_{ii}$ in this case is a straightforward extension of the result given above. From (5.40) we have

$$\hat{\mathbf{R}}_{ii} = \mathrm{E}\left\{ \begin{bmatrix} \mathbf{A}\bar{\alpha}\mathbf{s}_o[n] \\ \mathbf{A}\bar{\alpha}\mathbf{s}_o[n-1] \\ \vdots \\ \mathbf{A}\bar{\alpha}\mathbf{s}_o[n-(B-1)]) \end{bmatrix} \cdot \begin{bmatrix} \mathbf{A}\bar{\alpha}\mathbf{s}_o[n] \\ \mathbf{A}\bar{\alpha}\mathbf{s}_o[n-1] \\ \vdots \\ \mathbf{A}\bar{\alpha}\mathbf{s}_o[n-(B-1)]) \end{bmatrix}^H \right\} + \sigma_n^2 \mathbf{I}_{mB} \tag{5.43}$$

After expanding terms we obtain

$$\hat{\mathbf{R}}_{ii} = \begin{bmatrix} \mathbf{R}_i(0,0) & \mathbf{R}_i(0,1) & \cdots & \mathbf{R}_i(0,B-1) \\ \mathbf{R}_i(1,0) & \mathbf{R}_i(1,1) & \cdots & \mathbf{R}_i(1,B-1) \\ \vdots & & \ddots & \vdots \\ \mathbf{R}_i(B-1,0) & \mathbf{R}_i(B-1,1) & \cdots & \mathbf{R}_i(B-1,B-1) \end{bmatrix} + \sigma_n^2 \mathbf{I}_{mB} \tag{5.44}$$

where

$$\mathbf{R}_i(k,l) = \mathbf{A}\bar{\alpha}\mathbf{R}_{sso}(k,l)\bar{\alpha}^H\mathbf{A}^H. \tag{5.45}$$

and

$$\mathbf{R}_{sso}(k,l) = \mathrm{E}\left\{\mathbf{s}_o[n-k]\mathbf{s}_o^H[n-l]\right\} \tag{5.46}$$

The $(i,j)^{th}$ entry of $\mathbf{R}_{sso}(k,l)$ is given by

$$R_{i,j}(k,l) = R_d((\tau_j + lT_s) - (\tau_l + kT_s)) - R_d^*(\tau_i + kT_s - \tau_r)R_d(\tau_j + lT_s - \tau_r). \tag{5.47}$$

In calculating $\hat{\mathbf{R}}_{ii}$ one should make use of the hermitian symmetry of the matrix to reduce the required number of computations.

5.5 Independent Spatial/Temporal Filtering (ISTF)

The joint space-time receiver structure analyzed in the previous section provides the optimum output SINR of any linear structure which operates on multiple time samples of the signals present at the antenna array elements. However, due to the large number of weights which are jointly adapted, the complexity of this receiver structure may prohibit a practical implementation. One technique that can be used to reduce the complexity of joint space-time filters is to adapt the weights of each beamformer of a each tap independently of the other taps. The intermediate output signals are then aligned, scaled, and combined. This receiver structure is shown in Fig. 5.1 where Δ represents a unit delay.

Let $\mathbf{w}_l$ denote the weight vector applied to $\mathbf{x}[n+l]$, such that $z_l[n] = \mathbf{w}_l^H\mathbf{x}[n-l]$ is the lth beamformer output. The STF processor output may be expressed as

$$y[n] = c_0 z_0[n] + c_1 z_1[n] + \cdots + c_{B-1} z_{B-1}[n] \tag{5.48}$$

where c_i is the complex weight applied to the ith tap. The optimum weight vector at the lth tap is well known to be given by

$$\mathbf{w}_l = \mathbf{R}_{ii}(l)^{-1}\mathbf{v}_l \tag{5.49}$$

where $\mathbf{v}_l$ is the effective spatial signature vector and $R_{ii}(l)$ is the effective interference plus noise covariance matrix of the lth tap. From the results in the previous section we have

$$\mathbf{v}_l = \mathbf{A}\bar{\alpha}\mathbf{R}_d(l) \tag{5.50}$$

and

$$\mathbf{R}_{ii}(l) = \mathbf{R}_i(l,l) \tag{5.51}$$

Define the vector

$$\mathbf{z}[n] = \begin{bmatrix} z_0[n] \\ z_1[n] \\ \vdots \\ z_{B-1}[n] \end{bmatrix} = \begin{bmatrix} \mathbf{w}_0^H\mathbf{x}[n] \\ \mathbf{w}_1^H\mathbf{x}[n-1] \\ \vdots \\ \mathbf{w}_{B-1}^H\mathbf{x}[n-(B-1)] \end{bmatrix} = \begin{bmatrix} \mathbf{w}_0^H\mathbf{A}\bar{\alpha}\mathbf{s}[n] \\ \mathbf{w}_0^H\mathbf{A}\bar{\alpha}\mathbf{s}[n-1] \\ \vdots \\ \mathbf{w}_0^H\mathbf{A}\bar{\alpha}\mathbf{s}[n-(B-1)] \end{bmatrix} \tag{5.52}$$

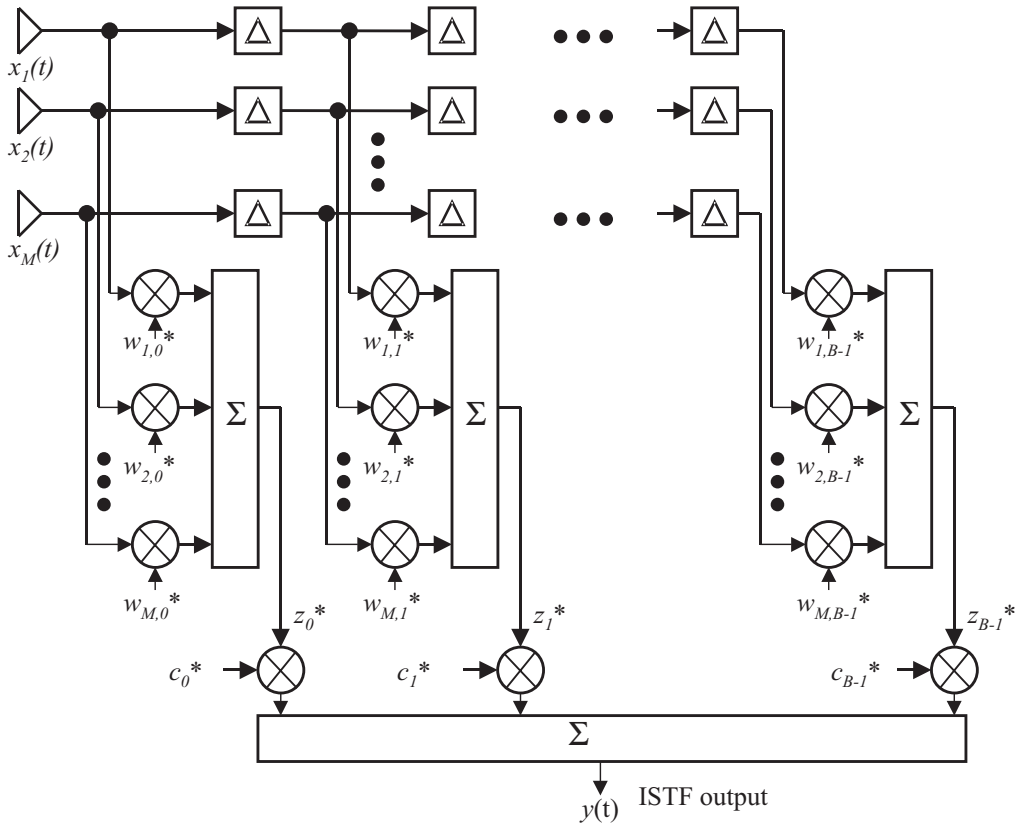

Figure 5.1: Independent Spatial/Temporal Filtering (ISTF) receiver structure.

Using the decomposition of $\mathbf{s}[n]$ given in (5.32) above, we may write

$$\mathbf{z}[n] = \begin{bmatrix} \mathbf{w}_0^H \mathbf{A}\bar{\alpha}\mathbf{R}_d(0) \\ \mathbf{w}_1^H \mathbf{A}\bar{\alpha}\mathbf{R}_d(1) \\ \vdots \\ \mathbf{w}_{B-1}^H \mathbf{A}\bar{\alpha}\mathbf{s}[n-(B-1)]\mathbf{R}_d(B-1) \end{bmatrix} d[n] + \hat{\eta}[n] = \hat{\mathbf{v}}d[n] + \hat{\eta}[n] \tag{5.53}$$

where

$$\hat{\mathbf{v}} = \begin{bmatrix} \mathbf{w}_0^H \mathbf{A}\bar{\alpha}\mathbf{R}_d(0) \\ \mathbf{w}_1^H \mathbf{A}\bar{\alpha}\mathbf{R}_d(1) \\ \vdots \\ \mathbf{w}_{B-1}^H \mathbf{A}\bar{\alpha}\mathbf{R}_d(B-1)) \end{bmatrix} \tag{5.54}$$

and

$$\hat{\eta}(n) = \begin{bmatrix} \mathbf{w}_0^H \mathbf{A}\bar{\alpha}\mathbf{s}_o[n] \\ \mathbf{w}_1^H \mathbf{A}\bar{\alpha}\mathbf{s}_o[n-1] \\ \vdots \\ \mathbf{w}_{B-1}^H \mathbf{A}\bar{\alpha}\mathbf{s}_o[n-(B-1)]) \end{bmatrix} + \begin{bmatrix} \mathbf{w}_0^H \eta[n] \\ \mathbf{w}_1^H \eta[n-1] \\ \vdots \\ \mathbf{w}_{B-1}^H \eta[n-(B-1)] \end{bmatrix} \tag{5.55}$$

The optimum output SINR becomes,

$$\text{SINR}_{ISTF} = \hat{\mathbf{v}}^H \hat{\mathbf{R}}_{ii}^{-1} \hat{\mathbf{v}}. \tag{5.56}$$

The i,jth component of the effective interference plus noise covariance matrix becomes

$$R_{i,j} = \begin{cases} \mathbf{w}_i^H \mathbf{R}(i,j)\mathbf{w}_j & : \text{for } i \neq j \\ \mathbf{w}_i^H \mathbf{R}(i,i)\mathbf{w}_i + \sigma_n^2 \mathbf{w}_i^H \mathbf{w}_i & : \text{for } i = j \end{cases} \tag{5.57}$$

where $\mathbf{R}(i,j)$ is defined above by (5.45).

5.6 Independent Temporal/Spatial Filtering (ITSF)

An alternative sub-optimum approach is to first adapt the temporal filter of each element independently of one another, and then combine the resulting outputs as shown in Fig. 5.2. In this case it is convenient to define the row vector $\mathbf{A}_m$ as the mth row of $\mathbf{A}$, so that the signal present on the mth antenna element may be expressed as

$$x_m[n] = \mathbf{A}_m \bar{\alpha} \mathbf{s}[n]. \tag{5.58}$$

Next we define the signal vector,

$$\mathbf{x}_m[n] = \begin{bmatrix} x_m[n] \\ x_m[n-1] \\ \vdots \\ x_m[n-(B-1)] \end{bmatrix} = \begin{bmatrix} \mathbf{A}_m \bar{\alpha} \mathbf{s}[n] \\ \mathbf{A}_m \bar{\alpha} \mathbf{s}[n-1] \\ \vdots \\ \mathbf{A}_m \bar{\alpha} \mathbf{s}[n-(B-1)] \end{bmatrix} \tag{5.59}$$

Let $\mathbf{c}_m$ denote the weight vector applied to the data vector of element m so that the mth equalizer output may be expressed as

$$Z_m[n] = \mathbf{c}_m^H \mathbf{x}_m[n] \tag{5.60}$$

Again it is well known that the optimum weight vector is given by

$$\mathbf{c}_m = \mathbf{R}_{ii}(m)^{-1} \mathbf{v}_m \tag{5.61}$$

where now $\mathbf{v}_m$ and $\mathbf{R}_{ii}(m)$ are the effective spatial signature vector and interference plus noise covariance matrices of the vector $x_m[n]$. Carrying out the signal decomposition, we find that the effective spatial signature vector is given by

$$\mathbf{v}_m = \begin{bmatrix} \mathbf{A}_m \bar{\alpha} \mathbf{R}_d(0) \\ \mathbf{A}_m \bar{\alpha} \mathbf{R}_d(1) \\ \vdots \\ \mathbf{A}_m \bar{\alpha} \mathbf{R}_d(B-1) \end{bmatrix}. \tag{5.62}$$

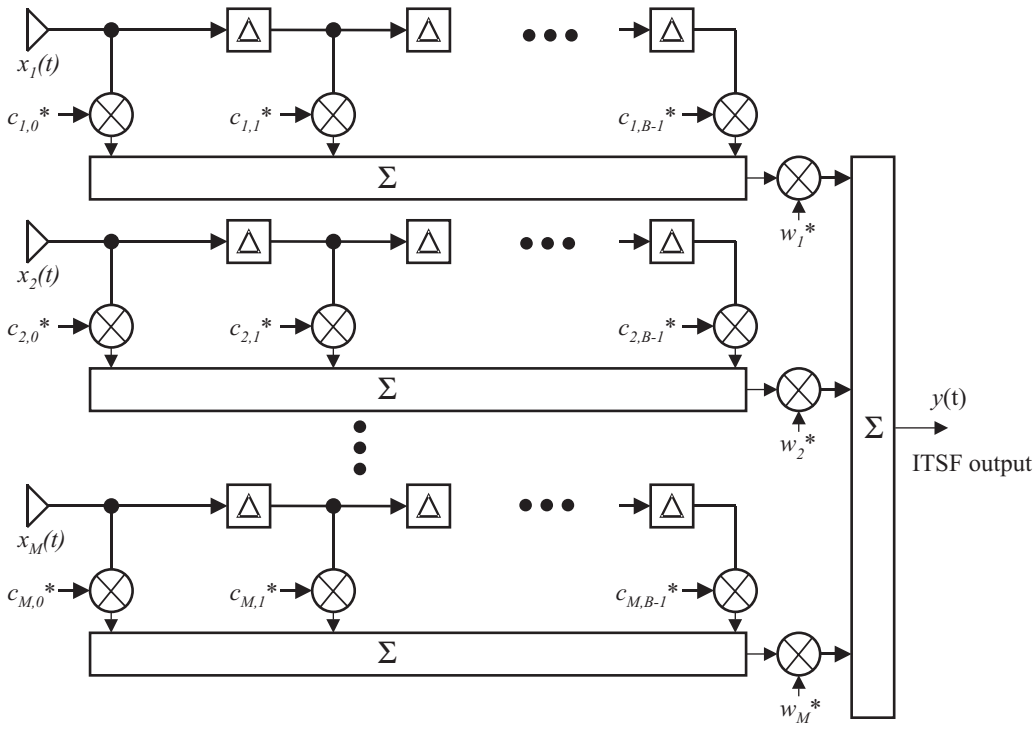

Figure 5.2: Independent Temporal/Spatial Filtering (ITSF) receiver structure.

Likewise, the interference plus noise covariance matrix is given by

$$\mathbf{R}_{ii}(m) = \begin{bmatrix} R_m(0,0) & R_m(0,1) & \cdots & R_m(0,B-1) \\ R_m(1,0) & R_m(1,1) & \cdots & R_m(1,B-1) \\ \vdots & & \ddots & \vdots \\ R_m(B-1,0) & R_m(B-1,1) & \cdots & R_m(B-1,B-1) \end{bmatrix} + \sigma_n^2 \mathbf{I}_B \tag{5.63}$$

where

$$R_m(k,l) = \mathbf{A}_m \bar{\alpha} R_{sso}(k,l) \bar{\alpha}^H \mathbf{A}_m^H \tag{5.64}$$

where $\mathbf{R}_{sso}$ is defined in (5.46).

The vector of intermediate equalizer outputs is given by

$$\mathbf{Z}[n] = \begin{bmatrix} Z_1[n] \\ Z_2[n] \\ \vdots \\ Z_M[n] \end{bmatrix} = \begin{bmatrix} \mathbf{c}_1^H \mathbf{x}_1[n] \\ \mathbf{c}_2^H \mathbf{x}_2[n] \\ \vdots \\ \mathbf{c}_M^H \mathbf{x}_M[n] \end{bmatrix} \tag{5.65}$$

The effective signature vector $\mathbf{Z}[n]$ is given by

$$\hat{\mathbf{v}}_z = \begin{bmatrix} \mathbf{c}_1^H \mathbf{v}_1 \\ \mathbf{c}_2^H \mathbf{v}_2 \\ \vdots \\ \mathbf{c}_M^H \mathbf{v}_M \end{bmatrix}. \tag{5.66}$$

Likewise, the the i,jth component of effective interference plus noise covariance matrix, $\hat{R}_{iiz}$ is given by

$$\hat{R}_{iiz}(i,j)\mathbf{c}_i^H\mathbf{A}_i\bar{\alpha}R_{sso}(i-1,j-1)\bar{\alpha}^H\mathbf{A}_j^H\mathbf{c}_j^H. \tag{5.67}$$

Finally, the optimum output SINR of this receiver structure is given by

$$\text{SINR}_{ITSF} = \hat{\mathbf{v}}_z{}^H\hat{\mathbf{R}}_{iiz}^{-1}\hat{\mathbf{v}}_z. \tag{5.68}$$

5.7 Simulation Results

In this section we use the closed formed expressions derived above for the optimum output SINR to evaluate the performance of various receiver structures in different multipath environments. The simulation results below assume BPSK signaling with square pulse shapes. In this case the autocorrelation function of the transmitted signal is given by

$$R_d(\tau) = \text{E}\left\{s(t)s^*(t-\tau)\right\} = \begin{cases} 1-|\tau|/T_b & : \text{for } |\tau| < T_b \\ 0 & : else \end{cases}, \tag{5.69}$$

where T_b is the symbol duration. For the case of the sampled signals, the sampled autocorrelation function should be used. When several samples are taken per symbol, then the continuous autocorrelation function provides a good approximation to the sampled autocorrelation function. For convenience, we will use the continuous autocorrelation to approximate the sampled autocorrelation function. Note that the sampled autocorrelation function will also depend upon where the samples occur within each symbol as well as on the number of samples per symbol. For each of the temporal filter structures it is assumed that the LOS component is aligned with the last tap in the receiver structure.

5.7.1 Validation of Results

In this section we validate the derivations above by comparing the closed formed expressions for each of the receiver structures described above with simulation results. For the simulated results, 100 data bits were generated with a sampling rate of two samples per bit. The sample matrix inverse algorithm was used to find the weight vector to apply to the data. For each data point, 1000 Monte Carlo trials were run.

The SINR at the array output is estimated from the cross-correlation of the array output, $y[k]$, with the reference signal, $d[k]$. The sampled cross-correlation of the two sequences is given by $\mathbf{r}_{yd} = \frac{1}{K}\sum_{k=1}^{K} y[k]d[k]^*$, where K denotes the number of samples over which the cross-correlation is estimated. The power in the reference signal is $R_{dd} = \frac{1}{K}\sum_{k=1}^{K} d[k]d^*[k]$. Using these relations, the power in the array output that is correlated with the desired signal, is given by $P_c = |\mathbf{r}_{yd}|^2/R_{dd}$, where it is necessary to divide by R_{dd} to remove the dependence of $\mathbf{r}_{yd}$ on the amplitude of the reference signal. Next, the interference and noise power is found by subtracting

the desired signal power, P_c, from the total power in the array output, $R_{yy} = \frac{1}{K}\sum_{k=1}^{K} d[k]d^*[k]$, to give SINR $= P_c/(R_{yy} - P_c)$.

Figures 5.3 through 5.7 show the simulated and analytical output SINR results for each of the receiver structures described above, as well as for the two important special cases of narrowband spatial filter and single channel temporal filter. The simulated values are shown as squares, whereas the analytical results are solid lines. The results are for a two element array with half wavelength spacing. For the temporal filter structure, ten taps are used. The results assume two multipath signal components, one with zero excess delay, and one with an excess delay equal to one symbol duration. The angle of arrival of the first path is broadside the array, and the angle of the second path is varied from 0 to 90 degrees. The SNR of each path is 30 dB. Finally, for each of the 1000 trials, random phases are assumed to the two paths. The path amplitudes are set equal to one. In all cases there is almost identical agreement between the two sets of results.

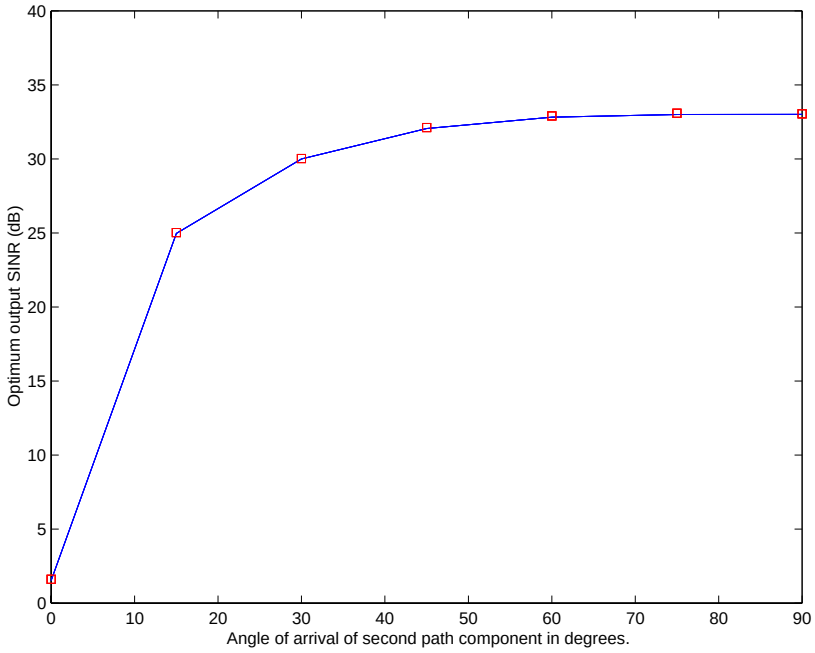

Figure 5.3: Validation of optimum output SINR for spatial filter.

5.7.2 Two-Ray Model

In this section the optimum output SINR assuming a two ray channel model is plotted for each of the receiver structures described above. Again a two element antenna array with half wavelength spacing is used. For the temporal receiver structures, 10 taps are assumed, with half a symbol spacing between taps. The amplitude of both paths is set equal to one, but the phase is selected from a uniform distribution from 0 to 2π. A total of 10,000 trials are run for each set of channel parameters and the average optimum output SINR is computed.

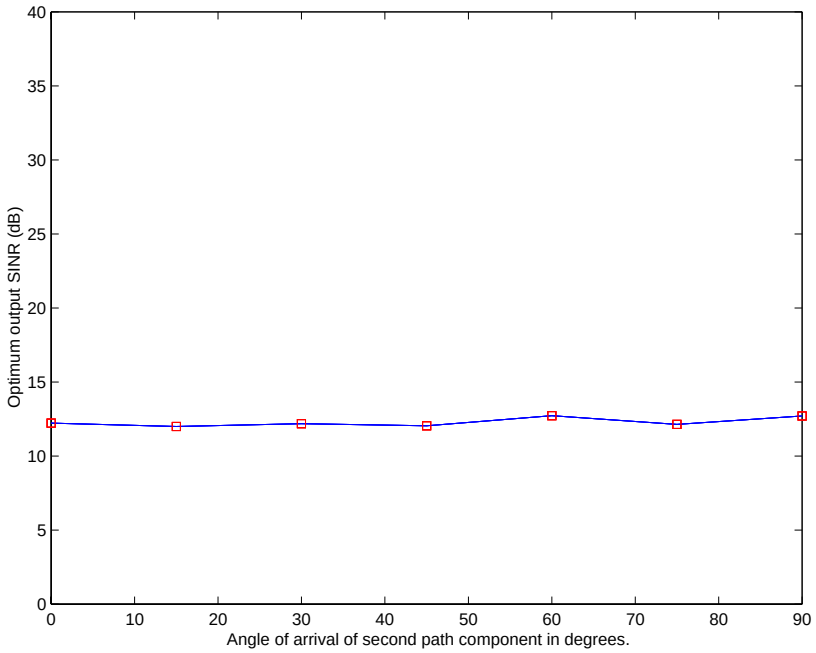

Figure 5.4: Validation of optimum output SINR for temporal filter.

In Figs. 5.8 and 5.9 the delay of the second path component is varied over the range from zero excess delay to an excess delay equal to one symbol duration. In Fig. 5.8 both signals arrive broadside the array. In this case, spatial processing is not capable of reducing intersymbol interference, and hence the spatial processing output SINR is nearly identical to the input SINR. When the delay of the second path approaches the symbol duration, then it becomes uncorrelated with the direct path. Since, both paths have equal power, the output SINR approaches 0 dB for spatial processing alone. However, for the receiver structures utilizing temporal processing, the impact of the intersymbol interference is not as great.

In Fig. 5.8 the second path is end-fire the array, and therefore spatial processing is useful in mitigating the intersymbol interference which occurs when the second path becomes uncorrelated with the first. In this case, the JSTF and the ISTF have nearly identical performance. As seen by comparing Fig. 5.8 with Fig. 5.9 the performance of the temporal filter is unaffected by the angle of arrival information.

The presence of the increase in the output SINR in Figs. 5.8 and 5.9 which occurs at a normalized delay of 0.5 is due to the fact that at this delay the second multipath signal is perfectly aligned with the desired signal at the second tap in the temporal receiver structures. This is due to the fact that here we assume that there is half a symbol duration between the taps in the receiver. At the other signal delays the second path is not perfectly aligned with any tap and hence it is only partially correlated with the desired signal at each tap. As expected when the second path has a higher correlation with the desired signal on a given tap the output SINR is higher.

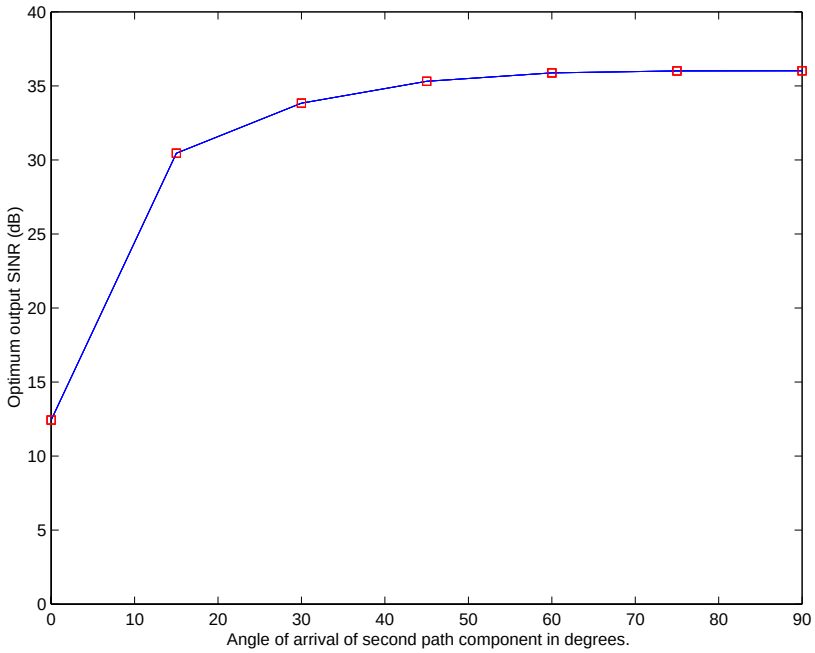

Figure 5.5: Validation of optimum output SINR for joint space time filter.

5.7.3 Circular Model

In this section the SINR CDF that results assuming a circular channel model with 5 scattering components, $D = 1000m$ and $R = 100m$ is found assuming symbol durations of $T_d = 10^{-5}$ sec and $T_d = 10^{-6}$ sec. The circular model is used to generate the channel angle of arrival and time of arrival parameters. The path amplitudes are all set equal to one. Random phases are assigned to each path from a uniform distribution over the range of $[0, 2\pi]$. A total of 10000 Monte Carlo trials, and the corresponding SINR CDF curves are found. The results are shown in Figs. 5.12 and 5.13. For the case when $T_d = 10^{-5}$ sec the channel is nearly flat fading, and therefore little is to be gained by temporal processing.

5.7.4 Liberti's Elliptical Model

In this section the SINR CDF that results assuming Liberti's elliptical channel model with 5 scattering components nd $\tau_m = 4\mu sec$ is found assuming symbol durations of $T_d = 10^{-5}$ sec and $T_d = 10^{-6}$ sec. In this case the angle of arrival and time of arrival parameters are obtained using the elliptical channel model. Again, The path amplitudes are all set equal to one and random phases are assigned to each path from a uniform distribution over the range of $[0, 2\pi]$. The SINR CDF curves are obtained from 10000 Monte Carlo trials. The results are shown in Figs. 5.14 and 5.15. Again, when $T_d = 10^{-5}$ sec there is little benefit from the temporal receiver structures. However, when $T_d = 10^{-6}$ sec there is a significant performance enhance obtained from temporal processing.

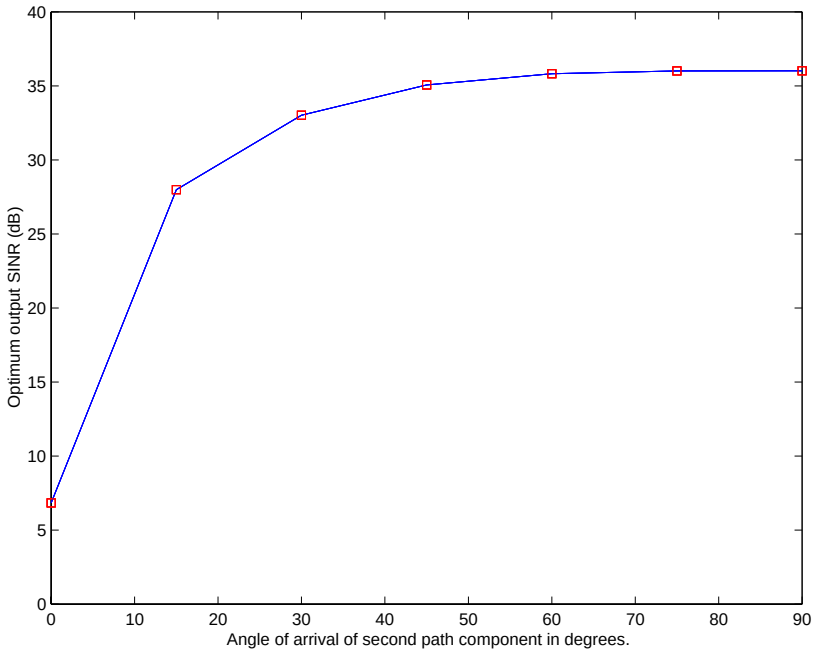

Figure 5.6: Validation of optimum output SINR for independent space/time filter.

5.8 Conclusions

In this chapter the optimum output SINR is derived for various space/time receiver structures in the presence of frequency selective fading channels. The results are used to predict the performance of the receiver structures in two ray, circular, and elliptical channel models.

As expected joint space-time processing provides the maximum output SINR of any of the receiver structures. The relative performance of temporal and spatial filters is dependent upon the parameters of the channel. When signal components arrive with a small separation angle between them then spatial processing is not as effective as when there is a large separation angle. The spatial processing receiver structures are also sensitive to the signal delays, since the signal delays will determine the level of correlation of the particular path with the desired signal. In contrast for temporal processing there is no dependence on the angle of arrival properties of the channel. For the sub-optimum space-time processing structures, it is found that the ISTF generally performs much better than the ITSF for most of the channel conditions considered. In fact, the ISTF typically achieves performance close to that of joint space-time processing.

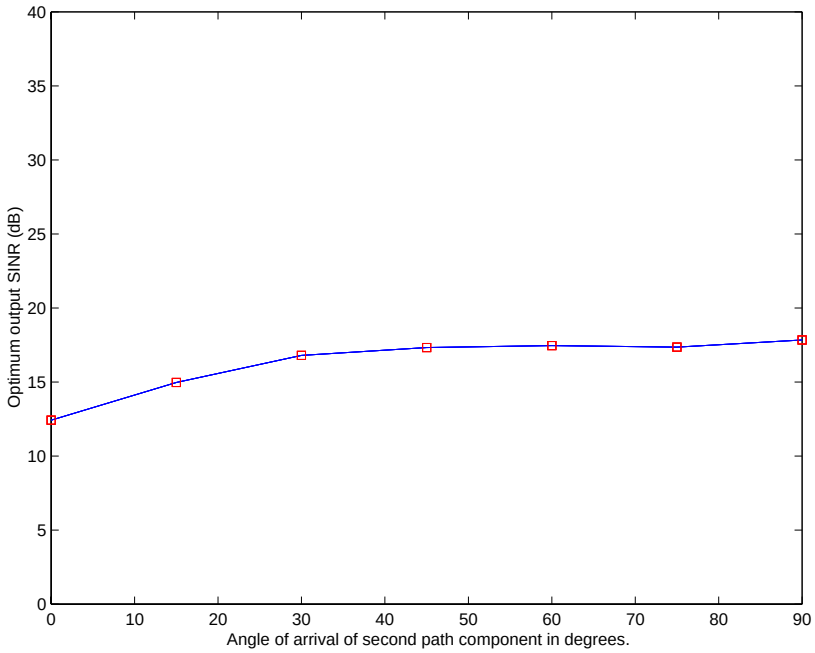

Figure 5.7: Validation of optimum output SINR for independent time/space filter.

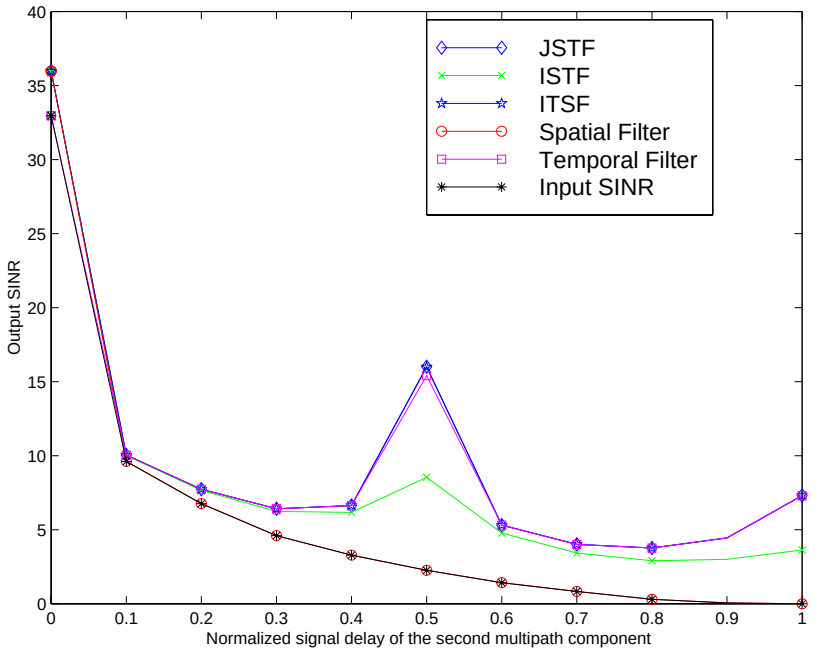

Figure 5.8: Optimum output SINR versus normalized delay of the second multipath component, when both signals are arriving from broadside the two elements.

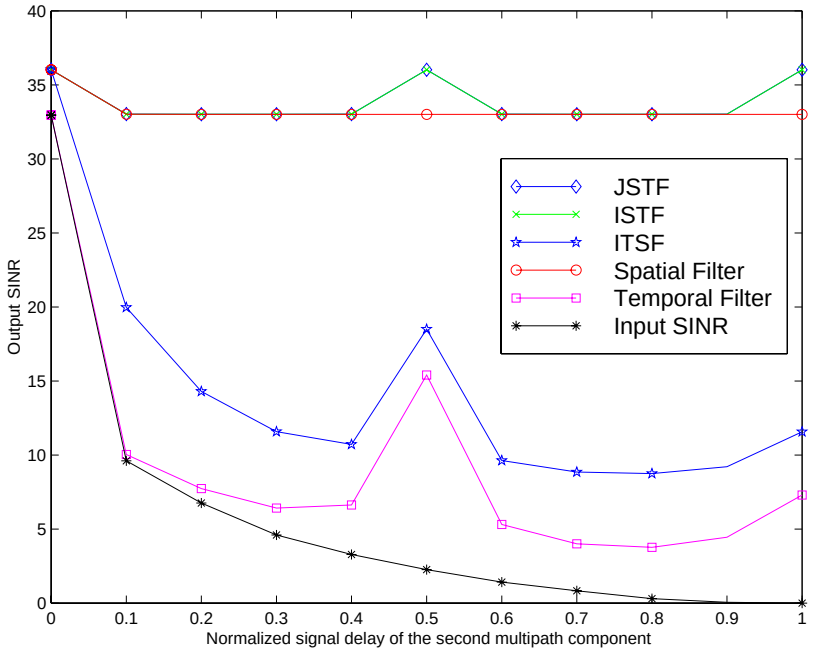

Figure 5.9: Optimum output SINR versus normalized delay of the second multipath component, when one signal is arriving from broadside and the second signal is arriving perpendicular to the line between the two elements.

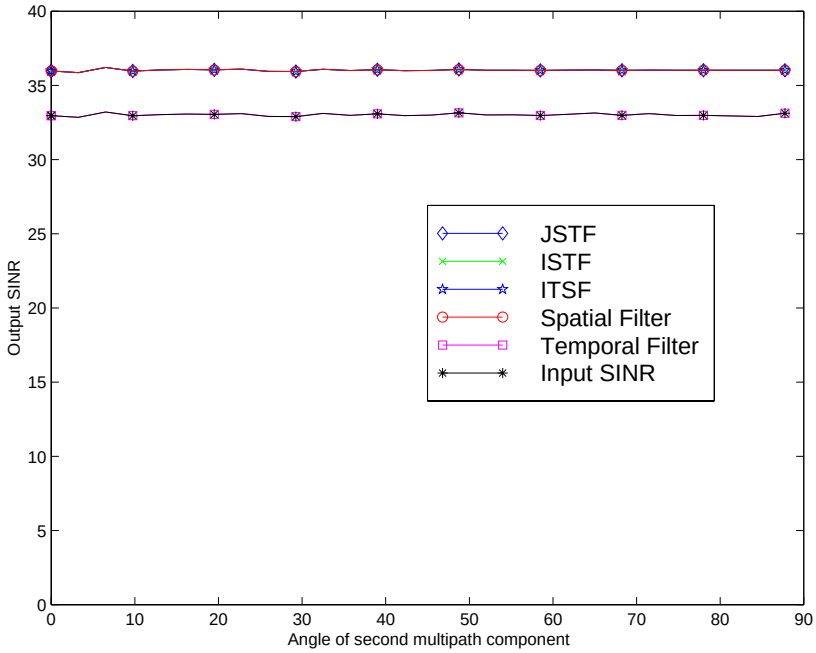

Figure 5.10: Optimum output SINR versus angle of arrival of the second multipath component, when both signals have zero excess path delay.

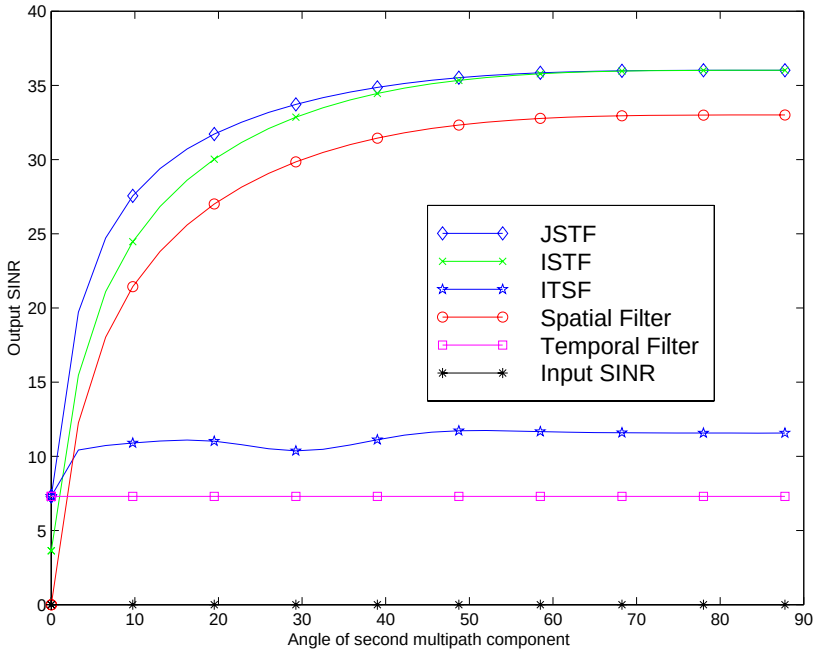

Figure 5.11: Optimum output SINR versus angle of arrival of the second multipath component, when the excess delay of the second signal is one symbol period.

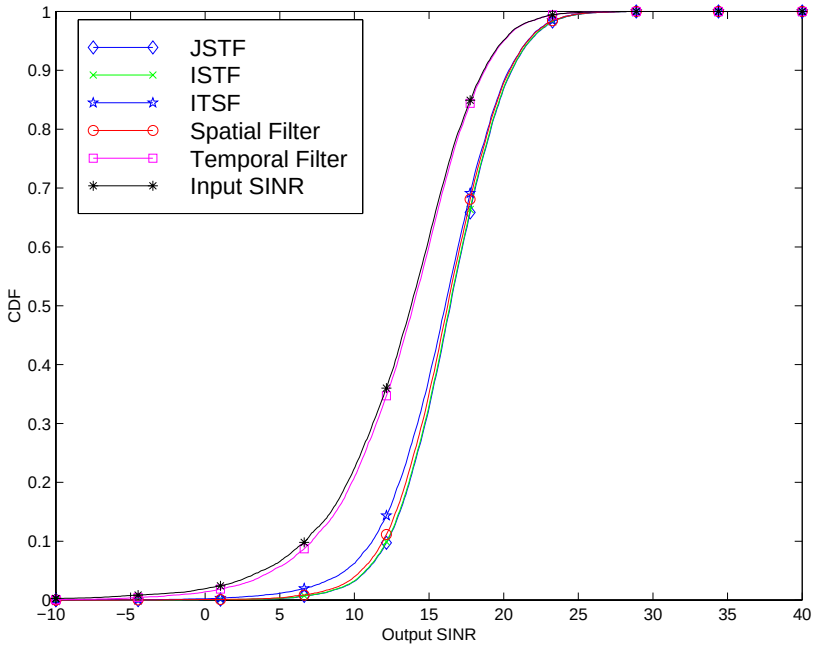

Figure 5.12: Optimum output SINR CDF assuming a circular scattering model with $D = 1000$ m, $R = 100$ m, and $T_d = 10^{-5}$ sec.

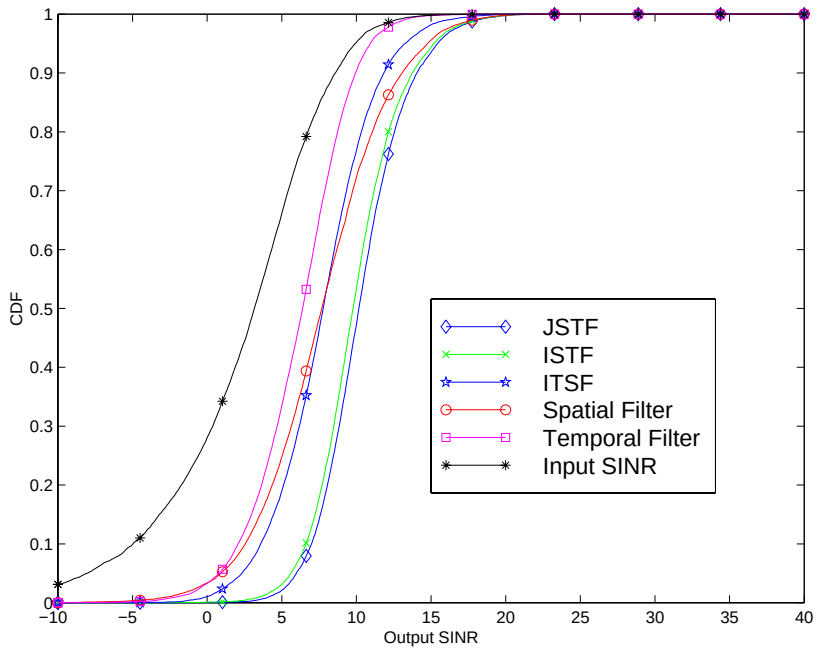

Figure 5.13: Optimum output SINR CDF assuming a circular scattering model with $D = 1000$ m, $R = 100$ m, and $T_d = 10^{-6}$ sec.

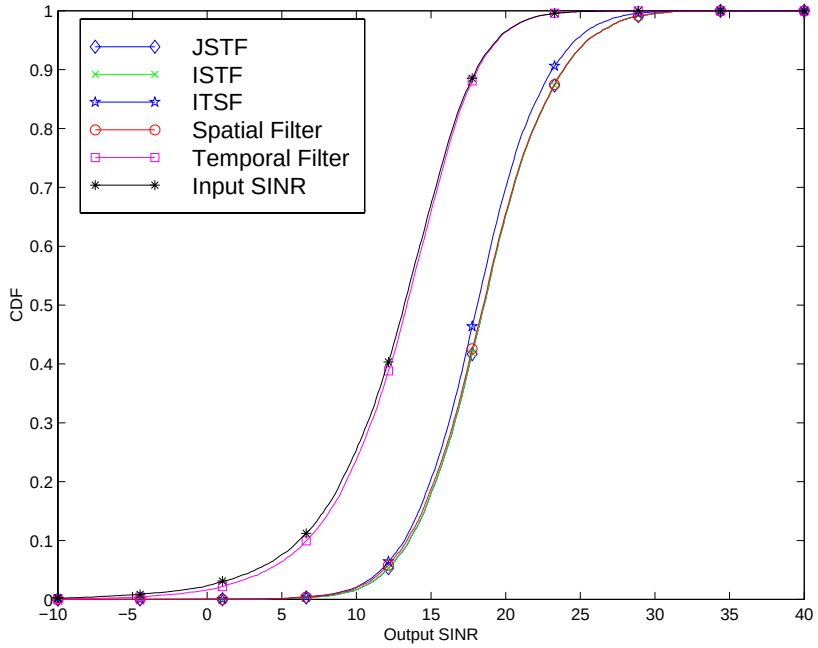

Figure 5.14: Optimum output SINR CDF assuming a elliptical scattering model with $D = 1000$ m, $\tau_m = 4\mu sec$, and Td=10^{-5} sec.

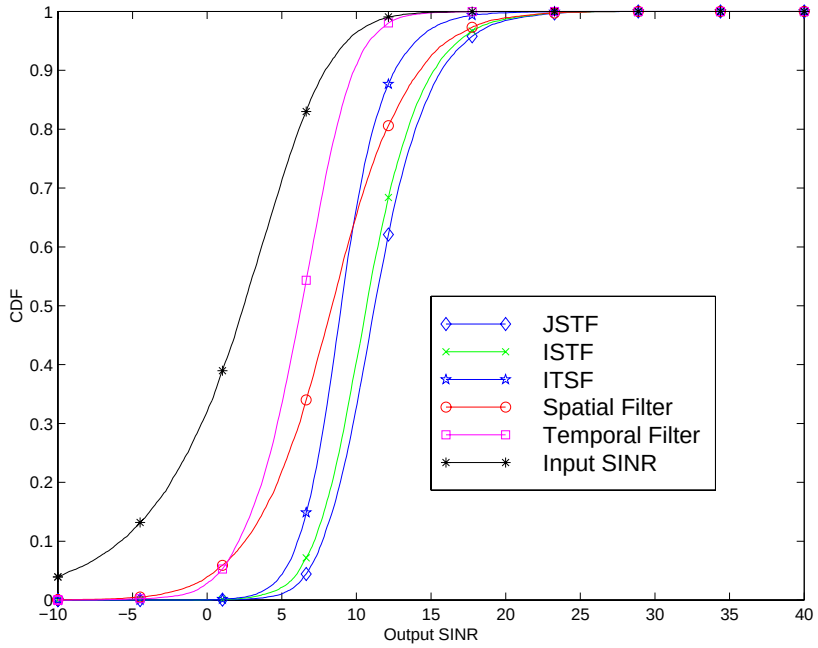

Figure 5.15: Optimum output SINR CDF assuming a elliptical scattering model with $D = 1000$ m, $\tau_m = 4\mu sec$, and Td=10^{-6} sec.

Chapter 6

MPRG Antenna Array Testbed

While theoretical channel models are useful for analysis and simulation purposes, there is no substitute for actual measured data. In practice channel models should be derived from either physical considerations, or from measured data. However, only when these models are validated through extensive measurement campaigns is there any confidence in their usefulness in modeling actual channels. To obtain measured channel data, as well as providing a demonstration tool for antenna array concepts, the MPRG has designed and developed the MPRG Antenna Array Testbed (MAAT). This system is used to make the antenna array measurements presented in Chapter 8. It has also been used to demonstrate receive diversity, transmit diversity, interference cancellation, and angle of arrival capabilities.

In this chapter the details of the MAAT system are described. Section 6.1 describes the array hardware and software. In Section 6.2 the bore-sighting procedure that is currently being used is discussed. Finally in Section 6.3 the stability of the array hardware is considered.

6.1 MPRG Measurement System

A high level block diagram of the MAAT system is shown in Fig. 6.1. Details of the analog tuner are given in Fig. 6.2. The system RF carrier frequency is tunable from 2035 to 2065 MHz. The antenna elements making up the eight element array are quarter wavelength monopoles, which are configured as either uniform linear array or uniform circular array with $\lambda/2$ spacing. The RF section of the receiver consists of an RF bandpass filter, a low noise amplifier, and a mixer. Each of the mixers is fed by an amplified common local oscillator output operating at 68 MHz below the selected carrier frequency. A one to eight signal splitter is used to provide the required eight oscillator signals. The output of the mixer contains the the signal modulated onto an IF frequency of 68 MHz. This signal is then bandpass filtered, further amplified, and then fed to the Sigtek ST-114 Digital Turner card. The Sigtek boards consists of an A/D converter followed by a digital downconversion subsection. The outputs of the Sigtek boards are the baseband I-Q signal components of the received signal quantized to 16 bits each. Further details regarding the RF and IF front-end system specifications are given in [50].

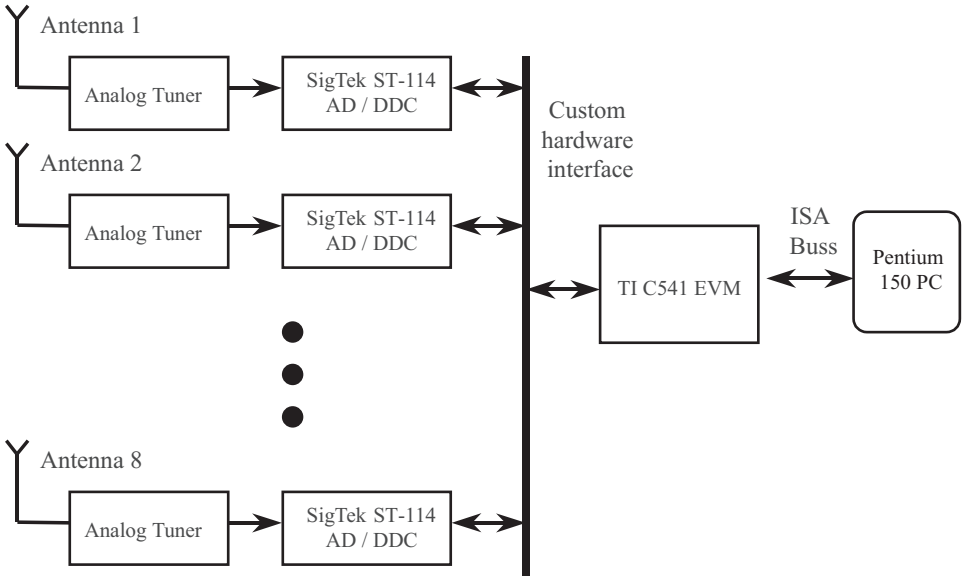

Figure 6.1: MPRG measurement system block diagram.

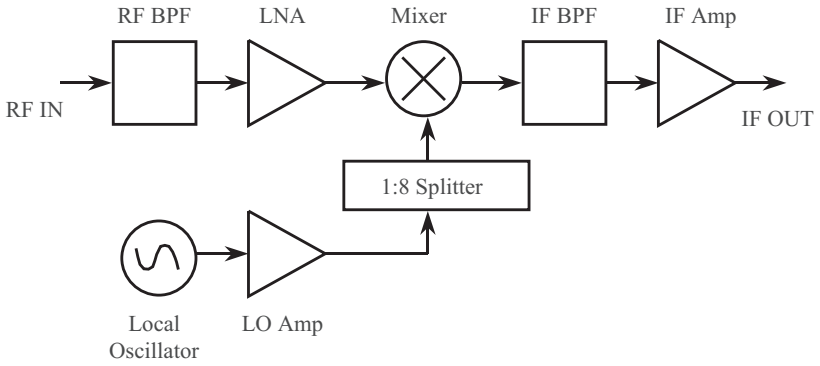

Figure 6.2: Analog filter block diagram.

The current collection system utilizes a TI320EVM board which is mounted on the ISA buss of the controlling PC. Data are collected and then stored in the onboard memory at variable sampling rates. The sampling frequency is presently limited by the TI DSP processing speed. Sampling rates as high as 125kHz are possible when data from all eight elements is collected.[1] The sampling rate may be increased inversely with the number of elements. Additionally, the duration of a continuous data collect is limited by the size of the memory on the TI DSP EVM. With the current collection program, there are 60416 addresses available for storing data. Each time sample requires 2 addresses for I and Q times the number of elements. When all eight elements are in use, a continuous data collect of 3776 samples is possible. Larger collection durations are possible when fewer elements are sampled.

When the memory on the TI320EVM board is filled, handshaking occurs with the host PC to

[1]This limitation will be reduced by utilizing a faster DSP in future systems.

retrieve the data. The PC interface is composed of a Visual Basic GUI, C-code TI-DSP interface software, and supporting Matlab code. The Visual Basic program is capable of controlling the TI-DSP execution, calling the required C-functions for data retrieval, and processing data with the Matlab engine.

The hardware interface between the Sigtek DDC boards and the TI320EVM board, the construction of the uniform circular antenna array, and the required software described above are original contributions of this work.

6.2 Array Boresighting Procedure

In this section we describe the array boresighting procedure that is being used with the MAAT to allow angle of arrival measurements to be made. Most direction finding algorithms require knowledge of the array manifold, the set of array response vectors as a function of angle of arrival. The array manifold is often estimated using expensive and time consuming array calibration procedures. An alternative is to bore-sight the array and then calculate the array manifold assuming that the antenna array is ideal.

Array calibration errors occur due to element position uncertainties, mutual coupling effects, and unknown amplitude and phase responses of the array hardware [51]. Our concern here is on the latter. In the absence of full array manifold measurements, it is often possible to use the location of the antenna elements to estimate the array manifold by assuming that the array is ideal. However, for this method to be successful, it is important that the amplitude and phase responses of the various branches of the array be known or accurately estimated. It is not uncommon for two branches to have drastically different phase responses due to the subtle differences in the individual hardware components making up each branch of the array.

One common method of estimating the amplitude and phase responses of the antenna array is to place a transmitter at a known angle of arrival relative to the array. The resulting phase responses can be compared against the known phase response of an ideal array. The difference in these two responses can be used as an estimate of the antenna array hardware phase shifts. In some instances it may not be possible to eliminate multipath propagation which will cause unknown phase shifts in the received signal vector. In this case subspace based techniques can still be used to estimate the calibration errors [51, 52]. Another disadvantage of this approach is the need for careful placement of the transmitter in the far field of the array. Additional approaches include using knowledge of a prominent reflector in the environment [53, 54], using multiple scattering sources [54], and using blind techniques [55, 56].

Another commonly used approach is to connect an RF signal generator to a multi-channel signal splitter, the outputs of which are connected to the input of the RF components of the array [57, 58]. Ideally signals with identical phase will be injected into the various branches of the array, and the measured array outputs can be used to determine the hardware amplitude and phase response. However, in practice it is possible that the difference in the signal phases at the output of the power splitter measures a few degrees. To accurately estimate the hardware amplitude and phase response of the array hardware, any phase differences in the channels of

the splitter must be found.

The calibration procedure we are using involves first estimating the relative amplitude and phase responses of the splitter. Next, the splitter calibration information is used to remove the effect of the splitter, such that the compensated data corresponds to the output of an ideal splitter. Finally, the relative amplitude and phase responses of the array hardware are estimated and removed from the data.

6.2.1 Hardware Setup

Our antenna array bore-sighting measurement setup is shown in Figure 6.3. An RF signal generator is connected to a Mini-Circuits ZB8PD-4 splitter, the outputs of which are fed into the eight channels of the MAAT. The Mini-Circuits splitter has a maximum unbalanced phase of ten degrees and a maximum unbalanced amplitude of 0.9dB between any two different output channels (see the Mini-Circuits RF/IF Designer's Handbook, p2-24).

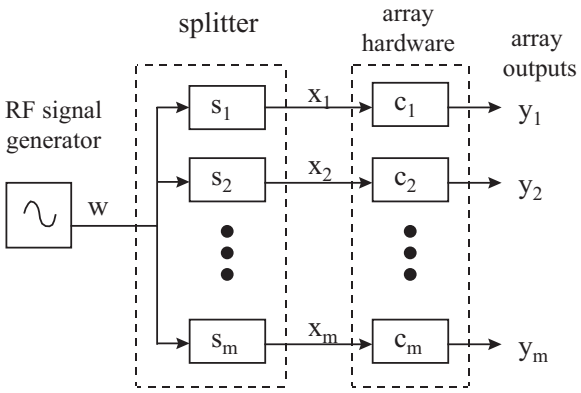

Figure 6.3: Array Bore-sighting Measurement Setup

6.2.2 Splitter Calibration

In this section a method of estimating the non-ideal amplitude and phase response of the signal splitter is described. Only the relative response of the branches of the splitter with respect to a reference branch is needed. Due to the high frequency of the RF signals measuring the phase at the splitter outputs directly may not be possible without the availability of expensive measurement equipment.

The procedure involves taking two measurements for each branch of the splitter, and switching the cables at the output of the splitter after the first measurement. Figures 6.4 and 6.5 show the setups for determining the relative amplitude and phase response of the reference branch (channel 1) with respect to the rth branch.

Let $y_1(k)$ and $y_r(k)$ denote the measured array outputs from the first measurement shown in Fig. 6.4 and let $z_1(k)$ and $z_r(k)$ denote the measured array outputs from the second measurement

as shown in Fig. 6.5. Also, let $w_1(k)$ and $w_2(k)$ denote the input to the splitter for first and second measurements respectively.

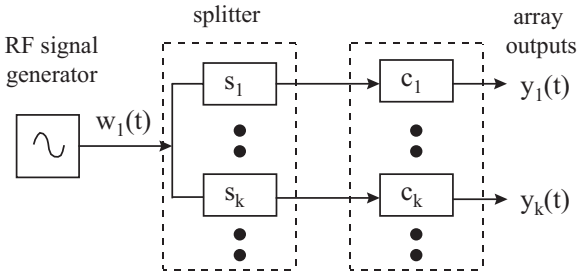

Figure 6.4: Setup for First Measurement

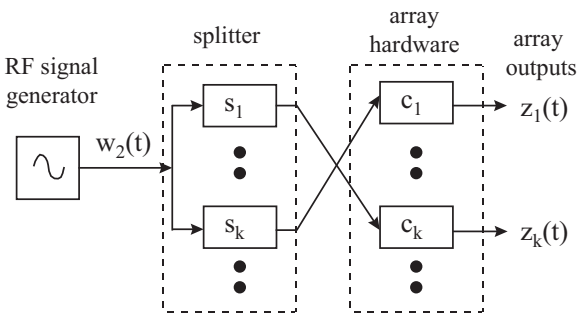

Figure 6.5: Setup for Second Measurement

Denoting the complex baseband response of the rth splitter branch by s_r, the measured outputs are given by

$$y_1(k) = c_1 s_1 w_1(k) + n_1(k) \tag{6.1}$$
$$y_r(k) = c_r s_r w_1(k) + n_2(k) \tag{6.2}$$
$$z_1(k) = c_1 s_r w_2(k) + n_3(k) \tag{6.3}$$
$$z_r(k) = c_r s_1 w_2(k) + n_4(k) \tag{6.4}$$

where $n_i(k)$ represents additive receiver noise. It is assumed that the following conditions hold:

$$\mathrm{E}\{n_i(k)\} = 0 \text{ for each } i \tag{6.5}$$
$$\mathrm{E}\{n_i(k) n_j(k)\} = 0 \text{ for } i \neq j \tag{6.6}$$
$$\mathrm{E}\{|n_i(k)|^2\} = \sigma_n^2 \text{ for each } i. \tag{6.7}$$

Our objective is to find the ratio $q_r = s_1/s_r$ by which we can multiply the received data to compensate for the relative amplitude and phase response of the rth splitter branch. Let

$$\mathbf{y}_{1r}(k) = \begin{bmatrix} y_1(k) \\ y_r(k) \end{bmatrix} \tag{6.8}$$

and

$$\mathbf{z}_{1r}(k) = \begin{bmatrix} z_1(k) \\ z_r(k) \end{bmatrix} \tag{6.9}$$

The estimated covariance matrices of $\mathbf{y}_{1r}$ and $\mathbf{z}_{1r}$ are given by

$$\hat{\mathbf{R}}_{yr} = \frac{1}{N}\sum_{k=1}^{N}\mathbf{y}_{1r}(k)\mathbf{y}_{1r}^{H}(k) \tag{6.10}$$

and

$$\hat{\mathbf{R}}_{zr} = \frac{1}{N}\sum_{k=1}^{N}\mathbf{z}_{1r}(k)\mathbf{z}_{1r}^{H}(k) \tag{6.11}$$

respectively, where $(.)^H$ denotes the hermitian operation. From (6.1) and (6.2) it can easily be shown that the dominant eigenvector of $\hat{\mathbf{R}}_{yr}$ is given by

$$\mathbf{e}_{yr} = \begin{bmatrix} c_1 s_1 \\ c_r s_r \end{bmatrix} \tag{6.12}$$

Likewise from (6.3) and (6.4) the dominant eigenvector of $\hat{\mathbf{R}}_{zr}$ is given by

$$\mathbf{e}_{zr} = \begin{bmatrix} c_1 s_r \\ c_r s_1 \end{bmatrix} \tag{6.13}$$

Normalizing the eigenvectors such that the first element is one, we obtain

$$\acute{\mathbf{e}}_{yr} = \begin{bmatrix} 1 \\ c_r s_r / c_1 s_1 \end{bmatrix} \tag{6.14}$$

and

$$\acute{\mathbf{e}}_{zr} = \begin{bmatrix} 1 \\ c_r s_1 / c_1 s_r \end{bmatrix} \tag{6.15}$$

Dividing the second component of $\acute{\mathbf{e}}_{zr}$ by the second component of $\acute{\mathbf{e}}_{yr}$ we obtain

$$\left(\frac{s_1}{s_r}\right)^2 = \gamma_r \tag{6.16}$$

where for convenience we define

$$\gamma_r = \frac{\acute{\mathbf{e}}_{zr}(2)}{\acute{\mathbf{e}}_{yr}(2)} \tag{6.17}$$

In solving (6.16) for $q_r = s_1/s_r$, we must account for all possible complex roots since γ_r is itself complex. Therefore, the two possible solutions to (6.16) are

$$|\gamma_r|^{1/2} e^{j\psi_r/2} \text{ and } |\gamma_r|^{1/2} e^{j(\psi_r/2+\pi)} \tag{6.18}$$

where $\psi_r = atan(\frac{Imag\{\gamma_r\}}{Real\{\gamma_r\}})$ is the phase of γ_r. Hence, there is an ambiguity of π in the phase of q_r. However, by assuming that the splitter is nearly ideal, we choose the solution with the minimum phase magnitude, i.e., we choose the solution q_r with phase between $-\pi/2$ and $\pi/2$. Measured results given in Table 6.1 below indicate that the relative phases of the splitter are small, and therefore choosing the phase as described is valid.

After the values q_r have been determined for all of the branches of the splitter, the non-ideal nature of the splitter can be compensated for by multiplying the rth channel output by q_r prior to estimating the antenna array amplitude and phase response. The splitter compensated array output is given by

$$\acute{\mathbf{y}}(k) = \begin{bmatrix} q_1 y_1(k) \\ q_2 y_2(k) \\ \vdots \\ q_m y_m(k) \end{bmatrix} = \begin{bmatrix} c_1(k) \\ c_2(k) \\ \vdots \\ c_m(k) \end{bmatrix} x_1(k) + \acute{\mathbf{n}}(k) \tag{6.19}$$

where $\acute{\mathbf{n}}(k) = [q_1 n_t(k)\ q_2 n_2(k)\ \cdots\ q_m n_m(k)]^T$ and $x_1(k) = s_1 w(k)$. Defining $\mathbf{c} = [c_1\ c_2\ \cdots\ c_m]^T$ then

$$\acute{\mathbf{y}}(k) = \mathbf{c} x_1(k) + \acute{\mathbf{n}}(k) \tag{6.20}$$

The resulting splitter compensated array output can be used to calibrate the array hardware as described in Section 6.2.3.

6.2.3 Hardware Amplitude and Phase Compensation

The signal amplitude and phase differences between array channels that remain after applying the splitter calibration procedure described above are due to subtle differences in the array hardware. It is these amplitude and phase differences that must be calibrated for accurate angle of arrival estimation.

The covariance matrix of the splitter compensated array output given in (6.19) is given by

$$\hat{\mathbf{R}}_{yy} = \frac{1}{N} \sum_{k=1}^{N} \acute{\mathbf{y}}(k) \acute{\mathbf{y}}^H(k) = \mathbf{R}_{ss} + \mathbf{R}_{nn} \tag{6.21}$$

where

$$\mathbf{R}_{ss} = \mathbf{c}\mathbf{c}^H \frac{1}{N} \sum_{k=1}^{N} |x_1(k)|^2 \tag{6.22}$$

and

$$\mathbf{R}_{nn} = \frac{1}{N} \sum_{k=1}^{N} \acute{\mathbf{n}}(k) \acute{\mathbf{n}}^H(k) \tag{6.23}$$

Provided that $|q_i| = |q_j|$ for all i, j, $\mathbf{R}_{nn}$ is an identity matrix. In this case $\mathbf{c}$ may be estimated to within a complex scalar from the dominant eigenvector of $\mathbf{R}_{yy}$. Otherwise, it should be estimated from the dominant eigenvector of $\mathbf{R}_{ss} = \mathbf{R}_{yy} - \mathbf{R}_{nn}$. In practice, with the signal being directly injected into the array hardware from a signal generator, the SNR will be sufficiently high so that the impact of noise may be neglected. Under this condition, the dominant eigenvector of R_{yy} is given by

$$\mathbf{e}_1 = \alpha \mathbf{c} \tag{6.24}$$

where α is an arbitrary complex constant. The relative phase response of branch 1 with respect to branch r, which is given by

$$r_r = \frac{c_1}{c_r} \tag{6.25}$$

is then found by dividing the first element of $\mathbf{e}_1$ by the rth element of $\mathbf{e}_1$.

Compensating for the amplitude and phase differences of the array hardware is accomplished by multiplying each of the rth received signals by r_r, since

$$\begin{bmatrix} r_1 y_1(k) \\ r_2 y_2(k) \\ \vdots \\ r_m y_m(k) \end{bmatrix} = \begin{bmatrix} r_1 c_1 x_1(k) \\ r_2 c_2 x_2(k) \\ \vdots \\ r_m c_m x_m(k) \end{bmatrix} = c_1 \begin{bmatrix} x_1(k) \\ x_2(k) \\ \vdots \\ x_m(k) \end{bmatrix} \tag{6.26}$$

is simply a scaled value of the incident signal vector. The input of each channel is scaled by the same amount, and therefore the relative amplitudes and phases at the input are maintained at the compensated array output.

6.2.4 Boresighting Results

In this section results are presented that were obtained using the procedures above to calibrate the splitter and then the antenna array. For each branch of the splitter, 3500 samples of data were collected from which q_r was calculated for each port. After the splitter was calibrated, the array hardware was calibrated by first multiplying the received data by the splitter calibration vector and then finding c_r as described in Section 6.2.3. The resulting compensation factors are shown in Tables 6.1 and 6.2 for the splitter and array hardware respectively.

While the relative splitter amplitudes are all nearly ideal (approximately equal to one), the measured relative splitter phases can be as high as 2.5 degrees. If one were to assume that the splitter were ideal, these phase shifts would mistakenly be included in the array hardware calibration factor.

The relative amplitude and phase of channel 1 with the various branches of the array are given in Table 6.2. Both the amplitude and phase responses of the array vary quite drastically from element to element indicating the need for array calibration.

Table 6.1: Splitter Calibration: amplitude and phase of q_r

element	amplitude	phase (degrees)
1	1	0
2	1.0306	-2.3635
3	1.0221	-1.2335
4	0.9879	0.5413
5	0.9663	-1.6064
6	0.9916	-2.6834
7	1.0478	-2.4947
8	1.0081	0.6186

The final test to determine the effectiveness of the calibration procedure described above involves angle of arrival measurements. Using our eight element uniform linear antenna array,

Table 6.2: Array Hardware Calibration: amplitude and phase of c_r

element	amplitude	phase (degrees)
1	1	0
2	1.0290	2.3033
3	1.2792	29.2297
4	1.2287	-19.5121
5	1.3461	-13.1873
6	1.1890	67.4705
7	1.1956	20.3478
8	1.7972	49.0068

measurements were made at fifteen degree increments over the entire 360 degree range. The transmit antenna was a stub loaded helix antenna with an antenna gain of approximately 10 dB. The transmit antenna was mounted on a wall pointing in the direction of the antenna array. The array was placed at a distance of 8.3m from the transmitter at a height of 2m. The array was rotated manually using a calibrated paper which was tapped onto the top of the array and a string which was tied from the center of the array to the transmit antenna. Due to the measurement setup, the true angle of arrival may differ from the desired amount by as much as a degree or two. Additionally, although a fairly open area was used for the measurement setup, it was not possible to eliminate multipath completely. The multipath makes it impossible to measure the array manifold directly. Regardless of these limitations, the measurements are still useful to obtain approximate measures of performance of the angle of arrival estimates.

The angle of arrival is estimated from the data using the classical delay and sum method [1]. The estimated angle of arrival is given by

$$\hat{\theta} = \arg\max_{\theta} \left(\mathbf{a}^H(\theta) \mathbf{R}_{xx} \mathbf{a}(\theta) \right) \tag{6.27}$$

where $\mathbf{a}(\theta)$ denotes the array response vector in the direction of θ and $\mathbf{R}_{xx}$ is the sample array covariance matrix. The errors of the angle of arrival estimates from ideal are shown in Fig. 6.6 versus the actual angle relative to the array broadside. As shown in the Fig. 6.6 all of the angle of arrival estimates are within six degrees, with smaller errors occurring when the transmitter is broad-side the array. The ability to obtain fairly accurate estimates of the angle of arrival indicates that by assuming an ideal array manifold one is able to obtain reasonable estimates of the actual array manifold provided that the amplitude and phase response of the array hardware is calibrated.

6.3 Antenna Array Hardware Stability

Motivated by the need to know how often the array hardware amplitude and phase responses must be calibrated several measurement studies were conducted. First the amplitude and phase responses of the antenna array hardware were measured over a ten hour period, starting with the system in a cold state. Next, the impact of cable motion of the cables which connect the

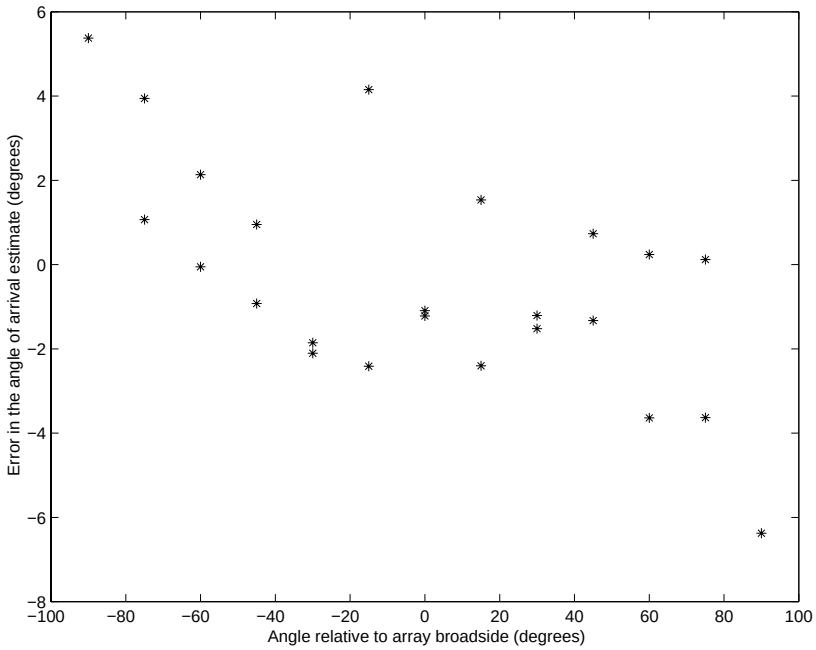

Figure 6.6: Measured errors in the angle of arrival measurements.

antenna element to the RF front-end was studied. Several measurements were made with the cables being bent or twisted between successive measurements. The impact of input signal level both with and without a variable AGC were considered. Finally, the impact of re-initializing the Sigtek ST-114 software has on amplitude and phase response is considered.

This report is organized as follows. Section 6.3.1 describes the measurement setup which is used for all of the measurements reported here. In Section 6.3.2 the stability of the array hardware response over time is considered. Sections 6.3.3 and 6.3.4 consider the impact of moving and reconnected the cables respectively. In Section 6.3.5 we consider the impact of input signal level on the hardware phase response. Section 6.3.6 is concerned with the variation of the array with input frequency. Section 6.3.7 shows results when the Sigtek ST-114 software is restarted. Finally, 6.3.8 summarizes the results of the stability measurements.

6.3.1 Stability Measurement Setup

The measurement system shown in Figure 6.3 was used to measure the stability of the array hardware and cable connections. The signal splitter is used in place of actual antenna elements to avoid unwanted variations in the environment.

For each measurement point reported, 3500 samples of data were collected at a 100kHz sampling rate. The signature vector of the data was collected as the normalized dominant eigenvector of the array covariance matrix scaled by the square root of the dominant eigenvalue. Scaling by the square root of the dominant eigenvalue allows the original signal amplitudes to be maintained.

The amplitude measurements reported below correspond to the measured amplitudes of the complex baseband data. The system is configured such that the maximum amplitude of the received signal is equal to one. The amplitude variations should be compared against the mean signal values shown in Fig. 6.7.

6.3.2 Time Stability

To determine the response of the antenna array hardware versus time, the signature vector of the array data was found at 10 second intervals for a period of 10 hours. The measurements started when the system was in a cold state, having been turned off for several hours prior to conducting the measurements. Figures 6.7 and 6.8 show the amplitude and phase responses of the antenna array hardware versus time. The phase responses shown in Fig. 6.8 are the demeaned signal phases referenced to channel 1 [2]. The corresponding demeaned amplitude and phase responses are shown in Figs. 6.9 and 6.10, respectively. A close-up of the demeaned amplitude and phase responses over the measurement period from 5 to 10 hours are shown in Figs. 6.11 and 6.12, respectively. As shown in Fig. 6.12 the relative phase variation is less than half a degree over the course of 5 hours.

The results indicate that a period of approximately 2.5 hours is needed until the array hardware stabilizes. However, even during this warm-up period the variations in the array hardware responses do not vary drastically. There is however a noticeable decrease in the variation of the array hardware responses after the warm-up period. The standard deviation of the amplitude and phase responses measured over the period from 5 to 10 hours are shown in Table 6.3. The values are fairly low indicating good stability of the array hardware over time.

Table 6.3: Standard deviation of the array hardware amplitude and phase stability versus time after warm-up period.

element	amplitude standard deviation	phase standard deviation (degrees)
1	0.000266	0.000000
2	0.000169	0.040289
3	0.000156	0.051239
4	0.000165	0.053611
5	0.000166	0.081976
6	0.000177	0.096358
7	0.000165	0.072256
8	0.000151	0.063971

6.3.3 Cable Motion Effects

In this section the variation of the array response caused by motion of the cables which connect the antenna element to the RF front end is considered. Five measurements were made with the

[2]The demeaned values are obtained by subtracting the mean of the signal from the signal.

cables being moved between each measurement. The corresponding demeaned amplitude and phase response of the array are shown in Figs. 6.13 and 6.14, respectively. Clearly, motion of the cables has an impact on the response of the array. The standard deviation of the amplitude and phase variations for each channel are given in Table 6.4. These values are several times greater than those observed above in Table 6.3, and therefore the large variations are indeed a result of cable variations, not time instability of the array hardware.

Table 6.4: Standard deviation of the array hardware amplitude and phase stability with cable motion.

element	amplitude standard deviation	phase standard deviation (degrees)
1	0.000643	0.000000
2	0.000638	0.547946
3	0.000416	0.271570
4	0.001270	0.841320
5	0.001405	0.782231
6	0.000238	0.255651
7	0.000525	0.437774
8	0.000274	0.401955

6.3.4 Cable Connections

The currently used boresighting procedure requires that the cables be disconnected from the splitter and then attached to the antenna element. A question of interest is how sensitive is the array response to the connection made by the cable. Again, five measurements were made, with the cables loosened and then tightened with a wrench between each trial. Loosening and tightening the cable connections did cause slight variations in the cable placement, and hence some of the variation may be attributed to this effect as well. The resulting demeaned amplitude and phase responses of the array are shown in Figs. 6.15 and 6.16. The corresponding standard deviations are given in Table 6.5. Surprisingly the standard deviation in the amplitude are greater than those found above for cable motion. However, in this case the standard deviation in phase is generally less than those due to cable motion. There is a noticeable difference in the standard deviation observed here with the ones found above for the variation of the array versus time. The measured values were obtained when a wrench was used to tighten the connection. If the cables are tightened by hand one might expect even larger variation in the amplitude and phase response of the array.

6.3.5 Input Signal Level

In this section we consider the relative phase responses of the array versus input signal level with and without a variable AGC. Figure 6.17 shows the demeaned relative phase response of the array for various input signal levels when the AGC is held fixed at 20dB. There are noticeable phase variations versus signal level. The standard deviation of the phase response over all of the measurements is given in Table 6.5. The corresponding plot and standard deviation values

Table 6.5: Standard deviation of the array hardware amplitude and phase stability with each cable being reconnected after each measurement.

element	amplitude standard deviation	phase standard deviation (degrees)
1	0.003082	0.000000
2	0.002721	0.053289
3	0.001776	0.682610
4	0.003314	0.038999
5	0.002925	0.687956
6	0.002298	0.062027
7	0.002295	0.041503
8	0.001788	0.083567

are given in Fig. 6.18 and Table 6.7 for the case when the AGC gain is automatically adjusted from 0dB to 95dB. Again, there is a significant phase variation.

Table 6.6: Standard deviation of the array hardware amplitude and phase stability over a range of input signal levels.

element	phase standard deviation (degrees)
1	0.000000
2	0.622423
3	1.418892
4	0.233498
5	0.217019
6	0.415027
7	2.621754
8	1.278324

Table 6.7: Standard deviation of the array hardware amplitude and phase stability over a range of input signal levels with AGC on.

element	phase standard deviation (degrees)
1	0.000000
2	0.511937
3	1.412915
4	0.218746
5	0.198953
6	0.358341
7	2.676416
8	1.152367

6.3.6 Baseband Input Frequency

The response of the array versus the baseband input signal frequency is considered here. With the AGC fixed at 20dB of gain, the input frequency was varied from 1 kHz to 25kHz in 1 kHz increments. The resulting amplitude and demeaned phase responses are shown in Figs. 6.19 and 6.20 below. In this case the phase shows very little variation with frequency, whereas the amplitude varies significantly. This variation in the signal amplitude is the result of the filters in the SigTek card.

6.3.7 Restarting AD/DDC Card Software

In the current configuration, changing AGC settings and/or sampling rate requires that the Sigtek ST-114 AD/DDC card software is restarted. In this section we study the impact of this operation on array calibration. Again, five measurements were made with the Sigtek ST-114 software being restarted between each measurement. The demeaned amplitude and absolute relative phase responses are shown in Figs. 6.21 and 6.22. As seen in Fig. 6.22 restarting the software has an enormous impact on the phase, and therefore array boresighting procedure must be done each time the software is restarted.

6.3.8 Summary of Stability Measurements

The measurement results presented above provide information regarding the stability of the array response to time, cable motion, cable connection, input signal level, carrier frequency, and software restarting. The array hardware response is found to be relatively constant with time after an initial warm-up period of approximately 2.5 hours. It was found that cable motion and cable connection have a noticeable but yet small impact on the array response. The amplitude response changed significantly with input frequency, while the phase changed only a little. Finally, it was found that restarting the software puts the channels in random relative phases which may cause drastic changes to the phase response.

6.4 Conclusions

In this chapter the MAAT that is used to collect measured data is described. The procedure for bore-sighting the array is presented along with angle of arrival measurement results that indicate it's effectiveness. It is found that the angle of arrival estimates are all within six degrees of the true angle of arrival, with the majority of the estimates being within two degrees of the true values.

Finally the stability of the array hardware was studied. The key result involving the stability of the array hardware is that it is relatively constant with time after an initial warm-up period of approximately 2.5 hours.

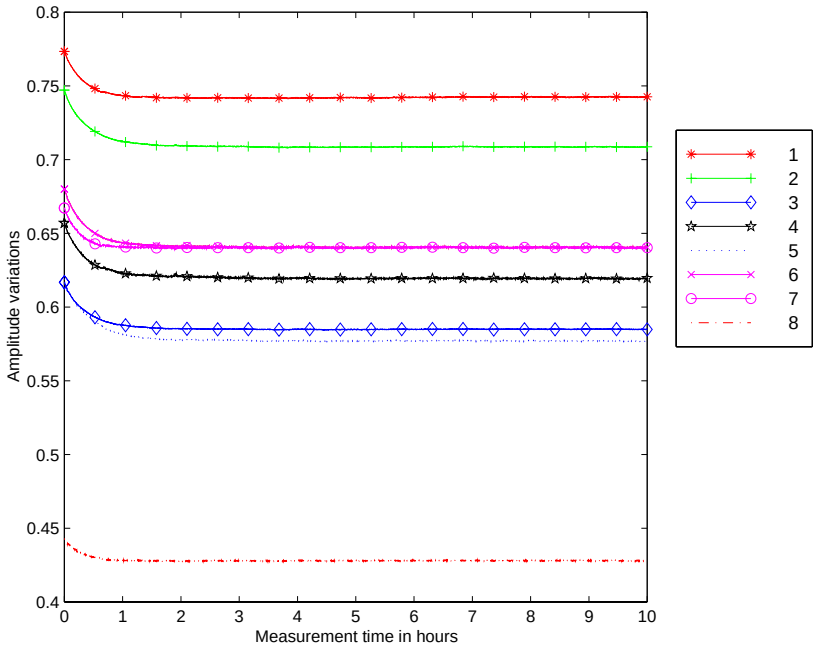

Figure 6.7: Amplitude response of the array hardware versus time.

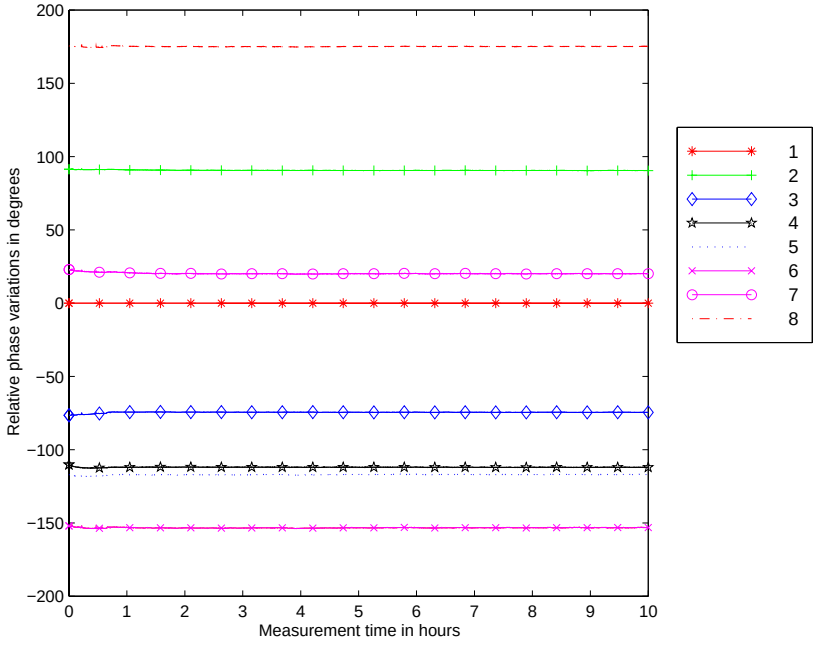

Figure 6.8: Relative phase of the array hardware versus time.

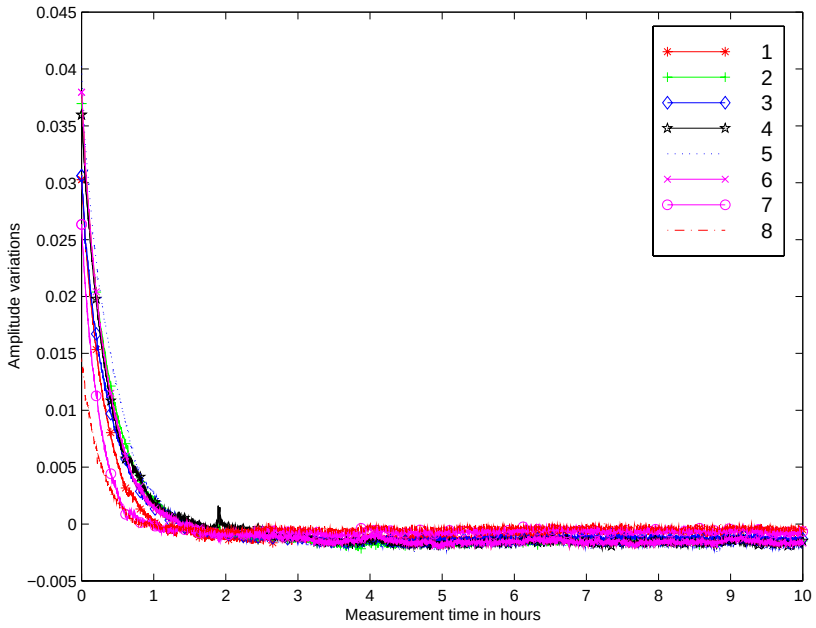

Figure 6.9: Demeaned amplitude response of the array hardware versus time.

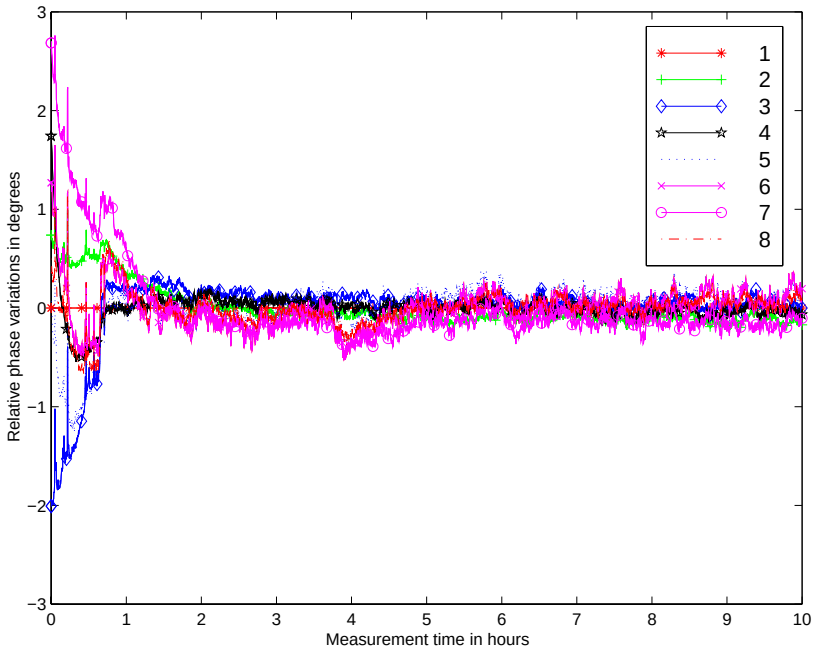

Figure 6.10: Demeaned relative phase of the array hardware versus time.

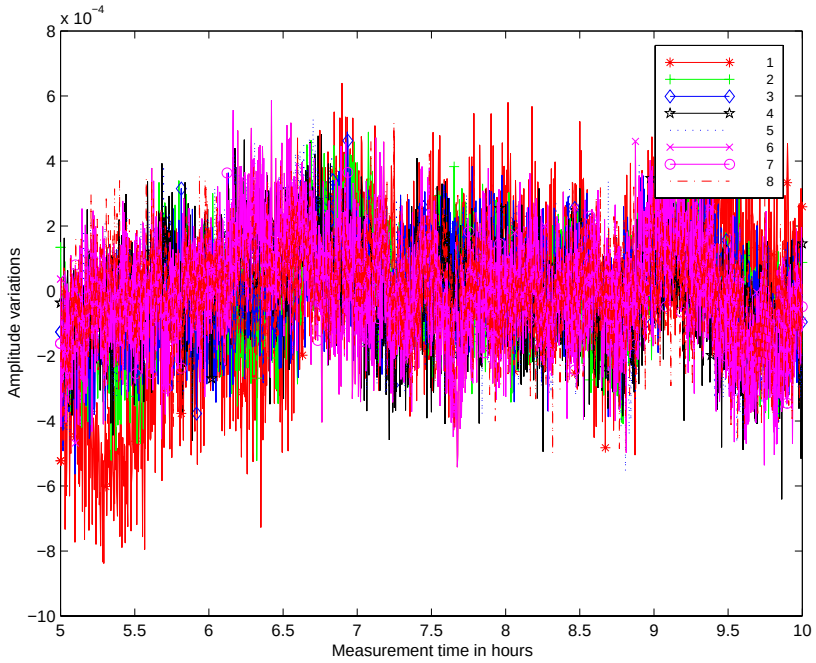

Figure 6.11: Demeaned amplitude response of the array hardware versus time for the time period of 5 to 10 hours.

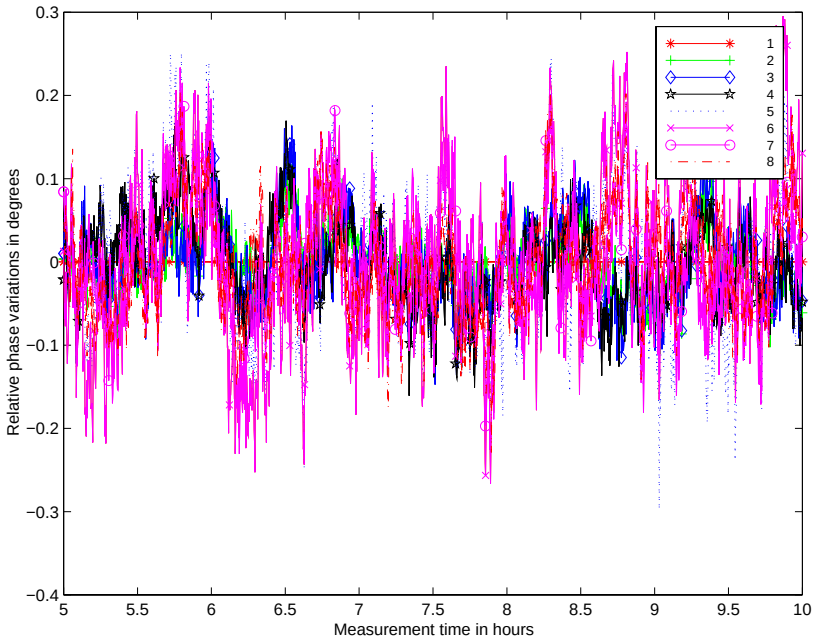

Figure 6.12: Demeaned relative phase of the array hardware versus time for the time period of 5 to 10 hours.

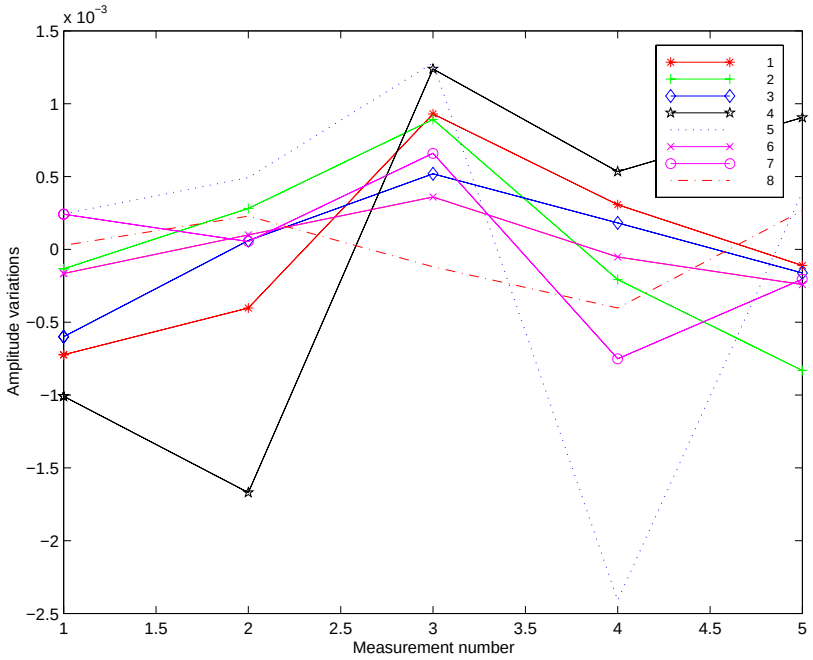

Figure 6.13: Demeaned amplitude response of the array hardware with cable motion.

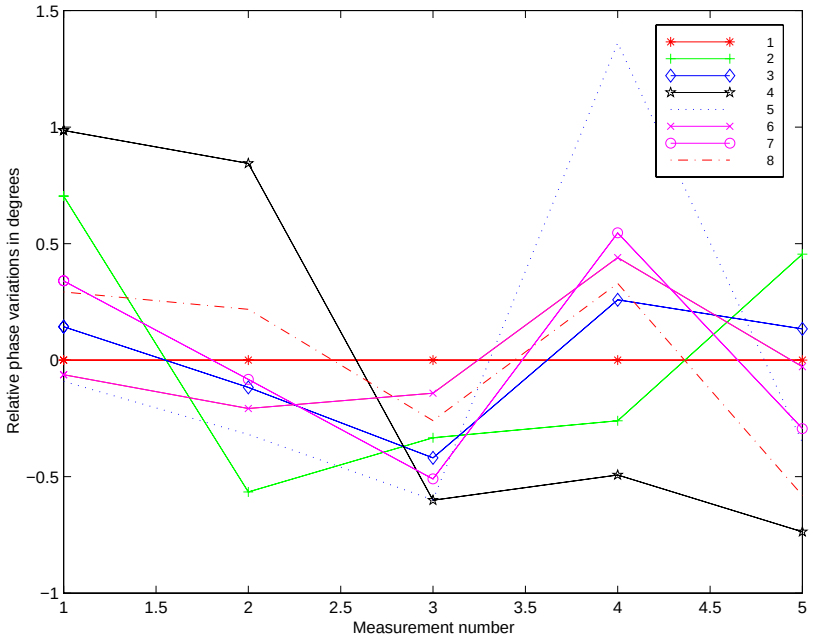

Figure 6.14: Demeaned relative phase of the array hardware with cable motion.

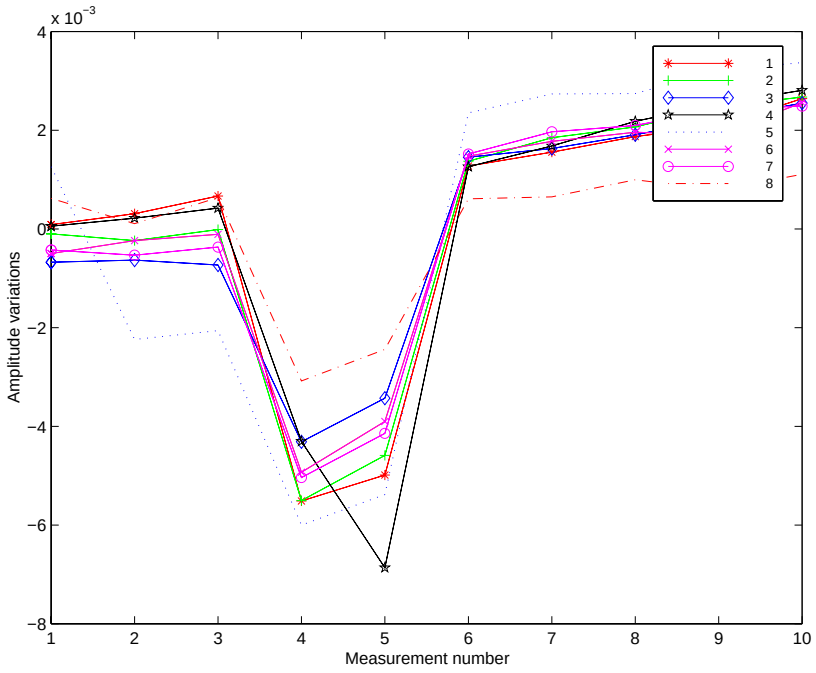

Figure 6.15: Demeaned amplitude response of the array hardware with each cable being reconnected after each measurement.

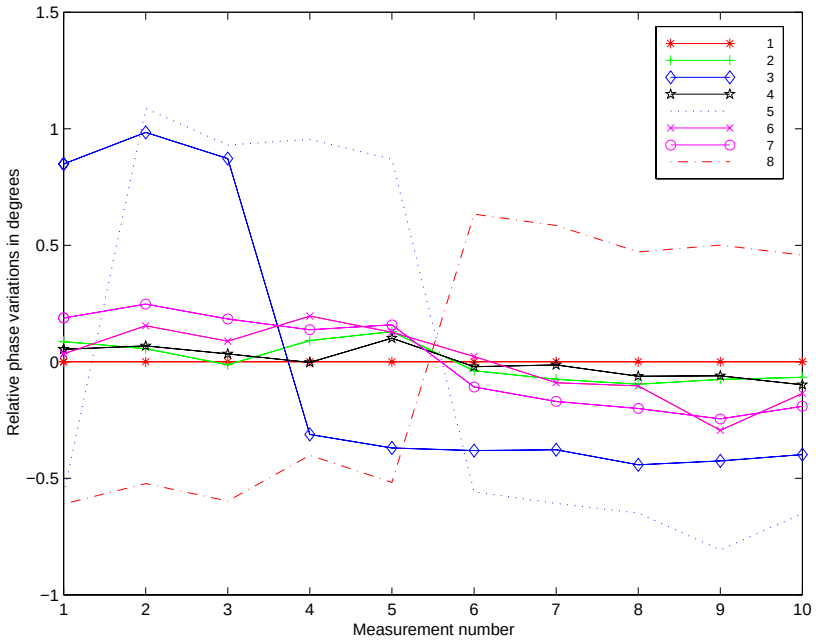

Figure 6.16: Demeaned relative phase of the array hardware with each cable being reconnected after each measurement.

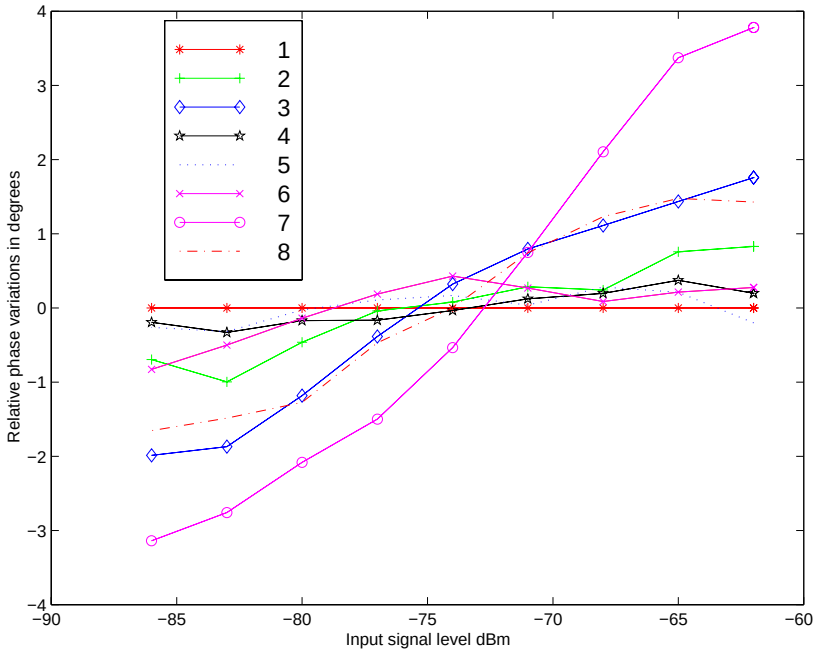

Figure 6.17: Demeaned relative phase of the array hardware for various input signal levels.

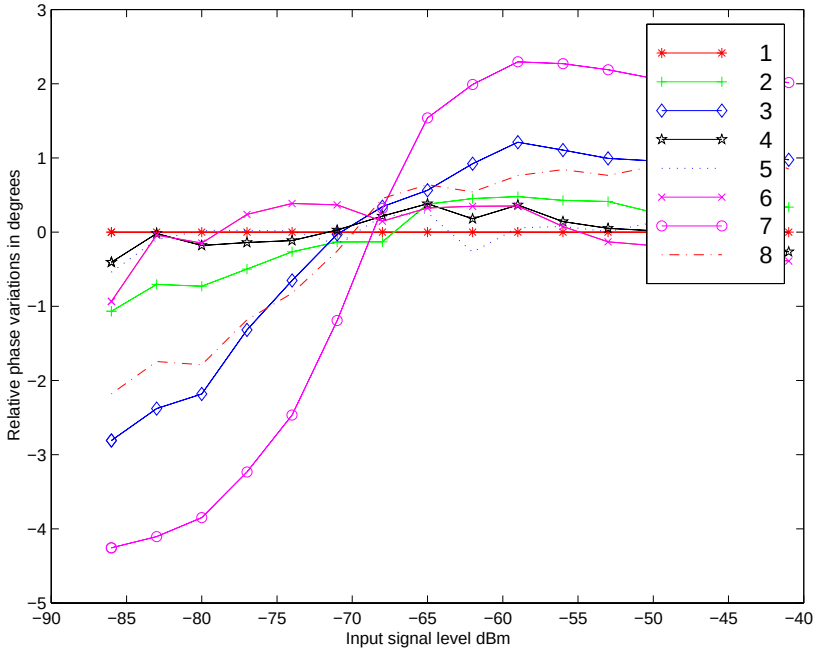

Figure 6.18: Demeaned relative phase of the array hardware for various input signal levels with AGC on.

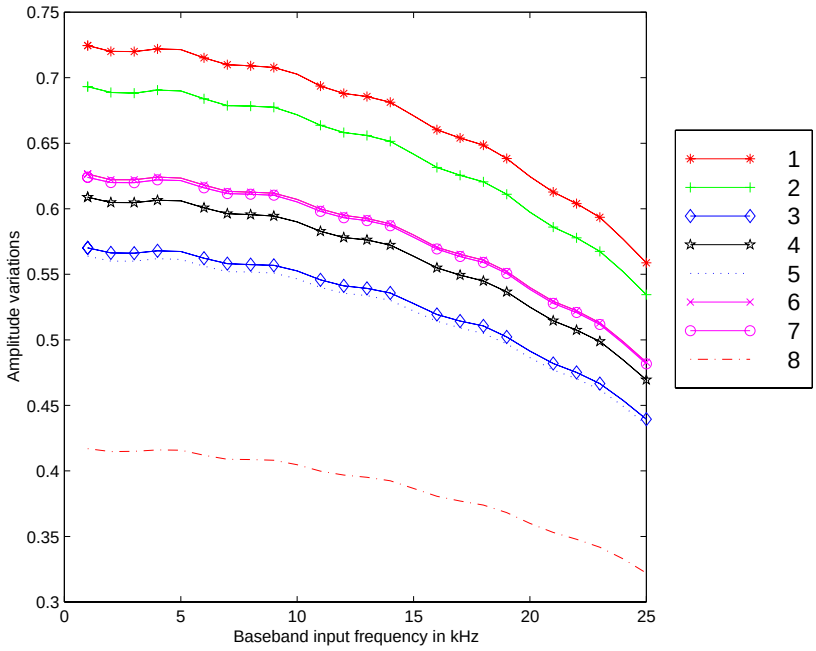

Figure 6.19: Amplitude response of the array hardware versus baseband input frequency.

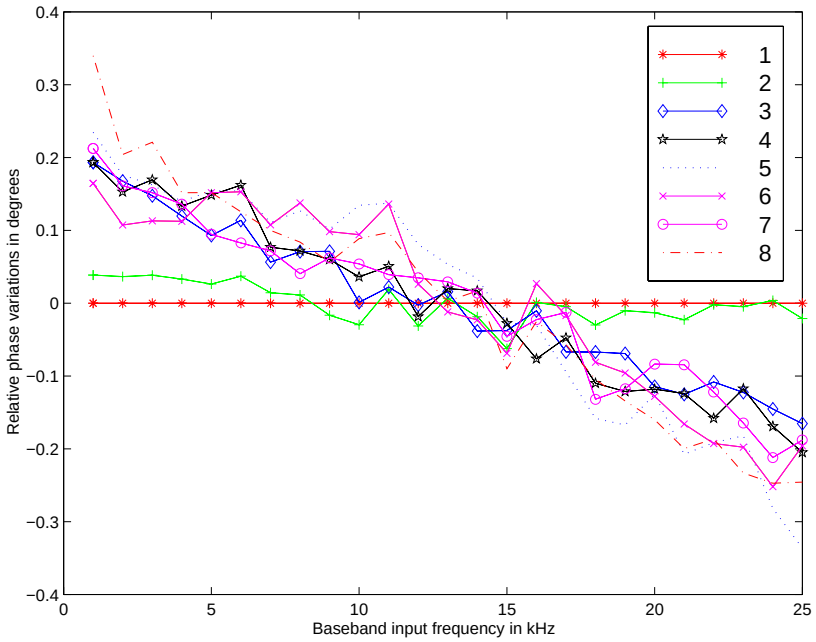

Figure 6.20: Demeaned relative phase of the array hardware versus baseband input frequency.

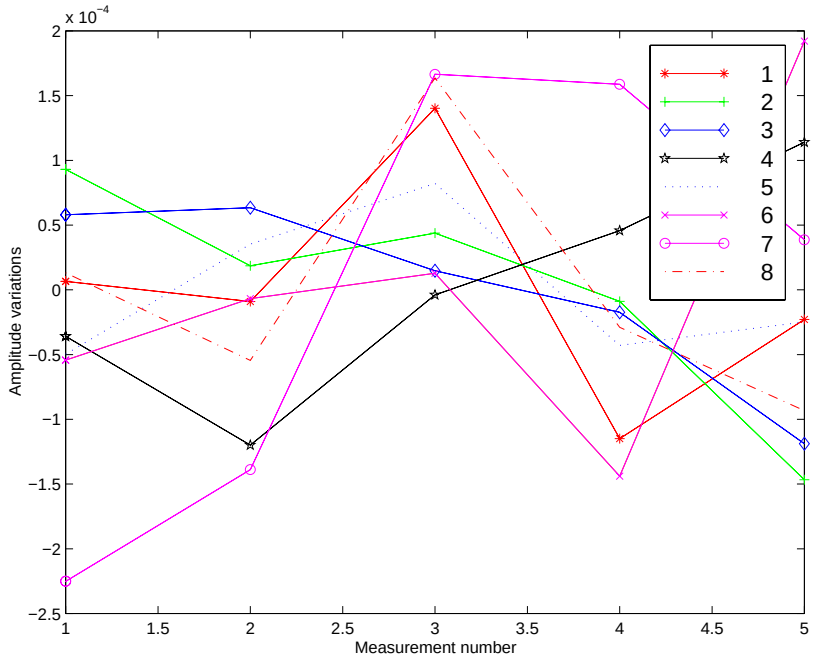

Figure 6.21: Demeaned amplitude response of the array hardware with the software being restarted after each measurement.

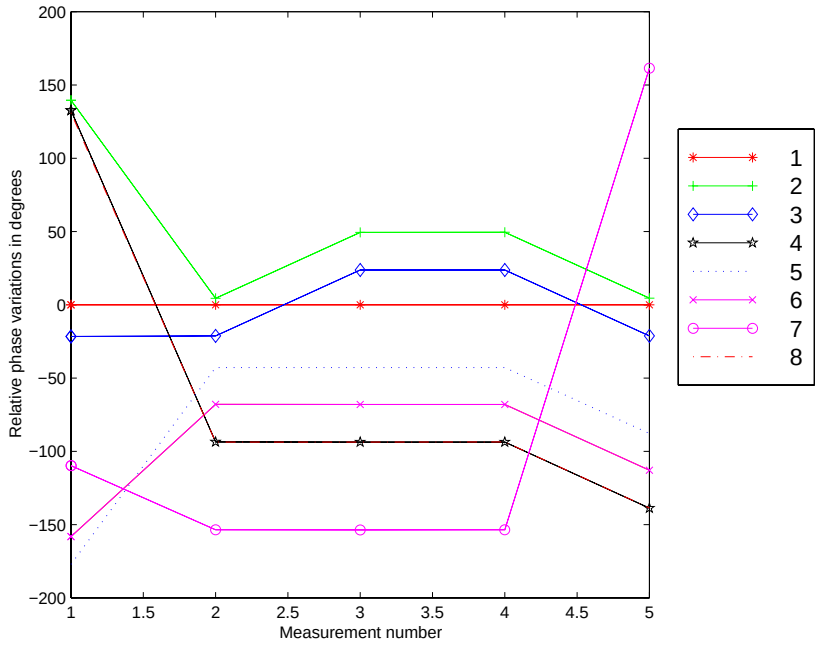

Figure 6.22: Demeaned relative phase of the array hardware with the software being restarted after each measurement.

Chapter 7

Survey of Antenna Array Propagation Studies

This chapter provides a survey of antenna array propagation measurements that have been reported in the literature. The main focus of the papers selected for inclusion in this survey is on array propagation results, not processing algorithms. Papers which describe how measurements may be processed, but include no real measurement results are not covered here.

The derivation of the relationships between each of the metrics defined regarding the changes in the spatial signature vectors is an original contribution of this work.

In general the propagation measurements involving antenna array receivers that have been made include the following: (1) signal cross-correlations observed at different antennas, (2) changes in the spatial signature vectors, (3) angle spread measurements, and (4) joint angle and time of arrival measurements. Each of these measurement types are covered in the corresponding sections below.

7.1 Signal Cross-correlation Coefficients

Measurements of the cross-correlation coefficients of the signals observed at multiple antenna elements were originally motivated by the need to evaluate diversity combining systems. These types of measurements are now also of interest in the more general case of generic array processing. It can be shown that the ideal SINR achievable with an array is a function of the array correlation matrix which itself is determined by the signal cross-correlations observed across the array.

In practice one may measure the cross-correlation coefficients of the complex signals, the signal envelopes, or the signal powers [59]. The complex signal correlation coefficient may be expressed as [60]

$$\rho_s = \frac{\mathrm{E}[V_1 V_2^*]}{\sqrt{\mathrm{E}[V_1 V_1^*]\mathrm{E}[V_2 V_2^*]}}, \tag{7.1}$$

where V_1 and V_2 are the zero-mean complex voltages measured at the two antenna elements. The signal envelope is defined as the absolute value of the complex baseband voltage. The signal envelope correlation coefficient may be expressed as [59]

$$\rho_e = \frac{\mathrm{E}\left[e_1 e_2\right]}{\sqrt{\mathrm{E}\left[e_1 e_1\right]\mathrm{E}\left[e_2 e_2\right]}}, \tag{7.2}$$

where e_1 and e_2 are the zero meaned signal envelopes. Finally, the signal power correlation coefficient may be expressed as [59]

$$\rho_p = \frac{\mathrm{E}\left[S_1 S_2\right]}{\sqrt{\mathrm{E}\left[S_1 S_1\right]\mathrm{E}\left[S_2 S_2\right]}}, \tag{7.3}$$

where S_1 and S_2 are the zero meaned signal powers. Of these the envelope correlation coefficient is the most widely reported measurement used to evaluate diversity systems. Approximate relationships have been found between the different forms of the correlation coefficients. In Rayleigh fading environments it is often assumed that $|\rho_s|^2 \approx \rho_e$ [61, 62, 59]. Also, it has been found that $\rho_e \approx \rho_p$ [61, 63, 59].

Typically, it is assumed that the variation in received signal amplitude is due to both short term and long term fading. Long term fading also known as shadowing is caused by differences observed in the environment as the mobile travels a distance of several wavelengths. Short term fading is caused by the constructive and destructive combining of several multipath components. In order to obtain meaningful estimates of the signal envelope correlations it is important to remove the changes in the mean signal strength caused by long term fading. Normalization of the data is accomplished by computing the moving average of the signal over the path of several wavelengths. The moving average over a window of length $2L$ is given by [64],

$$m(t) = \frac{1}{2L}\int_{t-L}^{t+L} e(\tau)d\tau. \tag{7.4}$$

The normalized signal envelope is given by

$$e_0(t) = \frac{e(t)}{m(t)}. \tag{7.5}$$

Proper selection of the window size $2L$ is important [65]. If the window size is too small then the estimate of the local mean will be poor due to insufficient data. If the window size is too large, the estimated local mean may not reflect the changes that are occurring due to slow fading. Typical measurement lengths of the local mean correspond to the mobile traveling a distance of 5 to 20 wavelengths [59].

It is well known that for diversity combining systems that a smaller value of the cross-correlation coefficient yields an increased diversity gain. Physically this may be explained as follows. When there is little correlation between the signal fading envelopes, then the likelihood that both signals will experience a deep fade is small. Therefore, one may expect that at least one of the elements has a strong signal. On the other hand if there is a high cross-correlation coefficient, then it is likely that both signals will experience a deep fade simultaneously. In this case neither

branch has sufficient signal strength for the diversity system to yield a strong output. It has been shown that cross-correlation values of 0.7 or less provide adequate diversity gain [10].

Original diversity measurements were used not only to determine the performance of diversity systems, but also to determine the required element separation to achieve sufficient decorrelation. It is know that the required element spacing is highly dependent upon the propagation environment and antenna heights.

Several measurement studies have focused on the required separation of antennas at the base station. In [66] it was found that 70 wavelength separation was needed for in-line and 15 to 20 wavelengths for broadside propagation. General trends that were observed include that the correlation coefficient increased when the mean angle of arrival approached the in-line case. Also the correlation coefficient decreased with increased element spacing. Additionally, it was found that local scattering in the vicinity of the base station also decreased the correlation coefficient.

In [65] both horizontal and vertical separation of the antenna elements were considered. It was found that a vertical separation of the elements typically resulted in smaller correlation values which were less sensitive to the mean angle of arrival at the base station. Again, it was found that the correlation coefficient decreased with an increase in antenna separation and as the mean angle of arrival approached array broadside.

Extensive measurements of envelope correlation and diversity gain for the 1800 MHz band were reported in [67]. In this study horizontal separation of the elements provided smaller correlation values as compared to vertical separation. It was found that 20λ was needed for horizontal separation. Additionally, empirical results were given for diversity gain as a function of the cross correlation coefficient and the mean signal level difference of the two branches.

Finally, results given in [12] indicate that the correlation coefficient is also highly dependent upon antenna height. This is an indirect result of there being less of an observable angle spread when the antenna is placed above local scattering objects.

At the mobile, the angular spread of the incoming signal is it typically much larger and hence smaller antenna separations are needed than those required at the base station. Until recently it was thought that separations of at least 0.2λ were needed to obtain a good degree of decorrelation. This result was based on the assumptionthat multipath were uniformly distributed about the mobile and that the antennas were omni-directional with no mutual coupling. However, recent measurement studies of closely spaced antenna elements [68, 69, 64, 70, 59] have shown that antenna separations less than a tenth of a wavelength may be sufficient. The much smaller correlation values obtained in these studies are attributed to the mutual coupling which exists between two closely spaced elements [69].

7.2 Changes in the Spatial Signature Vector

Measurements involving the change in the spatial signature vector (SSV) have been reported in [71–74]. The SSV which is defined in Section 2.3 determines the overall array response of a

single user due to multipath in the presence of flat fading. The amount by which it changes as the mobile moves determines the required algorithm update rate needed to track the environment. The rate of change of the SSV as a function of position also provides information regarding the displacement of two users required for the antenna array system to be able to separate their signals. In general the greater the difference between the signature vectors of two users the more easily the users may be separated. If the spatial signature vector changes quickly with a change in distance, then two users that are relatively close in proximity may still adequately be separated.

In [71] changes in the spatial signature vector were related to the projection angle between the two signature vectors. In particular the difference between the two signature vectors, $\mathbf{v}_1$ and $\mathbf{v}_2$, was defined as

$$\Delta \mathbf{v}_s = \sin^2 \theta_p \tag{7.6}$$

where

$$\theta_p = \operatorname{acos}\left(\frac{|\mathbf{v}_1^H \mathbf{v}_2|}{\|\mathbf{v}_1\| \|\mathbf{v}_2\|} \right), \tag{7.7}$$

is the projection angle between $\mathbf{v}_1$ and $\mathbf{v}_2$. From the definition of $\Delta \mathbf{v}_s$ we find that as the angle between the two vectors approaches $\pi/2$ the measured difference in the vectors increases. Similarly, when the angle between the two vectors is small, $\Delta \mathbf{v}_s$ is small.

Measurements were reported in [71] at 1.6 GHz, using a five element uniform array of dipoles with 10cm element spacing. For the measurements that were made with a stationary transmitter, the difference between the initial SSV and the current SSV was found. The results reported for a moving transmitter were based upon the difference between two adjacent SSVs. It was found that the SSV of a stationary mobile was stable for several minutes. However, for a moving transmitter, the spatial signature vectors changed fairly rapidly. In both cases, greater changes in the spatial signature vectors were observed when no line-of-sight component was present. Also it was found that the spatial signature changed dramatically with a change in carrier frequency of only 3.5%.

The results reported in [72] are similar to those found in [71]. In [72] the difference spatial signature vectors referred to as relative angle change was defined as

$$\Delta \mathbf{v}_a = \sqrt{1 - \left(\frac{|\mathbf{v}_1^H \mathbf{v}_2|}{\|\mathbf{v}_1\| \|\mathbf{v}_2\|} \right)^2}. \tag{7.8}$$

Measurements were made using an eight element uniform patch antenna array operating at 899 MHz. In [72] the authors studied the additional impact of both pedestrian and vehicular traffic in the vicinity of a stationary transmitter on the received SSV. It was found that while such traffic did cause changes in the spatial signature, the changes were not as great as those observed when the transmitter itself was in motion.

In [73] two metrics of the change in the SSV were defined, the relative angle change given by (7.8) above, and the relative amplitude change which is given by

$$\text{Relative Amplitude Change (dB)} = 20 \log_{10} \frac{\|\mathbf{v}_2\|}{\|\mathbf{v}_1\|} \tag{7.9}$$

An eight element uniform patch antenna array was used to collect measurement data. The results reported in [73] were similar to those presented in [71] and [72]. Again it was found that for even a small percentage change in the carrier frequency (<5%) the spatial signature vectors exhibited large angle and amplitude changes indicating that the uplink SSV cannot directly be used for beamforming on the downlink.

A common problem with the results reported in [71–73] for a moving transmitter is that the amount of change is given as a function of time, and yet the speed of the transmitter is not specified. Therefore, it is difficult to use these results to predict the change of the spatial signature vectors as the mobile moves a specified distance.

Another SSV measurement study was reported in [74]. Here the difference in two spatial signature vectors was defined as

$$\Delta \mathbf{v}_o = \mathbf{v}_2 - \left(\frac{\mathbf{v}_1^H \mathbf{v}_2}{\mathbf{v}_1^H \mathbf{v}_1} \right) \mathbf{v}_1, \tag{7.10}$$

which is the component of $\mathbf{v}_2$ that is orthogonal to $\mathbf{v}_1$. The rate of change in the normalized spatial signature is then defined as

$$\Delta \mathbf{v}_n = \frac{\|\Delta \mathbf{v}_o\|}{\|\mathbf{v}_2\| T_a}, \tag{7.11}$$

(where the error or typo in [74] has been corrected) which can be expressed

$$\Delta \mathbf{v}_n = \frac{\|\Delta \mathbf{v}_o\|}{\|\mathbf{v}_2\| T_a} = \frac{1}{T_a} \sqrt{1 - \left(\frac{|\mathbf{v}_1^H \mathbf{v}_2|}{\|\mathbf{v}_1\| \|\mathbf{v}_2\|} \right)^2}. \tag{7.12}$$

The relative percentage change of the SSV was determined as a function of vehicle speed. It was found that small changes (<5%) occurred for small speeds (<30 MPH), while at higher speeds the SSV changed over the range of 0 to 25% in 10 ms intervals. Only limited measurement points were presented and therefore more measurements are needed to further characterize the rates of change in the SSV.

7.2.1 Relationship between SSV Change Metrics

The metrics, $\Delta \mathbf{v}_s$, $\Delta \mathbf{v}_a$, and $\Delta \mathbf{v}_n$ are closely related. In this section the relationships between the various metrics are derived. First from comparison of (7.8) and (7.12) we find that

$$\Delta \mathbf{v}_n = \frac{1}{T_a} \Delta \mathbf{v}_a. \tag{7.13}$$

Next from (7.6) and (7.7) we may write

$$\Delta \mathbf{v}_s = \sin^2 \theta_p = 1 - \cos^2 \theta_p = 1 - \left(\frac{|\mathbf{v}_1^H \mathbf{v}_2|}{\|\mathbf{v}_1\| \|\mathbf{v}_2\|} \right)^2. \tag{7.14}$$

Comparing this result with (7.8) and (7.12) gives

$$\Delta \mathbf{v}_s = (\Delta \mathbf{v}_a)^2 = (T_a \Delta \mathbf{v}_n)^2. \tag{7.15}$$

All of the SSV change metrics may also be related to the cross-correlation between the two vectors $\mathbf{v}_1$ and $\mathbf{v}_2$ which is defined as

$$\rho_v = \frac{|\mathbf{v}_1^H \mathbf{v}_2|^2}{\|\mathbf{v}_1\|^2 \|\mathbf{v}_2\|^2}. \tag{7.16}$$

Using this definition it is easily shown that

$$\Delta \mathbf{v}_a = (1 - \rho_v)^{\frac{1}{2}} \tag{7.17}$$

$$\Delta \mathbf{v}_n = \frac{1}{T_a}(1 - \rho_v)^{\frac{1}{2}} \tag{7.18}$$

$$\Delta \mathbf{v}_s = 1 - \rho_v. \tag{7.19}$$

7.3 Angle of Arrival and Angle Spread

The angle spread of the received signal power of a single user is a critical parameter affecting the performance of antenna array systems. For diversity systems the required element spacing to decorrelate fading envelopes is known to be dependent upon the angle of arrival distribution of received multipath components. Also, it has been shown that angular spreading of the received signal allows two closely spaced transmitters to be separated by a receiving antenna array [75].

Typically the angle spread is defined by the square-root of the second central moment of the received signal power versus angle of arrival which is given by [76]

$$S_\theta = \sqrt{\int_{\bar{\theta}-\pi}^{\bar{\theta}+\pi} (\theta - \bar{\theta})^2 \frac{P(\theta)}{P_t} d\theta}, \tag{7.20}$$

where $P(\theta)$ is the received signal power in the direction of θ and $\bar{\theta}$ is the center of power which is analogous to center of mass in physics. The center of power is defined

$$\bar{\theta} = \int_{-\pi}^{\pi} \theta \frac{P(\theta)}{P_t} d\theta, \tag{7.21}$$

where P_t is the total received signal power given by

$$P_t = \int_{-\pi}^{\pi} P(\theta) d\theta. \tag{7.22}$$

When K discontinuous signal measurements are available the angle spread is defined

$$S_\theta = \sqrt{\sum_{i=1}^{K} (\theta_i - \bar{\theta})^2 \frac{P_i}{P_t}}, \tag{7.23}$$

where

$$\bar{\theta} = \sum_{i=1}^{K} \theta_i \frac{P_i}{P_t}, \tag{7.24}$$

and

$$P_t = \sum_{i=1}^{K} P_i. \tag{7.25}$$

An undesirable property of this definition of angle spread is that the resulting angle spread is dependent upon the choice of origin. This occurs because the definition of angle spread does not inherently account for the periodicity of $P(\theta)$. It can be shown that when $\overline{(\theta)} = 0$ the angle spread as defined by (7.20) attains its minima.

The definition of angle spread given above accounts for the received signal power from all possible angles of arrival. An alternative definition of the angle spread referred to as the path angle spread (PAS) is identical to the definition given above except that the limits of integration are set at the 3 dB points of the power-angle profile. The PAS is generally interpreted as the angle spread about the mean direction of a single scattering cluster, which are significantly less than the angle spread determined using the standard definition given by (7.20) [76].

Finally, if the powers of each received signal component are identical then the second central moment of the power-angle profile is equal to the variance of the angle of arrival itself. In this case the ratio $P(\theta)/P_t$ is equivalent to the probability density function of the angle of arrival $f_\theta(\theta)$. Under these conditions the angle spread as defined above is equal to the standard deviation of the angle of arrival itself.

A novel definition of angle spread was given in [77], where it is defined as

$$\Delta = \sqrt{1 - \frac{|F_1|^2}{|F_0|^2}} \tag{7.26}$$

where

$$F_n = \int_0^{2\pi} P(\theta) exp(jn\theta) d\theta \tag{7.27}$$

is the nth complex Fourier coefficient of $P(\theta)$. This definition has the nice attribute that the periodicity of $P(\theta)$ is naturally accounted for and hence the choice of origin is arbitrary. In [77] it was that fading rate measurements could be related to the angle spread of the channel.

Several studies reporting angle spread measurements have recently appeared in the literature [78, 76, 74, 79]. In general these measurements confirm that angle spread tends to decrease with an increase in T-R separation and/or an increase in antenna height. In [74] it was reported that the angle spread is greatest in urban areas, smaller in suburban areas, and the least in rural environments. In urban areas the angle spread ranged from approximately 50 to 100 degrees depending upon antenna height. For suburban environments the measured angle spread ranged from about 50 to 80 degrees and for rural environments the angle spread ranged from 10 to 50 degrees.

The results reported in [76] for suburban and urban environments indicate that the angle spread was typically between 20 to 50 degrees. Also in this study it was reported that the path angle spread ranged from 4 to 7 degrees.

Finally in [79] it was reported that a Laplacian distribution accurately matched the power angle spectrum. Additionally it was found that in rural areas the angle spread was correlated with T-R separation although in some locations the angle spread actually increased with an increase in T-R separation.

7.4 Joint Amplitude, Angle and Time of Arrival

Ultimately, we seek to characterize the joint amplitude, angle and time of arrival nature of the channel. The primary motivation here is for evaluation of wideband antenna array systems where both angle of arrival and time of arrival information is needed, although these measurements are also of interest to researchers searching for improved physical models of the wireless channel.

Recently a number of researchers have reported measurements involving joint angle and time of arrival information [80–88, 43]. Several different measurement methodologies have been used. One method is to use a rotating narrowbeam antenna which is connected to a wideband receiver [86, 43]. Another more common approach is to use a wideband antenna array [80–85]. Additionally, systems involving a moving array have been proposed where the angle of arrival information is determined from the Doppler shifts. A detailed discussion of these systems and subsequent processing methodology is beyond the scope of this report. The focus here is on reporting any relevant results as they relate to the actual propagation environment.

For suburban and urban environments it was found that there were generally five or fewer significant multipath components [80, 81]. Also it was found that the received signal power was concentrated near the line-of-sight direction even if the line-of-sight is obstructed [86]. Finally it was observed that the AOA and TOA properties of the received signals could be correlated with dominant features in the environment such as large buildings [88, 85]. In rural areas small delay and angle spreading was observed [86]. Finally for indoor propagation measurements, it was observed that the angle and time of arrival parameters were essentially independent and that the received signals were clustered in both time and angle of arrival [43].

Many of these joint AOA and TOA measurements that have appeared in the literature are only preliminary studies that are fairly limited in scope. Hence, there is still a great need for many more measurement campaigns of this type before all of the critical features of the space-time channel will be fully understood.

7.5 Summary

In Chapter 7 a survey of previous antenna array propagation measurements was given. The propagation measurement results presented include measurements of the envelope correlations

observed at two antenna elements, changes in spatial signature vectors, angle spread, and joint TOA-AOA channel properties. In all cases, many more measurement campaigns are needed to further characterize these important channel properties.

Chapter 8

Antenna Array Measurements

In this chapter we present data which was collected using the MAAT (See Chapter 6). The data is used to compare and contrast properties of the channel in various environments. Four main sets of data were collected. The first data set was collected in the hallway of the NEB building on the Virginia Tech campus. Its purpose was to demonstrate the capabilities of the MAAT system, and to study properties of the spatial channel as observed by an antenna array. The second set of data was collected in the MPRG office area. Using an automated track system to move the transmitter, it was possible to make a significant number of measurements with the transmitter located in various regions of the office area. Again, properties of the spatial channel were analyzed. The third and fourth data sets were collected outdoors between two large building on the Virginia Tech campus. The third and fourth data sets correspond to obstructed LOS and clear LOS channel conditions respectively. While the indoor data were collected using a uniform linear array, the outdoor data were collected using a circular antenna array. The motivation behind switching to the circular antenna array configuration was to remove the azimuth angle of arrival ambiguity which is present in the linear antenna array. Each of these different data sets is described in the corresponding sections below.

8.1 Preliminary Indoor Measurement Results

In this section some preliminary line-of-sight indoor antenna array propagation measurements are presented. Properties of the received signal envelopes, spatial signature vectors, and angle of arrival information are analyzed. It is found that over a distance of ten wavelengths, the properties of the received signal vector exhibit only small changes. This observation is thought to be a result of the presence of a significant line-of-sight signal component.

8.1.1 Measurement Setup

Measurements were made using the eight element ULA described in Chapter 6. The transmitter and receiver were located in the main hallway of the fourth floor of the New Engineering

Building at Virginia Tech at the locations shown in Figs. 8.1 and 8.2. The array was aligned such that broadside of the array pointed roughly in the direction of the transmitter, which was placed approximately 40m away. Both the transmitter and receiver antenna heights were approximately 1.5m.

Figure 8.1: Receiver (R) and transmitter (T) locations on the fourth floor New Engineering Building.

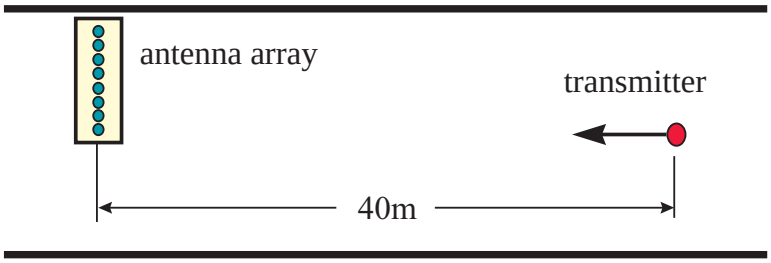

Figure 8.2: Closeup view of receiver and transmitter locations (not to scale).

The transmitter was held stationary while the receiver (also stationary) collected a block of continuous data. Snap shots of 3500 samples were collected for each transmitter location, using a sampling rate of 25kHz. The transmitter was then moved 1cm in the direction towards the receiving array. This process was repeated until the transmitter had traversed a distance of 150cm (slightly greater than ten wavelengths).

8.1.2 Signal Envelope Properties

For each block of data the average signal envelope observed by each antenna was found. The resulting normalized signal envelopes are shown in Fig. 8.3. The observed envelopes vary over a range of approximately 6dB as the transmitter traverses a distance of ten wavelengths. A possible explanation for the absence of deep fades is the fact that the measurements are made in a line-of-sight environment. Therefore, one should expect Ricean rather than Rayleigh fading.

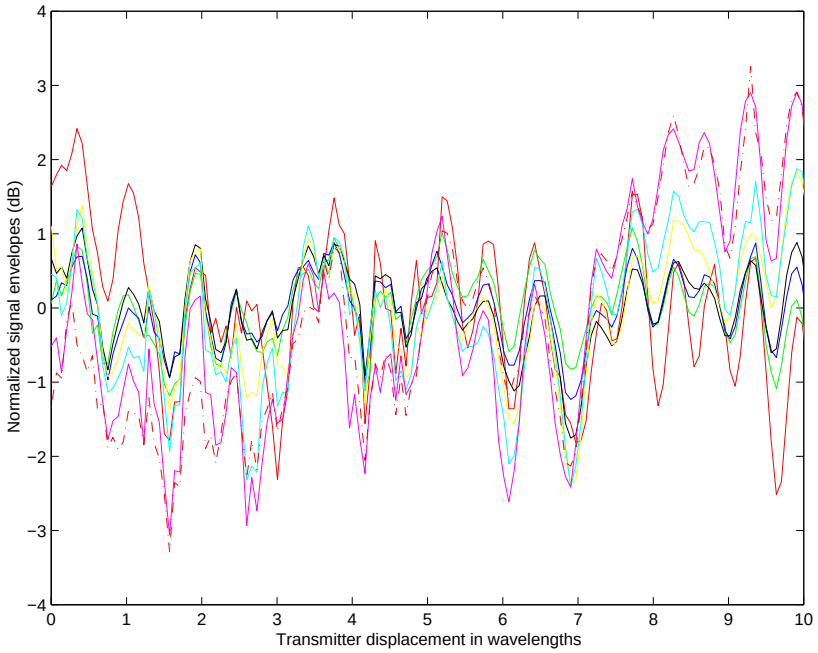

Figure 8.3: Average normalized signal envelopes versus transmitter displacement for indoor hallway measurements.

Envelope Cross-correlation Coefficients at the Receiver

An important property of the received signal envelopes is the cross-correlation coefficients between the envelopes present at each pair of antenna elements. As given by (7.2) above, the envelope cross-correlation coefficients between the ith and jth signal envelopes are defined as

$$\rho_e(i,j) = \frac{\mathrm{E}\left[e_i e_j\right]}{\sqrt{\mathrm{E}\left[e_i^2\right]\mathrm{E}\left[e_j^2\right]}}, \tag{8.1}$$

where e_i and e_j are the zero meaned signal envelopes. All of the envelope cross-correlation coefficients are conveniently expressed as a matrix where the i,jth component corresponds to $\rho_e(i,j)$. The envelope cross-correlation coefficient matrix of the measured data was found to be

$$\rho_e = \begin{bmatrix} 1.0000 & 0.7560 & 0.6602 & 0.6450 & 0.3814 & 0.3336 & 0.1057 & 0.0380 \\ 0.7560 & 1.0000 & 0.8859 & 0.6998 & 0.4618 & 0.5072 & 0.3749 & 0.3580 \\ 0.6602 & 0.8859 & 1.0000 & 0.9130 & 0.7302 & 0.7233 & 0.5586 & 0.4967 \\ 0.6450 & 0.6998 & 0.9130 & 1.0000 & 0.8608 & 0.7730 & 0.5393 & 0.4361 \\ 0.3814 & 0.4618 & 0.7302 & 0.8608 & 1.0000 & 0.9422 & 0.8002 & 0.7231 \\ 0.3336 & 0.5072 & 0.7233 & 0.7730 & 0.9422 & 1.0000 & 0.8918 & 0.8169 \\ 0.1057 & 0.3749 & 0.5586 & 0.5393 & 0.8002 & 0.8918 & 1.0000 & 0.9531 \\ 0.0380 & 0.3580 & 0.4967 & 0.4361 & 0.7231 & 0.8169 & 0.9531 & 1.0000 \end{bmatrix}.$$

The values along each diagonal are measures of the envelope cross-correlation coefficients for a given element spacing. These values maybe be plotted as a function of the element spacing

as shown in Fig. 8.4. Each data point is shown together with average value for the given separation distance. As expected the correlation coefficients decrease with an increase in antenna separation. From the figure it is found that an element separation of between 1 and 1.5 wavelengths is needed for the correlation coefficient values to be less than 0.7. Achieving a correlation coefficient of less than 0.7 is generally considered acceptable for obtaining a reasonable level of diversity gain.

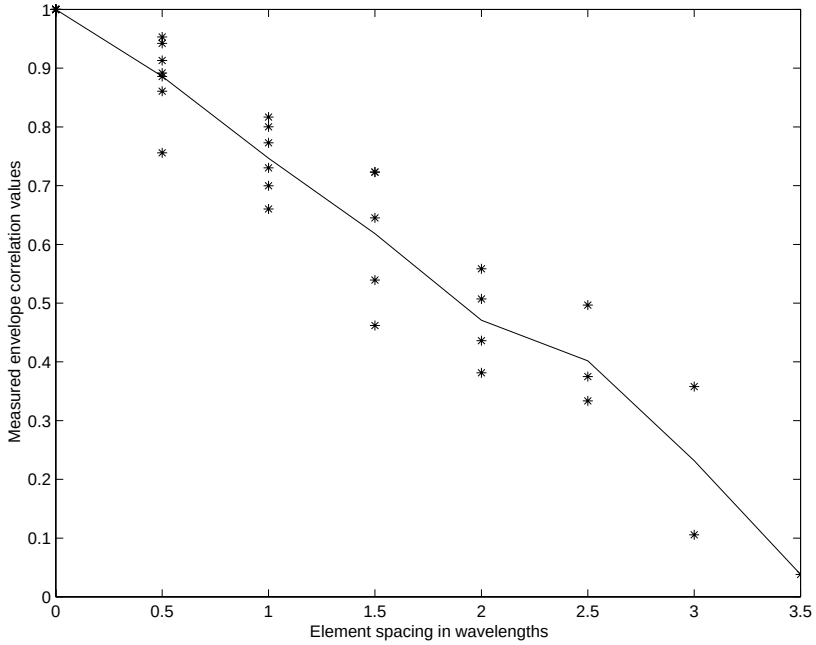

Figure 8.4: Envelope correlation values versus element spacing for indoor hallway measurements. Each '*' denotes a data point while the solid line shows the average.

8.1.3 Spatial Signature Vectors Properties

In this section, properties of the measured spatial signature vectors are investigated. The behavior of the spatial signature vectors as the transmitter moves in space fundamentally impacts system performance. The rate at which it changes with a change in location will determine the required convergent rate of applied adaptive algorithms as well as the ability of an array to separate two closely spaced users.

The spatial signature vectors are estimated from the received signal vector as follows. Recall from Section 2.3 that in a flat fading multipath signal environment the received signal vector for a single user may be expressed as

$$\mathbf{x}(t) = \mathbf{v}s(t) + \eta(t), \tag{8.2}$$

where $\mathbf{v}$ is the spatial signature vector, $s(t)$ is the complex baseband signal impinging upon the array, and $\eta(t)$ is additive noise. The corresponding array covariance matrix is given by

$$\mathbf{R}_{xx} = \mathrm{E}\left\{\mathbf{x}\mathbf{x}^H\right\} = \mathrm{E}\left\{\mathbf{v}s(t)s^H(t)\mathbf{v}^H\right\} + \mathbf{R}_{ii}. \tag{8.3}$$

Assuming that $\mathbf{v}$ is a constant and that $\mathbf{R}_{ii} = \sigma_n^2\mathbf{I}$, then

$$\mathbf{R}_{xx} = \mathbf{v}\mathrm{E}\left\{s(t)s^H(t)\right\}\mathbf{v}^H + \sigma_n^2\mathbf{I} = \mathbf{v}\mathbf{v}^H\mathrm{E}\left\{s(t)s^H(t)\right\} + \sigma_n^2\mathbf{I} = \mathbf{v}\mathbf{v}^H\sigma_s^2 + \sigma_n^2\mathbf{I} \tag{8.4}$$

where $\sigma_s^2 = \mathrm{E}\left\{s(t)s^H(t)\right\}$. That $\mathbf{v}$ is an eigenvector of $\mathbf{R}_{xx}$ is easily shown since,

$$\mathbf{R}_{xx}\mathbf{v} = (\mathbf{v}\mathbf{v}^H\sigma_s^2 + \sigma_n^2\mathbf{I})\mathbf{v} = \mathbf{v}(\mathbf{v}^H\mathbf{v})\sigma_s^2 + \sigma_n^2\mathbf{I}\mathbf{v} = [(\mathbf{v}^H\mathbf{v})\sigma_s^2 + \sigma_n^2]\mathbf{v}. \tag{8.5}$$

Therefore, $\mathbf{v}$ is an eigenvector of $\mathbf{R}_{xx}$ with a corresponding eigenvalue of

$$\lambda_1 = (\mathbf{v}^H\mathbf{v})\sigma_s^2 + \sigma_n^2. \tag{8.6}$$

The remaining eigenvectors are orthogonal to $\mathbf{v}$ and therefore,

$$\mathbf{R}_{xx}\mathbf{e}_i = (\mathbf{v}\mathbf{v}^H\sigma_s^2 + \sigma_n^2\mathbf{I})\mathbf{e}_i = \mathbf{v}(\mathbf{v}^H\mathbf{e}_i)\sigma_s^2 + \sigma_n^2\mathbf{I}\mathrm{e}_i = \sigma_n^2\mathbf{e}_i \tag{8.7}$$

where $\mathbf{e}_i$ is an eigenvector of $\mathbf{R}_{xx}$ not equal to $\mathbf{v}$. In this case, the corresponding eigenvalues are $\lambda_i = \sigma_n^2$. Since, $(\mathbf{v}^H\mathbf{v})\sigma_s^2 > 0$ then $\mathbf{v} = \mathbf{e}_1$ is the dominant eigenvector. In order to maintain amplitude information, the dominant eigenvector should be scaled appropriately. After scaling $\mathbf{e}_1$ such that $||\mathbf{e}_1||^2 = 1$ we find from (8.6) that the spatial signature vector may be estimated by

$$\hat{\mathbf{v}} = \sqrt{\lambda_1 - \lambda_M}\ \mathbf{e}_1 = \sqrt{[(\mathbf{v}^H\mathbf{v})\sigma_s^2 + \sigma_n^2] - \sigma_n^2}\ \mathbf{e}_1 = \sqrt{(\mathbf{v}^H\mathbf{v})\sigma_s^2}\ \mathbf{e}_1. \tag{8.8}$$

Estimating the spatial signature vector in this way guarantees that $||\hat{\mathbf{v}}||^2 = ||\mathbf{v}s(t)||^2$ as desired. The estimated spatial signature vector is scaled by σ_s. This scaling does not affect relative amplitude changes from measurement to measurement, provided that the transmit power remains fixed.

Figures 8.5 and 8.6 show the resulting amplitudes and relative phases of the spatial signature vectors versus transmitter displacement.[1] The phases are referenced to the first element in the array. As seen from the figure, only relatively small changes occur in the amplitudes of the spatial signature vector components. This finding is consistent with the small changes observed in the signal envelopes. There are however some significant changes in the phases, some varying as much as 25 degrees over the transmitter motion of 10 wavelengths.

Next we consider the rate of change of the spatial signature vectors as the transmitter moves. Various metrics have been proposed to quantify the difference in any two spatial signature vectors, all of which can be related to the normalized cross-correlation of two signature vectors as shown in Section 7.2 above. Therefore, we report here the cross-correlation values versus transmitter displacement. We define the normalized cross-correlation of two signature vectors $\mathbf{v}_1$ and $\mathbf{v}_2$ as

$$\rho_v = \frac{|\mathbf{v}_1^H\mathbf{v}_2|^2}{\|\mathbf{v}_1\|\|\mathbf{v}_2\|}. \tag{8.9}$$

The measured normalized cross-correlation values are shown in Fig. 8.7. All of the values are fairly high indicating that only small changes occur in the signature vectors as the transmitter

[1]The amplitude of channel eight was very small due to a bad connection at the antenna element. This problem will be corrected in future data collections.

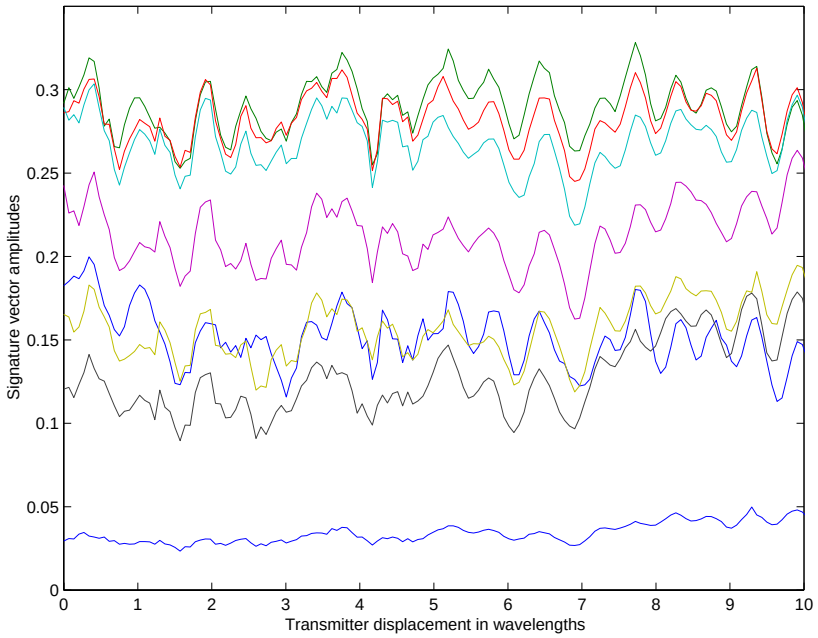

Figure 8.5: Amplitude of the components of the spatial signature vectors.

travels the distance of ten wavelengths. There is a slight decrease in the correlation values when the spatial signature vectors corresponding to greater separation distances are considered. The cdfs which result at various separation distances are shown in Fig. 8.8. The cdf for a separation of ten wavelengths is not smooth due to the limited amount of data points having this separation. Finally, the 5 and 95 percentage values of the CDF and the average normalized cross-correlation of the spatial signature vectors are shown in Fig. 8.9 versus the transmitter displacement in wavelengths. Again, one observes only a slight decrease in the correlation with an increase in the separation of the measurements of the two vectors.

Finally, it is well known that the ability of an antenna array to separate two closely spaced users is determined by the properties of their respective spatial signature vectors, as well as on their individual SNR's. It can be shown from (2.80) that for two equal power users in the presence of normalized background noise that the optimal output SINR is given by

$$\text{SINR}_{opt} = \mathbf{v}_1^H \mathbf{R}_{ii}^{-1} \mathbf{v}_1, \tag{8.10}$$

where $\mathbf{R}_{ii} = \mathbf{v}_2 \mathbf{v}_2^H + \sigma_n^2 \mathbf{I}_M$, $\mathbf{v}_1$ and $\mathbf{v}_2$ are the spatial signature vectors of user 1 and 2 respectively, and $\mathbf{I}_M$ is the M by M identity matrix. Using this expression the measured spatial signature vectors were used to find the distribution of optimum output SINR as a function of transmitter separation assuming a signal to noise ratio of 20 dB.

The results are shown in Fig. 8.10. The output SINR ranges from 0 dB for no antenna separation to nearly 15 dB for a user separation of ten wavelengths. For a separation of approximately ten wavelengths the output SINR reaches 15 dB indicating that the two signals are almost completely separated.

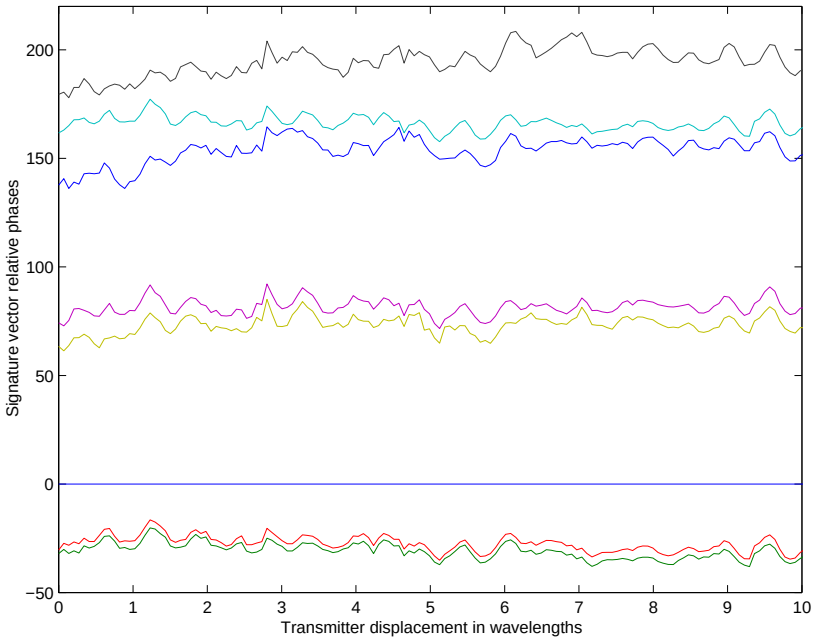

Figure 8.6: Relative phase of the components of the spatial signature vectors with respect to channel 1.

8.1.4 Angle of Arrival Characteristics

For antenna array systems the angle of arrival aspects of the channel are critically important to the system performance. As shown in Chapter 9, for the reverse link, the greater the angle spread of the multipath of a single user, the better the system performance. From the collected array data the power angle profile was estimated using

$$P(\theta) \approx |\mathbf{a}(\theta)^H \mathbf{R}_{xx} \mathbf{a}(\theta)|, \tag{8.11}$$

which is equivalent to pointing the array in each direction and measuring the received power. A plot of the estimated normalized received signal power versus the transmitter location is shown in Fig. 8.11. In Fig. 8.11 there appears to be two major signal components present in the channel. One should keep in mind the ambiguity in the array manifold which occurs with linear antenna arrays, which is the reason for showing only the range -90 to 90 degrees. Due to this limitation of the linear antenna array it is not possible to accurately estimate angle spread from the data.

8.1.5 Eigenvalue Distribution

The eigenvalue distribution is an important parameter of the spatial channel. The eigenvalue distribution is a function of several channel parameters including multipath coherence, number of multipath components, and angle of arrival distribution. For a discussion on the relationship between the eigenvalue distribution and channel parameters see Appendix C.

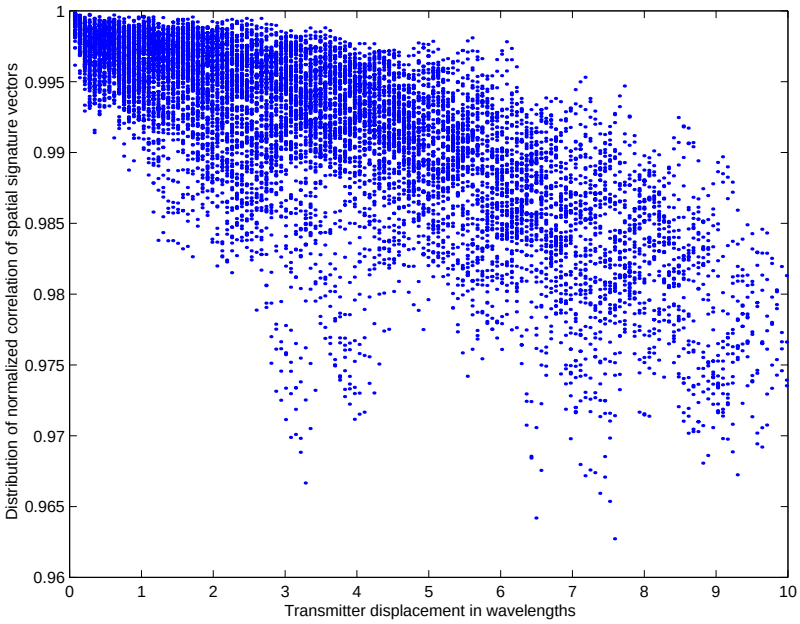

Figure 8.7: Distribution of SSV normalized cross-correlation values versus transmitter separation.

The eigenvalues of the covariance matrix corresponding to data collected over the entire distance traveled by the transmitter were found. The normalized eigenvalues are given in Table 8.1. [2] In this case the dominant eigenvalue is 25dB above the next largest eigenvalue. This is an indication of the lack of severe multipath conditions.

Table 8.1: Normalized eigenvalues of R_{xx} in the hallway.

i	λ_i	$10\log_{10}(\lambda_i)$
1	1.0000	0
2	0.0032	-25.0039
3	0.0008	-31.0877
4	0.0002	-37.7067
5	0.0001	-40.3993
6	0.0000	-43.4072
7	0.0000	-47.9508
8	0.0000	-51.7761

[2]The eigenvalues are normalized by the dominant eigenvalue.

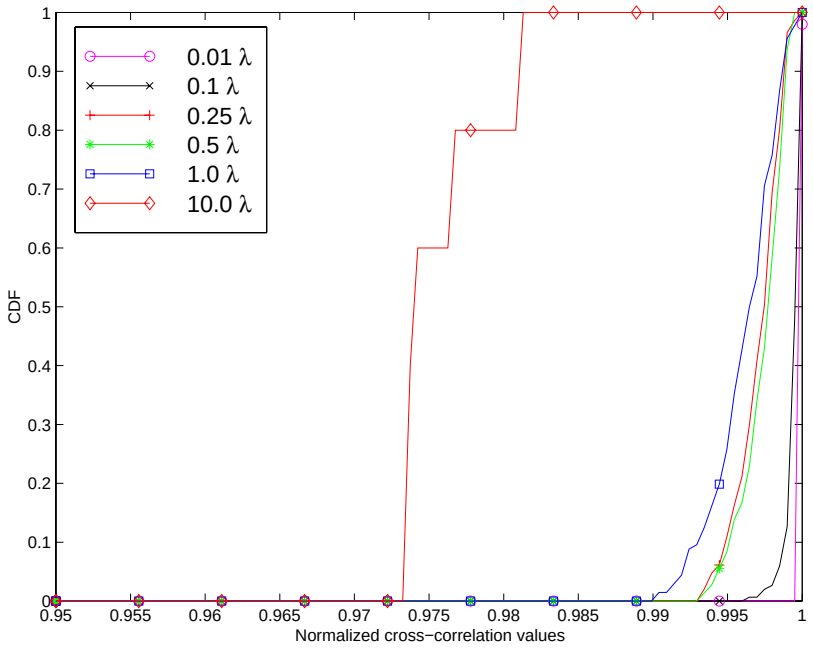

Figure 8.8: Normalized SSV cross-correlation CDF versus transmitter displacement for indoor hallway measurements.

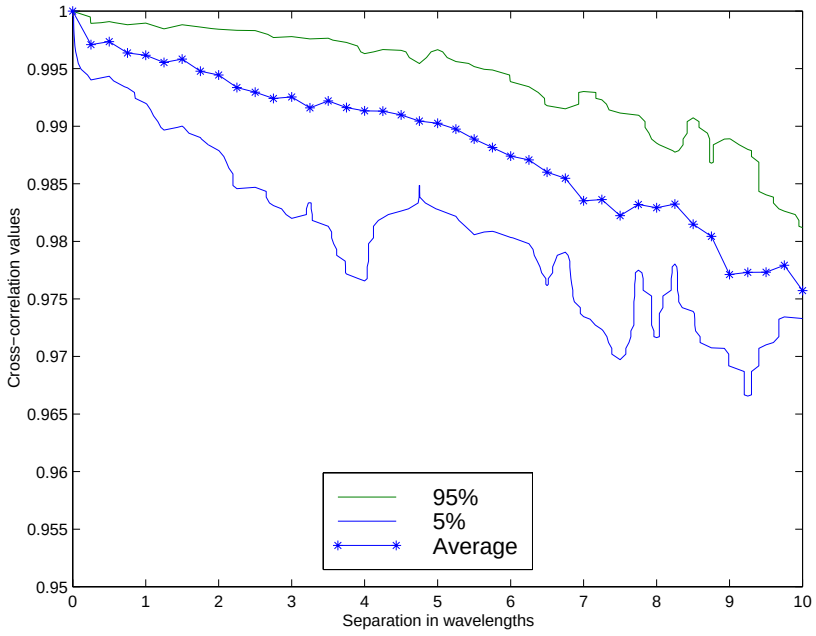

Figure 8.9: Normalized SSV cross-correlation CDF versus transmitter displacement for indoor hallway measurements.

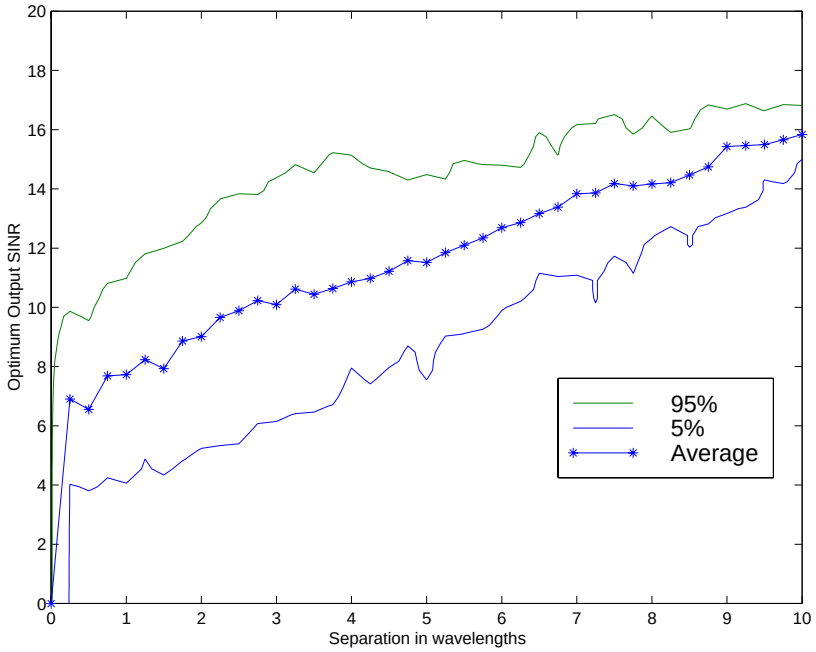

Figure 8.10: SINR distribution for two users with equal power each with 20 dB SNR versus user separation in wavelengths.

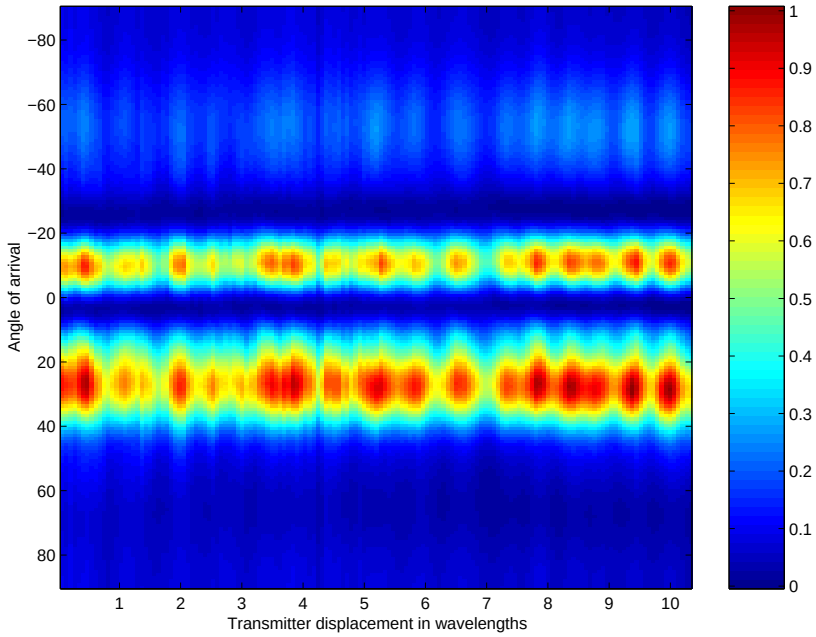

Figure 8.11: Normalized received signal power versus angle of arrival for various transmitter displacements.

8.2 Office Area Measurements

In this section measurements that were made in the MPRG office area are presented. Again we consider signal envelope correlation and changes in the spatial signature vectors versus transmitter displacement. As stated above the rate of change of the spatial signature vector will impact the required convergence rate of adaptive algorithms and the ability of an antenna array to separate to closely spaced users.

8.2.1 Measurement Setup

Measurements were made using the ULA configuration of the MAAT system described in Chapter 6. The transmitter and receiver were located in the MPRG office area on the fourth floor of the New Engineering Building at Virginia Tech as shown in Fig. 8.12. The antenna array remained stationary in the corner of the room at an angle of approximately 45 degrees relative to the wall. The transmitter was fastened to a linear positioning system. The linear positioning system moved the transmit antenna at a constant rate over a distance of 2m. Six different areas of the office area were selected for measurements labeled as A1 through A6 in Fig. 8.12. Areas 1 through 3 correspond to clear LOS measurements. For areas 4 through 6 the LOS was obstructed by cubical partitions. For each of these areas five trials over the 2m distance were run with the track being shifted a few inches between each trial. The positioner moved continuously as data was collected. For each 2m trace, 3776 evenly spaced vector samples were collected.

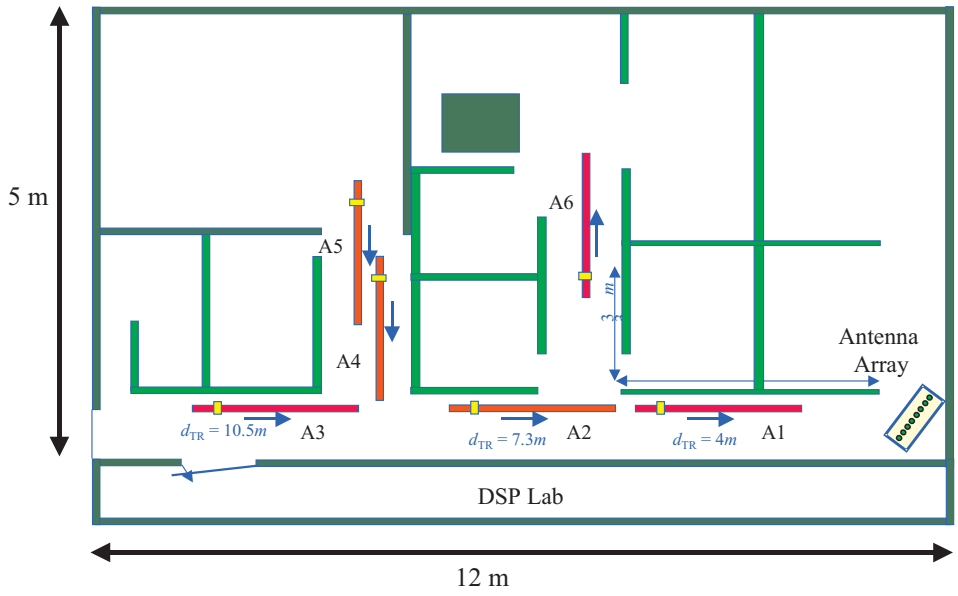

Figure 8.12: Antenna array and track positions for each set of measurements made in the MPRG office area.

8.2.2 Signal Envelope Properties

A representative plot of the signal envelopes collected in the office area is shown in Fig. 8.13. The plot shows the envelopes observed on the eight elements of the antenna array has the transmitter traverses a distance of five wavelengths. For each of the five measurements made in the six regions of the office area the cross-correlation between each pair of antenna elements was collected. The average over all 30 measurements is given by

$$\rho_e = \begin{bmatrix} 1.0000 & 0.0754 & 0.0656 & 0.0352 & 0.0484 & 0.0173 & 0.0202 & 0.0176 \\ 0.0754 & 1.0000 & 0.1501 & 0.0510 & 0.0934 & 0.0064 & -0.0019 & 0.0567 \\ 0.0656 & 0.1501 & 1.0000 & 0.2193 & 0.1099 & 0.0839 & 0.0543 & 0.0936 \\ 0.0352 & 0.0510 & 0.2193 & 1.0000 & 0.1880 & 0.0901 & 0.0697 & 0.0885 \\ 0.0484 & 0.0934 & 0.1099 & 0.1880 & 1.0000 & 0.1525 & 0.0636 & 0.1299 \\ 0.0173 & 0.0064 & 0.0839 & 0.0901 & 0.1525 & 1.0000 & 0.1989 & 0.0803 \\ 0.0202 & -0.0019 & 0.0543 & 0.0697 & 0.0636 & 0.1989 & 1.0000 & 0.2047 \\ 0.0176 & 0.0567 & 0.0936 & 0.0885 & 0.1299 & 0.0803 & 0.2047 & 1.0000 \end{bmatrix}.$$

Again, each diagonal contains the cross correlation values corresponding to a particular element separation distance. These values are plotted in Fig. 8.14 along with the average cross correlation for a given separation distance. In this case the cross correlation decreases rapidly with the element separation. In fact even for adjacent elements the envelope correlation is less than 0.3 for all pairs of elements.

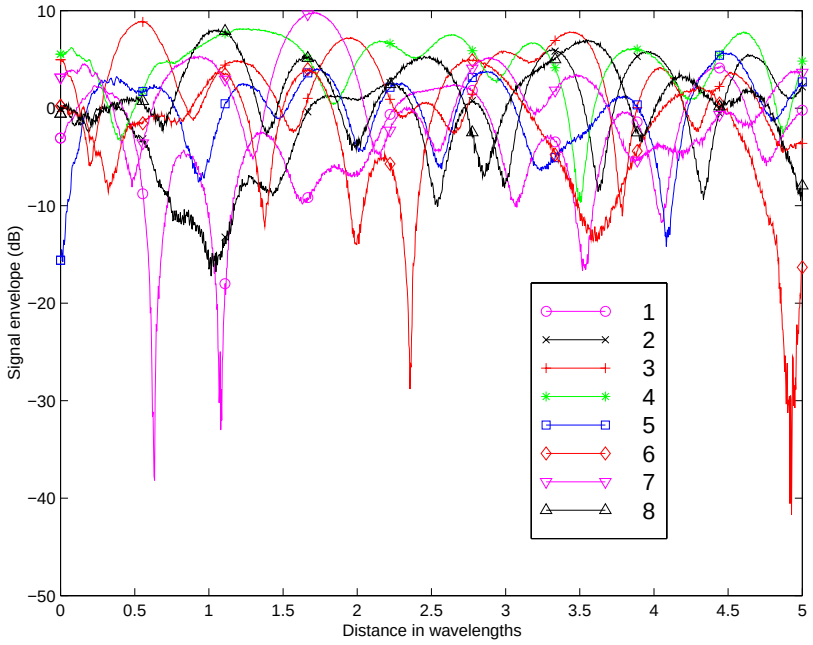

Figure 8.13: Normalized representative signal envelope for indoor office area measurements.

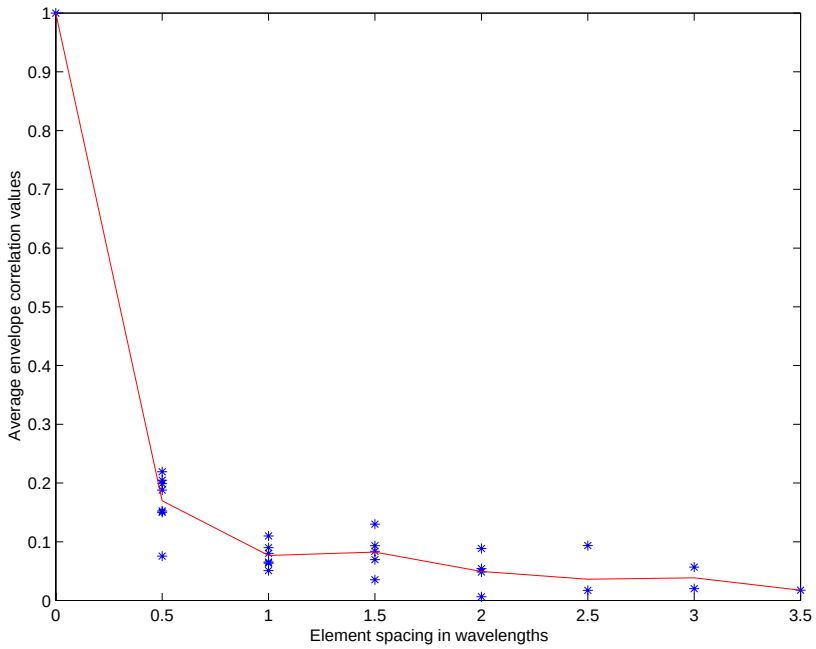

Figure 8.14: Envelope correlation values versus element spacing at the mobile for indoor office area measurements. The solid lines are the estimates obtained from each antenna element. The '-*' line is the average value.

8.2.3 Spatial Signature Vectors Properties

In this section we report properties of the normalized cross correlation between spatial signature vectors versus the transmitter displacement between measurements as defined in (8.9). The results are reported in Figs. 8.15 through 8.26 for each of the six regions in the room. Average results over all of the data collected in the office area are given in Figs. 8.27 and 8.28. For each area the SSV correlation cdfs are plotted for various transmitter displacements. Also shown are the 5 and 95 percentage points of the cdf and the average SSV correlation values versus transmitter displacement.

In general the measurements made with an obstructed LOS show a lower SSV correlation for a given transmitter displacement when compared to the clear LOS measurements. In all cases, it is found that the SSV decorrelate much more quickly in the office area than was found in the measurements made in the hallway. From Fig. 8.28 we find that when averaged over all of the data that the SSV is fairly decorrelated with a transmitter displacement on the order of one to two wavelengths. Furthermore, there is little difference between the SSV correlation values for five and ten wavelengths, indicating that the vectors are nearly as decorrelated as they will get with a transmitter displacement of only five wavelengths.

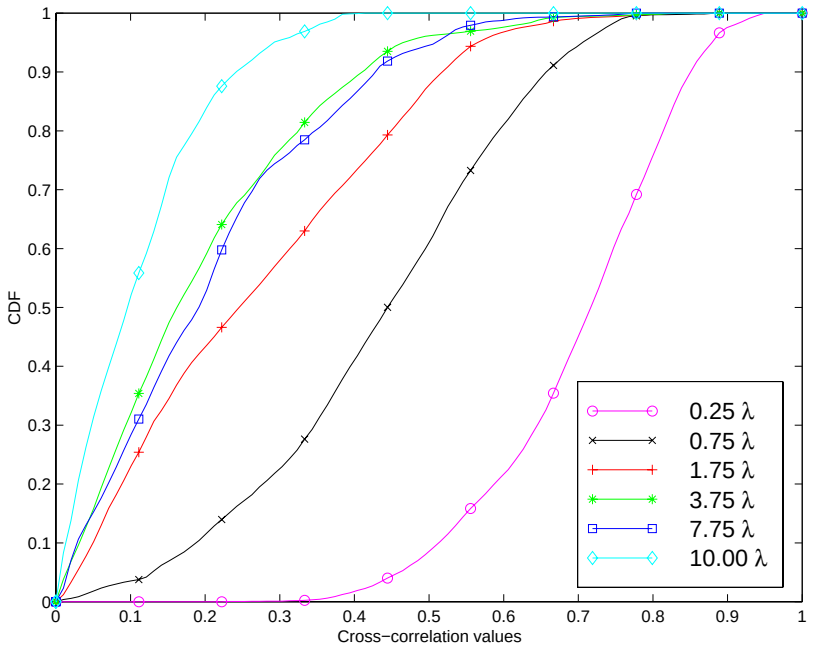

Figure 8.15: Normalized SSV cross-correlation CDF versus transmitter displacement for area 1.

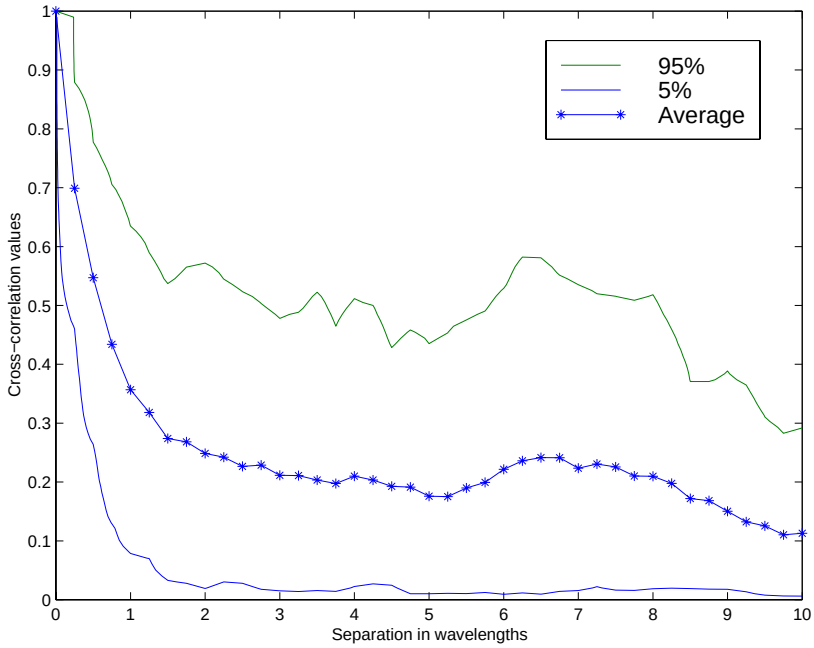

Figure 8.16: Normalized SSV cross-correlation CDF versus transmitter displacement for area 1.

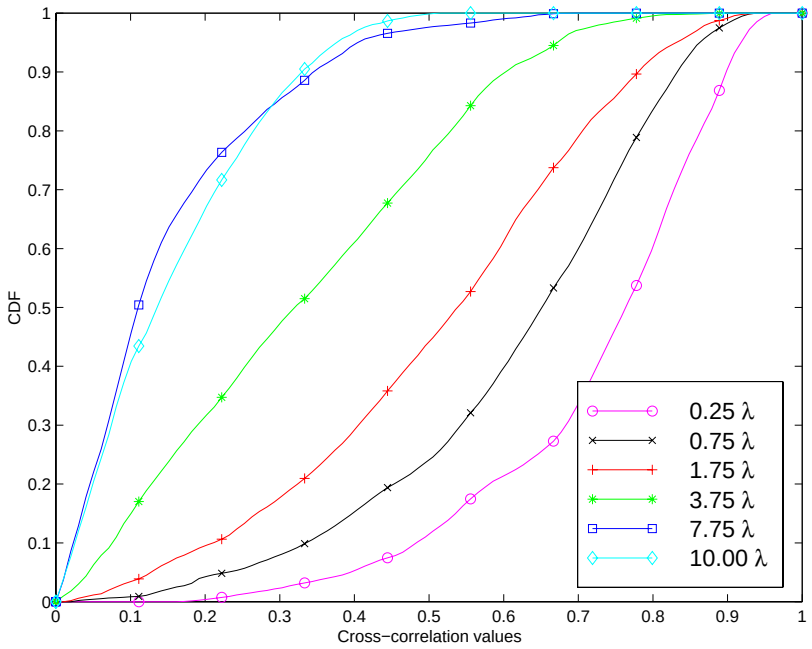

Figure 8.17: Normalized SSV cross-correlation CDF versus transmitter displacement for area 2.

8.2.4 Eigenvalue Distribution

The average normalized eigenvalues for both the LOS and obstructed LOS measurement areas are given in Tables 8.2 and 8.3, respectively. In both cases the ratio of the largest to the smallest eigenvalue is much less than what was observed for the hallway data. When comparing the clear LOS with the obstructed LOS one finds that there is less variation in the eigenvalues of the obstructed LOS. This result is consistent with the fact that in a more severe multipath channel, the eigenvalue spread decreases.

Table 8.2: Average normalized eigenvalues of R_{xx} for LOS cases in the office area.

i	λ_i	$10\log_{10}(\lambda_i)$
1	1.0000	0
2	0.4214	-3.7527
3	0.2469	-6.0756
4	0.1298	-8.8677
5	0.0756	-11.2154
6	0.0515	-12.8794
7	0.0309	-15.0996
8	0.0176	-17.5523

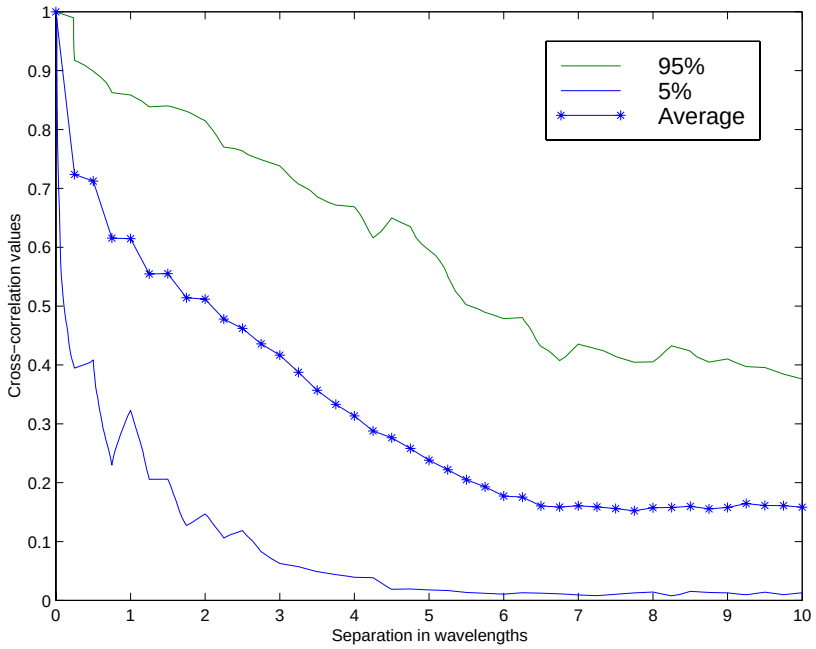

Figure 8.18: Normalized SSV cross-correlation CDF versus transmitter displacement for area 2.

Table 8.3: Average normalized eigenvalues of R_{xx} for obstructed LOS cases in the office area.

i	λ_i	$10\log_{10}(\lambda_i)$
1	1.0000	0
2	0.5006	-3.0051
3	0.3358	-4.7391
4	0.2545	-5.9431
5	0.1775	-7.5075
6	0.1223	-9.1242
7	0.0789	-11.0293
8	0.0443	-13.5353

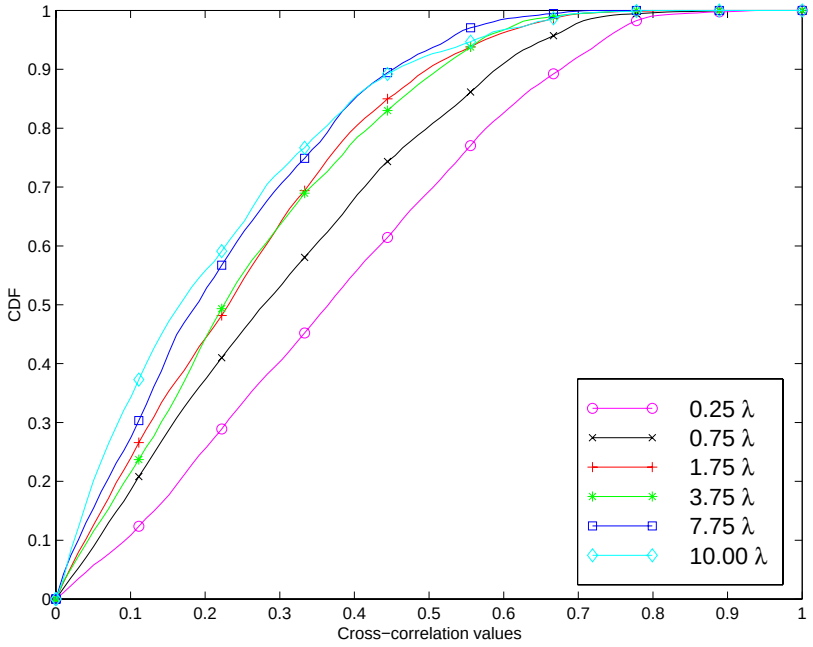

Figure 8.19: Normalized SSV cross-correlation CDF versus transmitter displacement for area 3.

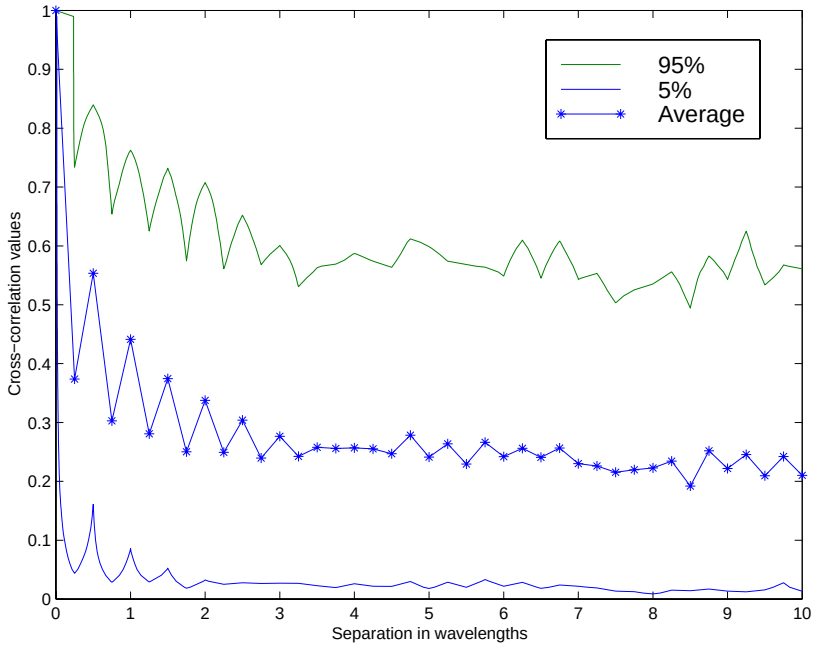

Figure 8.20: Normalized SSV cross-correlation CDF versus transmitter displacement for area 3.

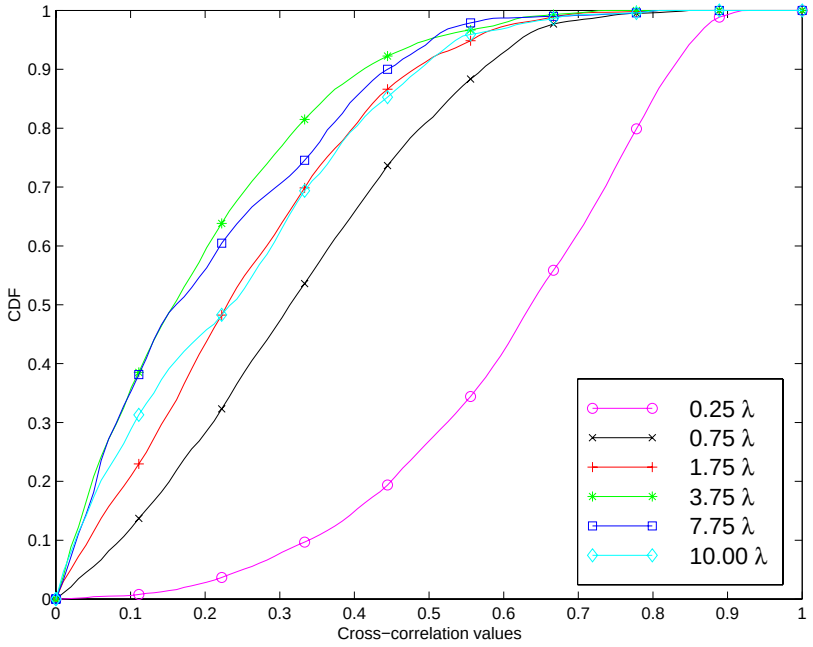

Figure 8.21: Normalized SSV cross-correlation CDF versus transmitter displacement for area 4.

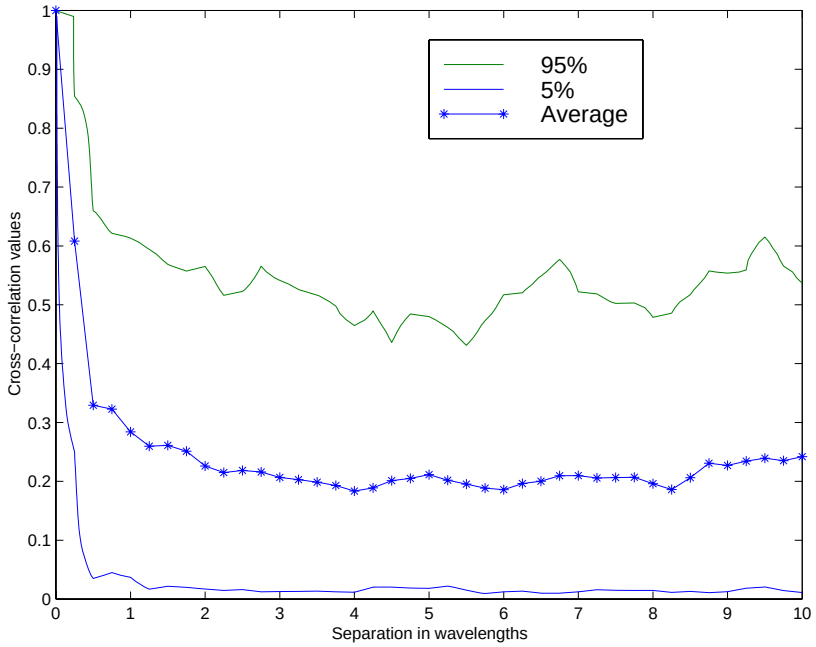

Figure 8.22: Normalized SSV cross-correlation CDF versus transmitter displacement for area 4.

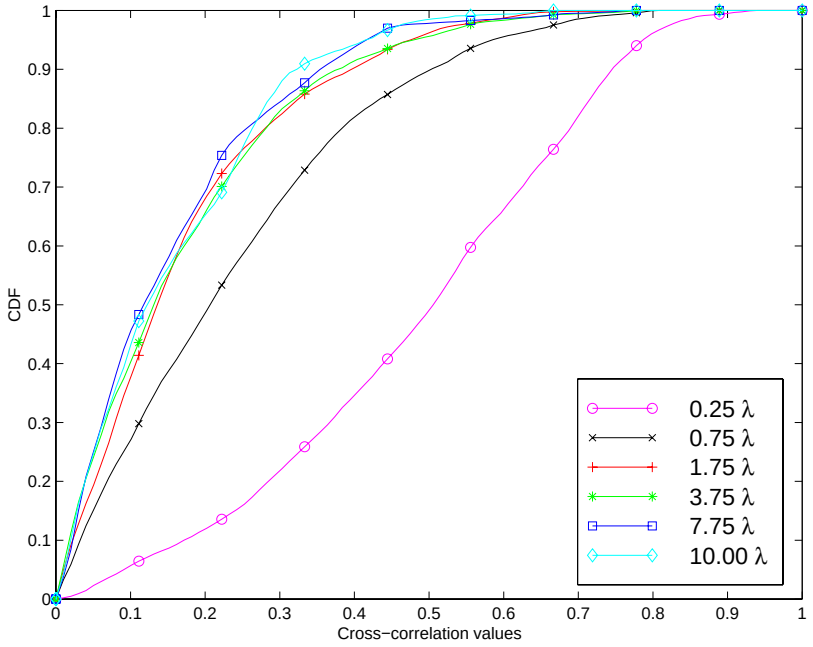

Figure 8.23: Normalized SSV cross-correlation CDF versus transmitter displacement for area 5.

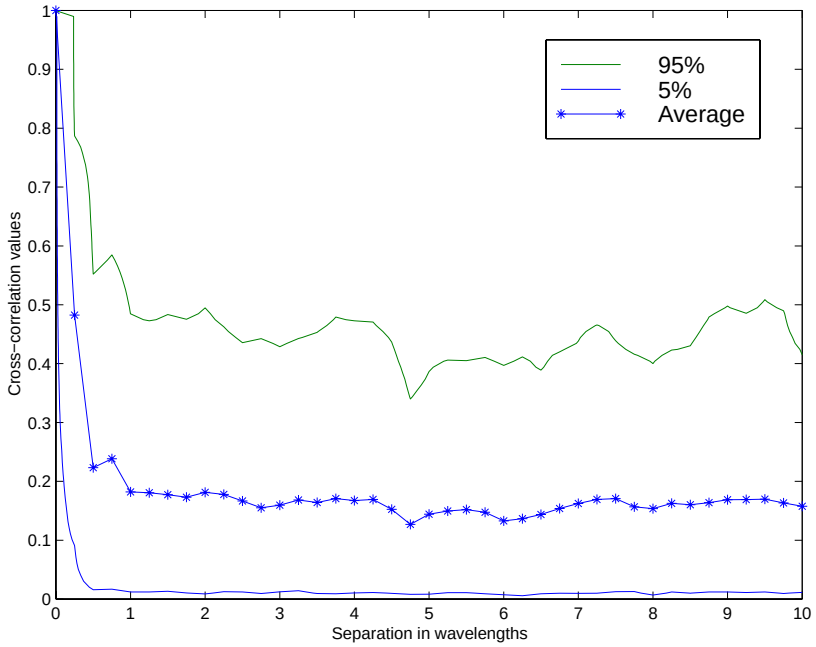

Figure 8.24: Normalized SSV cross-correlation CDF versus transmitter displacement for area 5.

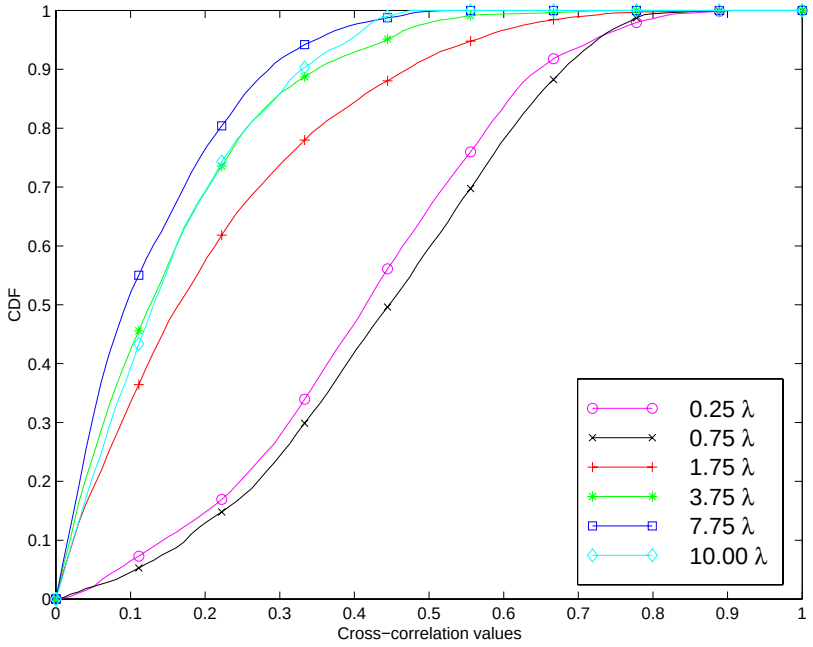

Figure 8.25: Normalized SSV cross-correlation CDF versus transmitter displacement for area 6.

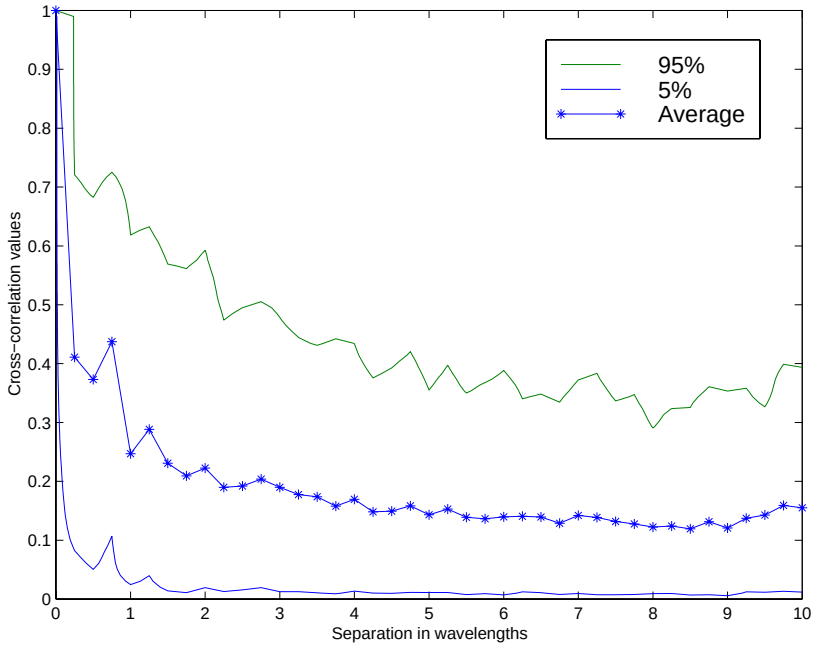

Figure 8.26: Normalized SSV cross-correlation CDF versus transmitter displacement for area 6.

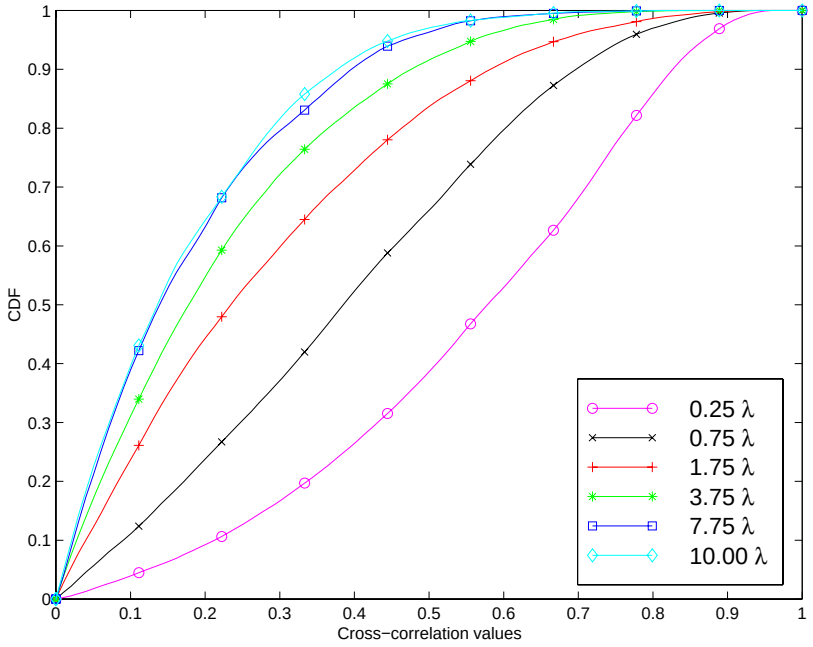

Figure 8.27: Normalized SSV cross-correlation CDF versus transmitter displacement averaged over all measurements.

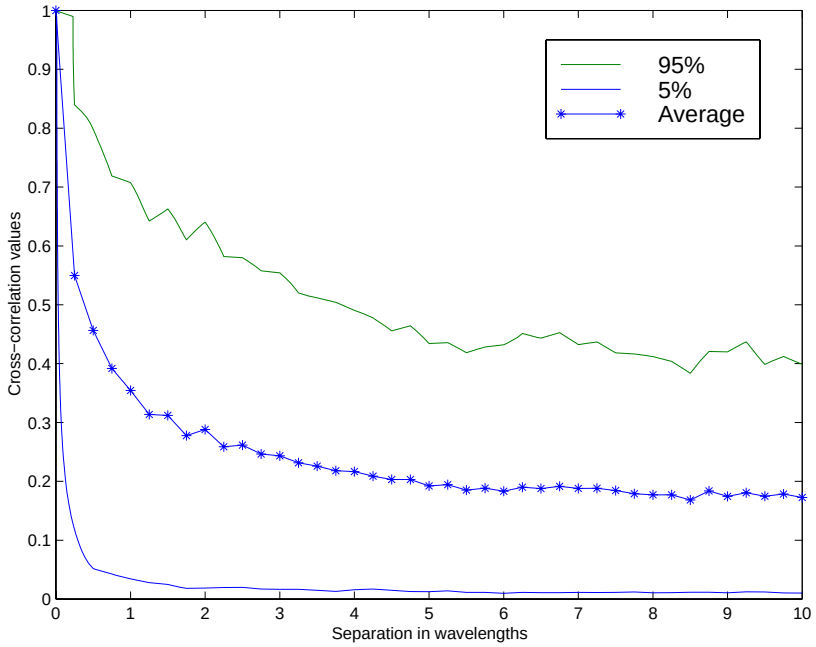

Figure 8.28: Normalized SSV cross-correlation CDF versus transmitter displacement averaged over all measurements.

8.3 Outdoor Obstructed LOS Measurements

8.3.1 Measurement Setup

The uniform circular antenna array configuration of the MAAT was used to collect outdoor antenna array data at the locations indicated in Figs. 8.29 and 8.30. The area labeled Tx1 indicates the position of the transmitter used to make obstructed LOS measurements. The data collected for this case is considered in this section. The area labeled Tx2 indicates the position of the transmitter used to make clear LOS measurements. The clear LOS measurements are analyzed in the next section. The antenna array receiver was positioned at the location labeled Rx.

For each set of data the transmitter was moved along the linear positioner approximately a distance of 2m while data was collected. Five runs down the track were made at each location, with the positioner shifted roughly a half wavelength to the side between each measurement. Over the 2m distance, 3500 samples of the received signal vector were collected.

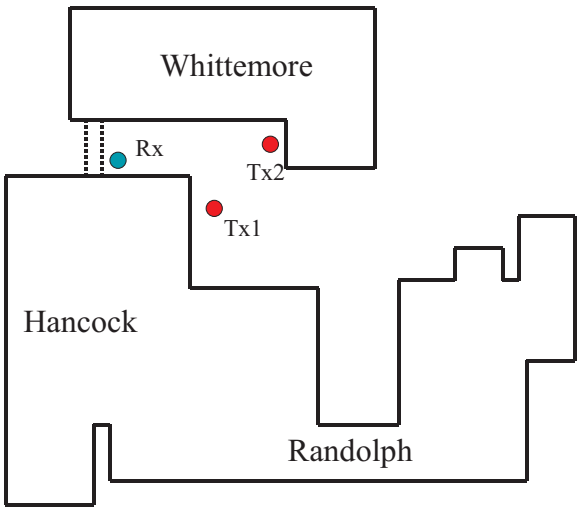

Figure 8.29: Receiver and transmitter locations for the outdoor measurements made on the Virginia Tech campus.

8.3.2 Signal Envelope Properties

For each of the measurements the signal envelopes were found. Figure 8.31 shows a set of representative signal envelopes observed on the eight elements of the antenna array as the transmitter moved a distance of five wavelengths. The envelopes show significant fading with power variations as high as 25dB or more over the five wavelength distance. The distance between deep nulls of each channel is roughly one wavelength.

Again, the envelope cross-correlation values over the five measurement trials were found for each pair of antenna elements. The corresponding cross correlation coefficient matrix is given

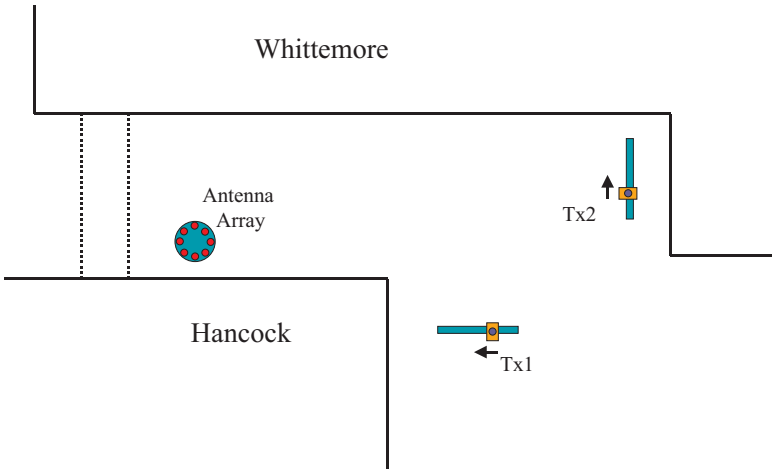

Figure 8.30: Closeup view of receiver and transmitter locations (not to scale).

by

$$\rho_e = \begin{bmatrix} 1.0000 & -0.1713 & 0.4308 & 0.3253 & -0.0006 & 0.0044 & 0.1759 & -0.0334 \\ -0.1713 & 1.0000 & 0.0178 & -0.0911 & 0.1208 & 0.1065 & -0.0735 & 0.2056 \\ 0.4308 & 0.0178 & 1.0000 & 0.4479 & -0.0009 & 0.1895 & -0.0375 & -0.0712 \\ 0.3253 & -0.0911 & 0.4479 & 1.0000 & 0.0638 & 0.1093 & 0.2007 & 0.1649 \\ -0.0006 & 0.1208 & -0.0009 & 0.0638 & 1.0000 & 0.1676 & 0.4084 & 0.3212 \\ 0.0044 & 0.1065 & 0.1895 & 0.1093 & 0.1676 & 1.0000 & 0.3869 & 0.2224 \\ 0.1759 & -0.0735 & -0.0375 & 0.2007 & 0.4084 & 0.3869 & 1.0000 & 0.4914 \\ -0.0334 & 0.2056 & -0.0712 & 0.1649 & 0.3212 & 0.2224 & 0.4914 & 1.0000 \end{bmatrix}.$$

All of the off diagonal entries of ρ_e is less than 0.5 in magnitude. Again, each diagonal of ρ_e corresponds to the correlation of the signal envelopes for a particular element separation. Table 8.4 shows the separation distance between the elements along each of the diagonal entries of ρ_e, assuming that diagonal 1 corresponds to the main diagonal.

Table 8.4: Element spacing versus diagonal number for uniform circular array with adjacent element spacing of half a wavelength.

Diagonal Number	Element Separation
1	0
2	0.5000
3	0.9239
4	1.2071
5	1.3066
6	1.2071
7	0.9239
8	0.5000

The correlation values are plotted versus the element separation in Fig. 8.32 along with the

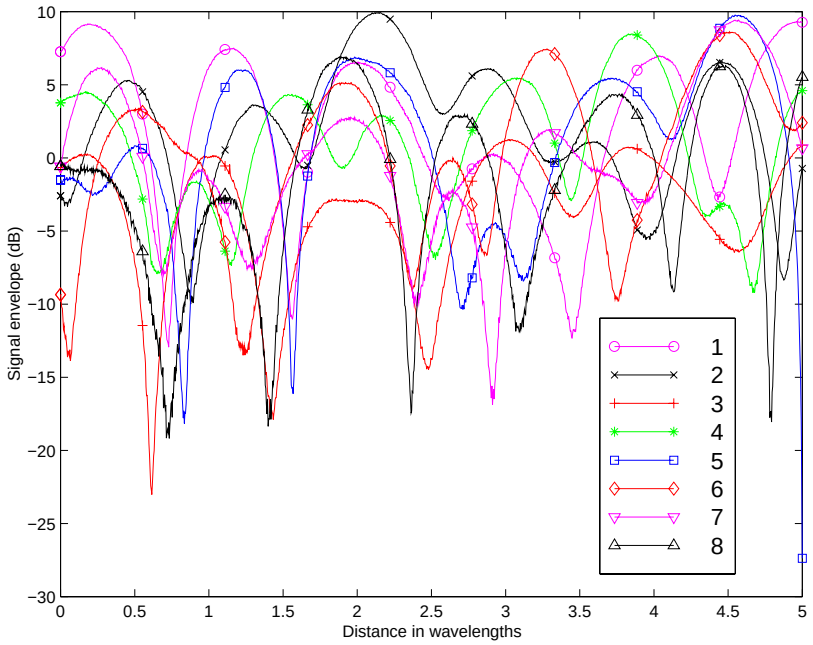

Figure 8.31: Normalized representative signal envelope for outdoor obstructed LOS measurements.

average correlation. The figures indicates that even for only half a wavelength element spacing there are small envelope correlation values. This result suggests that for this environment small element spacings would provide significant diversity gain.

8.3.3 Spatial Signature Vectors Properties

The cdfs for the SSV correlation values as defined in (8.9) versus transmitter displacement were found from the five sets of measurements. The resulting cdfs are shown in Fig. 8.33 for various transmitter displacement values. The results in Fig. 8.33 indicate that the SSV decorrelate to low values with transmitter displacements on the order of half of a wavelength. This is an expected result when one considers the variation of the fading envelopes observed over half a wavelength transmitter displacement. Figure 8.34 shows the 5 and 95 percentage points of the cdf and the average SSV correlation values versus transmitter displacement. The curves level off beyond one wavelength indicating that the correlation of the SSVs at one wavelength is nearly the same as the correlation of the SSVs at ten wavelengths. Returning to Fig. 8.33 we see that for ten wavelengths transmitter displacement that the SSV correlation values are nearly uniformly distributed from 0 to 0.65. This is indicated by the near linear shape of the corresponding cdf curve over this range.

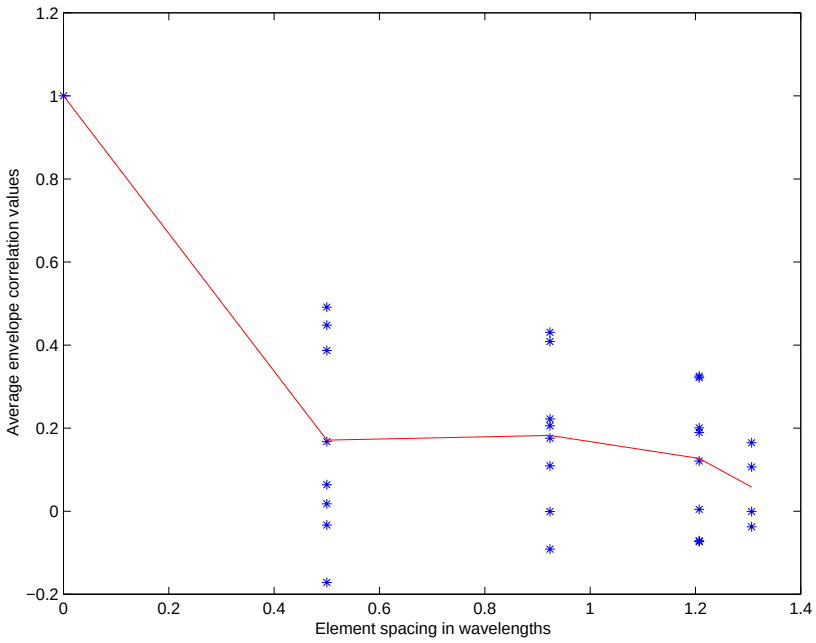

Figure 8.32: Envelope correlation values versus element spacing at the mobile for outdoor obstructed LOS measurements. The solid lines are the estimates obtained from each antenna element. The '-*' line is the average value.

8.3.4 Eigenvalue Distribution

The average normalized eigenvalues for the outdoor obstructed LOS measurements are given in Table 8.5. Although the eigenvalue spread is greater here than was observed for the office measurements, the ratio of the dominant to the second largest eigenvalue is smaller. Again, the eigenvalue spread is much less than what was observed for the hallway data.

Table 8.5: Average normalized eigenvalues of R_{xx} for obstructed LOS outdoor measurements.

i	λ_i	$10\log_{10}(\lambda_i)$
1	1.0000	0
2	0.6272	-2.0258
3	0.2216	-6.5444
4	0.1295	-8.8762
5	0.0746	-11.2702
6	0.0274	-15.6276
7	0.0153	-18.1596
8	0.0077	-21.1354

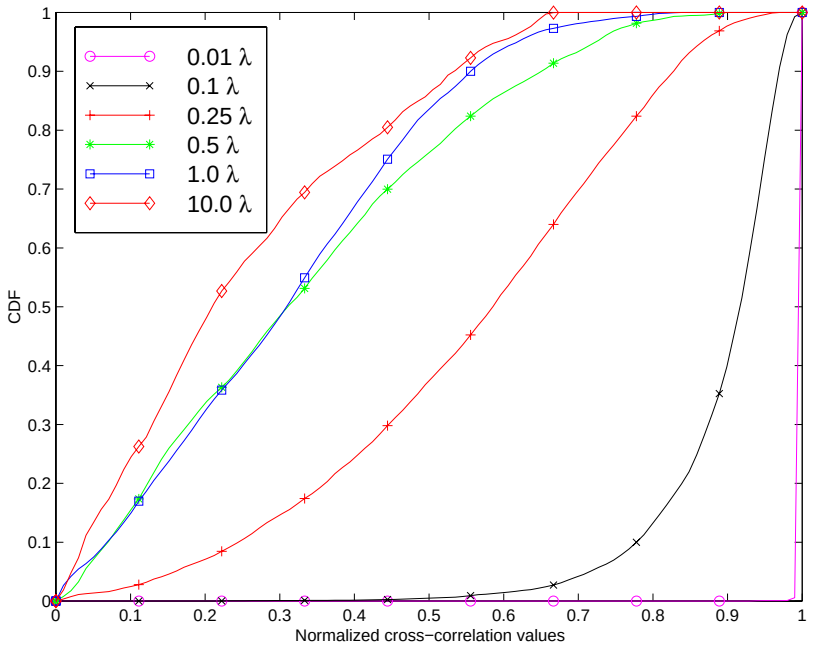

Figure 8.33: Normalized SSV cross-correlation CDF versus transmitter displacement for outdoor obstructed LOS measurements.

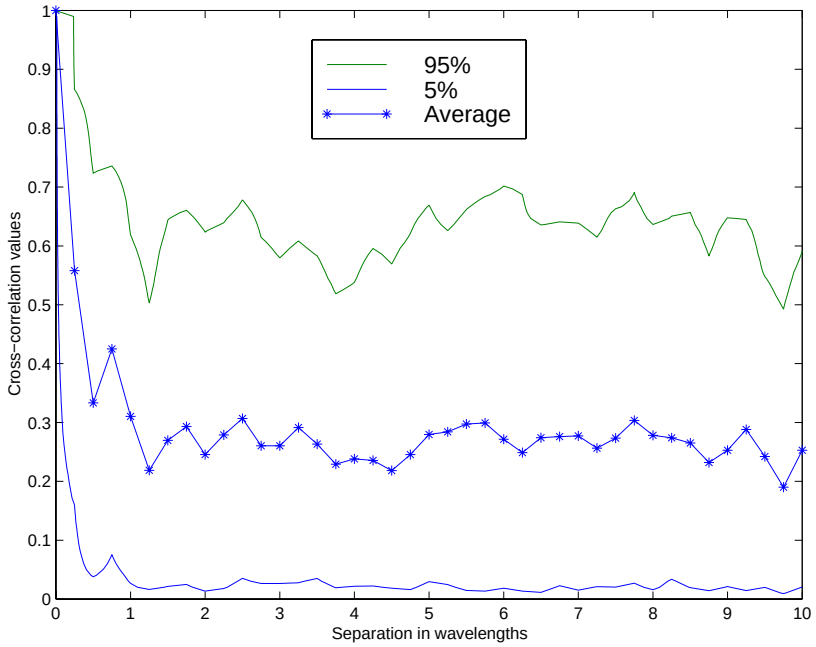

Figure 8.34: Normalized SSV cross-correlation CDF versus transmitter displacement for outdoor obstructed LOS measurements.

8.4 Outdoor Clear LOS Measurements

In this section the outdoor clear LOS measurements that were mentioned in the previous section are analyzed. As with the other data sets, the signal envelope correlation properties and the correlation of spatial signature vectors are considered.

8.4.1 Signal Envelope Properties

A representative plot of the signal envelopes received by the eight element circular array for a clear LOS environment are shown in Fig. 8.35 below. The figure shows moderate fading, with power variations on the order of only 10 to 15 dB on most elements over the distance of five wavelengths. Also, the transmitter displacement between deep fades exceeds a few wavelengths.

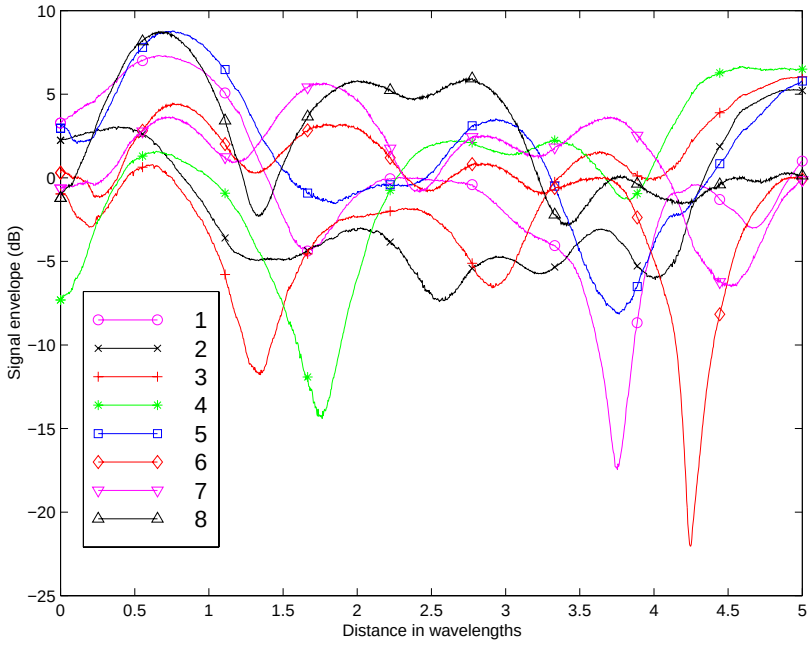

Figure 8.35: Normalized representative signal envelope for outdoor clear LOS measurements.

The corresponding matrix of cross-correlation coefficients averaged over the five measurements is given by

$$\rho_e = \begin{bmatrix} 1.0000 & 0.4890 & -0.0074 & 0.1531 & 0.6225 & 0.0359 & -0.0800 & 0.1595 \\ 0.4890 & 1.0000 & 0.4469 & 0.4744 & 0.6948 & -0.3775 & -0.4576 & -0.1874 \\ -0.0074 & 0.4469 & 1.0000 & 0.7962 & 0.0952 & -0.5861 & -0.4693 & -0.3654 \\ 0.1531 & 0.4744 & 0.7962 & 1.0000 & 0.2375 & -0.5952 & -0.4624 & -0.3004 \\ 0.6225 & 0.6948 & 0.0952 & 0.2375 & 1.0000 & -0.0228 & -0.0618 & 0.2541 \\ 0.0359 & -0.3775 & -0.5861 & -0.5952 & -0.0228 & 1.0000 & 0.7991 & 0.7546 \\ -0.0800 & -0.4576 & -0.4693 & -0.4624 & -0.0618 & 0.7991 & 1.0000 & 0.7342 \\ 0.1595 & -0.1874 & -0.3654 & -0.3004 & 0.2541 & 0.7546 & 0.7342 & 1.0000 \end{bmatrix}.$$

The off-diagonal entries of ρ_e are much higher in this case than that observed for the obstructed LOS environment. The correlation values are plotted versus the element separation in Fig. 8.36.

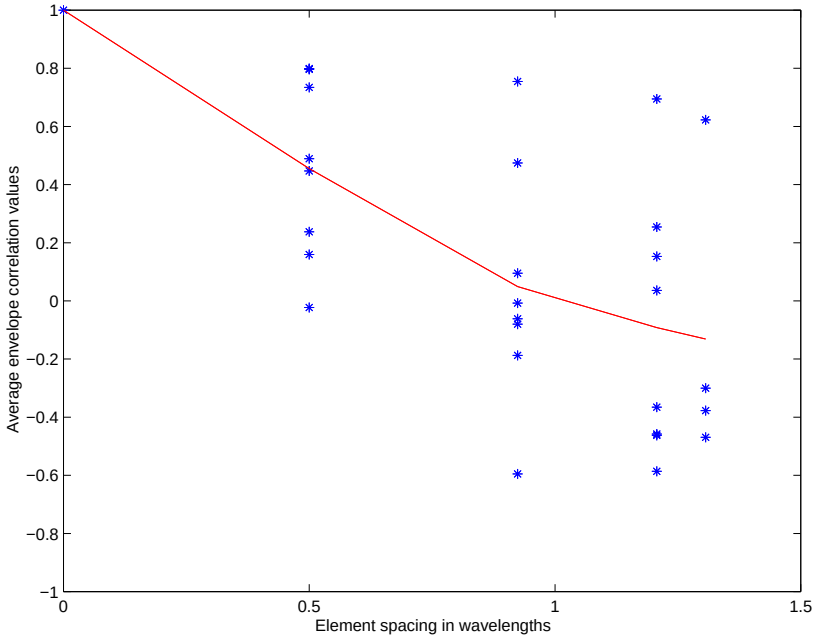

Figure 8.36: Envelope correlation values versus element spacing at the mobile for outdoor clear LOS measurements. The solid lines are the estimates obtained from each antenna element. The '-*' line is the average value.

8.4.2 Spatial Signature Vectors Properties

The cdfs of the normalized correlation values of the spatial signature vectors as defined in (8.9) were found for various transmitter displacements for the five clear LOS measurements that were made. The resulting cdfs are shown in Fig. 8.37 for various transmitter displacements. In this case the SSVs decorrelated much more slowly than was the case for the obstructed LOS measurements.

Figure 8.38 shows the 5 and 95 percentage points of the cdf and the average SSV correlation values versus transmitter displacement. An unexpected result is that the correlation of the SSVs is higher for transmitter displacements ranging from six to ten wavelengths then for the range of three to six wavelengths. One possible explanation for this observation is that there may be some periodic nature to the phase shifts of the various multipath components as the transmitter moves through space.

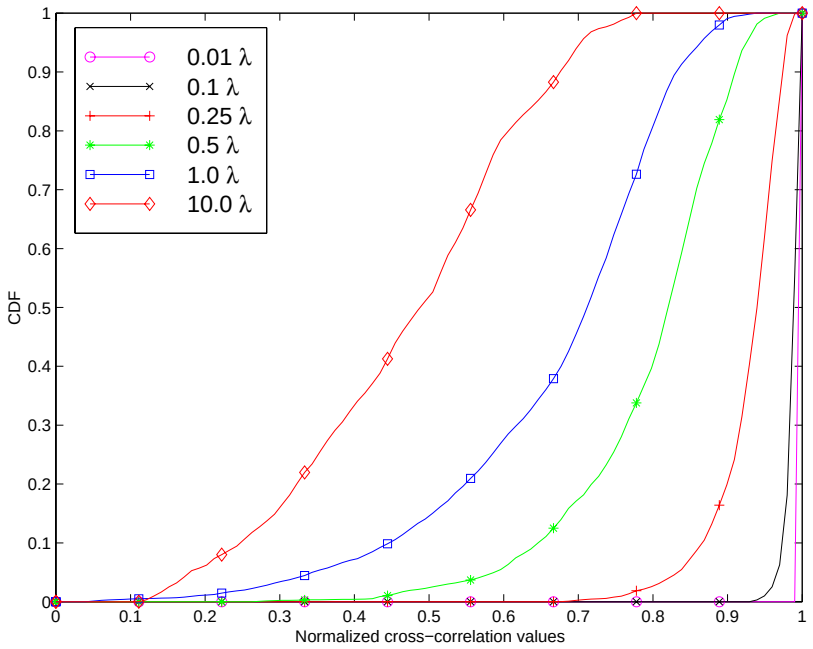

Figure 8.37: Normalized SSV cross-correlation CDF versus transmitter displacement for outdoor LOS obstructed measurements.

8.4.3 Eigenvalue Distribution

The average normalized eigenvalues for the clear LOS measurements are given in Tables 8.6. The eigenvalue spread here is greater than observed for the obstructed LOS measurements, but still less than that observed for the hallway data. Again, all of these results are consistent with the relationship between the eigenvalue distribution and the channel parameters.

Table 8.6: Average normalized eigenvalues of R_{xx} for clear LOS outdoor measurements.

i	λ_i	$10\log_{10}(\lambda_i)$
1	1.0000	0
2	0.3351	-4.7476
3	0.0446	-13.5018
4	0.0273	-15.6393
5	0.0163	-17.8878
6	0.0082	-20.8392
7	0.0022	-26.5041
8	0.0008	-31.0394

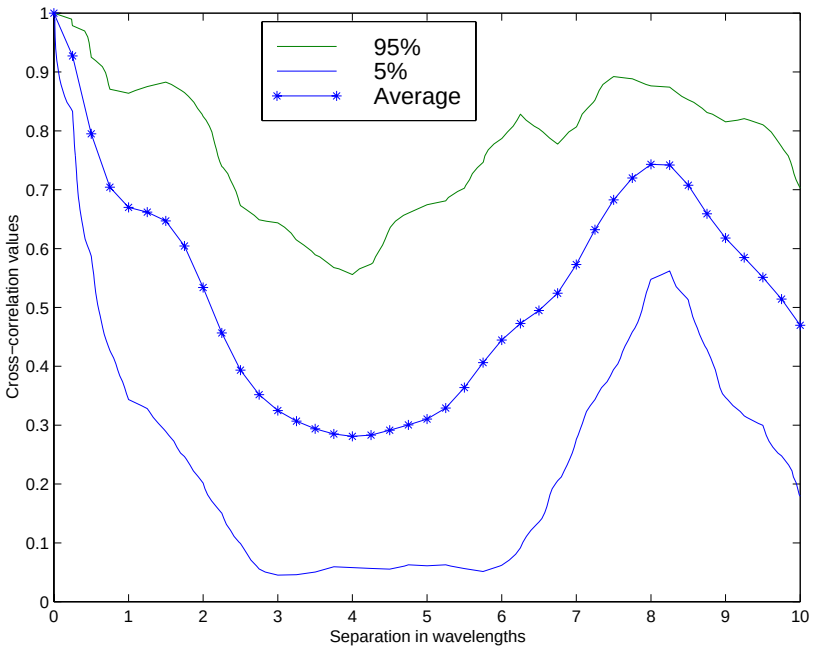

Figure 8.38: Normalized SSV cross-correlation CDF versus transmitter displacement for outdoor LOS obstructed measurements.

8.5 Summary

In this chapter antenna array measurements that were made in four drastically different propagation environments were studied. The focus of the analysis was the envelope correlations observed on each pair of sensors, the variations of the spatial signature vectors caused by a displacement of the transmitter, and eigenvalue distributions. In general the measured results were consistent with expected results.

It was found that in LOS environments, the fading was less severe, greater separation distances between antenna elements was needed for a specified envelope correlation value, the eigenvalue spread was smaller, and smaller changes were observed in spatial signature vectors for a given transmitter displacement as compared to obstructed LOS environments. This was especially true for the indoor LOS data collected in the hallway of the NEB.

The measurements show that there are dramatic differences in the properties of the received signal vectors with different environments. Therefore, it is essential that the environment is well understood before designing an antenna array system. In particular, in LOS environments greater element separations are needed to achieve the same level of diversity gain when compared to obstructed LOS environments. Additionally, since in a LOS environment the change in the spatial signature vectors is less for a given transmitter separation, greater user separation is needed for the same level of performance in an SDMA system. This also implies that the convergence of adaptive algorithms must be faster in an obstructed LOS environment, than in a clear LOS environment.

Chapter 9

Reverse Link Array Performance

In this chapter, the ability of an antenna array system to improve the signal to interference and noise ratio (SINR) is considered. The results shown here apply only to the reverse link, when the mobile uses a single transmit antenna and the base is equipped with an antenna array. The forward link is considered in the next chapter.

The chapter begins with a review of the ability of an array to cancel interference in both LOS and multipath environments from a linear algebra perspective. Then it is shown that in LOS environments it is only necessary to consider the angular domain, whereas in multipath environments one must consider the entire spatial domain. An example is given which highlights the differences between canceling interference and maximizing the output SINR.

The contributions made in this chapter involve the following simulations. Simulations are presented which demonstrate the ability of an array to separate two users which have identical AOA's for each path. The impact of angle spread on the ability of an array to separate two equal power users is studied. It is found that an increased angular spread tends to increase system performance.

9.1 Degrees of Freedom

It is a well known result that an M element antenna array has the ability to cancel $M-1$ or less interferers. In this section, this capability is reviewed using a linear algebra approach for both line-of-sight (LOS) and multipath environment.

9.1.1 Line-of-Sight Environment

For convenience, the definitions of notation given in Chapter 2 is repeated below. Let N denote the total number of users with signals impinging upon the array, and let $\mathbf{x}_k(t)$ denote the $M \times 1$ received signal vector corresponding to the kth user. In a LOS environment, $\mathbf{x}_k(t)$ may be

expressed

$$\mathbf{x}_k(t) = \alpha_k \mathbf{a}(\theta_k) s_k(t), \tag{9.1}$$

where α_k is the scalar complex path amplitude, $\mathbf{a}(\theta_k)$ is the array response vector in the direction of θ_k towards the kth user, and $s_k(t)$ is the complex baseband signal impinging upon the array.

The total received signal vector at the array is given by

$$\mathbf{x}(t) = \sum_{k=1}^{N} \mathbf{x}_k(t) + \eta(t), \tag{9.2}$$

where $\eta(t)$ accounts for receiver noise as well as background channel noise and is typically modeled as both spatially and temporarily white Gaussian noise.

The output of a narrowband antenna array is given by [1]

$$y = \mathbf{w}^H \mathbf{x} = [w_1^* \; w_2^* \; \cdots \; w_M^*] \begin{bmatrix} x_1 \\ x_2 \\ \vdots \\ x_M \end{bmatrix}, \tag{9.3}$$

where $\mathbf{w}$ is referred to as the weight vector, and $(.)^H$ denotes the hermitian operation (transpose complex conjugate). Temporarily, assume that there is no additive noise, i.e. $\eta(t) = 0$. Let $k = 1$ denote the desired user. The objective of the antenna array is to find $\mathbf{w}$ such that the following set of equations are satisfied,

$$\begin{aligned} \mathbf{w}^H \mathbf{a}(\theta_1) &= 1 \\ \mathbf{w}^H \mathbf{a}(\theta_2) &= 0 \\ &\vdots \\ \mathbf{w}^H \mathbf{a}(\theta_N) &= 0. \end{aligned} \tag{9.4}$$

Under this condition, and ignoring the noise term $\eta(t)$, the output of the array becomes $y(t) = \alpha_1 s_1(t)$. To understand when it is possible to solve (9.4) let us express (9.4) in matrix form as follows,

$$\begin{bmatrix} — \; \mathbf{a}^T(\theta_1) \; — \\ — \; \mathbf{a}^T(\theta_2) \; — \\ \vdots \\ — \; \mathbf{a}^T(\theta_N) \; — \end{bmatrix} \cdot \begin{bmatrix} w_1^* \\ w_2^* \\ \vdots \\ w_M^* \end{bmatrix} = \begin{bmatrix} 1 \\ 0 \\ \vdots \\ 0 \end{bmatrix}, \tag{9.5}$$

which may be expressed as

$$\mathbf{A}^T \mathbf{w}^* = \mathbf{C}, \tag{9.6}$$

where $\mathbf{A}$ is an $M \times N$ matrix given by

$$\mathbf{A} = \begin{bmatrix} \mathbf{a}(\theta_1) & \mathbf{a}(\theta_2) & \cdots & \mathbf{a}(\theta_N) \end{bmatrix} \tag{9.7}$$

[1] For notational convenience we have suppressed the implied dependence on t.

and

$$\mathbf{C} = \begin{bmatrix} 1 \\ 0 \\ \vdots \\ 0 \end{bmatrix}. \tag{9.8}$$

Taking the complex conjugate of both sides of (9.6) we have

$$\mathbf{A}^H \mathbf{w} = \mathbf{C}. \tag{9.9}$$

Hence, the ability of the antenna array to null interferers is related to the solution of a linear algebra problem. Depending upon the properties of the matrix $\mathbf{A}$, there can be either one solution, no solution, or infinitely many solutions.

When the number of users is less than the number of antenna elements, then there are an infinite number of solutions, provided that $\mathbf{a}(\theta_1)$ is not a scalar multiple of $\mathbf{a}(\theta_k)$ for $k \in \{2, 3, \cdots, M\}$. If $\mathbf{a}(\theta_1) = \mathbf{a}(\theta_k)$ for some $k \neq 1$ then there are no solutions.

When the number of users is equal to the number of antenna elements, a unique solution exists if all of the array response vectors are linearly independent. Generally, if the users have distinct angles of arrival then their array response vectors will be linearly independent. However, ambiguities in the array can cause two users with different angles of arrival to have the same array response vector. If two interferers have the same array response vector, then they may be treated as a single interferer and hence it is possible that an infinite number of solution exists. However, if an interferer has the same array response vector as the desired user then no solution exists. One should note though that if we consider the angle of arrival to have some continuous probability density function, then the probability that two users will have the same array response vector is zero.

Finally, when the number of users is greater than the number of antenna elements typically there will not be a solution to (9.9) since the number of equations exceeds the unknowns. However, if the desired user's signal is in the null space of the interferers subspace, then a solution still exists. This is possible if multiple interferers have the same array response vector due to ambiguities in the array or identical angles of arrival.

In the event that it is not possible to completely cancel all of the interferers, it is still possible to greatly improve the signal quality of the desired user.

9.1.2 Multipath Environment

As described in Chapter 2, in a flat fading multipath environment the received signal vector may be expressed as,

$$\mathbf{x}_k(t) = \left[\sum_{l=1}^{L_k} \alpha_{k,l} e^{-j\omega_c \tau_{k,l}} \mathbf{a}(\theta_{k,l}) \right] s_k(t) = \mathbf{v}_k s_k(t), \tag{9.10}$$

where

$$\mathbf{v}_k = \sum_{l=1}^{L_k} \alpha_{k,l} e^{-j\omega_c \tau_{k,l}} \mathbf{a}(\theta_{k,l}) \tag{9.11}$$

is the signature vector of user k. Using this model, nulling out the interference while still preserving the desired signal requires a solution of the following set of equations:

$$\begin{aligned} \mathbf{w}^H \mathbf{v}_1 &= 1 \\ \mathbf{w}^H \mathbf{v}_2 &= 0 \\ &\vdots \\ \mathbf{w}^H \mathbf{v}_N &= 0. \end{aligned} \tag{9.12}$$

This system of equations is identical to those given in (9.4) with the array response vector $\mathbf{a}(\theta_k)$ being replaced by the signature vector $\mathbf{v}_k$. For convenience we may express the system of equations in matrix form as

$$\mathbf{V}^H \mathbf{w} = \mathbf{C} \tag{9.13}$$

where

$$\mathbf{V} = \left[\begin{array}{cccc} \mathbf{v}_1 & \mathbf{v}_2 & \cdots & \mathbf{v}_N \end{array} \right] \tag{9.14}$$

and

$$\mathbf{C} = \left[\begin{array}{c} 1 \\ 0 \\ \vdots \\ 0 \end{array} \right]. \tag{9.15}$$

In this case, the existence of a solution to (9.13) depends upon the properties of $\mathbf{V}$. When the number of antenna elements exceeds the number of users a solution will exists provided that all of the signature vectors are linearly independent. If the number of antenna elements is less than the number of users, there are more equations than unknowns, and therefore typically no solutions exist.

When the channel has frequency selective fading, then each of the multipath signals must be treated as unique interfering signals, including the multipath components of the desired user. This leads to the following constraints on $\mathbf{w}$,

$$\begin{aligned} \mathbf{w}^H \mathbf{a}(\theta_{1,1}) &= 1 \\ \mathbf{w}^H \mathbf{a}(\theta_{k,l}) &= 0 \end{aligned}$$

for $k \in \{1, 2, \cdots, N\}$ and $l \in \{1, 2, \cdots, L_k\}$ with $k, l \neq 1, 1$. In this case the ability of the antenna array to cancel the interference is dependent upon the total number of multipath signals as opposed to the number of interferers. Typically, for narrowband antenna arrays, many more antenna elements are needed to achieve a specified level of performance in frequency selective environments than are needed in flat fading environments.

9.1.3 Angular versus Spatial Domains

In the previous two sections it was shown that an M element antenna array can typically cancel $M-1$ interferers for both LOS and flat fading multipath environments. In this section an example is used to show that these two different environments lead to different constraints on the beampattern. In particular, it will be shown that for LOS environments, it is possible to determine the system performance by observing the beampattern in the *angular domain*. That is, we may simply note how the magnitude of the beam pattern changes with angle of arrival, and restrict our attention to signals that have a received signal vector which is a scalar multiple of the array response vectors.

However, for multipath environments, the gain of the beampattern is less meaningful. In multipath environments it is not necessary to steer deep nulls in the directions of each of the interfering multipath components. In this case, we must consider the gain of the array in the direction of the individual signature vectors, which may lie anywhere in M dimensional space. Therefore, multipath environments require the consideration of the entire *spatial domain* of possible received signal vectors.

Consider the following two examples. In the first example we have a two element array with an element spacing of 0.5 λ, where λ is the carrier wavelength. There are two users in a LOS environment. The desired user and interferer have angles of arrival of 0 and 45 degrees with respect to array broadside, respectively. In this case the matrix $\mathbf{A}$ given in (9.7) is full rank, and therefore, we may find $\mathbf{w}$ using

$$\mathbf{w} = (\mathbf{A}^H)^{-1}\mathbf{C}. \tag{9.16}$$

The resulting beampattern is shown in Fig. 9.1. In this case, the beampattern has unity gain in the direction of the desired user and a null in the direction of the interferer.

In the second example, we have the same antenna array. However, in this case both of the users have two multipath components. The desired user has signal components at both 0 and 30 degrees. The interferer has multipath components at 5 and 45 degrees. In this case the matrix $\mathbf{V}$ given in (9.14) is full rank, and therefore

$$\mathbf{w} = (\mathbf{V}^H)^{-1}\mathbf{C}. \tag{9.17}$$

The resulting beampattern is shown in Fig. 9.2. In this case, it is not possible to determine the performance of the array from the magnitude of the beampattern. There are not nulls in the directions of the interferer's multipath at 5 and 45 degrees, but in fact the array has completely nulled out the interferer.

9.2 Maximizing SINR

In this section we consider a more practical approach, where rather than simply attempting to null interferers, our goal is to maximize the array output signal to interference and noise ratio (SINR). To understand why it is important to maximize SINR rather than just nulling

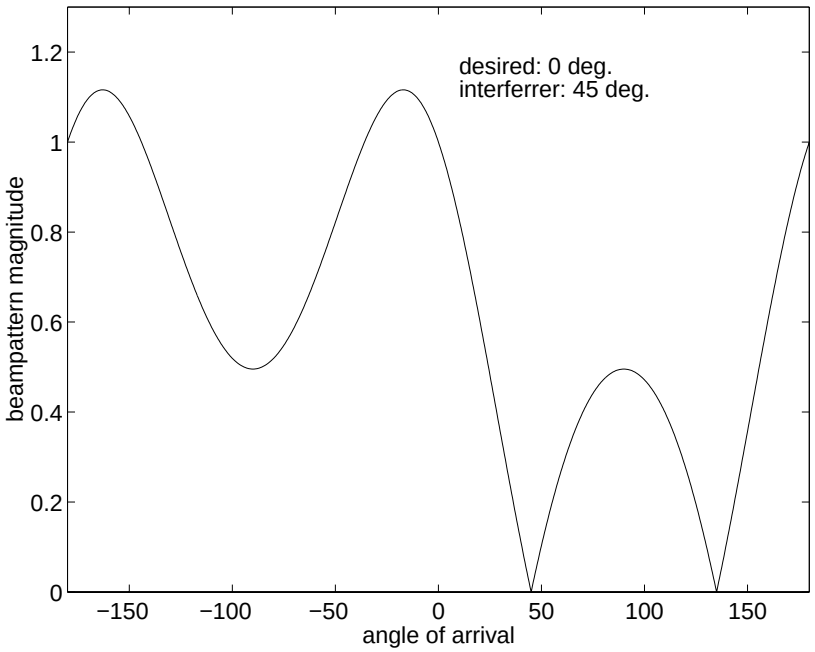

Figure 9.1: Beampattern, line-of-sight environment.

interference, we must account for the additive background or receiver noise term η. Consider the case when two equal power users in a LOS environment have nearly an identical line-of-bearing. Again, using a two element array with half wavelength spacing, let the desired user's AOA be 0 degrees relative to the array broadside, and let the interferer be at 5 degrees relative to the array broadside.

The beampattern which results using a null steering beamformer is shown in Fig. 9.3. A null is placed at 5 degrees as desired. However, the magnitude of the beampattern is small in the direction of the desired users as compared to its maximum value. This effect causes the spatially white additive noise to be enhanced, leading to a major reduction in the array output SINR. Effectively, by forcing a null in the direction of the interferer, the desired signal is inadvertently buried in the additive noise. Therefore, simply steering nulls at interferers does not guarantee good performance.

The array output in this case is given by $y(t) = s_1(t) + \mathbf{w}^H\eta$, which has a corresponding SINR of

$$\text{SINR} = \frac{\sigma_s^2}{\sigma_\eta^2 \mathbf{w}^H\mathbf{w}}, \tag{9.18}$$

where σ_s^2 is the power of the desired signal and σ_η^2 is the noise power. For the weight vector used to null the interferer, $\mathbf{w}^H\mathbf{w} = 26.8444$ which implies that

$$\text{SINR} = \frac{1}{26.8444}\frac{\sigma_s^2}{\sigma_\eta^2} = 0.0373\frac{\sigma_s^2}{\sigma_\eta^2}. \tag{9.19}$$

This result will be used to compare the performance of a null steering array to the optimum SINR approach.

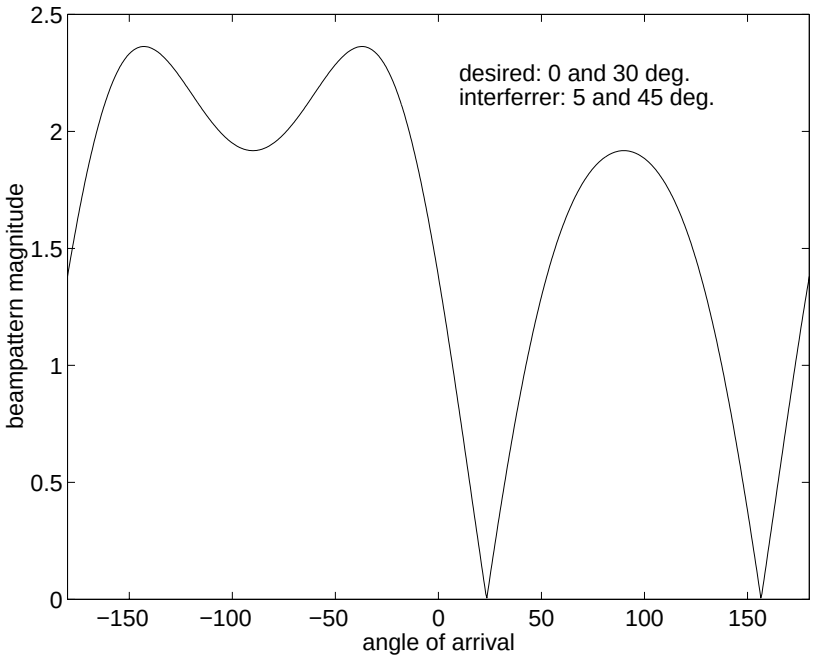

Figure 9.2: Beampattern, multipath environment.

An alternative approach which prevents the desired signal from being buried in the noise is to chose the weight vector to maximize the SINR directly. The solution of this problem in a LOS environment as derived in Section 2.6 above is given by

$$\mathbf{w}_{opt} = \beta \mathbf{R}_i^{-1} \mathbf{a}(\theta_1), \tag{9.20}$$

where β is a constant, $\mathbf{a}(\theta_1)$ is the array response vector in the direction of the desired user, and $\mathbf{R}_i$ is the interference plus noise correlation matrix. The resulting SINR is

$$\text{SINR}_{opt} = \sigma_s^2 \mathbf{a}^H(\theta_1) \mathbf{R}_i^{-1} \mathbf{a}^H(\theta_1). \tag{9.21}$$

In a multipath environment we obtain

$$\mathbf{w}_{opt} = \beta \mathbf{R}_i^{-1} \mathbf{v}_1, \tag{9.22}$$

where $\mathbf{v}_1$ is the signature vector of the desired user. The resulting SINR is

$$\text{SINR}_{opt} = \sigma_s^2 \mathbf{v}_1^H \mathbf{R}_i^{-1} \mathbf{v}_1. \tag{9.23}$$

Applying the maximum SINR solution to the example above with the desired user at broadside of the array and an equal power interferer at 5 degrees from broadside each with 10dB input SNR results in the beampattern shown in Fig. 9.4. The beampattern shows that the optimum weight vector does not simply steer a null at the interferer, since it must maintain a relatively high gain in the direction of the desired user.

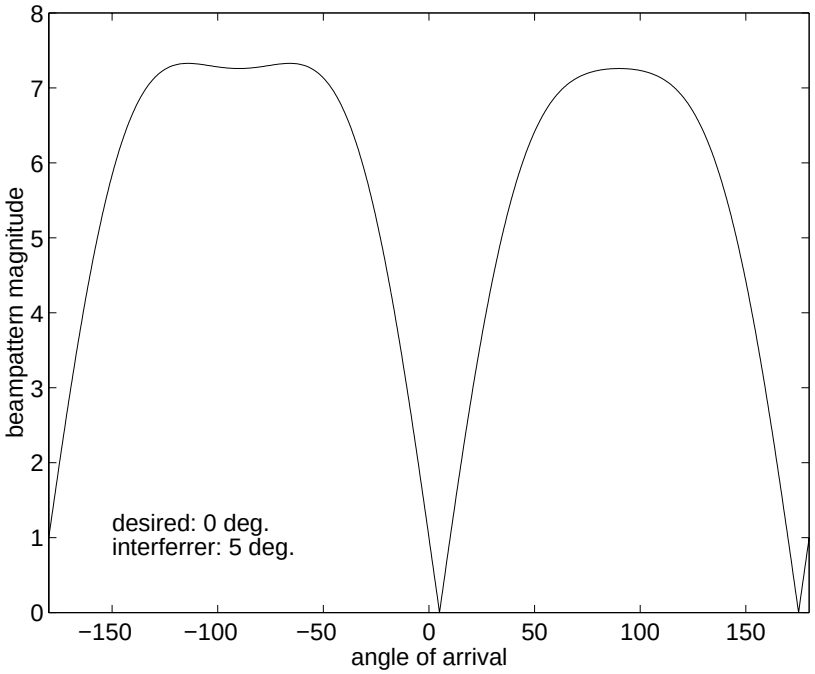

Figure 9.3: Beampattern for two closely spaced users, when null steering is used. Interferer at 5 degrees is nulled, but the gain towards the desired user at 0 degrees is small relative to the maximum gain.

The resulting output SINR versus input SNR is shown in Fig. 9.5. Also shown is the output SINR obtained using the null steering approach. When the input SNR is small, the null steering approach which does not account for the additive noise performs poorly. The difference in the performance levels diminishes as the input SNR increases, as should be expected since at a high SNR level, it becomes more important to null the interference than to maintain a high gain in the direction of the desired user. At an infinite input SNR both approaches would be identical.

9.3 Separation of Two Users with Identical AOA in a Multipath Environment

When multipath signals are present, the array output SINR is dependent upon the properties of the spatial signature vectors. Due to the differences in phases that occur for the different paths of different users it is theoretically possible to achieve a high level of SINR gain, even when the angles of arrival of the multipath of the desired user are identical to the angles of arrival of an interferer [89]. In SDMA systems with two closely spaced mobiles, the presence of several dominant reflectors in the environment may very well lead to identical angles of arrival for several paths of different mobiles. In this section the ability of an antenna array to separate two users which each have two multipath components, such that the AOA of the paths of the desired user are identical to those of the interferer is considered. The results presented here

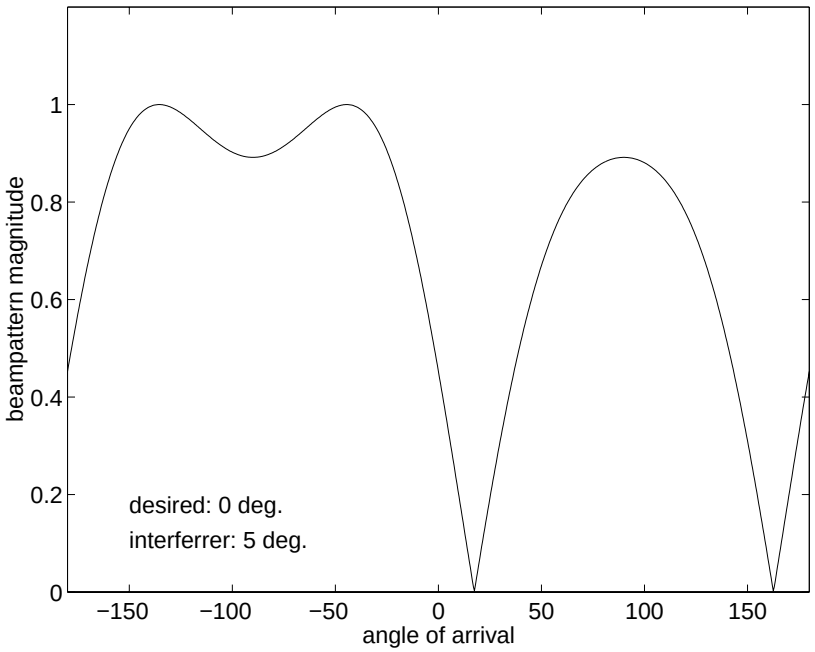

Figure 9.4: Beampattern of optimum beamformer.

could also be used to evaluate the performance of systems which utilize antenna arrays at the mobile, since the angle distribution of the paths transmitted from the various antenna elements is likely to be the same.

The signal model is

$$\mathbf{x}(t) = \mathbf{x}_1(t) + \mathbf{x}_2(t) + \eta(t), \tag{9.24}$$

where

$$\mathbf{x}_1(t) = \left[\alpha_{1,1}e^{-j\omega_c\tau_{1,1}}\mathbf{a}(\theta_{1,1}) + \alpha_{1,2}e^{-j\omega_c\tau_{1,2}}\mathbf{a}(\theta_{1,2})\right] s_1(t) = \mathbf{v}_1 s_1(t) \tag{9.25}$$

and

$$\mathbf{x}_2(t) = \left[\alpha_{2,1}e^{-j\omega_c\tau_{2,1}}\mathbf{a}(\theta_{2,1}) + \alpha_{2,2}e^{-j\omega_c\tau_{2,2}}\mathbf{a}(\theta_{2,2})\right] s_2(t) = \mathbf{v}_2 s_2(t) \tag{9.26}$$

are the received signal vectors for users 1 and 2 respectively, and $\eta(t)$ is additive white noise. For simplicity, assume that $\alpha_{1,1} = \alpha_{1,2} = \alpha_{2,1} = \alpha_{2,2} = 1$, $\theta_{1,1} = \theta_{2,1} = \theta_1$ and $\theta_{1,2} = \theta_{2,2} = \theta_2$. Furthermore, multiplication of $\mathbf{v}_1$ by a phase shift does not affect the output SINR, and therefore without loss of generality we may assume that $e^{-j\omega_c\tau_{1,1}} = e^{-j\omega_c\tau_{2,1}}$. Therefore, the above signal model may be reduced to

$$\mathbf{x}_1(t) = \left[\mathbf{a}(\theta_1) + e^{-j\psi_1}\mathbf{a}(\theta_2)\right] s_1(t) = \mathbf{v}_1 s_1(t) \tag{9.27}$$

and

$$\mathbf{x}_2(t) = \left[\mathbf{a}(\theta_1) + e^{-j\psi_2}\mathbf{a}(\theta_2)\right] s_2(t) = \mathbf{v}_2 s_2(t), \tag{9.28}$$

where $\psi_1 = \omega_c\tau_{1,1} - \omega_c\tau_{1,2}$ and $\psi_2 = \omega_c\tau_{2,1} - \omega_c\tau_{2,2}$. Assuming that ψ_1 and ψ_2 are random variables uniformly distributed over $[0, 2\pi]$, the resulting array output SINR cdf and the cor-

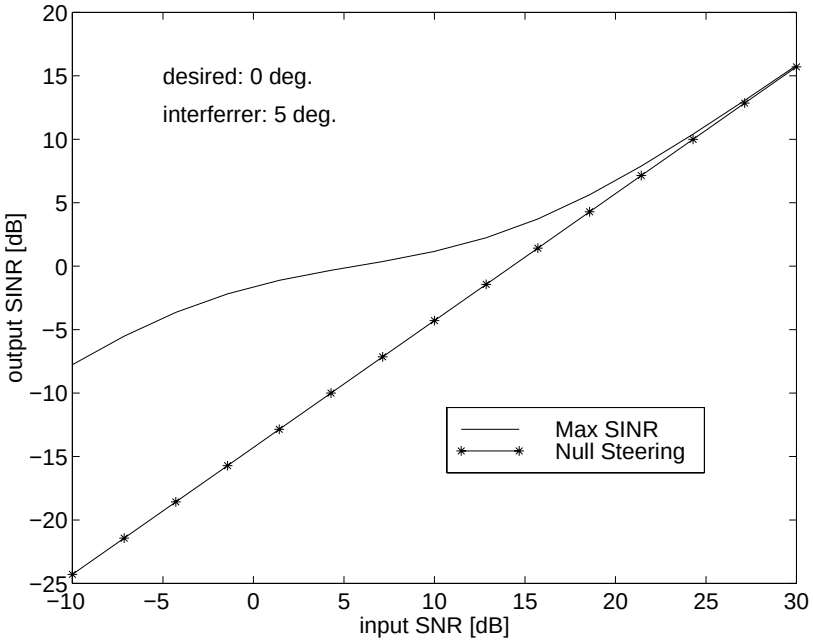

Figure 9.5: Comparison of the SINR performance of null steering and optimum beamforming.

responding array gain cdf may be found.[2] A critical parameter is $\Delta\theta = \theta_2 - \theta_1$ which is the angular separation of the two path components. For each of the simulations given below $\theta_1 = 0$ which is broadside the array.

Figure 9.6 shows the array output SINR cdf for various values of $\Delta\theta$ when the SNR is 20dB and a 4 element ULA with half wavelength spacing is employed.

Figure 9.7 shows the performance as a function of the number of antenna elements assuming a uniform linear array with $\lambda/2$ spacing. It is assumed that $\Delta\theta = 5$ degrees and the input SNR is 20 dB. The array output SINR is shown for array sizes of 1, 2, 4, and 8 element arrays.

Even though the two users have the exact same angles of arrival, it is still possible to provide a reasonable level of performance using an antenna array. When an 8 element array is used with $\Delta\theta = 5$ degrees, 90 percent of the time, the output SINR exceeds 10 dB. Therefore, it is indeed possible that multipath propagation is beneficial under certain circumstances.

9.4 Impact of Multipath on SINR Performance

In this section, the impact of multipath on the SINR performance is explored for the case when there are several randomly distributed multipath components about the LOS direction. Now, rather than having two identical angles of arrival, the AOA of each user are independently

[2]Array gain is defined as the ratio of the output SINR of an M element antenna array to the output SINR of a single antenna element system.

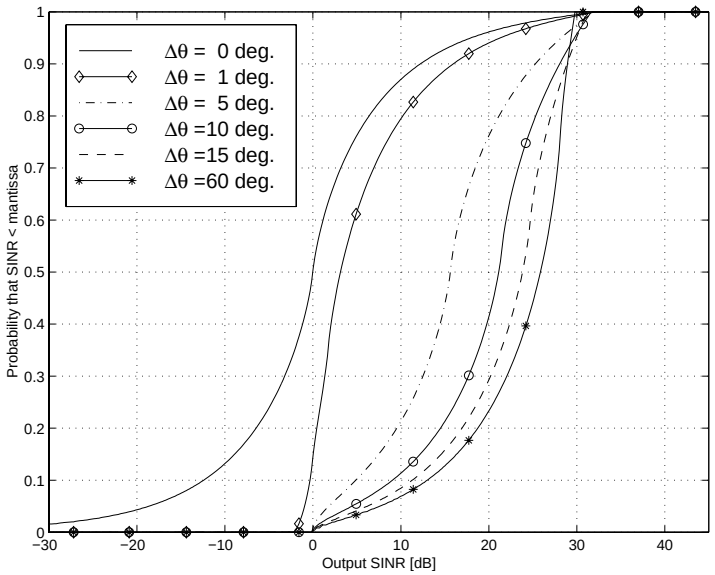

Figure 9.6: Output SINR cdf for various angular separations, $\Delta\theta$ between the two paths using a four element uniform linear array with half wavelength spacing.

Gaussian distributed about the LOS to the mobile. Again the environment being considered is that of two equal power users in a multipath environment with an SNR of 20 dB.

To show that angular spread may be beneficial, consider the case when there are five equal power multipath components that have a Gaussian distribution with standard deviation σ_a. In the absence of multipath two users that have an identical AOA can not be separated. However, when multipath is present, even if the two users are located at the same direction from the array it may still be possible to have sufficient array gain due to the differences in the user's signature vectors.

SINR cdf results for the case of two users that are broadside to the 4 element ULA are shown in Fig. 9.8. The results show that an increase in angle spread may cause a dramatic improvement in the SINR. Additionally it is found that despite the fact that the mobiles are in the same direction from the array, in the presence of multipath they may be separated. Even for small angle spreads a significant SINR improvement is obtained over the LOS case.

When the mobiles are further away from each other the impact of the angle spread is less dramatic. Figure 9.9 shows the resulting SINR cdf when User 1 is broadside the array and User 2 is 15 degrees from broadside. The difference in the performance for various angle spreads is quite small compared to the case when both users are broadside the array. Again, however, the SINR tends to improve with an increase in the angle spread.

From the previous two figures one may wonder what the impact that the angle spread has when the line-of-bearing to the mobiles is random over a large range of angles. It would appear that increasing the angle spread would improve system performance, since it has a small effect when users are well separated, and a dramatic effect when users are close together.

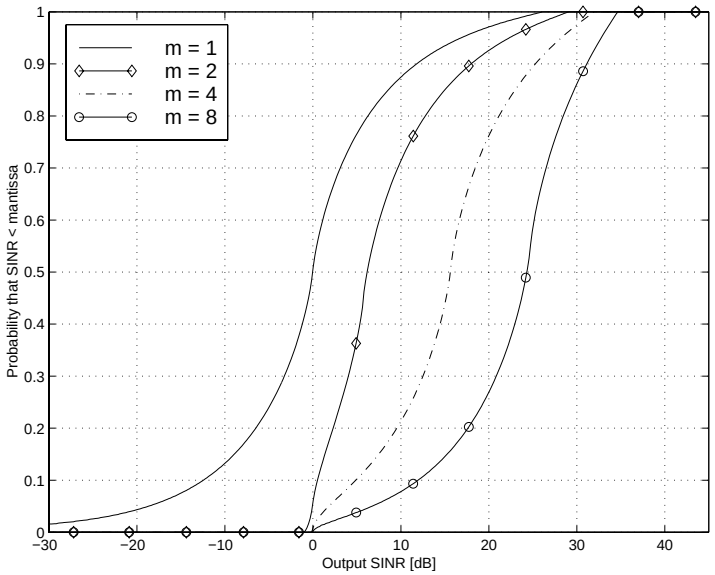

Figure 9.7: Output SINR cdf for various number of antenna elements for the case of $\Delta\theta = 5$.

In fact an increase in angle spread does improve performance of probably most interference cancellation systems. Figure 9.10 shows the SINR cdf for various angle spreads when a 4 element ULA, with 20 dB SNR, and two equal power users uniformly distributed over a 120 sector centered at the array broadside. Finally, Fig. 9.11 shows the SINR cdf when two users are uniformly distributed over a 120 degree sector with an angle spread of 5 degrees, an SNR of 20 dB, and a variable number of path components. As shown, the performance increases with an increase in the number of path components.

9.5 Summary

In LOS and flat fading environments it is typically possible to cancel $M - 1$ interferers using an array of M antenna elements. In frequency selective fading environments, each of the paths must be considered as individual interferers leading to a major reduction in the ability a narrowband array to cancel interference. Simply steering nulls in the directions of interference is not sufficient, since in doing so the SNR may suffer. In LOS environments the gain of the beampattern is meaningful. However, in multipath environments the beampattern is not a good indicator of system performance. Finally, multipath angular spread is often beneficial to interference cancellation antenna array systems, especially when two users have nearly the same line-of-bearing. SINR performance of the array increases with both angular spread, and the number of path components.

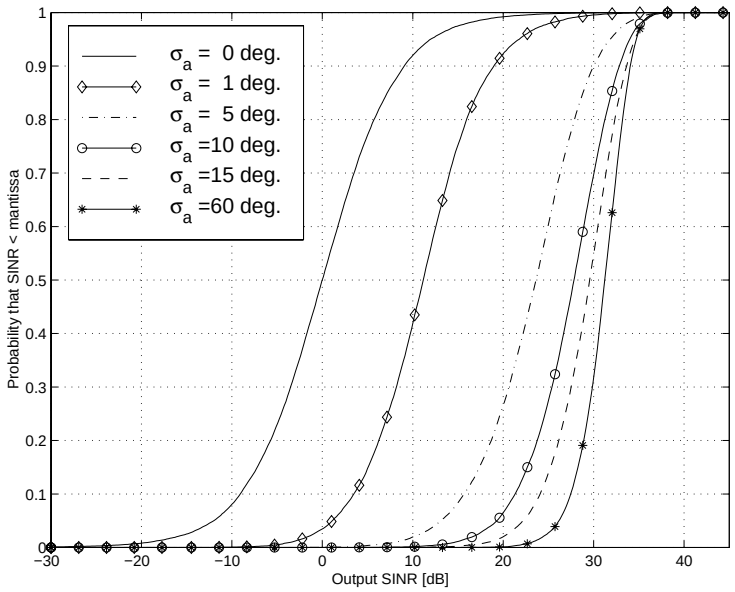

Figure 9.8: Output SINR cdf for various angle spreads with both users broadside the four element uniform linear array with half wavelength spacing.

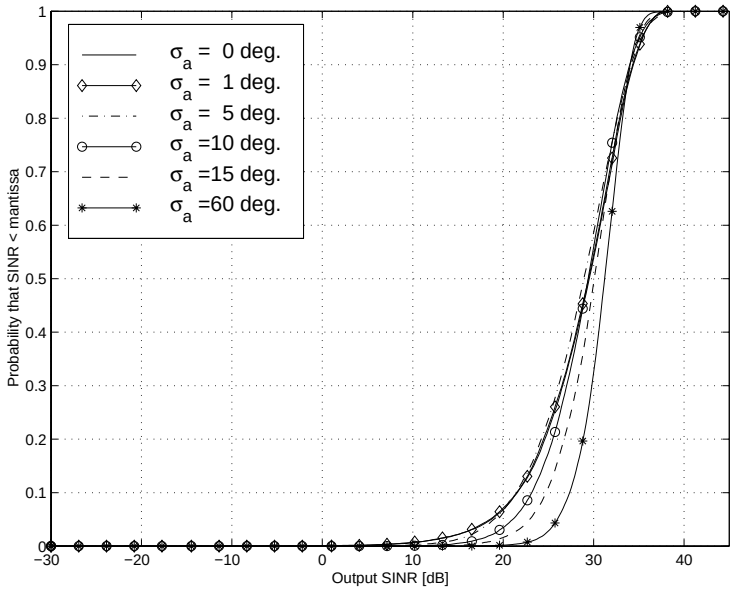

Figure 9.9: Output SINR cdf for various angle spreads with user 1 broadside the array and user 2 located at 15 degrees from broadside.

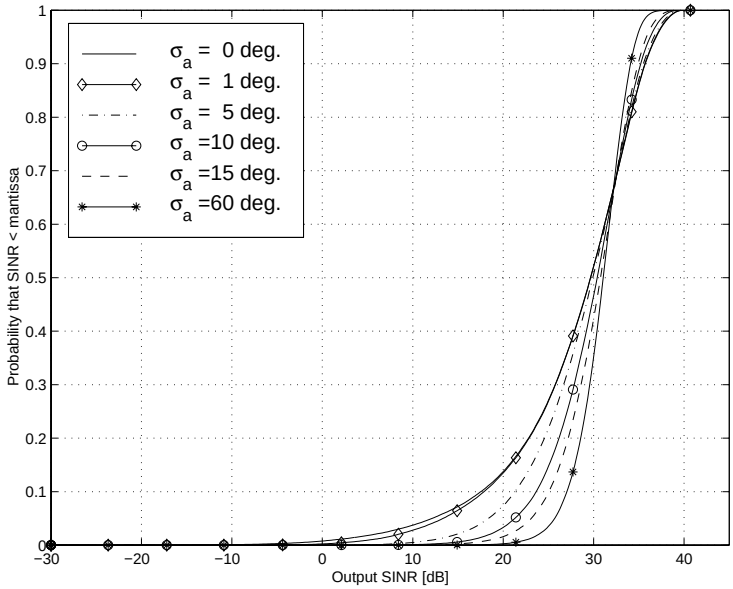

Figure 9.10: Output SINR cdf for various angle spreads with two users uniformly distributed over a 120 degree sector.

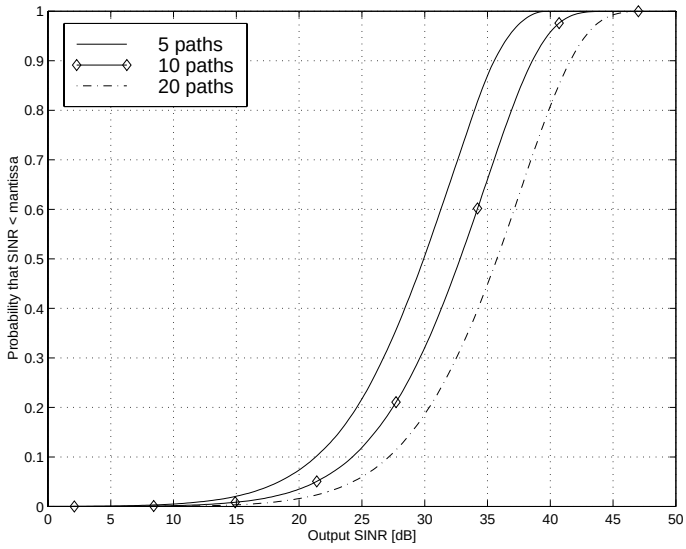

Figure 9.11: Output SINR cdf for various number of path components with two users uniformly distributed over a 120 degree sector.

Chapter 10

Forward Link Beamforming Techniques

The use of antenna arrays is thought to be one of the last remaining frontiers which will offer huge capacity gains over existing systems. Their ability to improve signal reception at the base station has been well documented. However, in order for the antenna arrays to provide increased system capacity, it is important that their use will also improve the forward link. Improving signal reception on the reverse link is relatively simple when compared to forward link implementations. In this chapter we review the various forward link beamforming techniques. Details of a forward link beamforming method which maximizes the received signal power at the mobile are given. The simulation results showing the relative performance of the dominant path selection method to the optimum performance is an original contribution of this work.

Several methods have been proposed for forward link beamforming [15]. In Section 10.1 a brief overview of the various methods is given. Simulation results for the maximum receive power method are presented in Section 10.2. Finally, Section 10.3 summarizes the chapter.

10.1 Survey of Forward Link Beamforming Techniques

10.1.1 Reverse Link Weight Vector

In TDD systems when the reverse link and forward link use the same carrier frequency it is possible to use the reverse link beamformer weights on the forward link [15]. In order for the reverse link and forward link propagation environments to be the same it is necessary for the reverse link and forward link transmissions to occur within the coherence time of the channel.

10.1.2 Feedback

For FDD systems differences in the carrier frequency cause drastic changes to the spatial signature vectors of the various users [71,72]. Therefore, different weights are needed for the reverse link and forward link. One method that may be used to determine the appropriate forward link weight vector involves the use of feedback from the mobile [90–92]. In this scheme probing signals are used to obtain an estimate of the path amplitude and phase from each antenna element to each mobile. The information is then feedback to the base station.

The weight vectors are found as follows. Define the estimated $M \times N$ complex channel matrix $\mathbf{C}$ such that the (i, n) component gives the complex channel gain from the ith transmitting element to the nth receiver, where M is the number of elements in the antenna array and N is the number of receivers [91]. Also, define the weight vector matrix,

$$\mathbf{W} = \left[\begin{array}{cccc} \mathbf{w}_1 & \mathbf{w}_2 & \cdots & \mathbf{w}_N \end{array} \right] \tag{10.1}$$

where $\mathbf{w}_i$ is the weight vector used to transmit the nth users signal. To prevent cross talk between users we require that

$$\mathbf{W}^H \mathbf{C} = \mathbf{I}_N \tag{10.2}$$

where $\mathbf{I}_N$ is the $N \times N$ identity matrix. This is achieved by selecting

$$\mathbf{W} = \mathbf{C}^{+H} \tag{10.3}$$

where $(.)^+$ denotes the pseudoinverse [91].

10.1.3 Optimum Beam Selection

When fixed multiple beam antennas are used, it is possible to transmit using the beam which had the strongest path on the reverse link [93,15]. In general fixed beam systems do not achieve the same level of performance as adaptive beamforming schemes, but they are often have much simpler implementations and for some environments provide performance which is close to that of a fully adaptive array [24].

10.1.4 Maximizing SINR using AOA Information

Several researchers have considered the use of AOA information in determining the forward link weight vector [94–100]. In essence the objective of these methods is to use AOA information of each user to maximize the ratio of power received at the desired user to the total power received at the interfered users [99]. When multipath signals are present it is not possible to maximize the instantaneous SINR. Instead these techniques attempt to maximize the mean SINR averaged over fast fading. In general the weight vector is found from a generalized eigenvalue problem of the form [95],

$$\mathbf{R}_{ss}\mathbf{w} = \lambda \mathbf{R}_{ii}\mathbf{w} \tag{10.4}$$

where $\mathbf{R}_{ss}$ is the array covariance matrix of the desired user averaged over fast fading, and $\mathbf{R}_{ii}$ is the sum of the interferers covariance matrix also averaged over fast fading. Both $\mathbf{R}_{ss}$ and

$\mathbf{R}_{ii}$ may be constructed using knowledge of the path amplitudes and angles of arrival for the desired user and interferers respectively.

10.1.5 Maximizing Received Signal Power Using AOA Information

It may not be practical to estimate the AOA of all users in the environment. As an alternative it is possible to select a weight vector which maximizes the received signal power at the mobile subject to the constraint on the total transmit power [101].

Consider the case when each multipath component experiences independent Rayleigh fading. Let p_i and θ_i denote the mean power level and angle of arrival of the ith path respectively. The received signal power at the mobile may then be expressed

$$P_r = \sum_{i=1}^{L} G(\theta_i) p_i \tag{10.5}$$

where $G(\theta_i)$ is the power gain of the antenna array in the direction of θ_i. The power of the multiple signal components is assumed additive since it is assumed that each path fades independently of the other paths, and hence is uncorrelated with them. The antenna gain is given by

$$G(\theta_i) = |\mathbf{w}^H \mathbf{a}(\theta_i)|^2 = \mathbf{w}^H \mathbf{a}(\theta_i)\mathbf{a}(\theta_i)^H \mathbf{w} \tag{10.6}$$

where $\mathbf{w}$ is the transmit weight vector and $\mathbf{a}(\theta_i)$ is the array response vector in the direction of θ_i. Substituting (10.6) into (10.5) gives

$$P_r = \sum_{i=1}^{L} \mathbf{w}^H \mathbf{a}(\theta_i)\mathbf{a}(\theta_i)^H \mathbf{w} p_i = \mathbf{w}^H \left[\sum_{i=1}^{L} \mathbf{a}(\theta_i)\mathbf{a}(\theta_i)^H p_i \right] \mathbf{w} = \mathbf{w}^H \mathbf{R}_{ss} \mathbf{w} \tag{10.7}$$

where

$$\mathbf{R}_{ss} = \sum_{i=1}^{L} \mathbf{a}(\theta_i)\mathbf{a}(\theta_i)^H p_i. \tag{10.8}$$

We seek the weight vector $\mathbf{w}$ which maximizes (10.7) subject to the constraint

$$\mathbf{w}^H \mathbf{w} = 1 \tag{10.9}$$

Using the method of Lagrange multipliers it is easily found that the desired weight vector is simply the dominant eigenvector of $\mathbf{R}_{ss}$, which may be constructed from estimates of path powers and angles of arrival [100]. Several properties of this method are explored through simulation in the following section.

10.2 Simulation of Maximum Received Power Method

In this section simulation results show the performance of the the maximum received power forward link beamforming method described in the previous section. Also, shown is the performance of a sub-optimum approach where only the dominant signal path is considered in the

calculation of the forward link weight vector. In this case the forward link weight vector is given by $\mathbf{w} = \mathbf{a}(\theta_1)$, where θ_1 is the multipath signal component with the largest power (dominant path component). It is found that the dominant path approach provides nearly identical signal power to the receiver when compared with the optimum approach which takes into account knowledge of all the multipath signal components.

For each of the simulations below 100 trials are simulated. The mobile is located broadside a ULA with half wavelength spacing. The angle of arrival of each multipath signal component is selected from a Gaussian distribution centered at array broadside. The path amplitudes of each multipath component are assumed to be equal. The simulation results are shown in Figs. 10.1 through 10.3 below. The results show the received signal power at the mobile relative to signal power that would be received if a single path component were present and an omni-direction transmit beampattern was used.

In Fig. 10.1 the received signal power at the mobile is plotted versus the number of antenna elements in the array for the case of two equal power signal components with angle of arrival values selected from a Gaussian distribution with a standard deviation of 10 degrees. Both the optimum and the dominant path received signal powers are shown. When only one element is present, the relative received signal power is 3 dB since two paths are present. The increase in the received signal power as the number of antenna elements increases is due to the improvement in antenna gain. For example with two antenna elements the relative received signal power increases by 3 dB over the single element case.

In Fig. 10.2 the relative received signal is plotted versus the number of multipath components in the environment for the case of an eight element ULA with half wavelength spacing, and an angle of arrival standard deviation of 10 degrees. The optimum, dominant path, and omni-direction cases are considered. Again, the beamforming towards the dominant path provides near optimum performance. As expected the relative received signal power at the mobile increases with an increase in the number of multipath signal components.

The relative received signal power versus angle spread of the channel is shown in Fig. 10.3 for the case of an eight element ULA and two multipath signal components. Again the performance of the dominant path selection is nearly optimum. In general the relative received signal power decreases with an increase in the angle spread. This is likely due to the fact that as the signal paths are further spread out it is more difficult to transmit power down both signal paths. For the dominant path selection, the decrease in the relative received signal power with an increase in angle spread is due to the decreased likelihood of the second path being in the mainbeam of the beampattern which points at the dominant path.

The results given here show only the improvement in the efficiency of the transmitter to direct its power towards the desired user. In practice one must consider the overall improvement in the SINR present at each user, the analysis of which would be dependent upon the angular distribution of the users relative to the base. In general, it would be expected that by efficiently transmitting power to the desired user that there would be less interference power received by other users. This is due to the fact that efficient transmission of signal power to the desired user would result in less power being transmitted in other directions in which other users may be present.

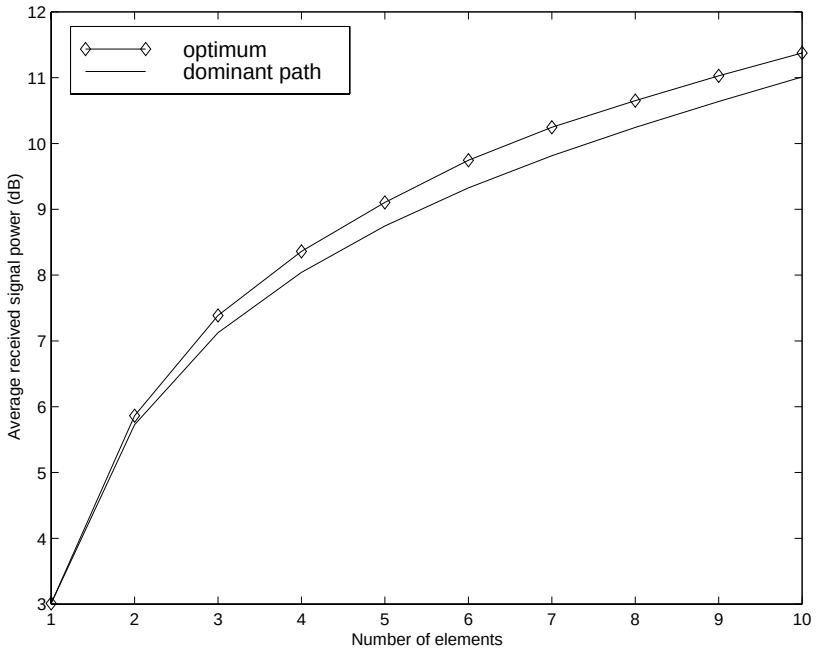

Figure 10.1: Average relative received signal power versus number of antenna elements in ULA (AS=10 deg., 2 equal power path components).

10.3 Conclusions

An overview of forward link beamforming methods was given. Details of a technique used to maximize the average received signal power at the mobile were given. Also proposed was a sub-optimum method which simply steers signal power in the direction of a dominant multipath component. Simulation results of the maximum received signal power method indicate that utilizing knowledge of only a single path gives near optimum performance. Also, as expected the received signal power increases with an increase in the number of antenna elements in the array and with an increase in the number of multipath components in the channel. Finally, it was found that the relative received signal power decreased with an increase in the angle spread of the signals relative to the base.

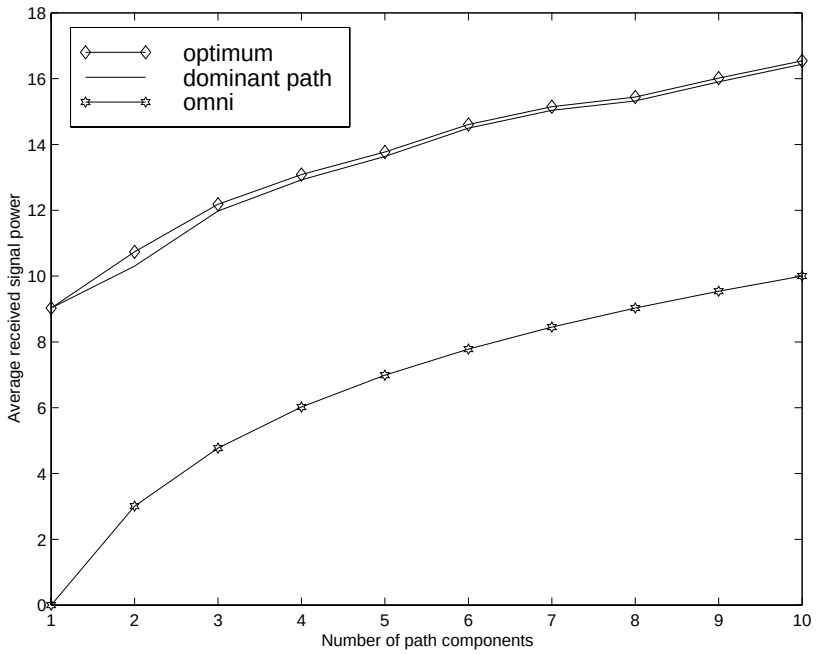

Figure 10.2: Average relative received signal power versus number of equal power path components (AS=10 deg., 8 element ULA).

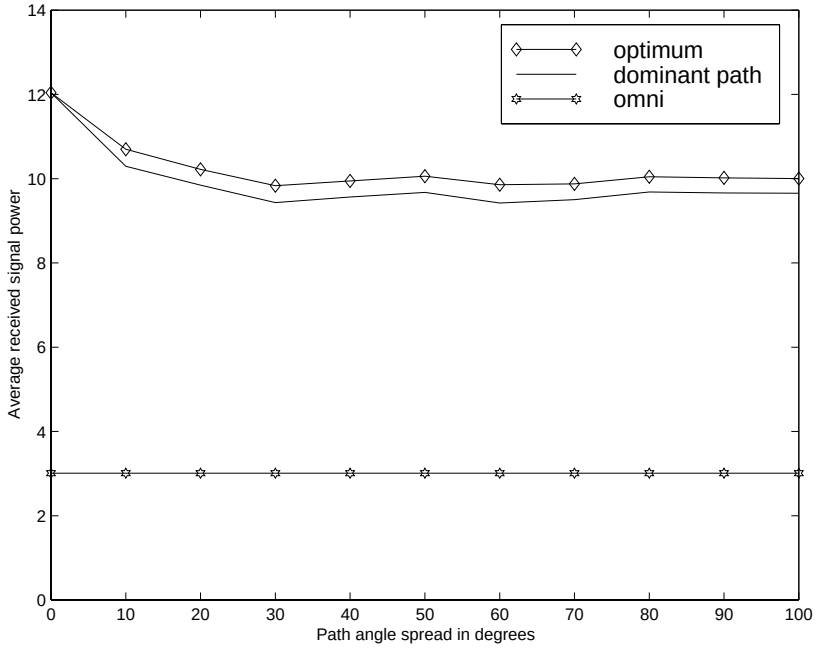

Figure 10.3: Average relative received signal power versus angle spread (8 element ULA, 2 equal power path components).

Chapter 11

Summary and Future Work

The focus of this research is on vector channel models and their relationship to the performance of antenna array systems. We summarize the results of this work in Section 11.1. In Section 11.2 we describe open research problems for future study. Final conclusions are discussed in Section 11.3.

11.1 Summary of Results

In Chapter 2 fundamentals of antenna array systems were covered. Signal models for both narrowband and wideband signals were reviewed. The definitions of adaptive beamforming and spatial diversity systems were given. The derivations of the optimum weight vector for the maximum SINR, minimum mean square error, minimum variance, and the maximum likelihood performance criteria were reviewed. Finally the ability of an antenna arrays to improve system capacity, extend maximum range, increase coverage, reduce mobile transmit power, improve signal quality, and increase data rates were explored.

A survey of several proposed vector channel models was given in Chapter 3. The models were classified into two classes, geometrically based and statistically based depending upon whether or not the location of scattering objects is specified by the model.

In Chapter 4 the joint TOA-AOA, marginal TOA, and marginal AOA probability density functions were derived for the circular and Liberti's elliptical scattering channel models. The Doppler spectrum which results when an exponential path-loss model was applied to the multipath components is also derived for both models.

In Chapter 5 a generalized optimum output SINR analysis was presented. The analytical derivation was based on the decomposition of the received signal vector into two signal components, one which is correlated with the desired signal and one which is not. Closed formed expressions are obtained for various space-time processing structures in frequency selective fading channels. The derived expressions are used to compare the performance of the receiver structures in various multipath channel conditions. It was found that the ISTF structure performs nearly as

well as the joint space-time processor under most conditions.

Details of the MPRG Antenna Array Testbed (MAAT) were presented in Chapter 6. A brief description of the antenna array hardware and software is given. The antenna array calibration procedure for compensating for the array hardware and signal splitter were presented. Measurements of the antenna array hardware amplitude and phase stability were presented.

In Chapter 7 a survey of previous antenna array propagation measurements were presented. The propagation measurement results include measurements of the envelope correlations observed at two antenna elements, changes in spatial signature vectors, angle spread, and joint TOA-AOA channel properties. It was shown that the various spatial signature vector change metrics could all be expressed in terms of the normalized cross correlation of the two vectors.

Measurement results obtained using the MAAT were presented in Chapter 8. Data was collected in four different channel environments including: indoor hallway, indoor office area, outdoor obstructed LOS, and outdoor clear LOS. The cross correlation of signal envelopes versus element spacing were reported for each of these environments. The cross correlation values were less in the indoor office area and the outdoor obstructed LOS than in the other measurement environments. Also, the correlation of the spatial signature vectors versus transmitter displacement were analyzed. Again, lower correlation values were found in the indoor office area and the outdoor obstructed LOS than in the other measurement environments. Finally, the eigenvalue distribution of the received array covariance matrix corresponding to data collected as the transmitter traversed a distance of 150 cm were reported. The eigenvalue spread was greater in the indoor office area and the outdoor obstructed LOS than in the other measurement environments. All of these results are consistent with expected results for the various channel conditions. Finally, the results may be used to determine the required convergent rate of adaptive algorithms, the required element spacing for diversity systems, and the performance of SDMA systems in each of the environments described above.

In Chapter 9, simulations showed the ability of an antenna array to separate two received signals. It was shown that an antenna array system can improve signal quality even if an interferer has multipath with identical AOA to that of the desired user. This situation is likely in SDMA applications where two users are in close proximity to one another. Also, it was shown that two user's with identical line-of-sight AOA can be adequately separated provided that the angular spreading of the users' multipath is sufficiently high. Finally, the impact of angle spread and number of path components was explored through simulation. It was found that the greater the angle spread and number of path components the greater the performance of the adaptive beamformer.

Finally, Chapter 10 presented an overview of forward link beamforming techniques. Simulation results showed the increase in received signal power at the mobile unit that is achievable using forward link beamforming.

11.2 Future Work

Finally, there are several areas of this work that could be extended through further research.

1. In Chapter 5 the simulations results assumed a BPSK signal format with no pulse shaping. The inclusion of pulse shaping will change the signal auto-correlation function and hence the optimum output SINR. Additional simulations studies which include pulse-shaping and other modulation schemes would provide further insight into the performance of the various receiver structures.

2. Due to time limitations only a limited amount of data could be collected and analyzed. Additional measurement campaigns to further characterize the vector channel in various environmental conditions would lead to greater confidence in the models.

3. Additional research could be performed to derive channel models from collected data in different environment conditions. Models that are derived from measured data could be used for simulation and analysis of antenna array systems.

4. The simulation studies presented in Chapter 9 show the performance of antenna array systems on the reverse link when two users are present. Additional simulation studies involving more users in various environmental conditions would provide additional insight into the impact that the channel parameters have on system performance.

5. Finally, the work presented here on forward link beamforming techniques was limited to determining the received signal power at the mobile. Additional simulations should be done to determine SINR improvement of the forward link beamforming techniques in various multipath environments. This would involve modeling the location of all users in the environment and taking into account co-channel interference from neighboring cells.

11.3 Conclusions

This research has studied multipath signal models for antenna array systems and their impact on system performance. Fundamental qualitative relationships were identified relating channel parameters to the ability of an antenna array to improve signal quality. Also, measurement results were presented indicating the variation of measured signal properties in various environments.

The results presented in this work have implications to wireless system design. First, the analytical results derived for the performance of the various space time processing structures will be useful in identifying an appropriate receiver structure for a particular multipath environment. Next, the measurement results can be used to determine the convergence rate of adaptive algorithms, and the required separation distance of users in an SDMA system. Finally, the simulation results on the performance of adaptive antenna on both the forward and reverse link are useful in identifying the relationship between channel parameters and system performance.

Antenna array systems are among one of the hottest research topics within wireless communications. Their use in future systems is inevitable. The efficient implementation of these systems will rely in part on accurate models for the signals received by an antenna array. In this work we have derived some fundamental results and have provided background information for the development and future study of these models.

Appendix A

Gradient of a Scalar Quantity

This appendix summarizes the key results related to taking the gradient of a scalar quantity with respect to a vector. Results are given for both real and complex vector quantities.

A.1 Gradient of a Scalar Quantity: Real

Defining Q to be a scalar which is a function of an m-dimensional column vector parameter $\mathbf{a}$ then the gradient $\nabla_{\mathbf{a}} Q$ is given by [16]

$$\nabla_{\mathbf{a}} Q = \begin{bmatrix} \frac{\partial Q}{\partial a_1} \\ \frac{\partial Q}{\partial a_2} \\ \vdots \\ \frac{\partial Q}{\partial a_m} \end{bmatrix} \tag{A.1}$$

From this definition, it is straight forward to derive the relationships in Table A.1, where $\mathbf{b}$ is also a real m-dimensional column vector, $\mathbf{B}$ is an $m \times m$ real matrix, and $\mathbf{B_s}$ is an $m \times m$ symmetric real matrix.

Table A.1: Gradient relationships for real vectors.

Quantity Q	Gradient $\nabla_{\mathbf{a}} Q$
$\mathbf{a}^T\mathbf{b}$	$\mathbf{b}$
$\mathbf{b}^T\mathbf{a}$	$\mathbf{b}$
$\mathbf{a}^T\mathbf{B}\mathbf{a}$	$(\mathbf{B}+\mathbf{B}^T)\mathbf{a}$
$\mathbf{a}^T\mathbf{B}_s\mathbf{a}$	$2\mathbf{B}_s\mathbf{a}$

A.2 Gradient of a Scalar Quantity: Complex.

When the vector $\mathbf{a}$ is complex it is more difficult to define the gradient. The trouble arises from the fact that the scalar quantity Q may depend upon $\mathbf{a}$ in such a way that Q is not analytic, since the complex conjugate of $\mathbf{a}$ is not an analytic function of [16].

Let us assume that Q is a function of a scalar

$$a = a_r + ja_i \tag{A.2}$$

and its conjugate

$$a^* = a_r - ja_i. \tag{A.3}$$

By adding (A.2) and (A.3) we find

$$a_r = \frac{a + a^*}{2} \tag{A.4}$$

Similarly, by subtracting (A.3) from (A.2) we have

$$a_i = \frac{a - a^*}{2j} \tag{A.5}$$

Applying the chain rule to $Q = f(a, a^*)$ gives

$$\frac{\partial Q}{\partial a} = \frac{\partial Q}{\partial a_r}\frac{\partial a_r}{\partial a} + \frac{\partial Q}{\partial a_i}\frac{\partial a_i}{\partial a} = \frac{1}{2}\left(\frac{\partial Q}{\partial a_r} - j\frac{\partial Q}{\partial a_i}\right) \tag{A.6}$$

and

$$\frac{\partial Q}{\partial a^*} = \frac{\partial Q}{\partial a_r}\frac{\partial a_r}{\partial a^*} + \frac{\partial Q}{\partial a_i}\frac{\partial a_i}{\partial a^*} = \frac{1}{2}\left(\frac{\partial Q}{\partial a_r} + j\frac{\partial Q}{\partial a_i}\right) \tag{A.7}$$

Generalizing to the case when Q depends on the vector quantity,

$$\mathbf{a} = \mathbf{a}_r + j\mathbf{a}_i \tag{A.8}$$

we find,

$$\nabla_{\mathbf{a}} Q = \frac{1}{2}\left(\nabla_{\mathbf{a}_r} Q - j\nabla_{\mathbf{a}_i} Q\right) \tag{A.9}$$

and

$$\nabla_{\mathbf{a}^*} Q = \frac{1}{2}\left(\nabla_{\mathbf{a}_r} Q + j\nabla_{\mathbf{a}_i} Q\right) \tag{A.10}$$

Applying these definitions it is possible to obtain the results given in Table A.2, where $\mathbf{b}$ is a complex length-m column vector, and $\mathbf{B}_h$ is Hermatian [16].

Table A.2: Gradient relationships for real vectors

Quantity Q	Gradient $\nabla_{\mathbf{a}} Q$	Gradient $\nabla_{\mathbf{a}^*} Q$
$\mathbf{a}^H\mathbf{b}$	0	$\mathbf{b}$
$\mathbf{b}^H\mathbf{a}$	$\mathbf{b}^*$	0
$\mathbf{a}^H\mathbf{B}_h\mathbf{a}$	$(\mathbf{B}_h\mathbf{a})^*$	$\mathbf{B}_h\mathbf{a}$

Appendix B

Woodbery's Identity

In this appendix the matrix inversion lemma (also referred to as Woodbery's Identity) is proven. The matrix inversion lemma asserts that for two positive definite m-by-m matrices $\mathbf{A}$ and $\mathbf{B}$, positive definite n-by-n matrix D, and an m-by-n matrix C, the following relationships between $\mathbf{A}$ and $\mathbf{A}^{-1}$ hold [102]: when

$$\mathbf{A} = \mathbf{B}^{-1} + \mathbf{C}\mathbf{D}^{-1}\mathbf{C}^{H} \tag{B.1}$$

then

$$\mathbf{A}^{-1} = \mathbf{B} - \mathbf{B}\mathbf{C}(\mathbf{D} + \mathbf{C}^{H}\mathbf{B}\mathbf{C})^{-1}\mathbf{C}^{H}\mathbf{B} \tag{B.2}$$

This is easily verified by multiplying (B.1) by (B.2) and showing that equality holds. The following steps show equality:

$$\begin{aligned}
\mathbf{A}\mathbf{A}^{-1} &= \left(\mathbf{B}^{-1} + \mathbf{C}\mathbf{D}^{-1}\mathbf{C}^{H}\right)\left(\mathbf{B} - \mathbf{B}\mathbf{C}(\mathbf{D} + \mathbf{C}^{H}\mathbf{B}\mathbf{C})^{-1}\mathbf{C}^{H}\mathbf{B}\right) \\
\mathbf{I}_m &= \mathbf{I}_m + \mathbf{C}\left[-(\mathbf{D} + \mathbf{C}^{H}\mathbf{B}\mathbf{C})^{-1} + \mathbf{D}^{-1} - \mathbf{D}^{-1}\mathbf{C}^{H}\mathbf{B}\mathbf{C}(\mathbf{D} + \mathbf{C}^{H}\mathbf{B}\mathbf{C})^{-1}\right]\mathbf{C}^{H}\mathbf{B} \\
\mathbf{I}_m &= \mathbf{I}_m + \mathbf{C}\left[-\mathbf{I}_n + \mathbf{D}^{-1}(\mathbf{D} + \mathbf{C}^{H}\mathbf{B}\mathbf{C}) - \mathbf{D}^{-1}\mathbf{C}^{H}\mathbf{B}\mathbf{C}\right](\mathbf{D} + \mathbf{C}^{H}\mathbf{B}\mathbf{C})^{-1}\mathbf{C}^{H}\mathbf{B} \\
\mathbf{I}_m &= \mathbf{I}_m + \mathbf{C}\left[-\mathbf{I}_n + \mathbf{D}^{-1}(\mathbf{D} + \mathbf{C}^{H}\mathbf{B}\mathbf{C}) - \mathbf{D}^{-1}\mathbf{C}^{H}\mathbf{B}\mathbf{C}\right](\mathbf{D} + \mathbf{C}^{H}\mathbf{B}\mathbf{C})^{-1}\mathbf{C}^{H}\mathbf{B} \\
\mathbf{I}_m &= \mathbf{I}_m + \mathbf{C}\left[-\mathbf{I}_n + \mathbf{I}_n + \mathbf{D}^{-1}\mathbf{C}^{H}\mathbf{B}\mathbf{C} - \mathbf{D}^{-1}\mathbf{C}^{H}\mathbf{B}\mathbf{C}\right](\mathbf{D} + \mathbf{C}^{H}\mathbf{B}\mathbf{C})^{-1}\mathbf{C}^{H}\mathbf{B} \\
\mathbf{I}_m &= \mathbf{I}_m
\end{aligned}$$

Appendix C

Importance of Eigenvalue Distribution

The eigenvalue distribution is an important parameter of the spatial channel. The eigenvalue distribution is a function of several channel parameters including multipath coherence, number of multipath components, and angle of arrival distribution. Further details about each of these are given in the corresponding sections below.

C.1 Notation

The length M received signal vector is denoted $\mathbf{x}(t)$. The M by M array covariance matrix is given by

$$\mathbf{R}_{xx} = \mathrm{E}\left\{\mathbf{x}(t)\mathbf{x}(t)^H\right\}. \tag{C.1}$$

Since, $\mathbf{R}_{xx}$ is a positive definite Hermitian symmetric matrix, then all of the eigenvalues of $\mathbf{R}_{xx}$ are positive and real. The eigenvectors are denoted by $\mathbf{e}_1, \mathbf{e}_2, \cdots, \mathbf{e}_M$, with corresponding eigenvalues of $\lambda_1, \lambda_2, \cdots, \lambda_M$, where $\lambda_1 > \lambda_2 > \cdots \lambda_M$. λ_1 is the largest or dominant eigenvalue and e_1 is the corresponding dominant eigenvector. Here we define the eigenspread of $\mathbf{R}_{xx}$ as the quantity λ_1/λ_M.

There are several factors that impact the eigenvalue distribution. We shall explore the relationships that exist between signal correlation, number of multipath components, and angle spread with the eigenvalue distribution of $\mathbf{R}_{xx}$.

In all of the simulations that follow, a four element uniform linear array is assumed with an element spacing of half a wavelength. Also, the variance of the additive noise is $\sigma_n^2 = 0.001$.

C.2 Multipath Correlation

First, consider the impact that correlation between multipath components has on the eigenvalues of $\mathbf{R}_{xx}$. Suppose that there are two multipath components, so that the received signal vector may be expressed,

$$\mathbf{x}(t) = \alpha_1(t)\mathbf{a}(\theta_1)s(t-\tau_1) + \alpha_2(t)\mathbf{a}(\theta_2)s(t-\tau_2) + \eta(t). \tag{C.2}$$

For convenience, let $s_1(t) = \alpha_1(t)s(t-\tau_1)$ and $s_2(t) = \alpha_2(t)s(t-\tau_2)$ and let $\mathbf{a}_1 = \mathbf{a}(\theta_1)$ and $\mathbf{a}_2 = \mathbf{a}(\theta_2)$. Then

$$\mathbf{x}(t) = \mathbf{a}_1 s_1(t) + \mathbf{a}_2 s_2(t). \tag{C.3}$$

Assuming that $s_1(t)$ and $s_2(t)$ are zero mean random processes, then the array correlation matrix is given by

$$\mathbf{R}_{xx} = \mathbf{a}_1\mathbf{a}_1^H \mathrm{E}\left\{|s_1(t)|^2\right\} + \mathbf{a}_1\mathbf{a}_2^H \mathrm{E}\left\{s_1(t)s_2^*(t)\right\} + \mathbf{a}_2\mathbf{a}_1^H \mathrm{E}\left\{s_1^*(t)s_2(t)\right\} + \mathbf{a}_2\mathbf{a}_2^H \mathrm{E}\left\{|s_2(t)|^2\right\} + \sigma_n^2\mathbf{I}_M \tag{C.4}$$

For convenience, let $\mathrm{E}\left\{|s_1(t)|^2\right\} = \mathrm{E}\left\{|s_2(t)|^2\right\} = 1$. Under this condition, then

$$\mathrm{E}\left\{s_1(t)s_2^*(t)\right\} = \rho \tag{C.5}$$

is the complex cross-correlation coefficient between $s_1(t)$ and $s_2(t)$. In general the value of $|\rho|$ will be dependent upon the signal delays $\tau_1(t)$ and $\tau_2(t)$, and the time varying nature of the path coefficients, $\alpha_1(t)$ and $\alpha_2(t)$.

The eigenvalues will dependent on the phase of ρ. To remove this dependence, for each value of $|\rho|$, the phase is integrated over $[0, 2\pi]$. Figure C.1 shows the two largest eigenvalues. The remaining two eigenvalues are equal to $\sigma_n^2 = .001$ Here it is assumed that $\theta_1 = 0$. The different colored curves are for various values of θ_2 as indicated in the legend. As expected when $|\rho|$ approaches one, then there is a single dominant eigenvalue. An interesting case occurs for $\theta_2 = 90$ degrees. In this case, $\mathbf{a}_1$ and $\mathbf{a}_2$ are orthogonal, and therefore when $|\rho| = 0$ then $\lambda_1 = \lambda_2$. One should note that the presence of a second significant eigenvalue indicates the presence of another mode of the received signal vector that the beamformer must apply a degree of freedom to for optimum performance. Figure C.2 is a plot of the average value $\frac{\lambda_1}{\lambda_2}$ versus $|\rho|$.

C.3 Number of Path Components and Angle Spread

In this section several simulations results are given that show the impact that the number of path components, the angle spread, and mean angle of arrival have on the eigenvalues of $\mathbf{R}_{xx}$. The simulations assume perfectly uncorrelated multipath the angle of arrival of which is selected from a Gaussian distribution with a standard deviation equal to the indicated angle spread. The results indicate that when uncorrelated multipath is present, the number of significant eigenvalues will equal the number of path components provided the array is not overloaded. Also it is shown that an increased angle spread tends to increase the eigenspread of R_{xx}. Figures C.3 through C.6 show the resulting eigenvalues versus angle spread obtained assuming

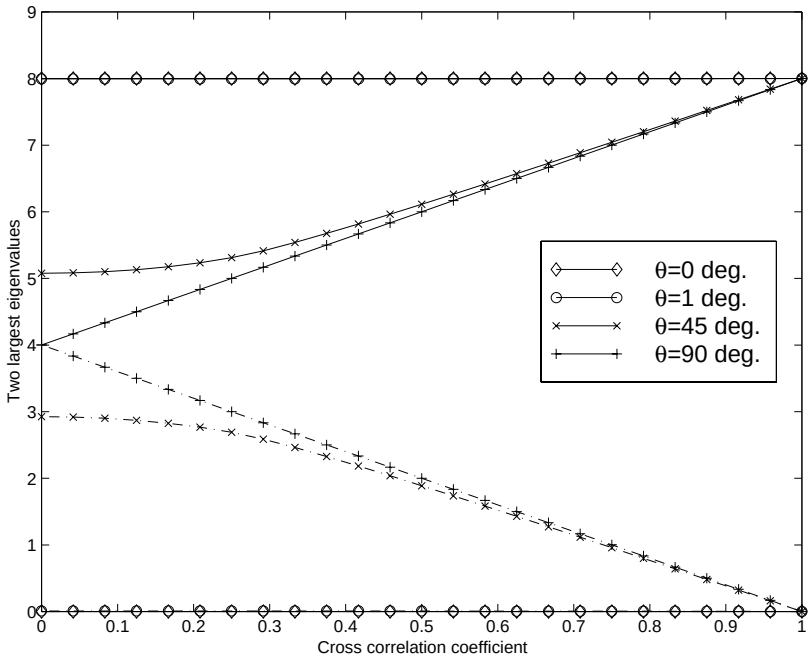

Figure C.1: Two largest eigenvalues of $\mathbf{R}_{xx}$ for two equal power multipath signals for various angles of arrival of the second path. The first path is broadside the array. The solid line is the dominant eigenvalue and the dashed line is the second largest eigenvalue.

unit power uncorrelated multipath. The value of θ_0 is the mean angle of arrival with respect to array broadside. As expected the eigenvalue spread decreases with an increase in angle spread, with an increase in the number of path components, and when the mean angle of arrival is closer to array broadside. All of these results are consistent with intuition regarding the correlation of fading envelopes in different environments. When correlation is low $\mathbf{R}_{xx}$ approaches an identity matrix and therefore the eigenvalues are nearly equal.

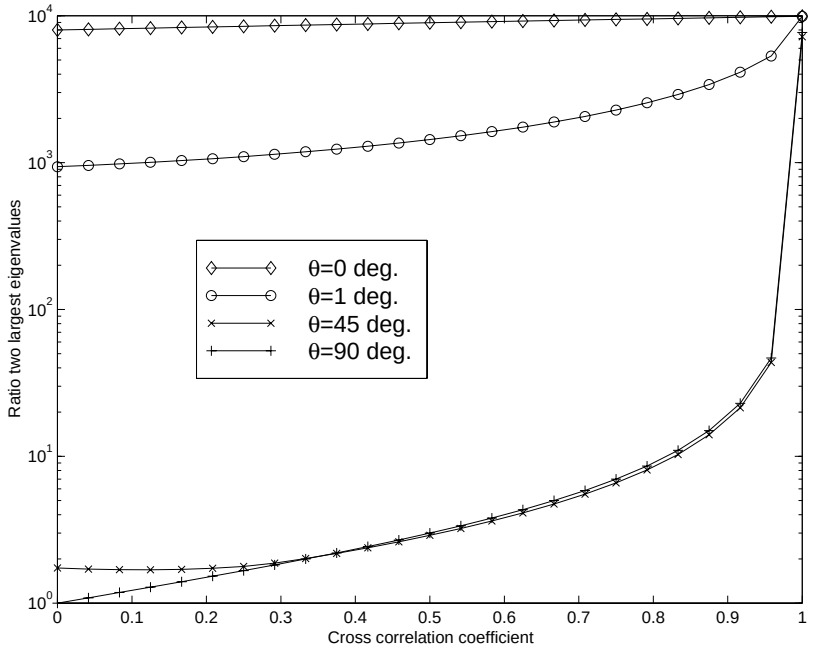

Figure C.2: Ratio of the two largest eigenvalues of $\mathbf{R}_{xx}$ for two equal power multipath signals for various angles of arrival of the second path. The first path is broadside the array.

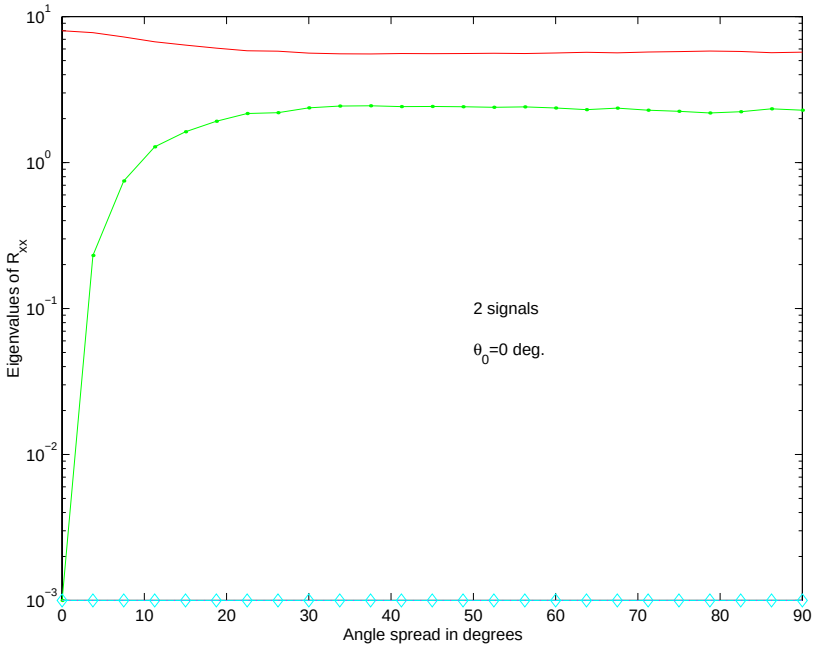

Figure C.3: Eigenvalues of $\mathbf{R}_{xx}$ with 2 unit power uncorrelated multipath components with a mean angle of arrival broadside the array versus angle spread.

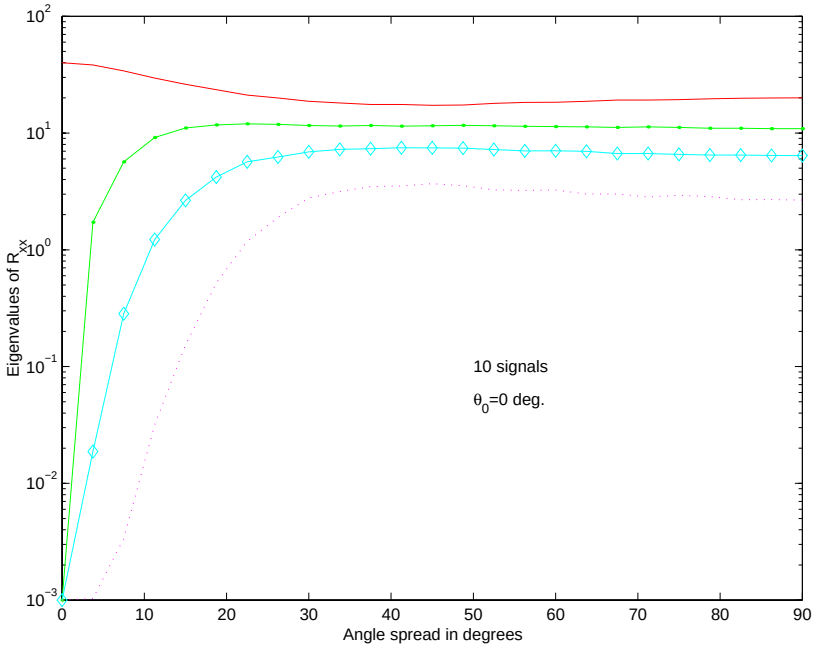

Figure C.4: Eigenvalues of $\mathbf{R}_{xx}$ with 10 unit power uncorrelated multipath components with a mean angle of arrival broadside the array versus angle spread.

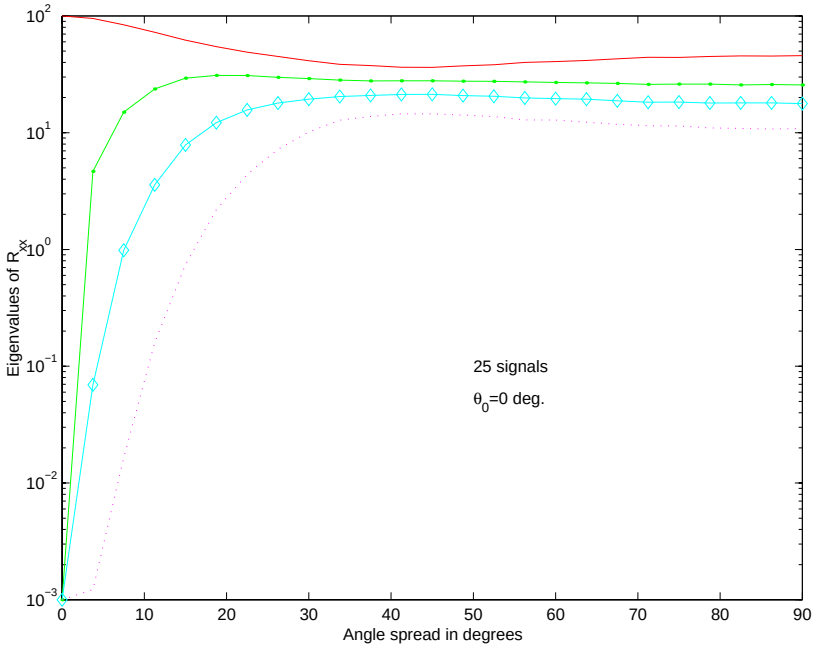

Figure C.5: Eigenvalues of $\mathbf{R}_{xx}$ with 25 unit power uncorrelated multipath components with a mean angle of arrival broadside the array versus angle spread.

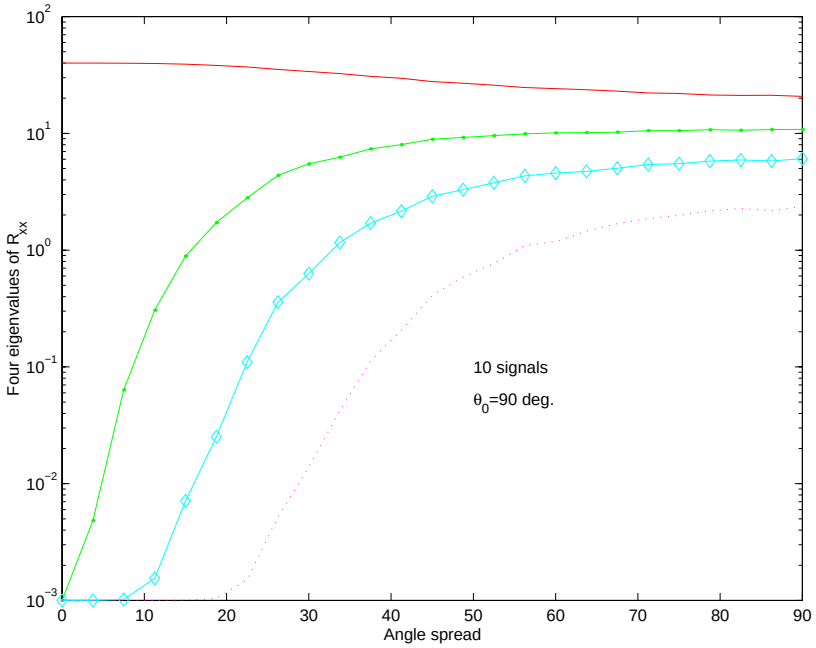

Figure C.6: Eigenvalues of $\mathbf{R}_{xx}$ with 10 unit power uncorrelated multipath components with a mean angle of arrival end-fire the array versus angle spread.

Bibliography

[1] D. H. Johnson and D. E. Dudgeon, *Array Signal Processing: Concepts and Techniques*. Englewood, New Jersey: Prentice Hall, 1993.

[2] R. Ertel, P. Cardieri, K. Sowerby, T. Rappaport, and J. Reed, "Overview of spatial channel models for antenna array communication systems," *IEEE Personal Communications Magazine*, pp. 10–22, Feb. 1998.

[3] J. Reed, R. Ertel, P. Cardieri, and T. Rappaport, "Vector channel models," *Fourth Workshop on Smart Antennas in Wireless Mobile Communications, Stanford University*, July 1997.

[4] R. B. Ertel and J. H. Reed, "Impact of path-los on the doppler spectrum for the geometrically based single bounce vector channel models," in *Proc., IEEE Veh. Tech. Conf.*, 1998.

[5] R. B. Ertel and J. H. Reed, "Angle and time of arrival statistics for the geometrically based single bounce vector channel models." accepted for publication in *IEEE Journal on Selected Areas in Communications*.

[6] R. B. Ertel, Z. Hu, and J. H. Reed, "Antenna array hardware amplitude and phase compensation
using baseband antenna array outputs," in *Proc., IEEE Veh. Tech. Conf.*, May 1999.

[7] D. K. Cheng, *Field and Wave Electronmagnetics*. New York: Addison-Wesley Publishing Company, 2nd ed., 1989.

[8] R. A. Monzingo and T. W. Miller, *Introduction to Adaptive Arrays*. New York: John Wiley & Sons, 1980.

[9] W. A. Gardner, ed., *Cyclostationarity in Communications and Signal Processing*. New York: The Institute of Electrical and Electronics Engineers, Inc., 1994.

[10] W. C. Jakes, ed., *Microwave Mobile Communications*. New York: IEEE Press, 1974.

[11] T. S. Rappaport, *Wireless Communications: Principles & Practice*. New York, New York: Prentice Hall PTR, 1996.

[12] W. C. Lee, *Mobile Communications Engineering: Theory and Applications*. McGraw-Hill, 2nd ed., 1997.

[13] J. D. Gibson, ed., *The Mobile Communications Handbook*. New York: IEEE Press, 1996.

[14] J. G. Proakis, *Digital Communications*. New York: McGraw-Hill Inc, second ed., 1989.

[15] J. Litva and T. K.-Y. Lo, *Digital Beamforming in Wireless Communications*. Boston: Artech House Publishers, 1996.

[16] C. W. Therrien, *Discrete Random Signals and Statistical Signal Processing*. Englewood, New Jersey: Prentice Hall, Inc., 1992.

[17] G. H. Golub and C. F. V. Loan, *Matrix Computations*. Baltimore: The John Hopkins University Press, 3 ed., 1996.

[18] A. Papoulis, *Probability, Random Variables, and Stochastic Processes*. New York: McGraw-Hill, Inc., 3rd ed., 1991.

[19] W. C. Y. Lee, *Mobile Cellular Telecommunications*. New York: McGraw Hill Publications, 1995.

[20] F. Tong and Y. Akaiwa, "Effects of beam tilting on bit-rate selection in mobile multipath channel," *IEEE Trans. Veh. Tech.*, vol. 46, pp. 257–261, May 1997.

[21] W. R. Braun and U. Dersch, "A physical mobile radio channel model," *IEEE Transactions on Vehicular Technology*, vol. 40, pp. 472–482, May 1991.

[22] A. J. Paulraj and C. B. Papadias, "Space-time processing for wireless communications," *IEEE Signal Processing Magazine*, pp. 49–83, Nov. 1997.

[23] A. J. Paulraj and B. C. Ng, "Space-time modems for wireless personal communications," *IEEE Personal Commun.*, pp. 36–48, Feb. 1998.

[24] J. C. Liberti, Jr. and T. S. Rappaport, *Analysis of CDMA Cellular Radio Systems Employing Adaptive Antennas*. PhD thesis, Virginia Polytechnic Institute and State University, Sept. 1995.

[25] J. C. Liberti and T. S. Rappaport, "A geometrically based model for line-of-sight multipath radio channels," in *Proc., IEEE Veh. Tech. Conf.*, pp. 844–848, Apr. 1996.

[26] P. Petrus, J. H. Reed, and T. S. Rappaport, "Geometrically based statistical channel model for macrocellular mobile environments," in *Proc., IEEE GLOBECOM*, pp. 1197–1201, 1996.

[27] P. Petrus, *Novel Adaptive Array Algorithms and Their Impact on Cellular System Capacity*. PhD thesis, Virginia Polytechnic Institute and State University, 1997.

[28] P. Petrus, J. H. Reed, and T. S. Rappaport, "Effects of directional antennas at the base station on the doppler spectrum," *Electronic Letters*, vol. 1, pp. 40–42, Mar. 1997.

[29] R. B. Ertel, "Statistical analysis of the geometrically based single bounce statistical channel models." unpublished notes, Apr. 1997.

[30] P. Zetterberg, "A downlink beam steering technique for GSM/DCS1800/PCS1900: Report version," tech. rep., Royal Institute of Technology, 1996.

[31] P. Zetterberg, P. Leth-Espensen, and P. Mogensen, "Propagation, beamsteering and uplink combining algorithms for cellular systems," *ACTS Mobile Communications Summit*, Nov. 1996. Royal Institute of Technology.

[32] P. Mogensen, P. Zetterberg, H. Dam, P. L. Espensen, S. L. Larsen, and K. Olesen, "Algorithms and antenna array recommendations," Tech. Rep. A020/AUC/A12/DR/P/1/xx-D2.1.2, Tsunami (II), September 1996.

[33] J. Blanz, P. Jung, and P. Baier, "A flexibly configurable statistical channel model for mobile radio systems with directional diversity," *AGARD SSP Symposium on Digital Communications Systems*, pp. 38.1–10, 1995.

[34] M. Lu, T. Lo, and J. Litva, "A physical spatio-temporal model of multipath propagation channels," in *Proc., IEEE Veh. Tech. Conf.*, 1997.

[35] J. S. Lee and L. E. Miller, "Error performance analysis of differential phase-shift-keyed/frequency-hopping spread-spectrum communication system in the partial-band jamming environments," *IEEE Transactions on Communications*, vol. COM-30, pp. 943–952, May 1982.

[36] W. C. Y. Lee, "Spectrum efficiency in cellular," *IEEE Transactions on Vehicular Technology*, vol. 38, pp. 69–75, May 1989.

[37] S. P. Stapleton, X. Carbo, and T. McKeen, "Spatial channel simulator for phased arrays," in *Proc., IEEE Veh. Tech. Conf.*, pp. 1789–1792, 1994.

[38] S. P. Stapleton, X. Carbo, and T. McKeen, "Tracking and diversity for a mobile communications base station array antenna," in *Proc., IEEE Veh. Tech. Conf.*, 1996.

[39] O. Norklit and J. B. Andersen, "Mobile radio environments and adaptive arrays," *PIMRC*, pp. 725–728, 1994.

[40] T. Fulghum and K. Molnar, "The Jake's fading model incorporating angular spread for a disk of scatterers," in *Proc., IEEE Veh. Tech. Conf.*, pp. 489–493, 1998.

[41] G. G. Raleigh and A. Paulraj, "Time varying vector channel estimation for adaptive spatial equalization," *Globecom*, pp. 218–224, 1995.

[42] D. Asztely, "On antenna arrays in mobile communication systems: Fast fading and GSM base station receiver algorithms," tech. rep., Royal Institute of Technology, Stockholm, Sweden, Mar. 1996. Royal Institute of Technology.

[43] Q. Spencer, M. Rice, B. Jeffs, and M. Jensen, "A statistical model for angle of arrival in indoor multipath propagation," in *Proc., IEEE Veh. Tech. Conf.*, 1997.

[44] Q. Spencer, M. Rice, B. Jeffs, and M. Jensen, "Indoor wideband time / angle of arrival multipath propagation results," in *Proc., IEEE Veh. Tech. Conf.*, 1997.

[45] B. P. Lathi, *Modern Digital and Analog Communication Systems*. Philadelphia: Holt, Rinehart and Winston, Inc., 2nd ed., 1989.

[46] G. B. Thomas, Jr. and R. L. Finney, *Calculus and Analytic Geometry*. New York: Addison-Wesley Publishing Company, 7th ed., 1988.

[47] F. Kronestedt, "A study of local scattering," Tech. Rep. T/B 94:050, Ericsson, 1994.

[48] D. R. Lide, ed., *Handbook of Chemistry and Physics*. Boston: CRC Press, Inc., 71st ed., 1990.

[49] A. L. Swindlehurst, S. Daas, and J. Yang, "Analysis of a decision directed beamformer," *IEEE Trans. Signal Proc.*, vol. 43, pp. 2920–2927, Dec. 1995.

[50] D. F. Breslin and J. H. Reed, "Adaptive antenna arrays applied to position location," Master's thesis, Virginia Tech, Aug. 1997.

[51] B. Ng, M. Er, and C. Kot, "Array gain/phase calibration techniques for adaptive beamforming and direction finding," in *IEE Proceedings - Radar, Sonar and Navigation*, vol. 141, Feb. 1994.

[52] F. McCarthy, R. Ridgway, and A. Paulraj, "Fast techniques for sensor array calibration," in *Asilomar Conference on Signals, Systems and Computers* (A. Singh, ed.), vol. 1, pp. 688–693, IEEE Comput. Soc. Press; Los Alamitos, CA, 1994.

[53] B. D. Steinberg, "The radio camera: Imaging with large aberrant arrays," in *Asilomar Conference on Signals, Systems and Computers* (D. Etter, ed.), pp. 78–81, IEEE Comput. Soc. Press; Washington, DC, 1987.

[54] B. Kang, H. M. Subbaram, and B. D. Steinberg, "Improved adaptive-beamforming target for self-calibrating a distorted phased array," *IEEE Transactions on Antennas and Propagation*, vol. 38, pp. 186–194, Feb. 1990.

[55] E. Baranoski and A. Steinhardt, "Localized subspace projection," *IEEE International Conference on Acoustics, Speech, and Signal Processing*, vol. 4, pp. 344–347, 1993.

[56] F. G. Robey and E. J. Baranoski, "Full space-time clutter covariance estimation," *IEEE International Conference on Acoustics, Speech, and Signal Processing*, vol. 3, pp. 1896–1899, 1995.

[57] G. V. Tsoulos and M. A. Beach, "Calibration and linearity issues for an adaptive antenna system," in *Proc., IEEE Veh. Tech. Conf.*, 1997.

[58] C. Passmann, G. Villino, and T. Wixforth, "A polarization plexible phased array antenna for a mobile communication sdma field trial," in *1997 IEEE MTT-S International Microwave Symposium Digest* (G. Koepf, ed.), vol. 2, pp. 595–598, IEEE; New York, NY, June 1997.

[59] J. S. Colburn, Y. Rahmat-Samii, M. A. Jensen, and G. J. Pottie, "Evaluation of personal communications dual-antenna handset diversity performance," *IEEE Trans. Veh. Tech.*, vol. 47, pp. 38.1–10, Aug. 1998.

[60] D. J. Y. Lee and C. Xu, "Capacity and trunking efficiency of smart antenna," in *Proc., IEEE Veh. Tech. Conf.*, 1997.

[61] J. N. Pierce and S. Stein, "Multiple diversity with nonindependent fading," *Proc. IRE*, pp. 89–104, 1960.

[62] M. T. Feeney and J. D. Parsons, "Cross-correlation between 900 MHz signals received on vertically separated antennas in small-cell mobile radio systems," *Proc. IEEE*, vol. 138, pp. 81–86, Apr. 1991.

[63] P. Eggers, J. Toftgard, and A. Oprea, "Antenna systems for base station diversity in urban small and micro cells," *IEEE J. Select. Areas Commun.*, vol. 7, pp. 1046–1057, Sept. 1993.

[64] M. LeFevre, M. A. Jensen, and M. D. Rice, "Indoor measurement of handset dual-antenna diversity performance," in *Proc., IEEE Veh. Tech. Conf.*, 1997.

[65] F. Adachi, M. T. Feeney, A. G. Williamsom, and J. D. Parsons, "Crosscorrelation between the envelopes of 900 MHz signals received at a mobile radio base station site," *IEE Proceedings*, vol. 133, pp. 506–512, Oct. 1986.

[66] W. C. Y. Lee, "Effects on correlation between two mobile radio base-station antennas," *IEEE Transactions on Vehicular Technology*, vol. COM-21, pp. 1214–1224, Nov. 1973.

[67] A. M. D. Turkmani, A. A. Arowojolu, P. A. Jefford, and C. J. Kellett, "An experimental evaluation of the performance of two-branch space and polarization diversity schemes at 1800 MHz," *IEEE Trans. Veh. Tech.*, vol. 44, pp. 318–326, May 1995.

[68] R. G. Vaughan and N. L. Scott, "Closely spaced monopoles for mobile communications," *Radio Science*, vol. 28, pp. 1259–1266, Nov.-Dec. 1993.

[69] K. Tsunekawa and K. Kagoshima, "Diversity performance analysis of two parallel dipole antennas mounted on a small metal body," *Electronics and Communications in Japan, Part 1*, vol. 76, no. 10, pp. 80–90, 1993.

[70] M. G. Douglas, M. Okoniewski, and M. A. Stuchly, "A planar diversity antenna for handheld PCS devices," *IEEE Trans. Veh. Tech.*, vol. 47, pp. 38.1–10, Aug. 1998.

[71] G. Xu, H. Liu, W. J. Vogel, H. P. Lin, and S. S. J. ang G. W. Torrence, "Experimental studies of space-division-multiple-acess schemes for spectral efficient wireless communications," in *Proc., IEEE Int. Conf. on Commun.*, May 1994.

[72] L. Bigler, H. Lin, S. Jeng, and G. Xu, "Experimental direction of arrival and spatial signature measurements at 900 MHz for smart antenna systems," in *Proc., IEEE Veh. Tech. Conf.*, vol. 1, (USA), pp. 55–58, IEEE; New York, NY, USA, 1995.

[73] S. S. Jeng, H. P. Lin, G. Xu, and W. J. Vogel, "Measurements of spatial signature of an antenna array," *IEEE International Symposium on Personal, Indoors and Mobile Radio Communications*, vol. 2, pp. 669–672, Sept. 1995.

[74] J. C. Liberti, "Measuring and modeling spatial radio channels for smart antenna systems," *submitted to Antennas and Propagation Society Conference*, June 1998.

[75] J. Salz and J. H. Winters, "Effect of fading correlation on adaptive arrays in digital mobile radio," *IEEE Transactions on Vehicular Technology*, vol. 43, pp. 1049–1057, Nov. 1994.

[76] J. Laiho-Steffens and A. Wacker, "Experimental evaluation of the two-dimensional mobile propagation environment at 2 GHz," in *Proc., IEEE Veh. Tech. Conf.*, pp. 2070–2074, 1997.

[77] G. D. Durgin and T. S. Rappaport, "Effects of multipath angular spread on the spatial cross-correlation of received voltage envelopes," in *Proc., IEEE Veh. Tech. Conf.*, 1999.

[78] P. C. F. Eggers, "Angular dispersive mobile radio environments sensed by highly directive base station antennas," *IEEE International Symposium on Personal, Indoors and Mobile Radio Communications*, vol. 2, pp. 522–526, Sept. 1995.

[79] J. B. Andersen, P. E. Mogensen, F. Frederiksen, K. Pedersen, and P. Leth-Espensen, "Propagation aspects of interference cancellation," *Fifth Workshop on Smart Antennas in Wireless Mobile Communications*, July 1998.

[80] J. Kenneday and S. Ellingson, "Smart antenna testbed for mobile wireless systems," in *Proc., Virginia Tech Symp. on Wireless Personal Commun.*, pp. (2–1)–(2–12), 1996.

[81] J. Kenneday, P. Harvey, M. Sullivan, and R. Minthorne, "Characterization of the cellular radio environment," *Microwave Journal*, p. 80, 1996.

[82] P. E. Mogensen, K. I. Pedersen, P. Leth-Espensen, B. Fleury, F. Frederiksen, K. Olesen, and S. L. Larsen, "Preliminary measurement results from an adaptive antenna array testbed for GSM/UMTS," in *Proc., IEEE Veh. Tech. Conf.*, vol. 3, pp. 1592–1596, 1997.

[83] J. Fuhl, J.-P. Rossi, and E. Bonek, "High-resolution 3-d direction-of-arrival determination for urban mobile radio," *IEEE Trans. Antennas and Propagation*, vol. 45, pp. 672–682, Apr. 1997.

[84] J.-P. Rossi, J.-P. Barbot, and A. J. Levy, "Theory and measurement of the angle of arrival and time delay of UHF radiowaves using a ring array," *IEEE Trans. Antennas and Propagation*, vol. 45, pp. 876–884, May 1997.

[85] K. Kalliola and P. Vainikainen, "Characterization system for radio channel of adaptive array antennas," in *Proc., IEEE PIMRC*, vol. 1, pp. 95–99, 1997.

[86] A. Klein, W. Mohr, R. Thomas, P. Weber, and B. Wirth, "Direction-of-arrival of partial waves in wideband mobile radio channels for intelligent antenna concepts," in *Proc., IEEE Veh. Tech. Conf.*, pp. 849–853, 1996.

[87] D. Adams, C. Ward, M. Smith, A. Jeffries, J. Hudson, and F. Overbury, "Macrocellular angle-of-arrival and delay propagation characteristics and their impact on smart antenna design and performance," *10th International Conf. On Antennas and Propagation*, pp. 2.129–2.131, Apr. 1997.

[88] H. J. Thomas, T. Ohgan, and M. Mizuno, "A novel dual antenna measurement of the angular distribution of received waves in the mobile radio environment as a function of position and delay time," *Proceedings IEEE Vehicular Technology Society*, vol. 1, pp. 546–549, 1992.

[89] J. H. Winters, "Smart antennas for wireless systems," *IEEE Personal Commun.*, pp. 23–27, Feb. 1998.

[90] D. Gerlach and A. Paulraj, "Base station transmitter antenna arrays with mobile to base feedback," in *Asilomar Conference*, pp. 1432–1436, 1993.

[91] D. Gerlach and A. Paulraj, "Adaptive transmitting antenna arrays with feedback," *IEEE Signal Processing Letters*, vol. 1, pp. 150–152, Oct. 1994.

[92] D. Gerlach and A. Paulraj, "Adaptive transmitting antenna methods for multipath environments," *IEEE Globecom*, pp. 425–429, 1994.

[93] J. H. Winters, C. C. Martin, and N. R. Sollenberger, "Forward link smart antennas and power control for IS-136," in *Proc., IEEE Veh. Tech. Conf.*, 1998.

[94] P. Zetterberg and B. Ottersten, "The spectrum efficiency of a basestation antenna array system for spatially selective transmission," *IEEE Transactions on Vehicular Technology*, vol. 44, pp. 651–660, Aug. 1994.

[95] P. Zetterberg and B. Ottersten, "The spectrum efficiency of a basestation antenna array system for spatially selective transmission," tech. rep., Royal Institute of Technology, 1994.

[96] P. Zetterberg, "On base station antenna array structures for downlink capacity enhancement in cellular mobile radio," tech. rep., Royal Institute of Technology, 1996.

[97] P. Zetterberg, "A comparison of two systems for down link communication with antenna arrays at the base," *IEEE Wireless Communicaiton Systems Symposium*, 1995.

[98] P. Zetterberg, "A downlink beam steering technique for GSM/DCS1800/PCS1900: Report version," tech. rep., Royal Institute of Technology, 1996.

[99] C. Farsakh and J. A. Nossek, "Channel allocation and downlink beamforming in an SDMA mobile radio system," in *Proc., IEEE PIMRC*, vol. 2, pp. 687–691, 1995.

[100] J. Goldberg and J. R. Fonollosa, "Downlink beamforming for cellular mobile communications," in *Proc., IEEE Veh. Tech. Conf.*, 1997.

[101] P. Zetterberg, H. Dam, F. Fredreksen, S. L. Larsen, P. L. Espensen, P. Mogensen, and K. Olesen, "Experimental investigation of capacity and quality enhancement of GSM using adaptive beamforming," in *Nordic Radio Seminar*, Aug. 1996.

[102] S. Haykin, *Adapive Filter Theory*. Upper Saddle River, New Jersey: Prentice Hall, third ed., 1996.

Publications

- Richard B. Ertel, *Spatial Filtering with Adaptive Antenna Array Algorithms in DS-CDMA Communications Systems*, M.S. Thesis, Pennsylvania State University, 1996.
- Richard B. Ertel and Stephan V. Schell, "Comparative Study of Adaptive Antenna Arrays in CDMA Communication Systems," *Virginia Tech's Sixth Symposium on Wireless Personal Communications*, pp. 10.1-12 , June 1996.
- Jeffrey Reed, Richard Ertel, Paulo Cardieri, and Theodore Rappaport, "Vector Channel Models," *Fourth Workshop on Smart Antennas in Wireless Mobile Communications*, Stanford University, July 24-25, 1997.
- R. B. Ertel, P. Cardieri, K. Sowerby, T.S. Rappaport, and J. H. Reed, "Overview of Spatial Channel Models for Adaptive Array Communication Systems," *IEEE Personal Communications Magazine*, pp. 10-22, Feb. 1998.
- Richard B. Ertel and Jeffrey H. Reed, "Impact of Path-loss on the Doppler Spectrum for the Geometrically Based Single Bounce Vector Channel Models," *Vehicular Technology Conference*, May 1998.
- P. Petrus, R. Ertel , and J. Reed, "Capacity Improvement Using Adaptive Arrays in an AMPS System," *IEEE Trans. on Vehicular Tech.*, vol. 47, no. 3, pp. 717-727, Aug. 1998.
- R. Ertel and J. Reed, "Generation of Two Equal Power Correlated Rayleigh Fading Envelopes," *IEEE Communications Letters*, Oct. 1998.
- Richard B. Ertel and Jeffrey H. Reed, "Angle and Time of Arrival Statistics for the Geometrically Based Single Bounce Vector Channel Models," accepted for publication in *IEEE Journal on Selected Areas in Communications*.
- Richard B. Ertel, Zhong Hu, and Jeffrey H. Reed, "Antenna Array Hardware Amplitude and Phase Compensation Using Baseband Antenna Array Outputs," *Vehicular Technology Conference*, May 1999.

Vita

Richard B. Ertel was born on March 9, 1971, in Allentown, Pennsylvania. He received his Associate of Arts in Engineering from Harrisburg Area Community College in 1991 with highest distinction. He then received his B.S.E.E. with highest honors and M.S.E.E. degrees from Penn State University in May 1993 and May 1996, respectively. He is currently a Bradley Fellow and research assistant at Virginia Tech where he is working at the MPRG with Dr. Jeff Reed on vector channel models and adaptive antenna arrays.

His work at Penn State included a research assistantship at the Applied Research Lab in the summer of 1996 working on source localization. In the summer of 1997 he worked for Southwestern Bell Technology Resources as a technical intern evaluating and implementing vector channel models.